University of Cape Town,
Hydrometallurgy Laboratory
Department of Chemical Engineering

A STUDY OF THE DECAY OF ACID CATIONIC ION EXCHANGE RESIN

University of Cape Town

By:

Allan Bernard Nesbitt

Supervisor:
Prof. Jochen Petersen

2016

Submitted in fulfilment of the requirements for the degree of Doctorate of Philosophy in Chemical Engineering at the Department of Chemical Engineering in the Faculty of the Built Environment

The copyright of this thesis vests in the author. No quotation from it or information derived from it is to be published without full acknowledgement of the source. The thesis is to be used for private study or non-commercial research purposes only.

Published by the University of Cape Town (UCT) in terms of the non-exclusive license granted to UCT by the author.

University of Cape Town

ACKNOWLEDGEMENTS

Thanks to my family Lee Nesbitt, Allan Michael, Nicholas John and Oliver William without whose support this would not have been possible.

Thanks to Matukela Maloka who took part in much of the test work, for all his efforts and patience.

Thanks to my supervisor Professor Jochen Petersen for his excellent support and patience and to Professor Jean-Paul Franzidis and the Minerals to Metals initiative for the kind financial support.

Thanks to Ms Johanna Van Deventer of Purolite® for her kind assistance and the supply of ion exchange resins used in this study.

DECLARATION

I, Allan Bernard Nesbitt, hereby declare that the work on which this thesis is based is my original work (except where acknowledgements indicate otherwise) and that neither the whole work nor any part of it has been, is being, or is to be submitted for another degree in this or any other university. I authorise the University to reproduce for the purpose of research either the whole or any portion of the contents in any manner whatsoever.

Signature: Date: 1/10/2016

ABSTRACT

A study was undertaken on the decay of acid ion exchange resin from both a qualitative and quantitative perspective. The qualitative study concentrated on observing the impact on resin strength of varying electrolyte concentrations and varying di-vinyl benzene contents, during the loading phase. The phenomenon of osmotic shock in addition to resin cracking and swelling is clearly observed. A further qualitative study bore out the change in resin rigidity as the resin is artificially degraded through repeated loadings and regenerations performed by using a specially constructed device that cyclically loads and regenerates resin up to 1000 times in a three week period. Loss of resin rigidity was observed under these circumstances and was measured by means of observing changes in degree of swelling/contraction and changes in translucence.

Quantitative study of the resin was limited to its characterisation through measurement of the equilibrium through the Mass-Action Law, capacity and resin kinetics. A study, of existing kinetic rigorous modelling methods and in particular the extensively published challenge of the multiple mechanism adsorption process, was undertaken. A rigorous model, that divorces the external and internal mass-transport parameters from the traditionally utilised lumped parameter, is proposed. All kinetic measurements were performed in a 1 litre closed circuit (finite system) consisting of a variable-pump, a five mL zero length column (ZLC) and a reservoir, allowing for the insertion of probes and sample extraction.

An original method of model simulation for the purposes of fitting to kinetic data was developed and consists of determining the resin surface concentration from flux data assuming the applicability of Newton's Law of Cooling to the ionic flux through the external laminar layer. Simulation of flux inside the resin was achieved by assuming an internal homogeneous environment and the applicability of the Nernst-Plank equation that combines transport effects of both Fick's Law of Diffusion and inter-ion electrical forces to the flux of both the adsorbing and desorbing ions simultaneously, during the transient adsorption process.

The parameters of the rigorous model are the intra-particle diffusion of both the adsorbing and desorbing ions ($\boldsymbol{D_i}$, $\boldsymbol{D_D}$) in addition to the mass transfer coefficient ($\boldsymbol{K_L}$) in the laminar layer at the surface at the resin/liquid interface. A full simulator was produced using Turbo Pascal software which was fitted to raw kinetic data using the Hook-Jeeves search algorithm.

After successfully fitting the simulation to fresh resin kinetic data and attaining reasonable parameter values that altered with turbulence and di-vinyl benzene content, the simulation was then fitted to kinetic data of decayed resin and changes in these parameters were observed as the resin aged.

While the mass transfer coefficient in the laminar dynamic layer was observed to only be affected by turbulence, the intra-particle diffusivity of the adsorbing ion was observed to increase with decay-induced decreased steric state inside the resin. The measured parameters changed as expected and therefore effectively explained the decay induced changes of the steric environment within the resin. Further the change in steric state of the decayed resin was also confirmed by both developed techniques; i.e. change in swelling/contraction and translucence. To confirm repeatability of these results two resin decay campaigns were undertaken in which resin was cycled 800 times with capacity and kinetic tests, at three different ZLC through pump rates being carried out every 100 cycles, with both achieving identical results.

From the fitting of the simulator to both fresh and decayed resin, it was observed that the intra-particle diffusivity of the desorbing ion ($\boldsymbol{D_D}$) seemed to have little effect on the fitting process with the Hook-Jeeves algorithm generally determining a value of at least three orders of magnitude higher than that of the adsorbing ion ($\boldsymbol{D_i}$). By establishing a boundary for the desorbing ion diffusivity, at approximately 3 orders of magnitude higher than the adsorbing ion diffusivity, it was found that PPMC fits of the simulator to the raw data were already good (PPMC > 0.99) based on the maxima achieved on the other two parameters.

The method proposed in this study of measuring the changes of resin parameters during decay, can be used in a rigorous simulation of the life cycle of any particular acid resin and could then be used as a useful tool for designers of contacting equipment to determine resin life expectancy in a particular application. This method is attractive as it can be carried out quickly and cheaply negating the necessity to carry out costly pilot plant studies.

CONTENTS

LIST OF SYMBOLS

a	Resin surface area (m^2)
B	Beginning concentration of adsorbing ions bulk solution (*mol/L*)
$\overline{C_T}$	Total specific concentration of active sites in the resin (*equiv./L*)
$\overline{C_A}, \overline{C_B}, \overline{C_C}$	Concentrations of species A, B, C inside the resin (*mol/L*)
$C_{D,t=0}$	Concentration of desorbing ion in solution at $t = 0$ (*mol/L*)
$C_{D,t=\infty}$	Concentration of desorbing ion in solution at $t = \infty$ (*mol/L*)
$\overline{C_D}$, C_D	Concentrations of the desorption ion in resin and liquid (*mol/L*)
$\overline{C_{i,avg}}$	Average concentration of i throughout the bead (*mol/L*)
$C_{i,bulk}$	Concentration of adsorbate in bulk solution (*mol/L*)
C_i^*	Concentration of adsorbate in solution at the resin surface (*mol/L*)
$\overline{C_i}$, C_i	Concentrations of the adsorption ion in resin and liquid (*mol/L*)
C_i^f, C_i^{eff}	Concentration of column influent and effluent (*mol/L*)
$C_{i,P}^{t+\Delta t}$	**C**oncentration in the shell being balanced at $t + \Delta t$ *(mol/L)*
$C_{i,P}^{t}$	**C**oncentration in the shell being balanced at t *(mol/L)*
$C_{i,P}^{t+\Delta t}, C_{i,P}^{t}$	**C**onc. in the shell of interest at $t + \Delta t$ and t respectively (*mol/L*)
$C_{i,O}^{t+\Delta t}, C_{i,O}^{t}$	Conc. outer shell to interest shell $t + \Delta t$ and t respectively (*mol/L*)
$C_{i,I}^{t+\Delta t}, C_{i,I}^{t}$	Conc. inner shell to interest shell $t + \Delta t$ and t respectively (*mol/L*)
$\overline{C_{i,sur}}$	Concentration of adsorbing ion in resin matrix at surface (*mol/L*)
D_{app}	Apparent diffusivity from Nernst Plank equation (m^2/s)
$D_{app,pi}$	Apparent diffusivity to inside shell from interest shell (m^2/s)
$D_{app,po}$	**A**pparent diffusivity to outside shell from interest shell (m^2/s)
D_i, D_D	Intrinsic diffusivity of adsorbing and desorbing ion (m^2/s)
$D_{i,D}$	Common adsorbing and desorbing diffusivity (m^2/s)
D_L	Free aqueous solution diffusivity (m^2/s)
E	End concentration of adsorbing ions in bulk solution (*mol/L*)
Err	Degree of error from optimum point (%) Equ.3-38
f	Volume fraction of the resin in the bed (dimensionless)
F	Faraday's constant (96 485 *C/mol*)
FWSR	Free Wet Settled Resin volume i.e. allowed settling naturally (*L*)
J_D, J_i	Mol flux of the desorbing, adsorbing ion respectively ($mol/dm^2.s$)
$J_{diff,i}, J_{diff,D}$	Mol flux caused by conc. gradients ad- , desorbing ions ($mol/dm^2.s$)
$J_{el,i}, J_{el,D}$	Mol flux caused by charge cloud for ad-, desorbing ions ($mol/dm^2.s$)
k_f, k_r	Forward and reverse rate constants respectively ($dm^3/mol.s$)
K_f	Overall mass transfer coefficient ($m^{-2}.s^{-1}$) Equ.2-9

K_L	Mass transfer coefficient (*m/s*)
K_0	Constant which can be equated to $Ln\left[N_i^a\right]_{t=0}$
K_1	Rate constant (s^{-1}) Equ.3-10
K_{sp}	Solubility constant (dimensionless)
L	Length of the column (*m*)
N_A	Specific Mass flux ($mol/dm^2.s$)
N_i	Flux of adsorbing ion across the interface ($mol/dm^2.s$)
N_i^a	Flux calculated from measured bulk concentrations ($mol/dm^2.s$)
N_{NaOH}	Concentration of NaOH titrant (*mol/mL*)
N_R	Number of resin beads (*dimensionless*)
O_{PPMC}	Optimum point PPMC value (dimensionless) Equ.3-38
P_{PPMC}	PPMC value at offset increment (dimensionless) Equ.3-38
Q	Capacity of resin (*equiv./L*) (*L of FWSR*)
R	Radius of the resin beads (*dm*)
R	Universal gas constant (8.314 *J/mol.K*)
r	Radial distance to the point mass balance is applied (*dm*)
r_{ib}	Radial distance to the inner boundary of the shell being balanced *(dm)*
r_{ob}	Radial distance to the outer boundary of the shell being balanced *(dm)*
r_{MI}	Radial distance to middle of inside shell to shell of interest *(dm)*
r_{MP}	Radial distance to middle of shell of interest (*dm*)
r_{MO}	Radial distance to middle of shell on outside of shell of interest *(dm)*
S	Magnitude of steric hindrance induced by crosslinking
T	Temperature (*K*)
t	Time *(s)*
Δt	Advance in time increment *(s)*
u	Volumetric flow rate of liquid through column (*mL/min*)
V	Linear superficial velocity (*dm/s*)
$\overline{V}$	Volume of resin (*L*)
V_C	Volume of bulk solution (m^3)
V_{blank}	Volume of NaOH added to neutralise the blank in titration (*mL*)
V_{NaOH}	Volume of NaOH added to neutralise the sample in titration (*mL*)
w	Is the sign (±) of the immovable charges (dimensionless)
W	Equilibrium factor (dimensionless) Equ.2-7
x_f	Mol fraction of solvent ≈ 1 in dilute solutions (*dimensionless*)
X_D	Equivalent mass fraction of desorbing ion in resin (dimensionless)

X_i	Equivalent mass fraction of adsorbing ion in resin (dimensionless)
Y_i	Molar mass fraction of adsorbing ion in resin (dimensionless)
Y	Calculated grey scale intensity value (dimensionless) (*0 – 214)*
z	Laminar layer thickness (*m*)
z_i, z_D	Valence of adsorbing and desorbing ion (*dimensionless*)
z_A, z_B, z_C	Valence of ions A, B, C inside the resin matrix (*dimensionless*)

Greek symbols

α	Equilibrium constant for the Mass-Action-Law (*dimensionless*)
β	Proportionality constant (dimensionless) Equ.2.11
δ	Ratio of adsorbing ion to desorbing ion diffusivity (dimensionless)
ε	Resin bed voidage (dimensionless)
φ	Charge cloud electrical potential (*J/C*)
μ	Fluid viscosity (*Pa.s*)
ρ	Fluid density (kg/m^3)
Γ	Fractional attainment of equilibrium Equ.2-6

Dimensionless numbers

Re	Reynolds Number	$[\rho(2\mathrm{R})V]/[\mu(1-\varepsilon)]$
Sh	Sherwood Number	$K_L 2\mathrm{R}/D_L$
Sc	Schmidt Number	$\mu/\rho D_L$

The dimensions of the given variables can vary in magnitude with application e.g. m^2/s can be dm^2/s in some instances.

LIST OF FIGURES

Campaign I

Campaign II

Combined Campaigns

LIST OF TABLES

1. INTRODUCTION

There are two types of ion exchange resin application, 1) demineralisation/purification and 2) mineral recovery through selective recovery and concentration. Although both are identical processes, the fundamental difference is in the product that is considered important, either the ions being absorbed, or the solution from which the ions have been absorbed. The resin represents a base or acid in solid particulate form that, after ad-sorption of ions from a solution, can be physically removed, thus allowing for recovery/regeneration in a separate solution.

1.1. Water purification

The application of ion exchange technology to water purification is a well-established process with a long history. The key challenge is to achieve very high efficiency of ion removal, invariably by means of using a combination of general purpose strong cationic resin followed by weak anionic resin, resulting in de-ionised water that has a necessary but limited use in industry, mostly as feed for steam plants. Paradoxically, the regeneration of the ion exchange resins requires use of strong acid and base solutions followed by neutralisation of the spent regenerant that in turn results in a concentrated electrolyte that requires disposal. In most cases the cheapest reagents for regeneration are sulphuric acid and lime, which results in the production of impure gypsum. It therefore can be stated that using ion exchange resin for treating foul water to make it potable or for desalination purposes is not ideal.

Of greater practical application are resins that reduce the hardness of water, i.e. remove calcium or magnesium and the associated anion. However, in specific cases if there are particular contaminants in the water e.g. arsenic, mercury, cadmium, nitrates, sulphates, iron, manganese, organics etc. resins can be used for selective removal. Removing these makes the water at least fit for release into a catchment basin or for further processing by more conventional means.

1.2. Recovery of minerals

The application of ion exchange resins to mineral recovery is a more recent development than water purification, with its earliest and most successful application being the recovery of uranium in the 1950s. Only from the 1980s do we find advances in ion exchange resin technology that resulted in the manufacture of complex resins that allow for application to specific types of mineral recovery, e.g. Minix and Aurex specifically manufactured for the recovery of gold.

After leaching the solution containing the metal ion is contacted with an appropriate resin type. There is no necessity to clarify the solution as the ore solids are generally < 100 µm while the resin particles are > 300 µm, allowing for the physical separation of the resin from the mineral slurry by screening. Examples of metals recovered in this manner are zinc at Anglo Platinum's base metal refinery in Rustenburg, South Africa and uranium at Rossing Uranium in Swakopmund, Namibia.

The use of ion exchange resin technology in mineral recovery is currently undergoing a renaissance. The nature of ion exchange resin, in that it is easily added to and removed from solution/slurry, lends itself to modularization of the process, and therefore application in remote areas where there is limited infrastructure and expertise, becomes attractive. There is general consensus that the management of water usage in a resin plant is vital. As the process is strictly driven by concentration gradients, and in the case of regeneration/elution the required gradients generally need to be high, the removal of excess regenerates is of paramount importance before returning the resin to an adsorption cycle. This can only be achieved by excess water usage which will have to be recycled to ensure plant efficiency.

However, as already mentioned, a difficulty with ion exchange technology is water management. The removal of excess regeneration-solution requires excessive wash water that can only be managed by a diligent water audit. In addition the brittle nature of the resin material can result in physical attrition as it passes through mechanical machinery such as screens, mixers or pumps. Resin decay via chemical attrition is also a challenge, particularly if the resin is exposed to powerful oxidizing solutions as is used in some regeneration processes.

Resin has advantages over other separation technologies such as activated carbon adsorption and solvent extraction (SX). Being entirely synthetic, the possibility of resins being made ion-specific is an advantage over activated carbon. Also the flammable nature of the solvents used in solvent extraction carries a high safety risk, requiring the installation of sophisticated fire protection systems.

Higher levels of expertise are also required to operate SX plants due to the complexity of the unit operation. In addition, the nature of solvent extraction contactors, which are generally set up in banks of smallish, efficient, alternating mixer/settler units, are only scaled up through replication. None of these challenges are present in ion exchange resin technology.

Another difficulty that ion exchange resin technology faces is the conservative nature of the mining industry, and it will be necessary to overcome a great deal of characteristic inertia that is commonly found with respect to the assimilation of new technologies. This may be due in part to evidence that resin can be poisoned or exhibit signs of decay/aging during the normal cyclic duty - a challenge that this thesis seeks to address. This is all the more acute when considering that, unfortunately, the cost of new resins is high when compared to existing technologies (activated carbon and solvent extraction), the greater expense being connected to the cost of purpose-specific resin development that has to be paid off.

1.3. Problem statement

During the design stage of an ion exchange plant there are normally three parties. The resin manufacturer who claims the superior performance of his resin, the design engineer who designs the contacting equipment to be used in a specific process and the client that risks the capital and eventually owns the process and any profits that will be forthcoming. Process feasibility and optimisation is not something the resin manufacturer will commit to, as he will argue that he has no say over the operation of the envisaged process, although he may have some experience with generic processes.

The design engineers will almost always require a pilot plant campaign, the data from which could be assimilated through mathematical models that will allow for the simulation of the process and the evaluation of various designs and configurations of contacting equipment.

Just as the resin manufacturer is constrained in the guarantees he gives, the design engineers will have to limit design to the data range measured during the campaign and will seek indemnity from blame for process failure in the event of any deviations from the parameters of that pilot plant system. This leaves the process owner with a risk factor that could be expensive if the plant is particularly large and if profitability depends on the recovery of a high-value low-grade mineral via ion exchange resin.

This is compounded by the fact that there is currently no theoretical backbone to resin decay despite there being much anecdotal and published data on the phenomenon. The overwhelming majority of test work has been done on fresh ion exchange resins for a limited number of cycles and the long-term effect of in-service decay of resin performance is poorly understood.

When selecting a resin for use in a recovery process, one of the greater capital costs on start-up is the resin inventory. If the resin life span in the particular duty is short, regular resin replacement could become a significant running cost and make the process financially unviable. This would be important information for the design engineer or those conducting the viability study. At this time there are no organisations that offer a service that will test a particular ion exchange resin, cyclically, in a particular duty over a large number of cycles. The only alternative is to construct a pilot plant, and then the potential to generalise the results in the form of a composite mathematical algorithm for the purposes of simulation, is remote. There is as such no tool for either measuring or estimating the state of resin decay, either directly or through prediction based on systematic models.

The general question that requires answering is, how often will the inventory of a particular resin, in a particular duty, need to be replaced? The specific question is how one models the decay of resin performance so as to give the design engineer a practical tool with which to design his resin contactor.

In section 16-5 of Perry's Handbook 7th edition the following statement is made with respect to design strategy; *"[important aspects include] an understanding of dispersive phenomena at the bed scale and, for regenerative processes, knowledge of* ***ageing characteristics*** *of the sorbent material, with consequent changes in sorption equilibrium*".

It is accepted that resin capacity is generally linked to number of active sites, and as these are broken down or oxidised the capacity is reduced. In addition, breakage of the co-polymer structure of the resin also results in the washing-out of active sites.

Normally, fresh resin is shown to perform well in a particular duty. However, with continued cycles, performance will probably decay with respect to kinetics and capacity. If poisoning of the resin brings this about through the adsorption of an ion that cannot easily be removed, then decay may be rapid and easily predictable with a minimum amount of laboratory work. Alternatively, if a slow reduction in active sites and associated loss of performance caused by cycles of swelling, mild osmotic shock and polymer-cleavage is the cause of decay, quantification of this phenomenon could be useful to the plant operator and especially to the design engineer who will probably have to design for a performance poorer that that of fresh resin.

1.4. Decay in resin performance

Little attention has been given to the modelling of the repeatable performance aspect of ion exchange resin; understandably, as there is so much emphasis on understanding the mechanism of adsorption, which is academically more interesting. But performance decay is a practical problem that the design engineer needs to have answered, and which this thesis seeks to put into perspective.

In any fixed bed arrangement, during the adsorption phase there is what is commonly referred to as the ‘Mass Transfer Zone’ or MTZ. This is the zone of ion exchange activity where the fluid upstream of this zone is effectively the same as the feed, and downstream of the zone effectively has the composition of the product i.e. is in equilibrium with the loaded resin. Through the zone, in a longitudinal direction with respect to fluid flow, the concentration of the adsorbing/desorbing species alters in profile effectively from the feed to the product concentrations. As it is not desirable that any adsorbed species be allowed to pass to product, the MTZ cannot be allowed to break through to effluent. This means that a portion of the bed cannot be used and if the size of the MTZ enlarges due to poorer kinetics or reduced capacity, less of the bed can now be used, ultimately leading to a situation where the effective bed

capacity deteriorates to the point where the bed becomes inoperative for the particular duty and the resin has to be replaced, see Fig.1-1.

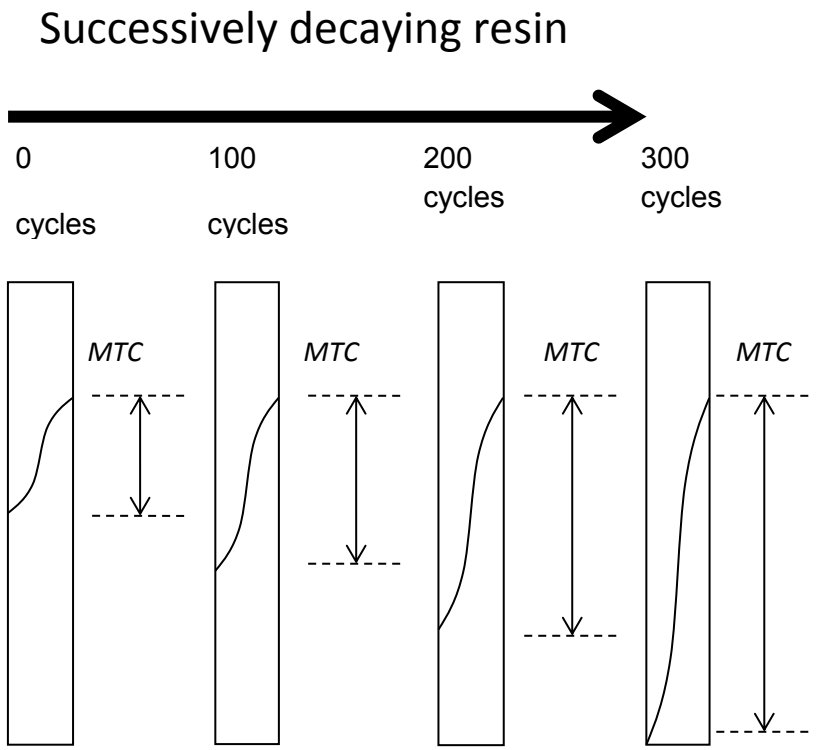

Fig.1-1 Expanding Mass Transfer Zone as the resin decays

The design of an ion exchange plant then requires a reasonable estimate of the decay of resin capacity and kinetics over time. It also requires an estimate of a point at which the resin is no longer performing adequately and requires an efficiently timed replacement. The multiple mechanisms of adsorption make for complicated modelling, as kinetic measurements are normally limited to bulk concentration measurements, which generally result in a lumped parameter modelling approach. Unless a rigorous kinetic modelling approach is used – there a number of schools of thought as to how this should be approached – there is no possibility of connecting a single ill-defined parameter to the decay state of the resin.

Intuitively, it can be postulated that resin decay generally occurs in one of, or a combination of, three ways;

- Repeated Swelling and contraction through cycles causes attrition in the copolymer matrix, and gradually structure is lost.

- Resin poisoning occurs with the adsorption of an ion that cannot be removed.

- Oxidation of the active sites occurs during the regeneration process resulting in the loss of capacity.

1.5. Intra-particle diffusion

The adsorption process consists of a number of mechanisms in series. Two of these mechanisms, which are well documented, are that of laminar layer resistance and intra-particle diffusion, both of which can play a role as controlling mechanism. Comprehensive characterisation of resin decay necessitates the measurement of intra-particle diffusion as it is the internal environment that will almost certainly undergo changes as the resin decays. Intra-particle diffusion cannot be measured directly. Hence a rigorous modelling approach will be necessary, incorporating a detailed intra-particle diffusion model in combination with a detailed surface diffusion model. This allows determination of discrete decay parameters with which to estimate resin life for design or measurement of degradedness.

1.6. Objectives

A model needs to be developed that advances the study of decayed resins by drawing on rigorous published/established transient models. Both heterogeneous and homogeneous intra-particle diffusion models have been postulated using both Fickian and Nernst-Plank diffusivity, but these have not been applied in a study of decayed resin. It will be a challenge to incorporate this model into an algorithm that combines it with models describing laminar layer diffusion in addition to equilibrium and swelling/contraction relationships.

To date most studies have either ignored either one mechanism or another, or have used an empirically obtained relationship to describe the laminar layer mechanism and combined this with an intra-particle diffusivity model. Given the lack of accuracy of empirical models, this approach is unlikely to be sufficient for the study of decaying resin.

A multiple mechanism model will need to be developed in combination with an experimental methodology that measures the parameters of these mechanisms directly from transient data and reduces the system to key parameters. By applying this algorithm to fresh resin, of varying steric environment, the determined intra-particle diffusivities can be compared to those determined by other researchers and act as a calibration. The next stage would be to artificially degrade the resin using a machine that automatically cycles the resin through multiple loadings and regenerations in a chemically aggressive environment. Further measurements of the intra-particle diffusion should indicate changes as a function of changes in steric environment, while laminar layer mass transfer coefficients should either remain constant or only change as a function of external turbulence.

1.7. Scope and limitations

The study will be limited to gel-type strong-acid polystyrene resins with varying divinylbenzene (DVB) cross-linking to highlight the impact of different DVB contents on intra-particle diffusivity. Resin decay will be limited to approximately half its capacity, decay being achieved by the use of Fenton's reaction at the active site which will be a sulphonic group. It is further envisaged that this study will be limited to Nernst-Plank mass transport with respect to measuring intra-particle diffusion.

1.8. Structure of thesis

A detailed literature review reports published examples of resin decay studies, reviews the history of transient modelling and the contemporary approaches to rigorous transient modelling techniques. A suggested modelling approach is then described, including a detailed description of the simulator and the search algorithm that will be employed.

A detailed description is given of the construction of a dedicated cycling machine that artificially degrades the resin in addition to the methods of kinetic, equilibrium and capacity measurement and other equipment employed, such as the closed circuit 'finite solution' testing circuit incorporating a 'zero length column' that confines the resin.

Finally, the results of the calibration and the measurements of intra-particle diffusion in decayed resins are presented proving the effectiveness of the model to simulate the transient adsorption process as it alters during resin decay in addition to independent confirmation of the internal decayed state of the resin.

2. LITERATURE SURVEY

2.1. Fundamentals of ion exchange resins

"The behaviour of ion exchanges in general depends on factors of an almost overwhelming variety" states Helfferich on the 100th page of his book, Ion Exchange Resin (Helfferich, 1962). Despite resin begin made of a highly defined, entirely synthetic substance, which intuitiveness would suggest presents less of a challenge than an amorphous natural adsorbent such as activated carbon or zeolite, there is still a substantial amount of work that needs to be done to elucidate the fundamentals. To appreciate the functioning of ion exchange resin, the behaviour of resin with respect to structure, transient adsorption, capacity and equilibrium needs to be studied in detail.

2.1.1. Structure

Ion exchange resin is essentially a copolymer structure manufactured into spherical particles/beads ranging in size from 300 to 1200 microns (Fig.2-1). The primary polymer used for the majority of resins is poly-styrene which is cross-linked with divinylbenzene (DVB) to give an in-soluble copolymer onto which active sites are grafted. Other types of primary monomers employed are methacrylate and acrylonitrile (Fig.2-2).

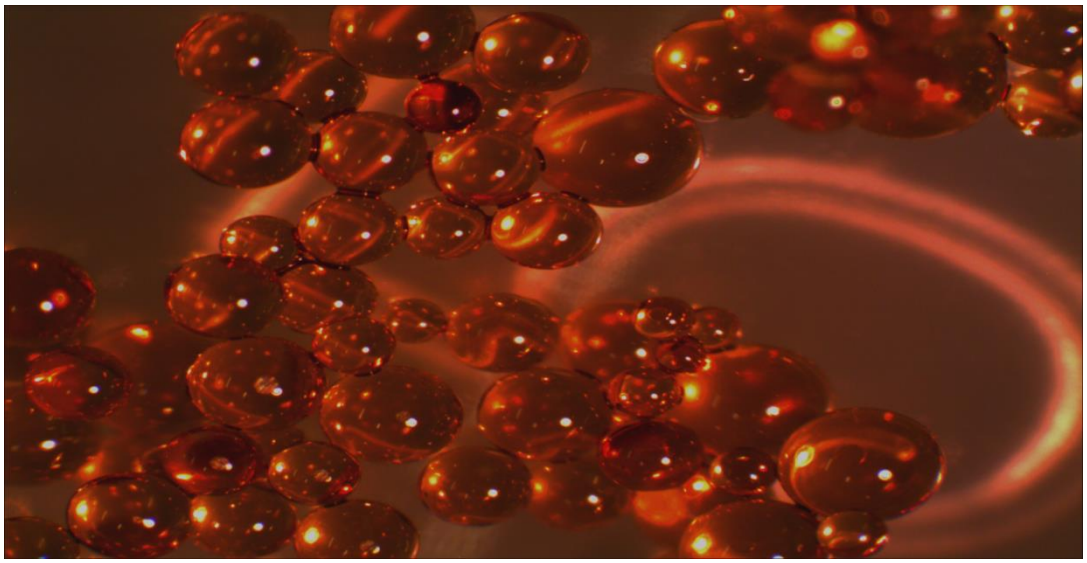

Fig.2-1 Strong acid resin beads under a microscope magnfied one hundred times

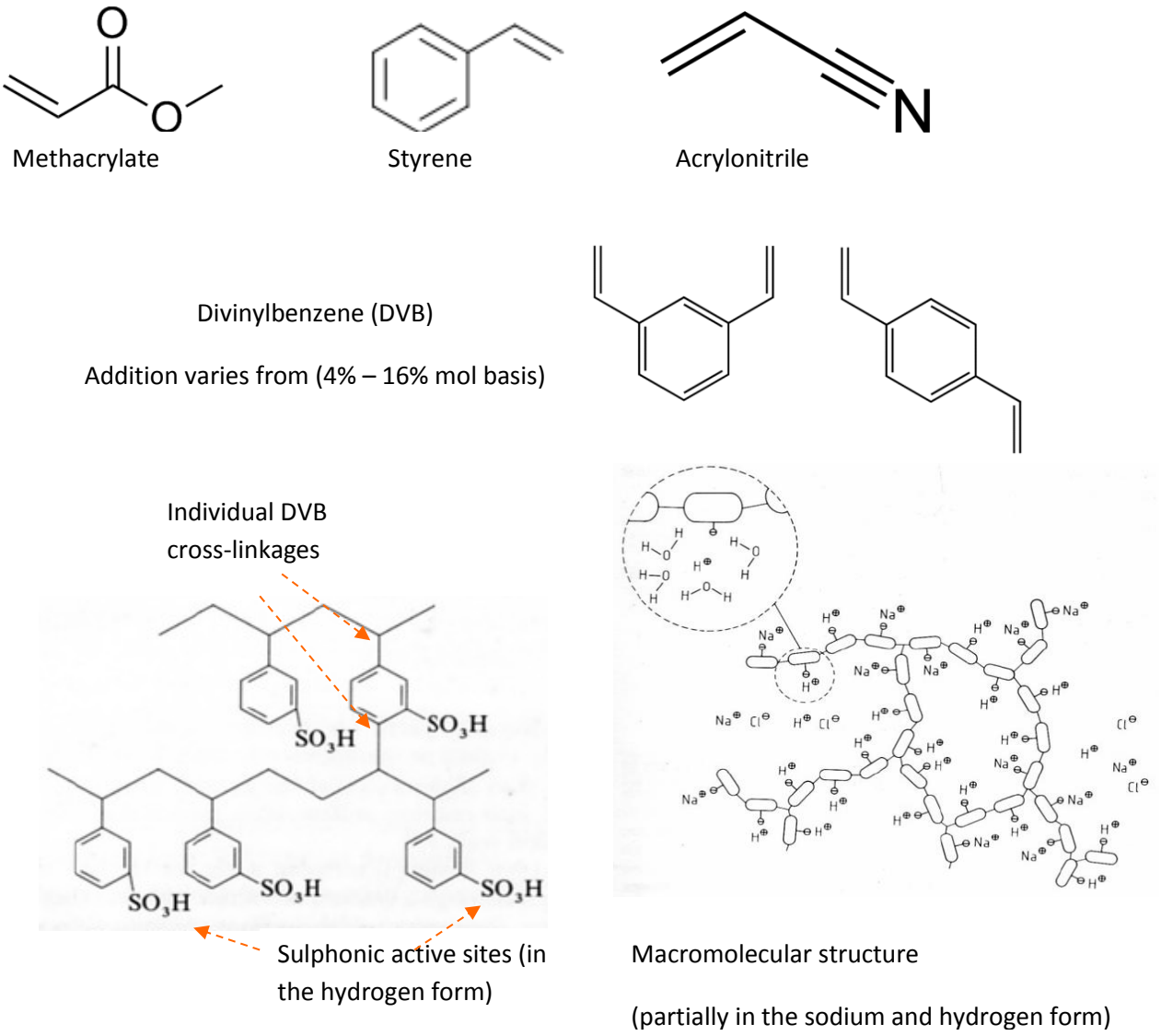

Fig.2-2 Various ion exchange resin molecular structures (De Dardel & Arden, 1989)

2.1.1.1. Cross-linking

An important aspect of the structure of the ion exchange bead is the degree of cross-linking that is controlled by the amount of divinylbenzene co-polymer addition. By adding a relatively low quantity of DVB (4% - 6%) a flexible structure is achieved that has the advantage of allowing for greater ion access but is lacking in strength and hence is more susceptible to osmotic shock. This is a phenomenon where large discrepancies in ionic concentration lead to powerful osmotic diffusion, effectively applying larger forces to the co-polymer substrate causing it to break. Rates of adsorption are also enhanced due to the

reduction in the steric environment inside the resin. By adding a greater quantity of DVB (8% - 16%) a sturdier structure is achieved that is less susceptible to osmotic shock but is rigid and less accommodating of larger ions.

2.1.1.2. Copolymer manufacture

The manufacture of the copolymer is normally achieved through the 'Pearl Polymerization Technique' (Helfferich, 1962). The monomers are introduced into an agitated aqueous solution with a stabilizer, maintained at a temperature in excess of 80^{o}C. The monomers polymerise into the copolymer shown in Fig.2-3

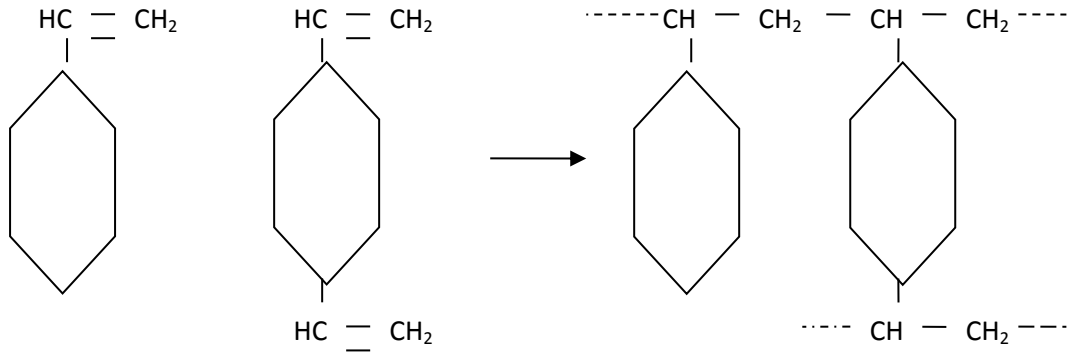

Fig.2-3 Styrene combined with Di-vinyl-benzene to form a copolymer matrix

The size of the droplets of copolymer formed depends chiefly on the nature of the suspension stabilizer added allowing for variance in bead size and distribution (Helfferich, 1962).

2.1.1.3. Active sites

Active sites are grafted onto the resin matrix. There are many different types but some of the more common are the following for acid resins,

$-SO_3^-$ $-COO^-$ $-PO_3^{2-}$ HPO_2^- SeO_3^- $-AsO_3^{2-}$

The active groups are grafted on to the copolymer by treatment with the applicable strong acid. In the case of the sulphonic group this is sulphuric acid but chloro-sulphuric acid can

also be used (Fig.2-4). Other acids can also be used such as carboxylic, phosphonic, phosphinic, selenoic, arsenic acids some of which require the use of catalysts and or oxidising agents during the grafting process (Helfferich, 1962).

The sulphonic active group ($-SO_3^-$) and the carboxylic ($-COO^-$) are the most common strong acid and weak acid active groups respectively. The dissociation constant for the sulphonic group ($-SO_3^-H^+$) is extremely high even at low pH's resulting in a strong acid resin, while in the case of the carboxylic group ($-COO^-H^+$) the hydrogen ion is held far more strongly giving a far lower dissociation constant and hence a weak acid resin is the result. Higher pH's are required for adsorption so as to allow for deprotonation of the carboxylic acid before it becomes available for the adsorption of alternate cationic species.

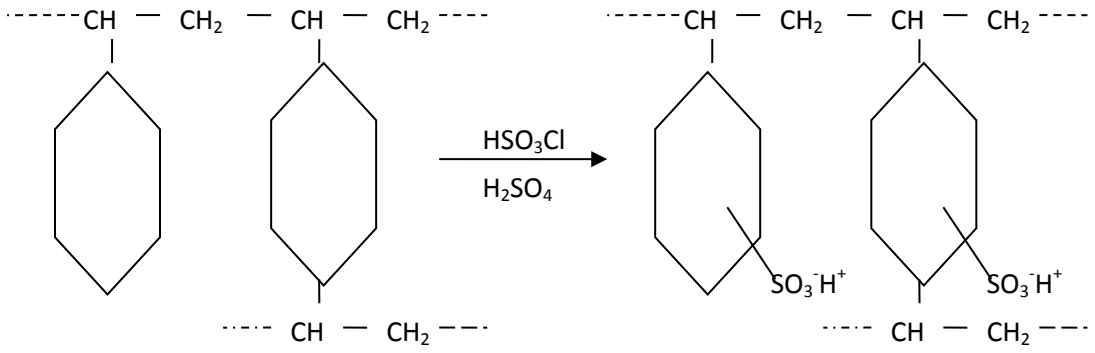

Fig.2-4 Grafting of sulphonic group onto each benzene ring of copolymer

It is notable that prior to the invention of ion exchange resin, anionic adsorption material, unlike cationic adsorption material such as zeolite was unknown as it did not occur naturally. Therefore the invention of anionic ion exchange resin was truly ground breaking (Helfferich, 1962). Typical active sites for anion/base resins are the following;

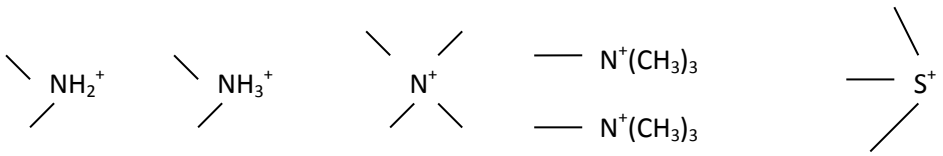

Anionic resins in general tend to be less stable and more susceptible to chemical and thermal degradation than cationic resins and therefore invariably have a shorter useful life span. Strong base ion exchange resin prepared with quaternary amine active sites tend to loose arms of the amine during normal duty resulting in a drop in base strength (Helfferich, 1962).

2.1.1.4. Gel type versus macroporous type resins

Traditionally there are two structures i.e. the gel type where the copolymer matrix is manufactured as a homogeneous structure and macroporous that has the copolymer structure riddled with pores of various sizes. Each of these structures has advantages and disadvantages. Gel type resins are easily manufactured, are cheaper and have higher capacities, however the homogeneous nature of the structure makes them more susceptible to osmotic shock. Generally the macroporous resins' heterogeneous structure tends to be more resistant to osmotic shock at the expense of capacity but the larger pores allow for the ingress of fine solids making them particularly vulnerable in a Resin In Pulp (RIP) environment. Macroporous resins are also slightly more expensive to produce.

2.1.1.5. Shallow Shell Technology

More recently Purolite has developed a structure which consists of an inert core in the centre of the resin bead also referred to as SST or Shallow Shell Technology (Fig.2-5). Purolite claims that it dramatically improves adsorption efficiency and also uses less regenerant during the regeneration process. The amount of wash water used is also substantially reduced. Purolite report that during the regeneration cycle the regenerant does not have to penetrate as deeply into the resin in the SST bead to remove all the adsorbed ions resulting in a quicker de-sorption, less regenerant usage and the avoidance of un-regenerated cores that could diffuse back to the surface during the wash water cycle resulting in leakage. Although these claims are unsubstantiated by independent researchers this development is an indication of the resin-producing industry's on-going attempts at progress.

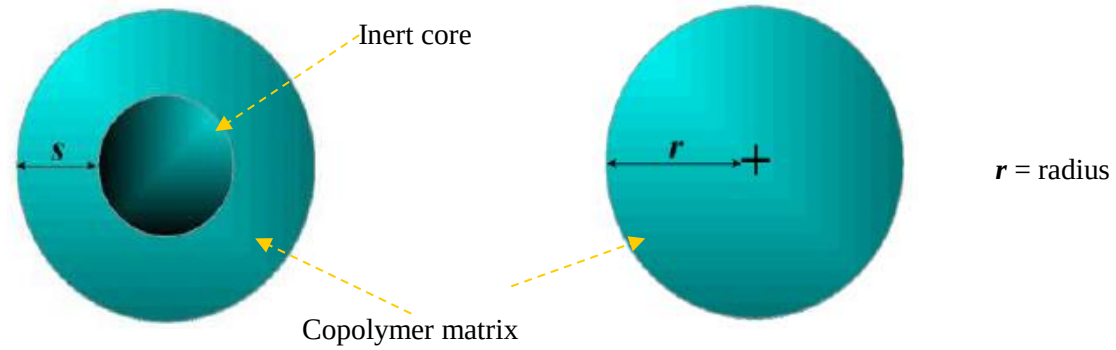

Fig.2-5 Shallow shell technology ion exchange resin

2.1.2. Different types of resin

2.1.2.1. Strong acid and base resins

The dissociation constants of the strong acid or base resins are high if one were to view these ion exchange resins as a liquid acid or base. From an adsorption perspective this means that in the case of a strong acid resin the sulphonic active site presents a negative charge and hence has an affinity for positively charged ions. Mono-valent ions readily latch to the active site, however these could be displaced by multivalent positively charged ions due to the higher charge density, resulting in the resin displaying an increase in affinity for ions with a higher valence positive charge, generally speaking. In the same way the strong base resin's active site, which is generally a secondary or tertiary amine, presents a positive charge which likewise readily adsorbs anions with an increasing affinity for ions with higher valences.

Generally, but not always, acid and base resins during the adsorption/regeneration cycle, alternate between the ions being adsorbed and a regenerative ion which is generally a mono-valent ion i.e. H^+ or Na^+ in the case of the acid resin and OH^- or Cl^- in the case of the base resin. To achieve displacement of adsorbed ions in exchange for mono-valent ions the regenerating solution needs to be high in concentration, usually of the order of one to two molar and have a high dissociation constant. One of the challenges of using base resins to adsorb metal-cyanides from solution is that to remove these metals it sometimes requires the

regeneration solution to have a higher oxidative level to assist with the breaking of the ionic bond between the metal and the active site, as would be achieved with the addition of hydrogen peroxide (Fernando *et al*, 2002). Excess oxidant can damage the resin active-site and structure.

For strong acid and base resins the concept of partial loading has to be considered, and is particularly important in a finite medium and is a function of the concentration of both the equilibrium adsorbing and desorbing ions present in solution that compete for active sites. In an infinite solution, where there is no build-up of desorbing ion, full capacity is likely to be achieved.

2.1.2.2. Weak acid and base resins

Weak acid and base resins are simply those where the dissociation constant is lower and hence the propensity for dissociation is less. In the case of acid resins the active sites are generally carboxylic groups and in the case of weak base resins, a primary amine. It's notable that a weak base active site has a lone pair of electrons associated with the nitrogen in the primary amine and this tends to adsorb H^+ ions resulting in the positive charge required to pick up the anion. Hence a weak base resin is seen to pick up entire acid molecules, first the H^+ and then the associated anion. This denotes that, streictly speaking, an ion exchange does not take place and the process would be better described as an adsorption. A weak base resin prior to adsorbing the acid is normally referred to as being in the free base form.

When generating deionised water, the standard approach is to firstly contact the impure water with a strong acid resin in the H^+ form, which results in the exchange of the H^+ for whatever undesirable cationic atom/molecule exists in the solution. This gives an acidic discharge containing H^+ now associated with the anions in the original feed solution. The next stage is to pass the acidic solution through a weak base resin where the entire acid is adsorbed, leaving deionised water.

2.1.2.3. Chelating resins

Somewhat more modern than acid/base exchangers, chelating resins use a different philosophy to immobilise ions. The word chelating comes from the ancient Greek word for 'Claw' and this essentially describes the action of two adjacent molecular ligands that make up the active site in this case.

Common chemical structures that make up these active sites are iminodiacetic acid, aminophosphoric and thiourea. Essentially the idea is to have a functional group with which metal ions would normally form strong complexes in solution. By choosing different types of ligands it is supposedly possible for the resin to have different affinities for different ions and hence the resin can be made highly selective.

2.1.3. Fibres

In addition to ion exchange copolymer material being manufactured into resin beads, it can also be manufactured into fibres, although the base material is identical to that of ion exchange resins (granular). The fibres have distinct advantages over the resins.

The manufacturing process of the fibres is more controlled, resulting in a final product of higher dimensional tolerances. Fibres typically can be made with diameters of 5 μm to 10 μm giving superior surface area for mass transfer over (granular) ion exchange resins, where diameters are seldom less than 300 μm.

Fibres by nature can be woven into a variety of different materials that allows for various technological designs e.g. filtration systems that provide both mechanical (physical) filtration and ion-exchange possibilities. Fibres lend themselves to continuous ion exchange processing as fibre manufactured into a rope can be mechanically passed through various contactors on a pulley system, representing adsorption washing and regeneration. Fibres are used extensively in gaseous filtration environments.

Fibres also have disadvantages over particulate resin as there are difficulties with bulk handling and sensitivity to mechanical damage. A disadvantage is that pressure drop across fibre beds tend to be higher than across particulate resin beds making them unsuitable for metallurgical recovery operations.

Fig.2-6 gives an indication of ion exchange fibres' used in industry and its application in different technologies.

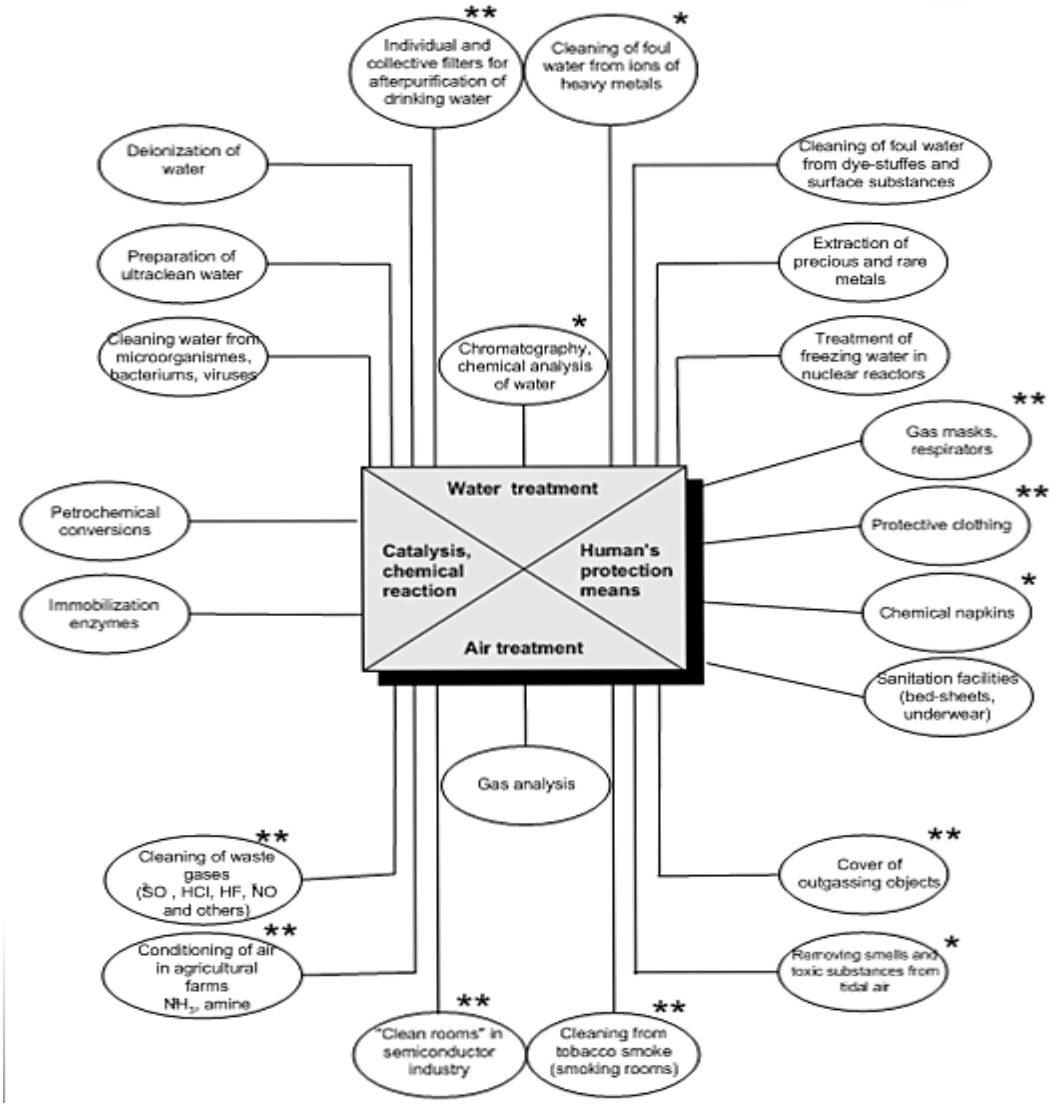

**Tested in a laboratory environment* ***Commercial application*

Fig.2-6 Applications for Fibre ion exchange technology (*Imatek&K Ltd*)

2.2. Defining resin performance

Determining the performance of a resin in an envisaged duty is of paramount importance given the vast number of different types of resins and applications. Generally, the first test performance indicator is an equilibrium test in which the resin affinity for a specific ion, as opposed to others in the same environment, is investigated. Testing routines are well established in the literature and invariably have an equilibrium curve/model as the output. Linked to this is the overall capacity of the resin for a particular ion, and this links into the environment in which it is being used.

Finally, the kinetics or rate of uptake of a particular ion becomes the final performance defining factor. An appropriately chosen, parameter-sensitive model is made to reflect the mechanism of the adsorption/ion exchange and once calibrated ultimately predicts the kinetic curve that is likely to be followed for the particular resin in a defined environment.

2.2.1. Resin capacity and equilibrium

The capacity of resin is generally measured in ‘equivalents per volume’ as there is considered to be a direct link between active sites and capacity, the co-polymer matrix of the resin being assumed homogeneous with respect to active site concentration. The term ‘equivalents’ is used and could be paralleled to the term ‘Normal’ in standard wet chemistry calculations. Essentially, equivalents per volume refers to the molar quantity of mono-valent ions adsorbed per unit volume, which implies that the quantity of divalent ions that the same resin could adsorb would be half as much i.e. double the number of active sites would now be required to accommodate the same amount of divalent atoms/molecules.

The volume of the resin can be linked to the density of the fixed ionic groups, with the number of ionic groups per bead being the only constant. However any swelling of the resin, a common phenomenon especially with strong acid resin in the H^+ form, will alter this specific capacity (Helfferich, 1962). The measurement of the actual volume of the resin also has its difficulties and is normally achieved and reported as Free-Wet-Settled-Volume

(*FWSV*) i.e. the resin is allowed to settle in a measuring flask and the volume recorded. The accurate measurement of this could be adversely impacted by the time left to settle, the temperature of the liquid (generally aqueous) and the pH of the solution.

Resin capacity and its measurement in equivalents/volume is in itself an imprecise element as it can vary with changes in electro-negativity of the absorbing ion and degree of conversion i.e. it links to equilibrium concentration and this is especially true for strong acid and base resins. The extent to which the continuous solution phase associated with the resin can be considered an infinite solution is also a factor that plays a role in the measurement, as it is only in a truly infinite solution i.e. no desorbing ion present, that maximum capacity can be determined. As most ion exchange resin applications are in either a fixed or fluidized bed arrangement through which the continuous medium passes, it is reasonable to assume that an infinite solution system exists in practice. However, it may not be desirable for the resin to be operated beyond its breakthrough point as this may mean loss of valuable ion being recovered or the discharge to product of undesirable ions in solution. Ultimately useful capacity is invariably less than actual capacity.

Another manner of describing resin capacity is that of equivalents per dry weight (milliMol-equivalents/gram) a measurement that requires the destruction of the resin for analytical purposes. Arguably the achieved measurement has a strong link to the mass of polymer present and it is necessary to make sure that there are no losses during the destruction process, particularly if it is via thermal desiccation. However, linking this value to the ion capacity of hydrated fresh resin, where only the difficult-to-measure volume of the resin bed is known, makes it a tenuous measurement at best. In a finite system where the quantity of resin and associated aqueous solution are constant, the equilibrium thus established between the desorbing and adsorbing ion would likely be disturbed if a quantity of resin were removed for the purposes of determining the MilliMole-quivalents/gram measurement, making this measurement inaccurate under these circumstances.

In the context of fundamental resin research, resin capacity and equilibrium have received far less attention from researchers than resin kinetics. Nevertheless for practical purposes some important aspects have to be considered as it was thought that capacity is a simple function of

the active sites. Any study of ion exchange resin that incorporates the resin capacity will have to take cognizance of these realities.

2.2.2. Kinetics of ion exchange

The study of the kinetics of ion exchange resin has received a substantial amount of attention over the last seventy years. Most of the studies have centred on discerning the mechanism of ion exchange/adsorption or defining an empirically determined utilitarian model that can be used for practical purposes over a wide range of system parameters. In the very early days gross assumptions were made which saw the ion exchange process in resin as being a subset of reversible reactions based on collision theory, thus linking it to ion and resin concentrations. This ultimately translated into second order decay models being used to simulate resin kinetics which did nothing to elucidate the mechanism of ion transfer. But certainly in the last forty years attention has been given to the development of more comprehensive transport models, quite often with multiple mechanisms in series.

One of the common assumptions is that mass transport into and out of the resin is controlled by the existence of a laminar dynamic layer of liquid adjacent to the surface of the resin bead, which for rough estimates has been proven to suffice. This assumption hangs on the proven theory based on empirical evidence of the existence of a universal laminar layer at a fluid solid interface. All mass transport through this layer occurs only via relatively slow diffusion possibly making this mechanism the controlling mechanism. But by definition this completely ignores the impact of the internal environment of the resin on mass transport. One of the great short-comings of this theory is that in practice it is necessary to evaluate the concentration gradient across this ill-defined laminar layer, and this can only be achieved by making a contradictory assumption that the concentration on the inside of the layer, i.e. on the surface of the resin, is zero. Such an assumption implies that the driving force behind the diffusion of the ions into the resin bead is zero, which is impossible. However, these studies are generally undertaken using early time kinetic data where the concentration at the surface may be very low and the laminar layer is assumed to be the controlling mechanism of transport into the resin.

Much more recently researchers have incorporated the concept of charge clouds inside the resin bead, generally through the use of the Nernst-Plank equation, and the impact this has on ionic-mass transport. The concentration of ions inside a resin bead is so high, generally two orders of magnitude higher than in the surrounding bulk liquid, that the impact of the charge cloud generated by both the adsorbing and desorbing ions has to be taken into account when evaluating transport behaviour within the resin.

As resin structural designs and active sites vary very much, and considering the variances in ion types, sizes and affinities, the rate of ionic uptake can be said to vary greatly from system to system. This makes the study of resin ion exchange kinetics essential for the designer of a resin contactor, particularly in an environment where the concentrations of the ions earmarked for adsorption are low, which is common in mineral processing.

As this thesis has, the objective, to develop an understanding of and the quantification of, the change in kinetics that occurs as a resin ages in its particular duty, it was considered that an appropriate literature survey would be to study the many proposed mechanisms of adsorption and the associated models. Of particular importance will be those models that have ionic flux within the resin bead as an important and controlling factor, as it is fair to assume that it is in this area that the greatest change in the resin, during decay, is likely to manifest itself. Quantifying this is likely to be a complex challenge and it is notable that Perry's (1997) handbook Ch16 page19 has the following to say about the modelling of diffusion inside a resin bead "Numerical data are sparse and disperse,… so that locally conducted experiments and interpretation must be used to great extent".

2.3. Resin contacting equipment

A further important aspect of resin technology is that of contactor design. Being a particulate solid, resin not only lends itself to easy separation from solutions but the associated resultant large surface area per unit volume translates into rapid mass flux onto/off the resin. However, as the resin must be regenerated in a completely different chemical environment to ensure

efficient operation, its application is cyclical in nature and this presents a challenge with respect to creating a continuous process.

The simplest form of contacting equipment is to immobilise the resin in tanks and alternate between a loading feed-liquid, from which dissociated ions need to be removed, and a regeneration solution followed by wash water. Fig.2-7 shows a simple three stage cycle that begins with the loading process (a) sodium being adsorbed from a feed solution and hydrogen passing into solution (down flow), (b) acid regeneration down-flow, (c) water back washing up-flow. After the washing stage the resin returns to the loading stage.

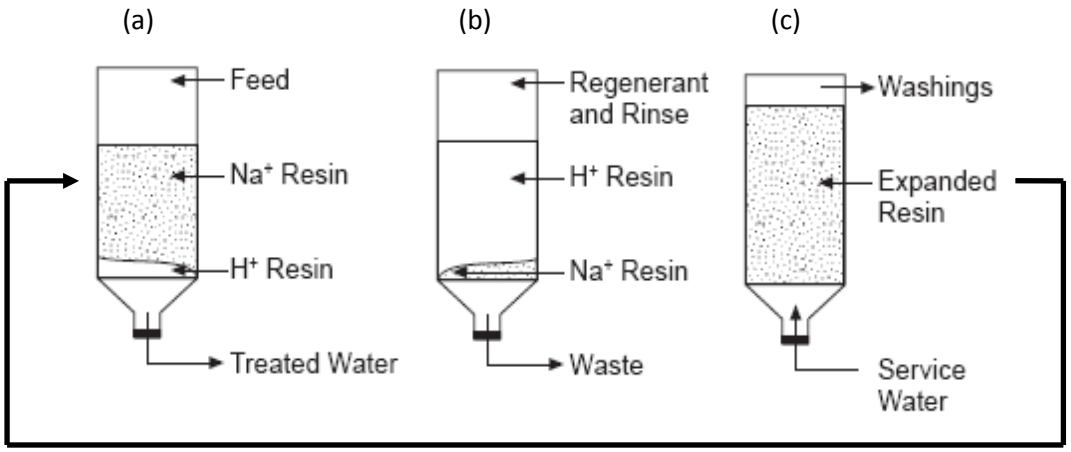

Fig.2-7 Loading (a), Regeneration (b), Washing (c) (*Dow Chemical Co.***)**

Use of either up-flow or down-flow configurations have both advantages and disadvantages. A down-flow configuration is common if the feed is clarified and the feed flow-rate relatively low. However, the pressure drop across the bed will be higher than that for up-flow and can increase fines build-up in the bed. Under these circumstances regeneration should be carried out in up-flow mode to displace entrained particles.

An up-flow configuration fluidizes the resin bed conveniently avoiding entrainment of particles. However, larger vessels are required to accommodate the expanded bed.

2.3.1. The carousel contactor system

The first level of continuous contactor is the passing of loading and regenerant liquids through a carousel of resin contactors (tanks), with the entry point of the loading and regenerant liquids rotating through a rotary valve (Fig.2-8).

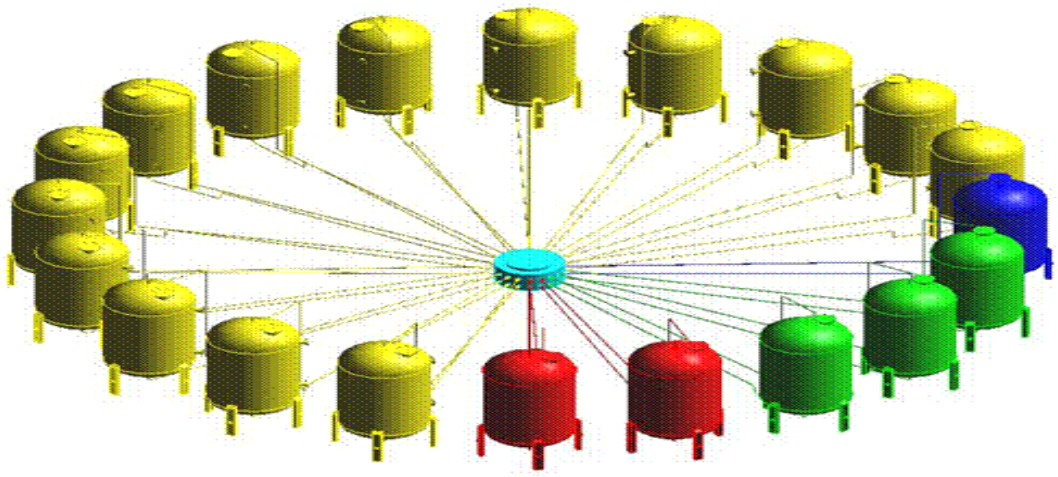

Fig.2-8 Rotary resin contactor system; (*Puritech Continuous Ion Exchange*)
Yellow = loading, Blue = elution, Green = regeneration, Red = washing

Although this method is practical and results in little physical movement of the resin, from a chemical engineering perspective, the efficiency is that of a batch process. In addition the challenge of fines being generated exists as the resin undergoes physical/chemical attrition, which, if a down-flow configuration is employed, ultimately results in an increase in pressure drop across the bed. An up flow configuration negates this difficulty although broken beads are likely to be flushed out of the system.

The resin's very high surface area per unit bed volume and limited longitudinal mixing of resin particles in both the fluidised bed and particularly fixed bed configurations, result in little radial concentration variation in the contactor. This translates into the longitudinal variation, or reaction zone length, being a strong function of the ion exchange kinetics and capacity. Ultimately a bed of ion exchange resin of sufficient longitudinal length approaches the behaviour of a moving ideal plug flow reactor, and it would be beneficial to capitalise on this phenomenon to achieve higher efficiencies. To achieve a genuine continuous contacting

device the ion exchange resin needs to be transported the longitudinal direction, counter-current to the flow of the continuous medium.

2.3.2. NIMCIX column contactor system

The unit-operation contactor that is the closest to being fully continuous is the Street-Cloete Column (Gomez-Vaillard & Kershenbaum, 1980), (Gomez-Vaillard *et al*, 1980), which today is commonly referred to as the NIMCIX column after the purchase of the patent by the National Institute of Metallurgy (NIM), Mintek's fore-runner.

Invented in the 1960's, it proposes a vertical column of contactor stages separated by perforated plates, the sizing of the perforations being such that the resin is fluidised in each stage, and then after a predetermined time, the flow of the continuous medium is switched to down flow and the resin in each stage passes to the stage below, through the perforations. See Fig.2-9. Once resin inventory of each stage has passed to the stage below the up flow is resumed and the cycle continues.

Thus a more or less stationary reaction zone is maintained with the length of the column contributing to full equilibrium being attained before liquid medium and resin are parted. During up-flow, the superficial velocity of the continuous medium is kept well above the terminal velocity of the resin beads insuring that a fluidized bed is achieved in each stage.

Eventually, once the resin reaches the bottom of the column it is dumped into a bin and transported to the top of a second column in which it undergoes elution/regeneration treatment. In effect this approach does not result in a perfectly continuous process but it is an improvement on the batch carousel method. However, from a practical perspective the large concentration gradient that is normally in place during the elution/regeneration allows for this part of the cycle to be conducted in a batch arrangement as the greater complexity of using a column negates the gains in efficiency.

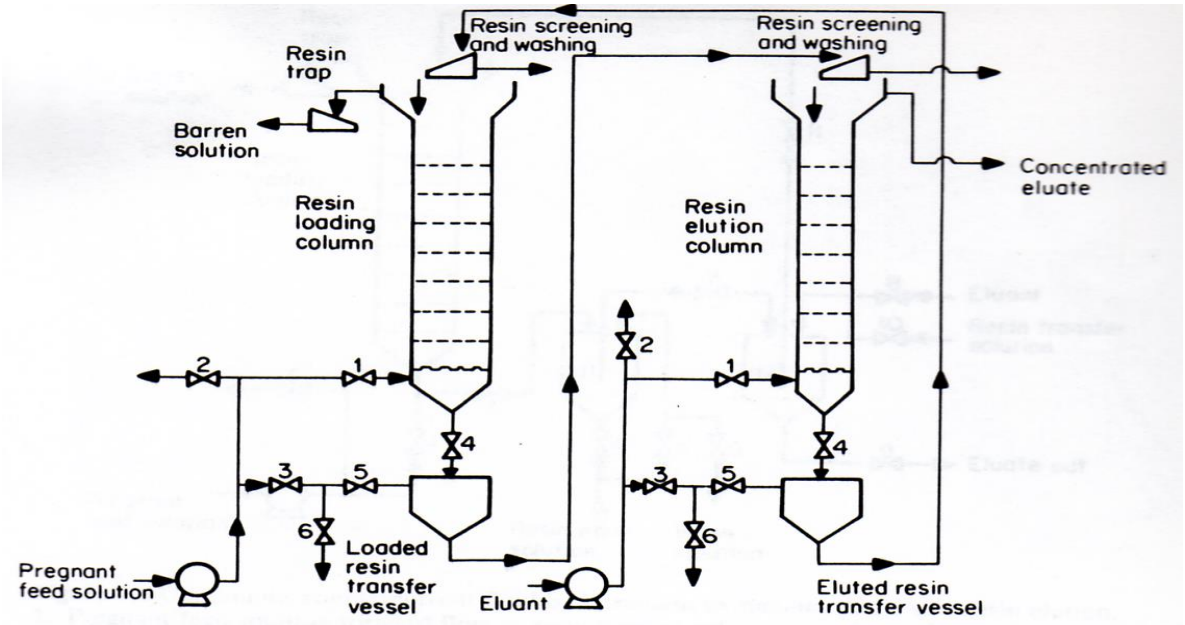

Fig.2-9 A NIMCIX loading and elution/regeneration column (*MINTEK*)

2.3.3. MetRIX contactor system

A much more modern contactor is that of the MetRIX plant that is currently still undergoing development for uranium recovery. It uses a cascade type of arrangement and sieve bends to separate out the resin from the pulp. It is envisaged that it could also be used for the recovery of other metals. The challenge associated with this type of contactor is the ingress of silica into the anionic resin particles (Yahorava *et al*., 2009), consequently resulting in pore blinding, slower kinetics and lower capacity, which is more of a short-coming of the resin than the contactor.

2.4. Ion exchange resins in the mineral processing industry

In the first decade of the 21st century a number of capital projects, involving ion exchange resin technology, appeared to be gaining momentum.

Paladin' s Langer Heinrich uranium recovery plant in Namibia, that was commissioned in 2006, is an example of a modern ion exchange processing plant that uses conventional fixed

bed ion exchange contactor columns. The plant has undergone a number of expansions since 2009 and its future seems assured. Langer Heinrich together with the far older Rossing mine, which also uses ion exchange resin for uranium recovery, have successfully contributed to making Namibia the fourth largest producer of uranium oxide.

French power company Areva's Trekkopje project, also in Namibia, is designed to recover uranium from low grade deposits and is another example of a modern application of ion exchange resin. This mineral processing plant makes use of the unique contacting system NIMCIX counter-current contactor technology developed by Mintek, a necessity given the low head grades, all of which goes to make this project unique in mineral processing. The initial construction timeline envisaged the plant being fully operational by 2012. However, geopolitical factors such as the drop in the price of uranium, the Fukushima disaster and the German government's policy of putting an end to power generation using nuclear fuels, led to Areva deciding to mothball the plant which is its status to date. It has never operated.

Bateman's MetRIX (Metal Recovery through Ion-eXchange) plant is a RIP (Resin In Pulp) plant that advantageously contacts the resin, counter currently, with an un-clarified pregnant uranium solution or leached pulp through a number of stages. The particulate nature of the resin, on average an order of magnitude larger than the particles of the pulp, negates the need to clarify the solution as the resin can be separated from the slurry. The resin/pulp separation is achieved using sieve bend technology and unlike other ion exchange applications the MetRIX process can be considered as genuinely continuous and could even approach the efficiency of a plug-flow reactor should a sufficient number of contacting units be used. One of the challenges with this technology is the life expectance, as the abrasive environment invariably compromises the resin's ability to maintain its adsorption efficiency (Yahorava *et al*., 2009).

Aside from uranium recovery there are also examples of ion exchange technology being used to recover base metals and platinum group metals. Examples of base metal recovery plants are Chambishi Metals and Mopani Copper Mine both situated in the copper belt in northern Zambia that use resins to recover nickel from a pregnant solution containing both nickel and cobalt. Generally, SX is used to recover the copper from the leach as the LIX reagent is highly selective and adsorbs copper even at low pH's, although there are examples of copper

recovery processes using resins such as the Vitrokele process (Fernando *et al*, 2008), which is used when copper is found in a gold bearing ore.

Impala platinum together with IBC Advanced Technologies have been successful in developing a resin that is used in the recovery of palladium. The technology used is commonly referred to as MRT (Molecular Recognition Technology) and the design of the resin and application is proprietary with little information in the public domain.

Modern ion exchange resins have become so sophisticated that manufacturers are able to claim their ion specificity. Minix (strong base) and Aurex (medium base) are two such resins that are topical and specific to gold – $Au(CN)_2^-$ ion - recovery. These are useful in systems that have highly carbonaceous ores disallowing the use of traditional CIP methods for the concentration of the valuable mineral and also where there are very high levels of base metals such as copper competing for the cyanide.

More recently there has been the successful development of an ion exchange Zn^{2+} removal plant at the Anglo American Base Metals Refinery in Rustenburg. The process uses an acid resin to remove the Zn^{2+}. Normally the trace presence of Zn^{2+} in a Ni^{2+}/Cu^{2+} recovery circuit can be ignored. However, because of the extremely low reduction potential of the Zn^{2+} it does not plate out in the tank house along with the other base metals causing it to build-up in the solvent extraction/electro-wining circuit. Therefore its removal using a resin process is deemed a necessity.

However, despite these successful technological breakthroughs, the process design engineer is left with a challenge to optimise or even determine feasibility of a specific process. This requires data beyond that supplied by the resin manufacturer such as the loss of ion capacity and alteration in kinetics of adsorption as the resin is used within a specific application.

Insuring that the adsorption and elution/regeneration process involving ion exchange resin can be systematically repeated often, without too rapid a decrease in efficiency, is extremely important. Lack of clarity in this area means accurate estimates of life expectancy will be impossible to make. Without a hard estimate of resin useful life the costing of a project

becomes impossible, especially considering that the cost of the ion exchange resin could constitute a significant capital expense. The cost of resin replacement during the course of the projects life will need to be accounted for.

2.5. Early modelling work (*pre 1965*)

Researchers have been posing various adsorption mechanisms for nearly 70 years going back to Boyd *et al*. (1947), resulting in a plethora of models. Although more recently published, rigorous models (Hasnat *et al.*, 1996) would appear to accurately predict only binary ion exchange, the complexity of these models leaves little doubt as to the difficulty of the challenge and it can be inferred that in this field of research there still lies much to be discovered. This can also be gleaned from the metamorphosis in proposed mechanisms that have been presented over the last five decades. Hasnat *et al's* (1996) heterogeneous model of co-ion intrusion is very different from that of Turner *et al*'s (1966) fifty-year-old model, which assumes Donnan exclusion and coupled diffusion coefficients in a homogeneous resin phase.

Another limiting factor to model development has been the ever-increasing computational requirements to simulate the more recently postulated more complex mechanisms. It is only because of technological advances allowing for the application of more complex computational methods that more rigorous testing of proposed mechanisms has been possible.

Still popular for its simplicity into the 1960s was the assumption that ion exchange kinetics was simply considered to follow a reversible second order reaction (Glaski, & Dranoff, 1963), being based on fundamental collision theory and governed by the concentrations of the electrolyte and the resin particles present in the system**.**

This is a simplistic approach derived from the 'reaction equation' of the counter ions (Equ.2-1) from which comes the rate of adsorption (Equ.2-2) that links to classic reactor theory. In the 1950s resin adsorption was thought of more in terms of a reaction, rather than a transport phenomenon. Although of no real theoretical value, for general purpose reporting, the theory

of adherence to second order kinetics could be used as a first estimate, especially if the system's equilibrium follows the Mass-Action-Law closely.

$$C_i + \overline{C_D} \leftrightarrow \overline{C_i} + C_D \qquad \alpha = \frac{\overline{C_i} \cdot C_D}{C_i \cdot \overline{C_D}} \tag{2-1}$$

$$\frac{dC_i}{dt} = k_f \overline{C_i} C_D - k_r C_i \overline{C_D} \tag{2-2}$$

Where

$\overline{C}_i, C_i$	Concentration of adsorbing ion on resin and in solution respectively
$\overline{C}_D, C_D$	Concentration of desorbing ion on resin and in solution respectively
α	Equilibrium constant
k_f, k_r	Forwards and reverse rate constants, respectively

The first published work on the rigorous mathematical modelling of ion exchange kinetics according to Helfferich (1962) seems to be that of Schulze (1915) who linked the kinetics of adsorption to ion diffusion which was quite revolutionary. It is generally accepted that most of the elementary work on diffusion modelling was carried out by Boyd *et al*, (1947) and Reichenberg, (1953). They approached the modelling of ion exchange kinetics through the application of 'Newton's Law of cooling' to diffusion through the imaginary dynamic laminar layer surrounding the resin bead in addition to the sequential mechanism of diffusion through the resin phase (Reichenberg, 1953), while assuming Donnan exclusion – ions with the same electrical charge as the active sites do not pass into the resin matrix - and that diffusion through the homogeneous resin phase is dictated by Fick's second law (Equ.2-3).

$$\frac{\partial \overline{C_i}}{\partial t} = D_i \nabla^2 \overline{C_i} \tag{2-3}$$

Where

t	Time
D_i	Intrinsic diffusivity of adsorbing ion

Despite the relative simplicity and elegance of this model, it has been proven to be reliable only over narrow and variable ranges (Helfferich, 1962). Incorporation into a spherical coordinate system and algebraic manipulation results in Equ.2-4. Further manipulation, assuming constant diffusivity throughout the resin phase, results in Equ.2-5;

$$\frac{\partial \overline{C_i}}{\partial t} = \frac{1}{r^2}\frac{\partial}{\partial r}\left(r^2 D_i \frac{\partial \overline{C_i}}{\partial r} \right) \qquad \textbf{2-4}$$

$$\frac{\partial \overline{C_i}}{\partial t} = D_i\left[\frac{\partial^2 \overline{C_i}}{\partial r^2} + \frac{2}{r}\frac{\partial \overline{C_i}}{\partial r} \right] \qquad \textbf{2-5}$$

Where

r Radial distance to the point at which mass balance is applied

Solving Equ.2-5 mathematically is relatively easy and a number of researchers have come up with applicable equations. Crank's equation (Helfferich, 1962) for an infinite solution system gives the fractional attainment of equilibrium (Γ) as a function of time and radial size of the resin particle (Equ.2-6).

$$\Gamma = 1 - \frac{6}{\pi^2}\sum_{n=1}^{\infty}\frac{1}{n^2}\exp\left(-\frac{D_i t \pi^2 n^2}{r^2} \right) \qquad \textbf{2-6}$$

For the finite solution system, that has to incorporate an equilibrium function, Paterson has postulated Equ.2-7 (Helfferich, 1962) that was originally derived for the equivalent heat transfer problem,

$$\Gamma = 1 - \frac{2}{3W}\sum_{n=1}^{\infty}\frac{\exp\left(G_n^2 \frac{D_i t}{r^2} \right)}{1 + \frac{G^2}{9W(W+1)}} \qquad \textbf{2-7}$$

where

G is the root of equation $G\cot G = 1 + \frac{G^2}{3W}$

W Equilibrium factor $\left(W = \frac{\overline{C_i}\overline{V}}{C_i V_C} \right)$

$\overline{V}, V_C$ Volume of the resin and the volume of the bulk solution respectively

Although these equations seem complicated they are easily simulated with software but their disadvantage is the assumption of a constant diffusivity. Should one wish to assume diffusivity to be a variable i.e. requiring a discrete solving of Equ.2-4, a comprehensive solution algorithm will be required.

Assuming the applicable chemical analyses are possible, this can be achieved with modern numerical algorithms such as finite element method, which can be solved either explicitly, implicitly, or by Crank-Nicholson methods. This was the status of ion exchange technology at the time computers began to have a major impact on the solving of complex systems.

Isotopic exchange, where diffusion is governed by Fick's law applied to ions in flux as they either leave or enter the resin bead, is the most basic approach to kinetic modelling of diffusion mechanisms. It assumes intra-particle homogeneity and no interaction between the charged ions. This approach is simple enough to allow it to be used for systems where a rough estimate is required of resin performance. In the early 1960s tackling this aspect of ion exchange simulation and modelling was considered still too complex for the calculative means available (Helfferich, 1962),

However, for the purposes of this study a more rigorous modelling approach needs to be used and through the last three decades a number of researchers have attempted to improve on the work of Boyd *et al*, (1947) and Reichenberg, (1953) attempting to bring in ionic electric charge interaction and also swelling characteristics of the resin. Later attempts were made to elucidate the multiple-mechanistic nature of the transient (Petruzzelli *et al*, 1987). In the previous 20 years, heterogeneous intra-particle environments have also been brought into the modelling and even attempts to incorporate the effects of charge cloud activity, close to the walls of the internal pores, on kinetics (Hasnat *et al*., 1996). The added complexity of these models would appear to detract from any practical application.

What is important in this study is to consider the practical nature of the resin decay phenomenon and therefore a comprehensive understanding of the scientific work conducted in resin adsorption modelling is necessary.

2.6. Ion exchange resin decay

Despite the vast amount of research undertaken and the plethora of models developed in ion exchange resin, many practical challenges remain. Ultimately, for engineering purposes, a model is only effective if it can be used in a practical application. The following reports indicate the difficulty associated with the phenomenon of ion exchange resin decay on which virtually no mathematical modelling has been done.

2.6.1. Reports of resin performance decay

2.6.1.1. Turner et al., 1966

Loss in ion exchange capacity during normal cyclic loading duty is not an uncommon phenomenon and has been reported by a number of researchers. Turner *et al*. (1966) appear to be the first to report a noticeable drop in resin capacity while doing experiments in an attempt to prove the applicability of the Nernst-Plank equation to ionic flux inside a cationic resin. The nature of the test work required that the resin be repeatedly loaded and regenerated causing resin degradation and ultimately a drop in performance. Although Turner *et al*, (1966) report the observation they proffer no explanation nor further detail on the number of cycles the resin experienced, which is unfortunate as this work was done in a controlled laboratory environment unlike the majority of reported resin decay events, which are taken from plant/production data.

2.6.1.2. Fleming & Hancock, 1979

The phenomenon of resin poisoning is well known and specific industrial systems have been reported (Fleming & Hancock, 1979). Poisoning of resin normally results in loss of capacity and poorer ion exchange kinetics and is normally the result of some trace species of ion in the loading solution that is not removed during the elution process, causing it to build up. In Fleming & Hancock's (1979) study, polymerization of the adsorbed cobaltic penta-cyanide mono aqua counter ion caused the robbing of capacity inside the resin and ultimately rendered the resin useless.

Fleming & Hancock's study is seminal and is often quoted as they were trying to solve a real economic challenge involving the loss of operational resin in a uranium plant. The study elucidated the mechanism of poisoning and proved beyond doubt that ion exchange resin cannot always be presented as a perfectly reversible reagent in a process.

2.6.1.3. Fernando et al., 2008

Another subset of decay is realized when resin is exposed to a highly oxidative environment which is sometimes required in a complex process (Fernando *et al*., 2008). Certain base metal cyanide complexes are known to hold tightly to active sites on the resin, with effective removal only being achieved by the presence of strongly oxidising solutions containing high concentrations of H_2SO_4 and H_2O_2. The degenerative effect on resin performance over repeated cyclic loadings is obvious and a case study has been reported by Fernando *et al* (2008) showing how the capacity and kinetics gradually decay.

Fernando *et al* (2008) also report that the presence of Fenton's reaction may also play a role in systematic breakdown of the resin. Fenton's reaction occurs when there is a transition metal - i.e. copper - in the presence of H_2O_2 that acts as a catalyst resulting in the formation of highly oxidative hydroxyl radicals. This is known to increase the rate of H_2O_2 oxidation of organics (*Geameay et al.*, 2004).

2.6.1.4. Williamson & Irving, 1996

Loss of capacity of a strong base resin has been documented by Williamson and Irving (1996) and is thought to be the result of the loss of quaternary and tertiary amines during normal cyclical use. However, this study indicates that thermal degradation can also play a role in this process. Unfortunately, their study had to make do with process data, disallowing rigorous scientific definition of the environment the resin is in.

2.6.1.5. Yahorava et al, 2009

Silica poisoning of strong base resins is a well-known phenomenon (Willimason & Irving, 1996). The paper of Yahorava *et al* (2009) does an in-depth study of the impact of silica poisoning on both macroporous and gel type resins and reports that both types are affected, with the gel type being more significantly affected, but that intrusion is more rapid in the macroporous resin. The resin was being used in a resin in pulp (RIP) pilot plant facility recovering uranium (U_3O_8), once again not allowing for a rigorous scientific definition of the environment that the resin is in.

Fig.2-10 is a comparison of two resins from different manufacturers designated '1' & '2', where 'M' designates macroporous and the 'G' gel type. A build-up of silica close to the outer surface of the resin appears to effectively throttle mass transport into/out-of the resin. Fig.2-11 shows the reduction in resin ionic capacity for each resin as the silica content increases and Fig.2-12 shows how with repeated loading cycles the nature of the kinetic curve changes which is to be expected as the resin becomes fouled with silica. Unfortunately, no systematic assessment of the fouled resin was made.

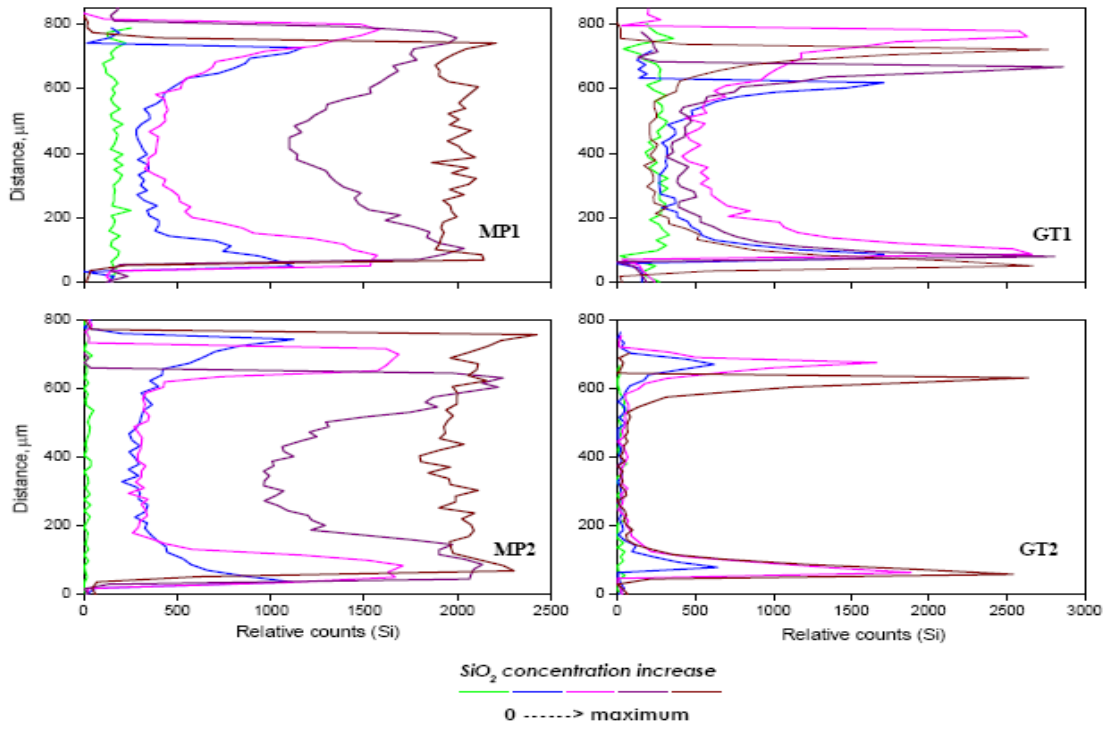

Fig.2-10 SEM silica detection on fouled resin, Yahorava *et al*, 2009

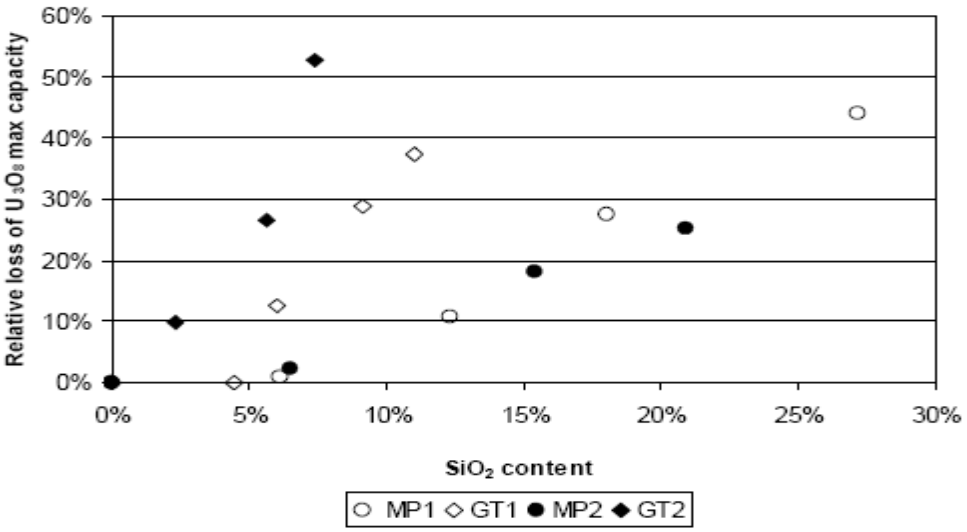

Fig.2-11 Loss of capacity due to silica poisoning, Yahorava *et al*, 2009

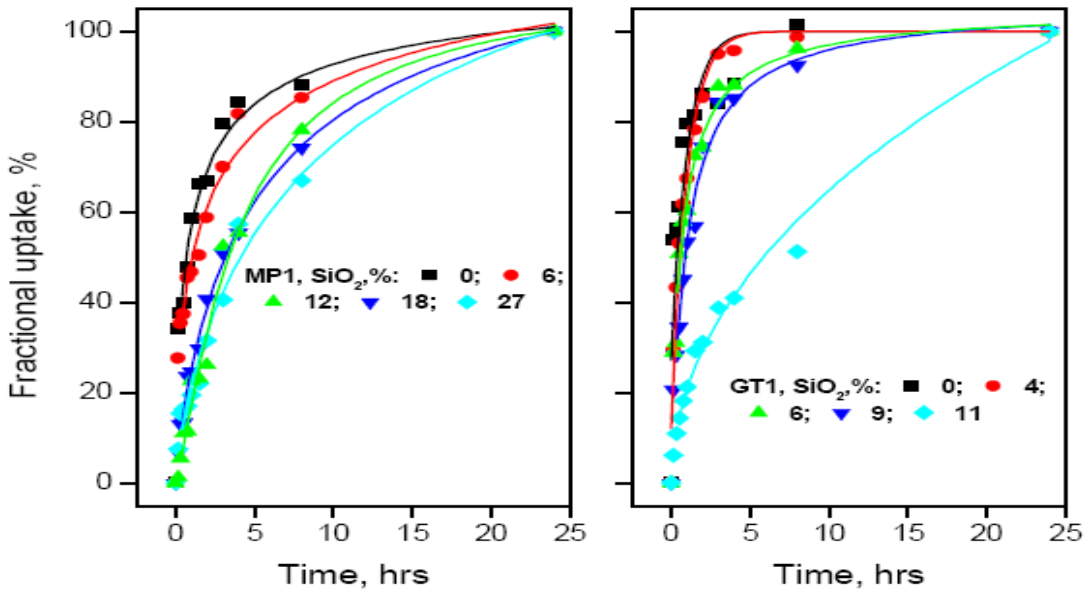

Fig.2-12 Uranium adsorption, for varying silica contents, Yahorava et al, 2009

2.6.2. Attempts to quantify resin decay

Although there have been a number of published papers about the decay in ion exchange resin performance during normal cyclic duty, there has been little attempt to produce a tool/algorithm that quantifies the decayed state of resin. The following is an example of an algorithm (Harries *et al*., 1986) that has been developed that gives a cut-off type scenario at which point a particular ion-exchange resin might be considered obsolete. There is also an attempt to use the Nernst-Plank model to measure changes in intra-particle diffusion as the resin ages (Nesbitt, 2010).

2.6.2.1. Harries 1986

Harries (1986) developed a method for the measurement of the decayed state of ion exchange resin. This technique was set up specifically for the ultra-pure water industry where efficiency of the resin is of paramount importance, given the necessity to maintain the ultra-pure water product purity at extremely high levels, and where any seepage of electrolyte to the effluent/product needs to be avoided.

However, this method is only attractive because of its simplicity (Gang-Choon Lee *et al*., 1997) and essentially consists of determining an overall 'Mass Transfer Coefficient' (MTC) derived from Newton's law of cooling, i.e. film diffusion applied over a concentration gradient that is found across the hydrodynamic laminar-layer adjacent to the resin bead surface. A dual resistance model is then assumed and an estimate of the secondary resistance inside the resin phase i.e. intra-particle diffusion, is then made.

The MTC method is based on a resin column mass balance (Equ.2-8) but is conducted in an extremely shallow bed effectively excluding the accumulation-in-the-fluid term.

$$\frac{V}{\varepsilon}\frac{\partial C_{i,bulk}}{\partial L} + \frac{\partial C_{i,bulk}}{\partial t} + f\left(\frac{1-\varepsilon}{\varepsilon}\right)\frac{\partial \overline{C_i}}{\partial t} = 0 \qquad \textbf{2-8}$$

Where

- ε Bed voidage
- V Superficial fluid velocity in the column
- $C_{i,bulk}$ Concentration of the ions in bulk solution
- L Column length
- f Volumetric fraction of the resin in the bed
- t Time
- $\overline{C_i}$ Concentration of adsorbing ion on the resin

A second mass balance (Equ.2-9) is made across the hydro-dynamic layer and is equated to the accumulation term for the solid phase in Equ.2-8.

$$\frac{\partial \overline{C_i}}{\partial t} = K_f a\left(C_{i,bulk} - C_i^*\right) \qquad \textbf{2-9}$$

Where

- K_f Overall mass transfer coefficient (MTC)
- a Resin surface area
- C_i^* Ion concentration in solution at the surface

In Equ.2-9 the surface liquid concentration (C_i*) is assumed to be zero. Substituting Equ.9 into equation Equ.2-8 and integrating with respect to column length ($\boldsymbol{L}$) and concentration along the bed and then solving for the mass transfer coefficient $\boldsymbol{K_f}$ results in Equ.2-10:

$$\boldsymbol{K}_f = \left[\frac{1}{6(1-\boldsymbol{\varepsilon})\boldsymbol{f}}\right]\frac{\boldsymbol{u}}{\boldsymbol{L}}\frac{6}{\boldsymbol{a}}\left[\ln\frac{\boldsymbol{C}_i^{\boldsymbol{eff}}}{\boldsymbol{C}_i^{\boldsymbol{f}}}\right] \qquad \textbf{2-10}$$

Where

$\boldsymbol{C}_i^{\boldsymbol{eff}}$ Ion concentration in the effluent of the column

$\boldsymbol{C}_i^{\boldsymbol{f}}$ Ion concentration in the column feed

It is from Equ.2-10 that the MTC ($\boldsymbol{K_f}$) is calculated for a given feed concentration ($\boldsymbol{C}_i^{\boldsymbol{f}}$) and effluent concentration ($\boldsymbol{C}_i^{\boldsymbol{eff}}$) and, as can clearly be seen from the derivation, this is based solely on the mass transfer coefficient associated with the hydro-dynamic laminar layer.

For the purposes of modelling the state of the degraded resin this model lends itself to empiricism while not elucidating on the inner state of the resin and its impact on kinetics. It is resin specific and the MTC must ultimately be a lumped parameter.

2.6.2.2. Foutch & Chowdiah 1992

Foutch & Chowdiah (1992) take the method of Harries (1986) further by using it to simulate effluent breakthrough curves of Cl^- ions as they pass out of a fixed bed arrangement. In so doing, they produce a tool that could assist plant operators to predict when resin may be past its usefulness.

As resin decays/fouls, the nature of the breakthrough curve becomes less sharp (Fig.2-13). This is to be expected, as the reaction zone in the resin bed expands longitudinally due to a decrease in resin capacity and the potential slowing down of the kinetics. This means that with continuous fouling the resin will eventually reach a state where the electrolyte is allowed to leak into the effluent effectively contaminating the product. As a resin fouls it gets to a

point where this situation is reached far too quickly and the resin can then be said to be un-usable particularly in an ultra-pure water application.

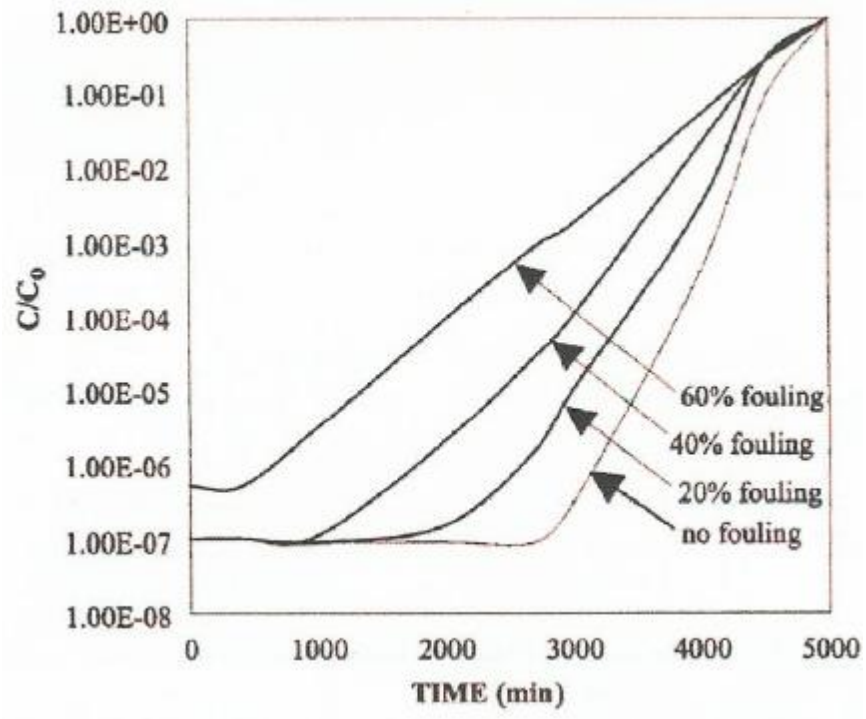

Fig.2-13 Aging resin successive breakthrough curves, Foutch & Chowdiah (1992)

Once again it's important to note that this method of measuring resin degradation, while useful, is based on the highly empirical model of Harries (1986) and hence can only be used in one particular application allowing for little variance in hydrodynamic environment.

2.6.2.3. Lee et al 1997

A study by Lee *et al*, 1997, that uses the method of Harries (1986) to characterize resin efficiency in an ultra-pure water application involved the study of resins from two 'Public Service Company of Oklahoma' power plants. This study was more scientific than previous studies and attempted to measure the overall MTCs of new and used resins from these power plants. Used resins were sampled from contactors that were charged with fresh resin between one and seven years prior.

This study points out the reality and these are that the overall MTC is largely a lumped parameter that can be used as a measure of resin performance. However, as little is known

about the controlling mechanism of mass transfer during the adsorption process, it is only likely to be useful in specific processes using specific resins and then only as a comparison to fresher resin. In this study, the MTCs of the old resin were found to have reduced by as much as 30% to 40% when compared to the MTCs of the fresh resin.

Sengupta *et al*, (2004) argue the shortcomings of the MTC method, especially its inability to distinguish between mass transport being controlled at the hydro-dynamic laminar layer or as it diffuses inside the particle to its active site. Intuitively, it is reasonable to postulate that intra-particle diffusion is likely to exhibit a larger change in mass-transport rates as the internal steric environment of the resin alters. Arguably, it is also possible that resin decay could lead to a possible change in controlling mechanism in favour of intra-particle diffusion, should fouling become significant.

Lee *et al* (1997) suggest that one approach to this challenge is to use established empirical Reynolds/Schmidt type models that predict mass transfer coefficients in the hydro-dynamic layer and then from the measured MTCs back-calculate the intra-particle mass transfer coefficients, the calculated value then being an indication of the resin degradation. This approach however, presents some difficulties in that a resin that degrades may alter in density and particle size which may in turn impact on the particle Reynolds number and hence on the predicted laminar layer mass transfer coefficient. Should there be a shift in the controlling mechanism as the resin ages this will also impact on this method.

Lee *et al*, (1997) did not attempt any correlation to the age/cycles-performed of the resin in their study. They simply did once off measurements comparing used and fresh resin, so no trend in measured MTC is reported as the resin degraded.

The method of Harries, (1986) is at best an empirical measurement that subsequent studies clearly showed could only be used in ultra-pure water applications where very high efficiencies are required and where a cut-off MTC can be defined below which a resin is declared incapable of achieving the required level of electrolyte removal. This makes the method unreliable to the study of resin degradation in general terms, especially if this degradation is a result of resin polymer matrix fouling or active site loss, which is far more likely to inherently impact intra-particle diffusion rates than diffusion across the hydrodynamic laminar-layer. Although ‘Newton’s Law of cooling’ type models have been

effectively used for film kinetics, as is the case for the (MTC) model, diffusion models are generally used for intra-particle mass-transfer kinetics (Gopala Rao *et al*., 1982).

2.6.2.4. Nesbitt 2010

An attempt to artificially degrade an ion exchange resin, systematically and in a controlled environment was undertaken by Nesbitt (2010), a study that was a precursor to this thesis. In that study cationic resin manufactured by Rohm and Haas 'Amberjet 1500H' was systematically degraded by continually cycling the resin, 900 times, through a loading of Cu^{2+} from a $CuSO_4$ solution and regenerating with a H_2SO_4/H_2O_2 mix in an attempt to cause Fenton's reaction to occur, which would effectively fast track the damage of the resin polymer matrix and active sites.

A machine was used to conduct this test work allowing for exact and rigorous definition of the resin's cyclical environment. Measurement of the intra-particle diffusion with successive cycles was then undertaking in a stirred batch reactor by performing kinetic tests and then fitting the Nernst-Plank model for intra-particle diffusion to the measured kinetic curves. The kinetic tests were then performed at different stirring speeds to alter the turbulence around the resin particles so as to discern the impact of the laminar dynamic resistance to mass transport, as it was theorised that alteration in turbulence is only likely to impact on the laminar layer resistance.

A systematic drop in resin capacity (Fig.2-14) was observed and a change in the nature of the kinetics (Fig.2-15). The kinetic curve showed that with successive cycles the 50% conversion point was reached more rapidly, pointing towards an increase in diffusion rates with resin decay. This is confirmed in Fig.2-16, where the intra-particle diffusion is shown to increase with successive cycles. Intuitively this makes sense as one is expecting the steric environment inside the resin to be breaking down i.e. becoming less dense and therefore offering less resistance to the diffusing ions.

Another important observation in the second case study conducted by Nesbitt (2010) was that with increasing turbulence i.e. greater mixing speeds, the increase in the calculated intra-particle diffusion with resin aging became more acute. Conversely, in the case of the Na/H

system at the lowest turbulence almost no change in intra-particle diffusivity was observed with aging, which led to the conclusion that with increasing turbulence the laminar layer resistance is reduced allowing for intra-particle mass transfer to play a greater role in the transient as a pure form of the Nernst-Plank intra-particle diffusion model was fitted to the data in this study, i.e. a model that ignores laminar layer resistance. Therefore the further assumption could be made that at the higher turbulences the measured intra-particle diffusions were more realistic.

Another difficulty in this study is that the turbulence around the resin beads is altered by using different stirring speeds in the batch reactor. Although this will likely change the turbulence i.e. Reynolds No., the actual measurement of the Reynolds No. that the resin beads experience is not easy to accomplish. It can only be assumed that for most of the time the resin beads experience a bulk continuous medium velocity of approximately bead terminal velocity as the beads have very little momentum/inertia and hence the change in Reynolds number with increasing stirring speed is likely to be only marginal.

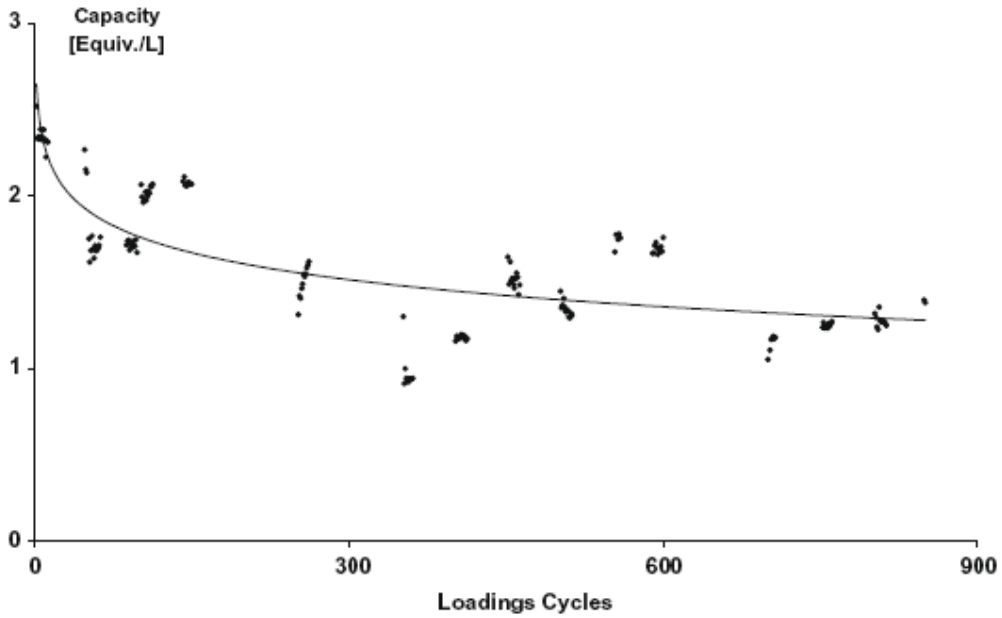

Fig.2-14 Resin capacity drop for Cu^{2+} ions with successive cycles (Nesbitt, 2010)

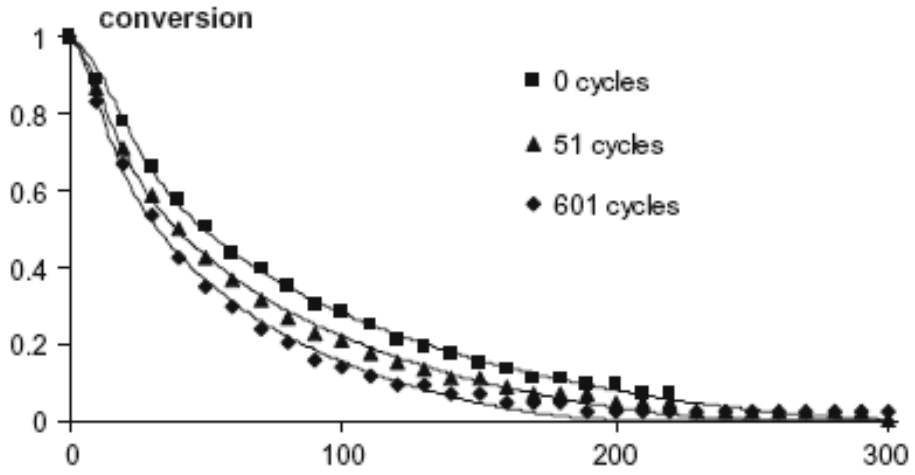

Fig.2-15 Kinetic adsorption curves for different numbers of cycles (Nesbitt, 2010)

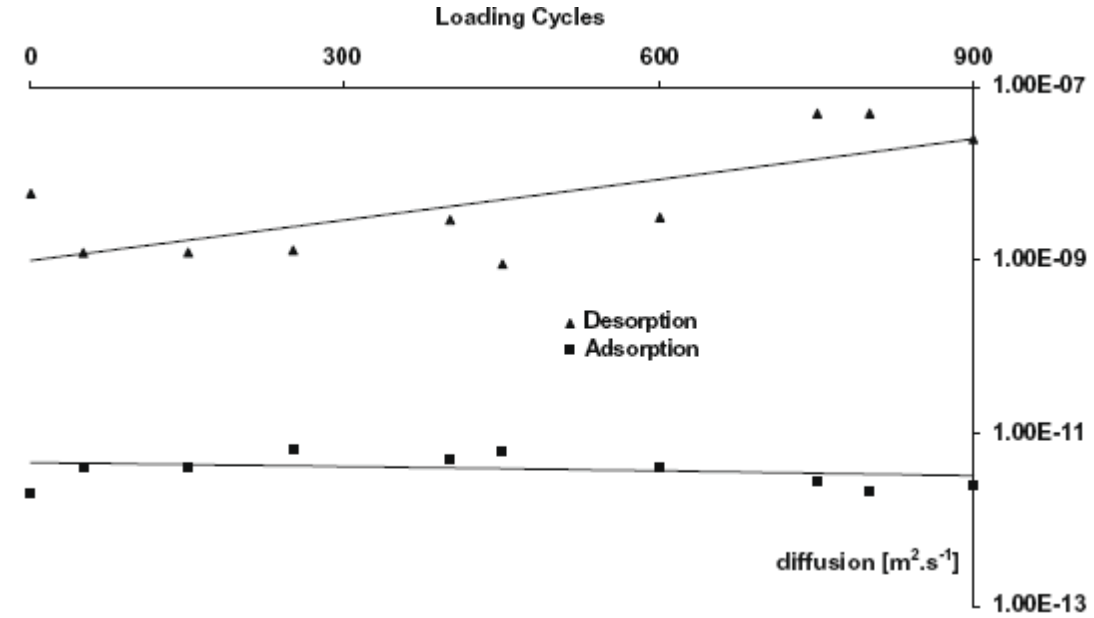

Fig.2-16 Intra-particle diffusion with increasing load cycles (Nesbitt, 2010)

The obvious conclusion that could be drawn from this work is that the adsorption process is complex and multi-mechanistic. Therefore rigorous modelling is the only way to move forward in any attempt to model resin decay.

2.7. Rigorous modelling of transient ion exchange systems

The researcher that embarks on the journey to mathematically model the mechanism of adsorption onto ion exchange resin quickly discovers the myriad number of variables that define the system. Various phenomena, each of which could be studied independently, could be listed as follows; swelling, osmotic forces, charge clouds, intra-particle diffusion, extra-particle diffusion, equilibrium states, kinetics, resin fluidisation properties, ion valence, ion affinity, variation in active site type, etc. etc.. Many of these have been studied over the past 50 years with clarification being achieved as greater rigorousness is used in the research. A fundamental principal in this kind of research is the classic assumption of the presence of controlling mechanisms.

2.7.1. Seven resistances theory

Helfferich (1962), together with Streat, (1982) and Sengupta *et al*, (2004) have described typical step processes, any of which could theoretically govern the mass transport during the transient. These various mechanisms are shown diagrammatically in Fig.2-17 and are described as follows;

1. Transport from the bulk solution to the liquid film boundary.
2. Transport through a stagnant liquid film to the resin phase boundary.
3. Transport across the liquid/resin interface.
4. Transport through the resin phase to the exchange site.
5. The exchange reaction of the contaminant ion for the ion on the exchange site.
6. Transport of the displaced ion through the resin phase out of the resin particle.
7. Diffusion of the displace ion from the exchanger surface into the bulk solution.

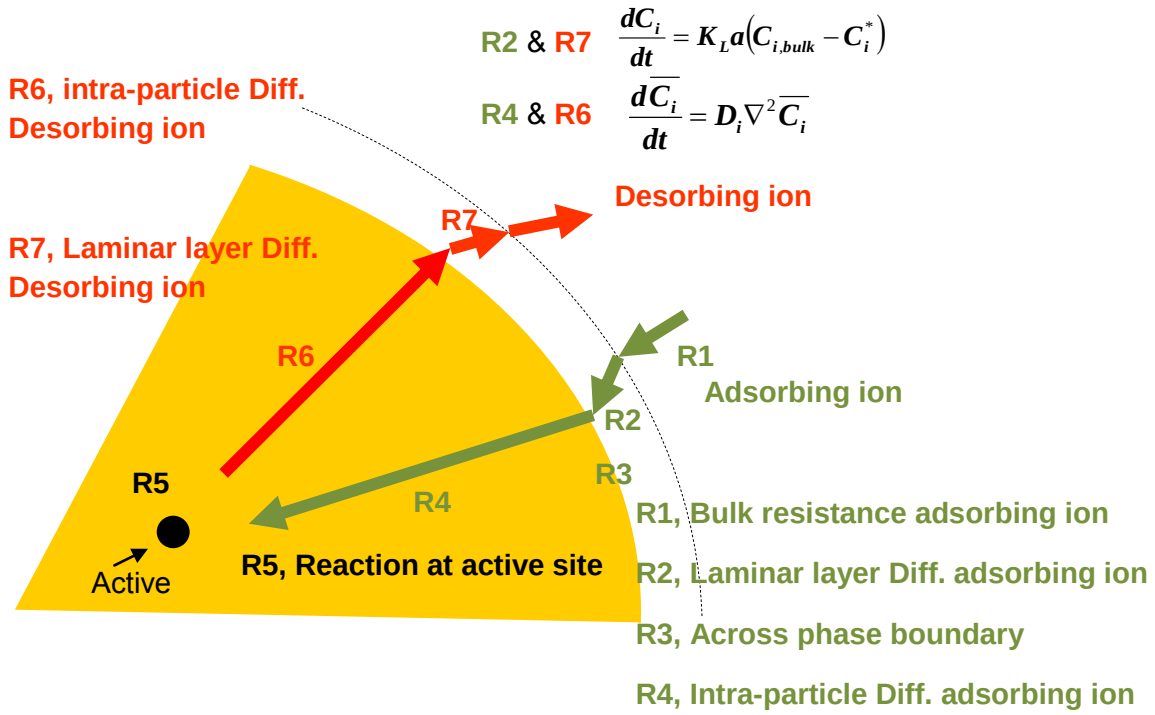

Fig.2-17 Schematic of sequential ion exchange mechanisms

The first mechanism is usually ignored as the required laminar-flow of the continuous medium through the resin bed is not known to occur in any conventional aqueous system. For the third mechanism, the resin phase concentration and the liquid phase concentration at the surface interface is always considered to be at equilibrium. The fifth mechanism rarely plays a role as reactions are almost always considered to be instantaneous. A study by Streat, (1982) drew the conclusion that there are difficulties separating reaction controlled from ultra-slow intra-particle diffusion. Mechanisms 7 and 6 are generally linked with mechanisms 2 and 4 respectively, as in the overwhelming majority of studies, ion fluxes within the resin and in the laminar hydrodynamic layer are assumed to be coupled by the electric potential caused by the differences in the ionic diffusivities and by the requirement of the no net current condition (Equ.2-14).

2.7.2. Studies in cross-linking

A further aspect of ion exchange research which bears relevance to this study is the phenomenon of studying the impact of the steric environment inside the resin on intra-particle diffusion.

2.7.2.1. Kataoka et al 1974

An attempt was made to put numbers to the relationship between the steric state inside an ion exchange resin bead and the intra-particle diffusion by Kataoka *et al* (1974). More specifically, they attempted to obtain a relationship between the degree of di-vinyl benzene (DVB) cross-linking and the intra-particle diffusion. In pursuit of this objective Kataoka *et al* (1974) measure the intra-particle diffusion in resins with 7 different DVB addition percentages i.e. 3%, 4%, 6%, 8%, 10%, 12% and 16%.

This work is considered important for the current study, and despite a number of reservations should be seen as early proof of the relationship. The equation that Kataoka *et al* (1974) proposes is given in Equ.2-11.

$$\frac{d\overline{D_i}}{\overline{D_i}} = -\beta dS \qquad \textbf{2-11}$$

Where

$\overline{D_i}$ Internal diffusivity of the adsorbing ion

β Proportionality constant

S Magnitude of steric hindrance induced by crosslinking

The model suggested by Kataoka *et al* (1974) indicates that, within boundaries, the diffusivity drops as the steric environment becomes denser. If the relationship is integrated (Equ.2-12a) with respect to change in steric state, Equ.2-12b is achieved. This shows an inverse proportionality between $\overline{D_i}$ and *S*, where when $S = 0$, $\overline{D_i}$ reaches some constant which should be equal to the free aqueous-solution diffusivity of the ion.

$$\int_{D_{s=0}}^{D_{s=s}} \frac{1}{D_i} dD_i = -\beta \int_{S=0}^{S=S} dS$$

2-12a&b

$$D_{i\,S=S} = D_{i\,S=0}\, e^{-\beta S}$$

Unfortunately $D_{S=0}$ does not equal the free diffusivity of the ion and Kataoka *et al* (1974) compensate for this by introducing Equ.2-13, where D_L is the free aqueous solution diffusivity, which shows that a factor β has to be introduced to make the model fit. With hindsight, it now becomes possible to present reasons for this inconsistency. It could be argued that the reason for this is because the resin is actually a copolymer matrix and the primary polymer – usually styrene – will still be present even if there is zero addition of DVB. In addition Kataoka *et al* (1974) completely ignore the impact of charge clouds on the intra-particle diffusivity

$$D_{i,S=0} = \beta \cdot D_L \qquad \textbf{2-13}$$

Kataoka *et al* (1974) show also that the effect of resin expansion plays a very significant role in the model relationship. Intra-particle diffusion measurement is highly dependent on the resin diameter.

The shortcoming of this work is essentially that they ignore the effect of the electro-magnetic forces acting between the adsorbing and desorbing ions, as all their work is based purely on the adsorbing ion. Seen from the perspective of empiricism the work has merit however, its level of complexity could be reduced with the same technological returns.

It is interesting to note that in the decade following the publication of this work the research group, at the University of Osaka, limited their research to calculating the intra-particle diffusivities of binary and ternary ionic systems (Yoshida & Kataoka, 1988). They use the Nernst-Plank model to estimate the ionic flux of the different ionic species inside the resin, effectively ignoring the swelling and contraction of the resin and without developing further the theory of the relationship between the steric environment and the intra-particle diffusion.

2.8. Modelling of transient adsorption behaviour (Nernst-Plank)

The majority of modern studies on intra-particle diffusion that assume the resin bead environment to be homogenous and the existence of a no-current condition (Equ.2-14), have adopted the Nernst-Plank model and apply it on spherical coordinates to determine the intra-particle diffusion i.e. Equ.2-17. (Kataoka & Yoshida, 1981), (Streat, 1982), (Petruzzelli *et al*, 1987a), (Petruzzelli *et al*, 1987b), (Hwang & Helfferich, 1987), (Yoshida & Kataoka, 1988), (Jones *et al*, 1993), (Rodriguez *et al*, 1998), (Rodriguez *et al*, 2002), (Valverde *et al*, 2004), (Valverde *et al*, 2005), (Nesbitt & Abrahams, 2005), (Nesbitt, 2010)

The coupling of ion fluxes is governed by the Nernst-Plank model (Equ.2-15), which, when reformulated for a two ion system (co-ions, adsorbing and desorbing) and assuming the law of 'superposition' for the generated charge cloud, gives us Equ.2-16. This is a form of Fick's first law using an apparent diffusivity in the resin matrix, comprised of the intrinsic diffusivities of the two ions (co-ions) their concentrations and their valence. The general assumption for flux in resin beads is radial symmetry (Equ.2-17).

$$J_i z_i + J_D z_D = 0 \qquad \textbf{2-14}$$

$$J_i = -D_i \left[\nabla \overline{C_i} + \frac{z_i \overline{C_i} F}{RT} \nabla \varphi \right] \qquad \textbf{2-15}$$

$$J_i = -\left[\frac{D_i D_D \left(z_i^2 \overline{C_i} + z_D^2 \overline{C_D} \right)}{z_i^2 \overline{C_i} D_i + z_D^2 \overline{C_D} D_D} \right] \nabla \overline{C_i} \qquad \textbf{2-16}$$

$$\frac{\partial \overline{C_i}}{\partial t} = D_i \frac{1}{r^2} \frac{\partial}{\partial r} \left[r^2 \frac{\partial \overline{C_i}}{\partial r} \right] \qquad \textbf{2-17}$$

Where

J_i Mass flux of the adsorbing ion

z_i, z_D Valence of the adsorbing and desorbing ion respectively

φ Charge cloud potential

R Universal gas constant

F Faraday's constant

One of the drawbacks of the Nernst-Plank model is its complexity. It is generally simulated by using discrete numerical methods that are impossible to undertake without the help of computer systems. Although the Nernst-Plank equation was first formulated by Helfferich (1962), it was only once substantial computational power became available in the mid to late 1970s that researchers were able to use numerical methods, to calculate intra-particle diffusivities (Nesbitt *et al*, 2005). Prior to this time researchers had to use analytically determined mathematical models that were limiting in their applicability.

From the late 1980s to the present, researchers appear to have not only accepted that adsorption is a diffusion driven process but also that it is dominated by combinations of mechanisms as first postulated by Petruzzelli *et al.* (1987a). This signifies that pursuit of rigorous modelling approach is likely to be complex. This is all the more severe if one considers that the only measurable variable in the transient is the bulk concentration. Nevertheless, the objective of measuring the impact of the alteration in steric environment on intra-particle diffusion calls for rigorous modelling and, at the outset, for a thorough study of recent attempts by other researchers to measure parameters of the system during the transient process of adsorption.

2.8.1. Kataoka & Yoshida, 1981

Kataoka & Yoshida (1981) conducted this study only on weak acid resin (Dowex CCR2). As the name implies, the dissociation of the H^+ ion from the active site of the weak acid resin, which is normally a carboxylic group ($COOH \rightarrow COO^- + H^+$), is extremely low and is of the order of $< 10^{-4}$. Therefore the adsorption mechanism is complicated requiring firstly a reaction with a hydroxyl group that accompanies the metal cation to the active site. The metal hydroxyl is then acid decomposed at the active site, the hydroxyl forming a water molecule

with the H^+ and allowing the Metal to be taken up by the active site. The overall reaction at the active site is shown in Equ.2-18 where the Me^+ represents the metal being adsorbed.

$$R-COOH + Me^+ + OH^- \rightarrow R-COOMe + H_2O \qquad \textbf{2-18}$$

This complicated mechanism implies that there needs to be some OH^- present in the solution, i.e. adsorption is unlikely to occur at a low pH value. The complicated mechanism also infers that the rate of reaction might be controlling and hence a reaction zone/plane is likely to form a moving boundary that slowly moves into the resin interior, a theory that had already been proven correct by (Holl & Sontheimer, 1977) but only in the case of resin regeneration, i.e. during H^+ adsorption cycle.

Central to Kataoka and Yoshida's (1981) study was to prove that the conversion of the resin could be described by the shrinking core model. They theorised that in the reacted shell of the resin during the transient, the hydroxyl ions (anions) and metal ions (cations) will be diffusing to the reaction boundary. They established their own model that combines the Shrinking Core Model, to describe the shrinking reaction boundary, together with the Nernst-Plank Model to govern the diffusion of the adsorbed metal ions along with the hydroxyl ions in the shell, i.e. on the outside of the reaction boundary. Few studies had been conducted on the mechanism of adsorptions in weak acids resins up to this time.

By fitting their model to kinetic data, they calculate the diffusion of Na^+ inside the converted shell of the resin and measure diffusion coefficients that are similar to those determined by other studies (Rodriguez *et al*, 1998); $D_{Na} = 1.47 \cdot 10^{-10}\ m^2/s$.

However, Kataoka & Yoshida, (1981) make statements that are difficult to accept in the light of conclusions made by later work. All adsorption test work is conducted at a Reynolds No. of 500 'to disallow any laminar layer control'. However, given the evidence (Petruzzelli *et al*, 1987) that the laminar layer always has some level of control this is unlikely.

A second statement made by Kataoka & Yoshida, (1981) is that they find that the diffusivity of sodium in Dowex CCR2 (the weak acid resin) is very similar to that measured in Dowex 50WX8 (a strong acid resin) and therefore diffusivities of other ions, measured in Dowex

50WX8 can also be assumed for Dowex CCR2. Given the very different capacities of these two different resins this is an unreasonable assumption.

2.8.2. Petruzzelli et al 1987a

An important addition to the understanding of the ion exchange transient behaviour is the work of Petruzzelli *et al* (1987) which proves conclusively that for most transient ion exchange systems both, laminar layer diffusion and intra-particle diffusion, control at different stages during the transient (Fig.2-18).,

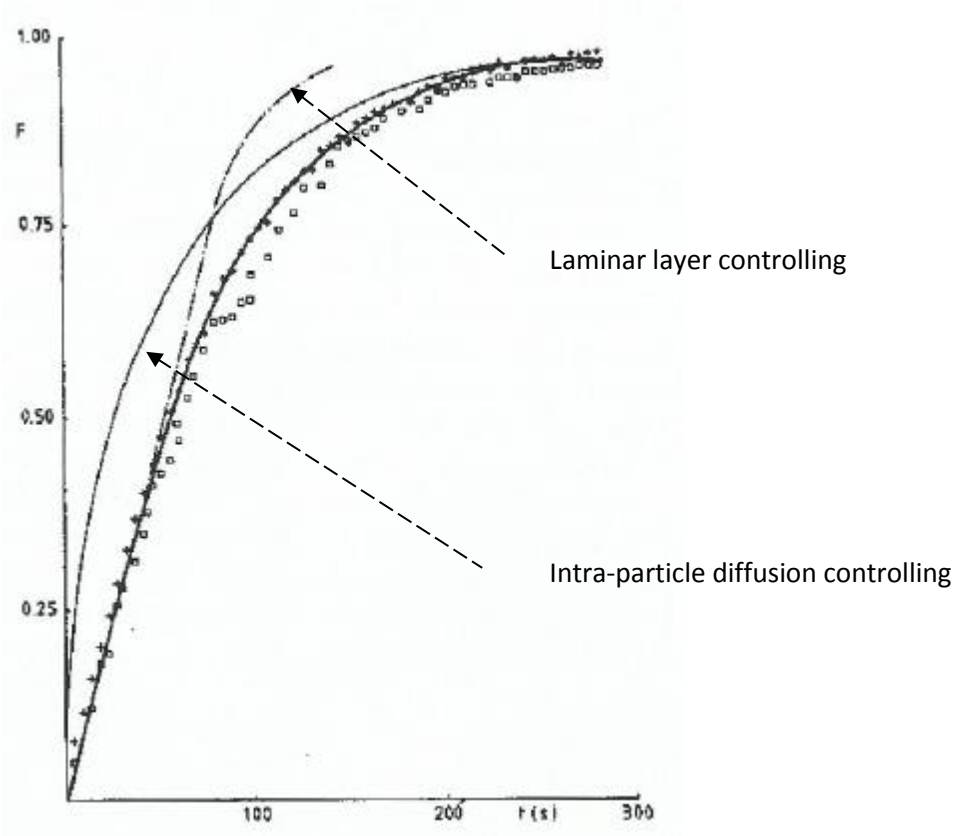

Fig.2-18 Adsorption kinetics with dual control (Petruzzelli *et al*, 1987a)

From Fig.2-18 it is possible to define three distinct sections of control mechanisms.

1. Laminar layer control during the early time data
2. Combined laminar diffusion and intra-particle diffusion control
3. Intra-particle diffusion control towards the end of the transient.

This discovery of Petruzzelli *et al*, (1987a) that both mechanisms control at different stages during the transient is an important piece of information in the puzzle to understand the transient behaviour of ion exchange resin, and it is vital information if one is trying to measure the intra-particle diffusion. Their work indicates the necessity of constructing a transient simulator that incorporates both laminar layer and intra-particle, diffusion mechanisms, which is complicated, and more recent rigorous modelling of ion exchange kinetics attempt this.

Petruzzelli *et al*'s (1987a) research appears to be the first to attempt to simultaneously incorporate both the intra-particle diffusivity and the laminar layer mass transfer resistance while assuming Nernst-Plank model behaviour within the resin bead. The laminar layer resistance was calculated by assuming a linear driving force law present in the liquid, comparable to a Newton's Law of cooling model. Further they link the laminar layer model and the intra-particle model through the 'Mass-Action-Law' by assuming equilibrium across the interface and zero accumulation of ions at the interface.

Their test work was carried out in a Kressman/Kitchener type reactor which consisted of immersing resin constrained in a cage that is attached to a high speed stirrer into an electrolyte, the rate of turn being approximately 3000 rpm. The Kressman/Kitchener (Kressman & Kitchener, 1949) reactor was originally constructed to perform interruption tests as it allows for the resin to be removed from a solution effectively interrupting a transient test. If discontinuity is observed when the resin is re-immersed it implies control by intra-particle diffusion. The advantage of this system is exacting control of the fluid turbulence surrounding the resin and hence constituted a useful tool to vary the impact on laminar layer control. However, calculating an exact Reynolds No. in the vicinity of the resin beads in an arrangement such as the Kressman/Kitchener type reactor is challenging.

The concentration of the electrolyte in the solution used by Petruzzelli *et al*, (1987a) was approximately 125 times higher than the highest concentration that could be attained from the release of all ions from the resin and this therefore they reason could be considered an infinite solution i.e. during the transient no significant change in bulk concentration.

The test work was carried out using resin IRA67 and a chlorine/sulphate system and proves that multi-mechanism control is present albeit only for this system. It's an example of an early attempt to simultaneously fit a rigorous model comprising duel resistances to data and measuring diffusion parameters that are of the same order of magnitude as achieved by other researchers. However, Petruzzelli *et al*, (1987a) do independently confirm the values that they achieve for intra-particle diffusion by comparing to an old analytical model developed by Grossman & Adamson (1952) that does not include the Nernst-Plank model but only Fickian diffusion.

2.8.3. Hwang & Helfferich 1987

Hwang & Helfferich's (1987) study is a strong indication of the development of computer systems that became available at the time, making it possible to simulate complicated mechanisms as mathematical algorithms. Their computer program was written in FORTRAN, the software language of choice for academic research at the time.

As part of the ongoing research into ion exchange kinetics, by broadening the application of Nernst-Plank equations to describe intra-particle diffusion Hwang & Helfferich (1987) extended the simulation of resin transient behaviour to multi-ion systems. Although their paper is an erudite advancement in the field of ion exchange transient simulation, the authors do not test their simulator against raw kinetic data and, by their own admission, also fail to incorporate any aspect of laminar layer resistance.

2.8.4. Petruzzelli et al, 1987b

In a further study, Petruzzelli *et al*, (1987b) confine their research to 1) Nernst-Plank intra-particle diffusion alone and 2) with reaction control. They also look at binary and multi-species systems. The paper essentially compares topical models of the time with no reference to real data. One observation they make is that there is no known example where the reaction is the sole controlling mechanism resolutely proving that transient ion exchange transport in resin is a diffusion controlled mechanism.

Although the authors specify that this study is an exercise in the evaluation of intra-particle diffusion models, it leaves out any reference to laminar layer control, which given practical realities has to be seen as a shortcoming.

However, two important statements are made which is an excellent indication of the level of scientific understanding of transient ion exchange systems at the time of publication and these amount to the following; for the scientist demanding greater accuracy, but not primarily interested in fundamentals of mass transfer, the Nernst-Plank theory still provides the best 'work horse' for systems without reaction. However, for the scientist, all available models will be unsatisfying when dealing in the fundamentals of mass transfer, which is motivation to keep searching for a simulation that is more rigorous but still manageable if applied to practical problem solving – a goal that may well prove elusive".

2.8.5. Rodriguez et al, 1998

The study of Rodriquez *et al*, (1998) is an example of measuring the diffusion inside a resin particle through the simulation of transient behaviour incorporating both the laminar layer resistance and that of intra-particle diffusion mechanisms. Rodriguez *et al*, (1998) incorporate the Nernst-Plank model (Equ.2-15) into their simulation of intra-particle adsorption/desorption diffusion behaviour and combine this with a Newton's Law of Cooling (Equ.2-9) type model describing the resistance at the resin liquid interface i.e. the dynamic laminar layer. They then link the two mechanisms by using an adapted form of the Mass-Action-Law for describing equilibrium.

However, Rodriquez *et al*, (1998) for ease of calculation, use a simplified form of the Nernst-Plank (Equ.2-19) that limits the simulator to mono-valent ions. In addition they fix the relationship between the intra-particle diffusivities of the exchanging ions by incorporating a fixed ratio (δ) between the associated diffusivities.

A distinct short coming of the simulation is its reliance on an empirical relationship model (Equ.2-21) postulated by Kataoka *et al*., (1973), to determine the laminar layer mass transfer coefficient used in the Newton's Law of cooling model (Equ.2-20), although it simplifies the

data fitting algorithm which then doesn't require a simultaneous search for parameters of both mechanisms.

$$J_i = -D_i\left[1+\frac{\overline{C_i}(1-\delta)}{\overline{C_T}+\overline{C_i}(\delta-1)}\right]\frac{\partial\overline{C_i}}{\partial r} \qquad \textbf{2-19}$$

$$D_{iD}\frac{\partial\overline{C_i}}{\partial r}\bigg|_{r=R} = K_L\left(C_i^* - C_{i,bulk}\right) \qquad \textbf{2-20}$$

$$\frac{K_L\varepsilon}{u} = 1.85\,Re^{-2/3}\,Sc^{-2/3}\left(\frac{1-\varepsilon}{\varepsilon}\right)^{-1/3} \qquad \textbf{2-21}$$

Where

- $\overline{C_T}$ Total number of equivalents on the resin
- δ Ratio of adsorbing ion diffusivity to desorbing ion diffusivity
- D_{iD} Combined diffusivity of adsorbing and desorbing ion
- Re Reynolds No.
- Sc Schmidt No.

The data used for the purposes of measuring parameters (e.g. intra-particle diffusivities) by mathematically fitting to the simulator were generated in a Zero Length Column (ZLC) with the reagents passing through once i.e. an infinite system arguably better than Petruzzelli *et al's* (1987) adapted version of the Kressman/Kitchener reactor.

An advantage of such a system is the consistency of the concentration gradients to which the resin is exposed as the bulk concentration of the adsorbing ion doesn't diminish once the adsorption process begins nor does the desorbing ion build up ultimately impacting equilibrium as would be the case with a finite system. A disadvantage of this system is the very low levels of desorbing ion concentration that need to be detected in the effluent of the ZLC.

Rodriguez *et al*. (1998) claim, and their recorded data proves it, that they observe a multi mechanism control and that they can measure intra-particle diffusion (self-diffusion coefficients) which they show to be constant for variance in feed flow rate to the ZLC. The

intra-particle diffusivities measured in IR120 strong acid resin which has an 8% divinylbenzene cross linking are; $1.35 \cdot 10^{-10}$ $m^2.s^{-1}$ for Na^+ and $5.6 \cdot 10^{-9}$ $m^2.s^{-1}$ for H^+ which are approximately an order of magnitude less than their free-water diffusivities.

Up to the late 1980s the research was geared towards the study of binary ion systems. An inevitable step was the systematic step up to multi-ion systems, research that proved to be an order of magnitude more complicated with respect to the application of the Nernst-Plank equation and the measurement of intra-particle diffusion.

2.8.6. Yoshida & Kataoka 1988

In this study Yoshida & Kataoka 1988 attempt to prove that it is possible to measure the intra-particle diffusivity of ions in ternary systems using the Nernst-Plank model. The three ions that they measured were H^+ /Na^+ /Zn^{2+} in Dowex 50WX10, a strong acid resin with a cross linking of 10% (10% Divinylbenzene addition).

They begin their study by reporting that in a former study (Kataoka & Yoshida 1987) they had measured the diffusivities of these ions in Dowex 50WX10, and these are given as hydrogen ion $D_H = 1.65 \cdot 10^{-11}$ ($m^2.s^{-1}$), $D_{Na} = 11.0 \cdot 10^{-11}$ ($m^2.s^{-1}$), $D_{Zn} = 0.962 \cdot 10^{-11}$ ($m^2.s^{-1}$). It is interesting to note that measured diffusion for sodium is about 40% slower than that reported by a similar study using Dowex 50WX8, the only difference between these two resins being the degree of Divinylbenzene addition i.e. the crosslinking. The lower cross linked resin (Dowex 50WX8) indicates a faster diffusivity which is not noted in this study but is pertinent to a study on resin decay.

In this study Yoshida & Kataoka 1988 not only show that it is possible to simulate a ternary system but can fit their simulation to raw data and obtain the diffusivities of the three ions presented above. They discover the secondary effect of where Na^+ is initially adsorbed and then dislodged by Zn^+, which is a divalent ion and for which the resin generally has a higher affinity than Na^+. The Na absorbs initially as its diffusivity is an order of magnitude faster than that of Zn^+. This study appears to be the first which uses finite differences to solve the Nernst Plank equation for all three ions.

2.8.7. Rodriquez et al., 2002

This paper is very similar to the authors' previous paper (Rodriquez *et al*, 1998) in that they use exactly the same approach to measure the intra-particle diffusion (Nernst-Plank based) of Na^+ and K^+ using a ZLC in a once through system i.e. an infinite system. The originality exists in an attempt to use different solvents i.e. methanol, ethanol and 2- propanol / water mixtures. The equilibrium is measured through the use of the Mass-Action-Law and the resistance in the laminar layer is once again assumed to be governed by Equ.2-21, just as in Rodriquez *et al* (1998), a distinct shortcoming as this means the mass transfer coefficient ($\boldsymbol{K_L}$) is derived from an empirically developed equation which could be inaccurate, as opposed to being determined directly from the raw data.

However, this research was important as resins in organic solvents swell less when compared to aqueous solution due to the lower degree of polarity, reducing the impact of resin swelling/shrinking on the intra-particle diffusion measurement. There is also varying solubility of the ions in the different solvent mixtures, making for improved selectively.

2.8.8. Valverde et al., 2004

Using the same ZLC technique described in *Rodriquez et al., (2002) and Rodriquez et al (1998)* the researchers attempt to measure the intra-particle diffusion of Cu^{2+}, Cd^{2+}, Zn^{2+}, paired with H^+, a quaternary system. Just as in the previous papers, the Mass-Action-Law is used to describe the equilibrium, and the laminar layer resistance is estimated by using Equ.2-21. As with the previous studies, this system is a finite system the only original aspect of the study is the measurement of the diffusion of divalent ions which makes the modelling marginally more of a challenge.

By the mid-2000s researches began to see the usual-assumption of the internal resin environment being 'homogenous', as being gross. In reality the internal environment consists of pores and co-polymer material and hence this could be described as the next logical technological frontier. Accepting that the resin internal environment is heterogeneous added another layer of complication to the simulation of mass transport inside the resin bead.

2.8.9. Valverde et al., 2005

In this paper the researchers attempt to apply their model to a macroporous resin where the Nernst-Plank equation is applied to both the pores and the copolymer matrix separately, and also incorporating a tortuosity factor which is assumed to be roughly the inverse of the resin porosity. Just as with previous studies the laminar layer resistance is calculated from Equ.2-21. This study can be described as an incremental advancement on the previous papers (Valverde *et al.*, 2004), (Rodriquez *et al., 1998), (Rodriquez et al., 2002).* However, the introduction of a tortuosity factor adds another parameter to the system and the question has to be asked if this truly amounts to any advancement on resin technology for practical purposes.

3. MODEL SIMULATION AND FITTING

3.1. Current approach to kinetic modelling

The rational approach chosen for this study is that of assuming that the most recent and widely accepted mechanistic modelling approach, of assuming a double resistances theory, is a reasonable simulation of transient mass transport on resin. It's essentially a two stage flux model with two well documented mechanisms operating in series.

During the course of the transient, three phases or fewer of mechanistic control are expected. An initial phase has ionic mass transfer across the laminar dynamic layer on the outside of the resin bead dominating the rate of flux. Thereafter a second phase begins where both ionic mass transfer across the laminar layer and the diffusion of ionic mass into and through the resin bead will both control the overall flux each to a greater or lesser extent. Finally, in the third phase, which likely occurs as the resin beads approach saturation, has the intra-particle diffusion controlling the rate of ionic mass transfer alone (Fig.3-1).

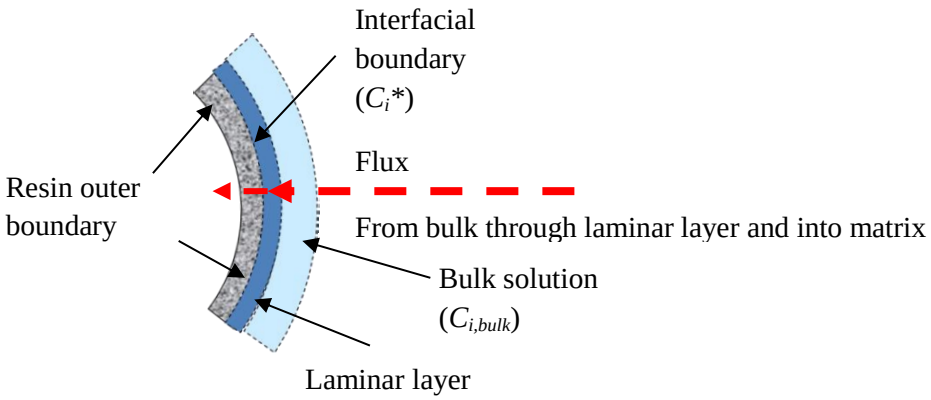

Fig.3-1 Ion flux through laminar layer and into resin matrix

Although the mechanisms have been well documented simulating it, for the purposes of fitting if to laboratory generated kinetic data, will be a challenge. The key, it is hypothesised, is the impossible to measure ionic concentration at the resin surface that, in a concentration driven mass transfer model, is the common variable in the driving forces of mass transfer on

both the inside and the outside of the resin. However, it is possible to measure mass flux through the laminar layer by calculating the change in bulk concentration with time as the disappearing (adsorbing) ions can only be passing through the laminar layer of the resin before passing through the surface and into the resin bead (Fig.3-1).

3.2. Mass transfer coefficient (K_L)

3.2.1. Diffusing solute through non-diffusing solvent

For the overwhelming majority of adsorption systems, the concentration of adsorbent will be low compared to the solvent of the continuous medium (i.e. < 5% on a mol basis). Therefore it is reasonable to assume that with respect to ionic-diffusion transport through the laminar dynamic layer, the adsorbent can be considered to be a substance (solute) diffusing through a non-diffusing medium (solvent).

The appropriate specific flux equation for substance A (adsorbate) diffusing through non-diffusing B (solvent) will be Equ.3-1.

$$N_i = -\frac{D_i}{z \cdot x_f}\left(C_{i,bulk} - C_i^*\right)\cdot 1000 \qquad \textbf{3-1}$$

where

N_i	Mass flux ($mol/m^2.s$)
D_i	Diffusivity (m^2/s)
z	Laminar layer thickness (m)
x_f	Mol fraction of solvent ≈ 1 in dilute solutions (*dimensionless*)
$C_{i,bulk}$	Concentration of adsorbate in bulk solution (mol/L)
C_i^*	Concentration of adsorbate in solution at the resin surface (mol/L)

If the resin beads are placed in a well-mixed finite-volume of continuous-medium solution (Fig.3-2), Equ.3-1 can be adapted to model the reduction in bulk ion concentration as the ion is adsorbed onto the resin. This is achieved by combining the diffusivity (D_i) with the abstract laminar layer thickness term (z) into a mass transfer coefficient (K_L), assuming that the

average molecular solution concentration is ≈ 55.5 mol/L i.e. $x_f \approx 1$ and incorporating the dimensions of the spherical resin bead and a closed circuit system, we achieve Equ.3-2, which contains the value for the surface concentration (C_i^*). The volume term (V_c) refers to the overall volume of the finite bulk fluid.

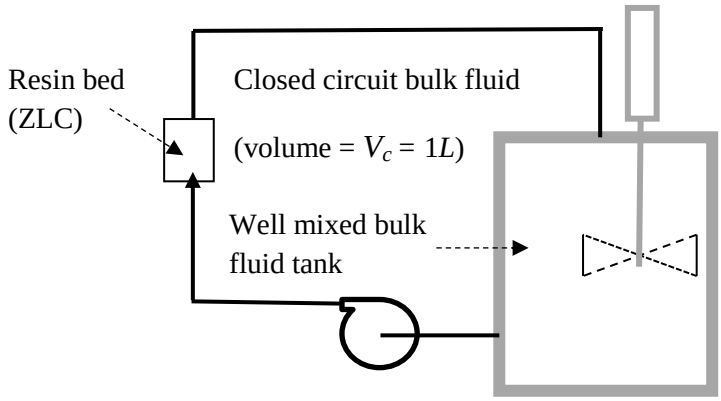

Fig.3-2 Resin bed associated with closed circuit bulk fluid (finite volume)

As all constants are measureable, these combined with the surface ionic concentration make it possible to calculate the mass transfer coefficient (K_L) (Equ.3-3) for a specific system, assuming that one is able to measure the surface concentration (C_i^*).

$$-\frac{dC_{i,bulk}}{dt} = K_L \frac{4\pi R^2 N_R}{V_C}(C_{i,bulk} - C_i^*) \qquad \textbf{3-2}$$

$$\frac{-\frac{dC_{i,bulk}}{dt}V_C}{4\pi R^2 N_R (C_{i,bulk} - C_i^*)} = K_L \qquad \textbf{3-3}$$

Where

- t Time (s)
- V_c Volume of bulk solution, i.e. in bulk solution (m^3)
- R Radius of the resin beads (m)
- N_R Number of resin beads present in the system (*dimensionless*)
- K_L Mass transfer coefficient (m/s)

Although, Equ.3-3 seems practical there are challenges in it application. Not the least of which is the requirement that the laminar layer be the controlling mechanism of the mass

transport through the laminar layer, effectively linking it to the rate of ion concentration reduction in the bulk.

3.2.2. Initial slope method

A well-documented method of determining the mass transfer coefficient constitutes measuring the slope of early time data from kinetic curves measured at different turbulences and seeking a correlation between rate of mass transfer (slope) through, and concentration gradient across (bulk ion concentration), the laminar layer, as shown in Fig.3-3.

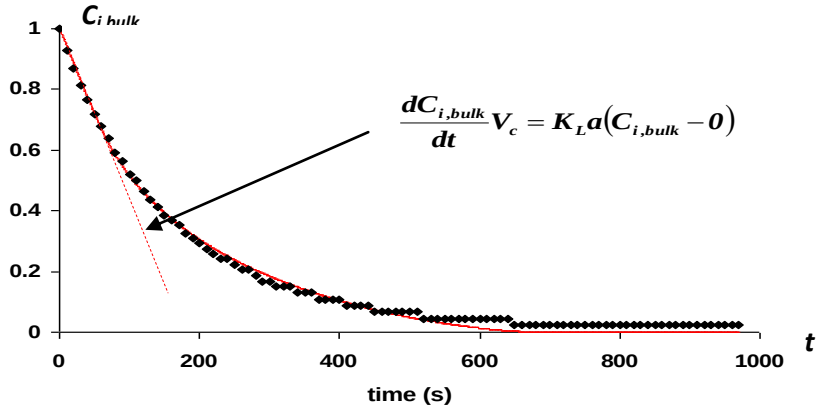

Fig.3-3 Laminar layer mass transfer coefficient (K_L) from initial slope data

A simplified Newton's Law of cooling model is assumed to be applicable as shown in Fig.3-3 (similar to Equ.3-2) where the '***a'*** is a combination of the systems parameters. Grouping all the constants as presented in Equ.3-2 gives Equ.3-4 from which a proportionality relationship can be deduced.

$$-\frac{dC_{i,bulk}}{dt} = \left(\frac{\left[4\pi R^2 N_R\right]K_L}{V_C}\right)\left(C_{i,bulk} - C_i^*\right) \quad \therefore \quad -\frac{dC_{i,bulk}}{dt} \propto \left(C_{i,bulk} - C_i^*\right) \qquad \textbf{3-4}$$

As can be seen from Equ.3-4, this model presents the reality that there will be a direct proportionality between the bulk concentration and the derivative of the bulk concentration of the adsorbing ion against time, suggesting that a first order decay function should be followed. It now becomes possible to rework Equ.3-4 in terms of the concentration of the

desorbing ion (C_D), the H^+ concentration in the bulk being easier to measure providing that there is no anion present with which the H^+ may form a complex.

The outcome of this is Equ.3-5 the derivation of which is presented in Annexure VI. It is therefore logically deduced that in the same finite system the derivative against time of the desorbing ion should also be proportional to the difference between the concentration of the desorbing ion at time t and the concentration of the desorbing ion at $t = \infty$ in the bulk solution (Equ.3-6).

$$-\frac{d\left(C_{D,t=\infty} - C_D\right)}{dt} \propto \left(C_{D,t=\infty} - C_D\right) \qquad \textbf{3-5}$$

Where

C_D Concentration of the desorbing ion in the bulk solution (*mol/L*)

$C_{D,t=\infty}$ Concentration of the desorbing ion in bulk at $t = \infty$. (*mol/L*)

From the final concentration/equilibrium measurement for each kinetic curve it becomes possible to rewrite Equ.3-5 in terms of conversion giving Equ.3-6 where $X_D = 1$ at $t = 0$ and $X_D \rightarrow 0$ as the transient approaches equilibrium.

$$-\frac{dX_D}{dt} \propto X_D \qquad \textbf{3-6}$$

Where

X_D $\left(C_{D,t=\infty} - C_D\right)/\left(C_{D,t=\infty} - C_{D,t=0}\right)$ resin conversion (dimensionless)

However, the method of initial slope measurement requires the assumption that the concentration of the ad-sorption ion on the surface of the resin bead – at the interface - is zero, allowing for the calculation of the driving force across the laminar layer from bulk concentrations only, i.e. $C_{i,bulk} - C_i^*$, where $C_i^* = 0$. For the purposes of using a concentration based model this is reasonable. Another automatic assumption therefor, is that mass transfer through the laminar dynamic layer is the only controlling mechanism during this early stage of the transient which might not be entirely realistic for highly turbulent environments.

For the relatively simple process of fitting a surface model to a kinetic curve these assumptions will suffice but when a second mechanism in series, diffusion inside the resin bead, is being simulated simultaneously, the zero concentration assumption at the surface is deficient as it then negates there being any flux into the resin. The particulate nature of the resin bead and the reality that most processes have the ion exchange resin undergoing a substantial, often total, conversion requires that the simulation and therefore the measurement of both serial mechanisms be undertaken simultaneously.

3.3. Calculating the concentration in solution at the interface (C_i^*)

The key factor in the simulation is the interface or ionic concentration at the resin surface (C_i^*). It is expected that its true value is never zero but is a floating value intrinsic to the driving force of both serial mechanisms, which augments/attenuates a mass flux across the laminar layer and simultaneously a flux into the resin interior, these two fluxes being equal to prevent either an excess or dearth of ionic mass at the interface.

Ultimately, it is assumed that the surface value approaches the final bulk concentration asymptotically and equilibrium with the concentration in the resin bead, simultaneously. The mass transfer coefficient determined in this manner is likely to be more realistic and will always be higher than that determined by the initial slope measurement technique, as the surface concentration will need to be higher than zero, thereby providing a lower driving force for mass transfer across the laminar layer which in turn requires a higher mass transfer coefficient to correlate this reduced driving force to the same measured mass flux across the laminar dynamic layer.

To determine the concentration in solution at the surface and assuming that Equ.3-7 is representative of the mechanism, it is necessary to first calculate the flux of ions (N_i) at time (t) across the interface from measured kinetic data. This can be done by taking the derivative of the measured bulk concentration ($-dC_{i,bulk}/dt$) verses time in the finite volume (V_C) and taking into account the interface surface area ($4\pi R^2 N_R$) and assuming that all ionic mass that leaves the bulk reports to the resin.

$$N_i = -\left.\frac{dC_{i,Bulk}}{dt}\right|_t \frac{V_C}{4\pi R^2 N_R} \cdot 1000 \qquad \textbf{3-7}$$

Where

N_i Flux of adsorbing ion across the interface ($mol/m^2.s$)

With a flux equation in place it then becomes possible to calculate the interface concentration (C^*_i) for any given value of mass transfer coefficient (K_L), given the bulk concentration at time ***t,*** by using Equ.3-8 which is derived directly from Newton's law of cooling (Equ.3-2).

$$C_i^* = C_{i,Bulk} - N_i / (1000 \cdot K_L) \qquad \textbf{3-8}$$

3.3.1. Determining a flux equation from raw kinetic data

In the present study our bulk concentration versus time data is measured in the laboratory using ion selective probes connected to computers, giving the advantage of high frequency reading, i.e. once every 10 seconds. However, only the log of the actual concentration was measured i.e. $p[H^+]$, which meant that any error was greatly amplified. Although this did not pose a challenge initially, when attempting to calculate a differential equation for the purposes of determining an ion flux its erratic behaviour becomes apparent. This is particularly acute close to the asymptote where minor erratic noise in concentration could result in large changes in flux and occasionally even return positive derivative values. Fig.3-4 is a typical example of a kinetic curve showing the decrease in concentration of the adsorbing ion in a closed-circuit type.

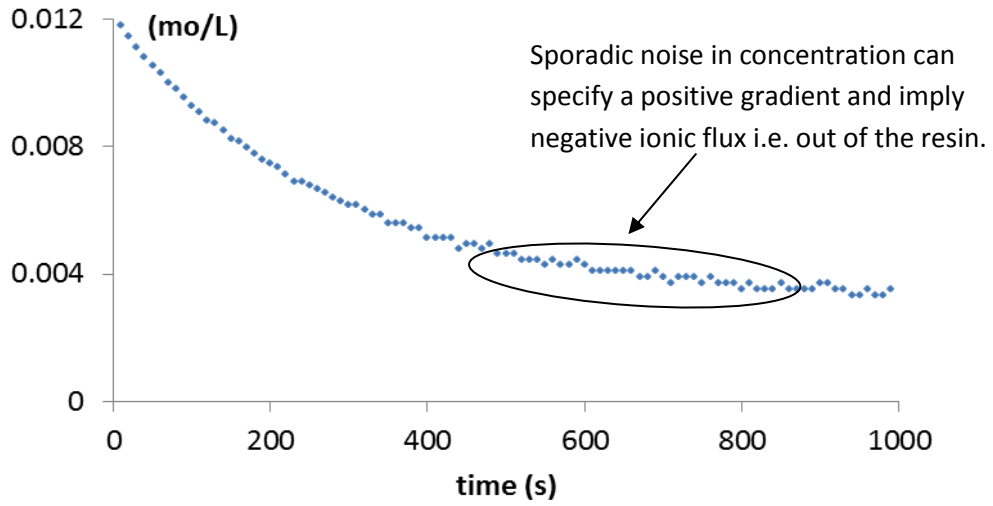

Fig.3-4 Typical bulk concentration kinetic data measured by probe

When the actual gradient is calculated from the bulk concentration curve using a simple differences method, extremely erratic data are calculated.

To overcome this difficulty a broadened form of Equ3-8 was used which incorporated an averaging technique that determined an average flux value for each data point as shown in Equ.3-9. This was calculated from the three bulk concentration data points recorded prior and post the point in time at which the flux is being calculated, all six bulk concentrations being equally weighted. This had the effect of greatly smoothing the curve although this implies that no flux values could be calculated for the first three and last three bulk concentration data points. Fig.3-5 shows the calculated flux value for the data shown in Fig.3-4, using Equ.3-9.

$$N_i^a = \frac{\left[\left.\frac{C_{i,bulk}}{dt}\right|_{t-3\Delta t} + \left.\frac{C_{i,bulk}}{dt}\right|_{t-2\Delta t} + \left.\frac{C_{i,bulk}}{dt}\right|_{t-\Delta t} + \left.\frac{C_{i,bulk}}{dt}\right|_{t+\Delta t} + \left.\frac{C_{i,bulk}}{dt}\right|_{t+2\Delta t} + \left.\frac{C_{i,bulk}}{dt}\right|_{t+3\Delta t}\right] V_C}{6\times 4\pi R^2 N_R} \quad \textbf{3-9}$$

Where

N_i^a flux calculated from adjacent measured bulk concentrations ($mol/m^2.s$)

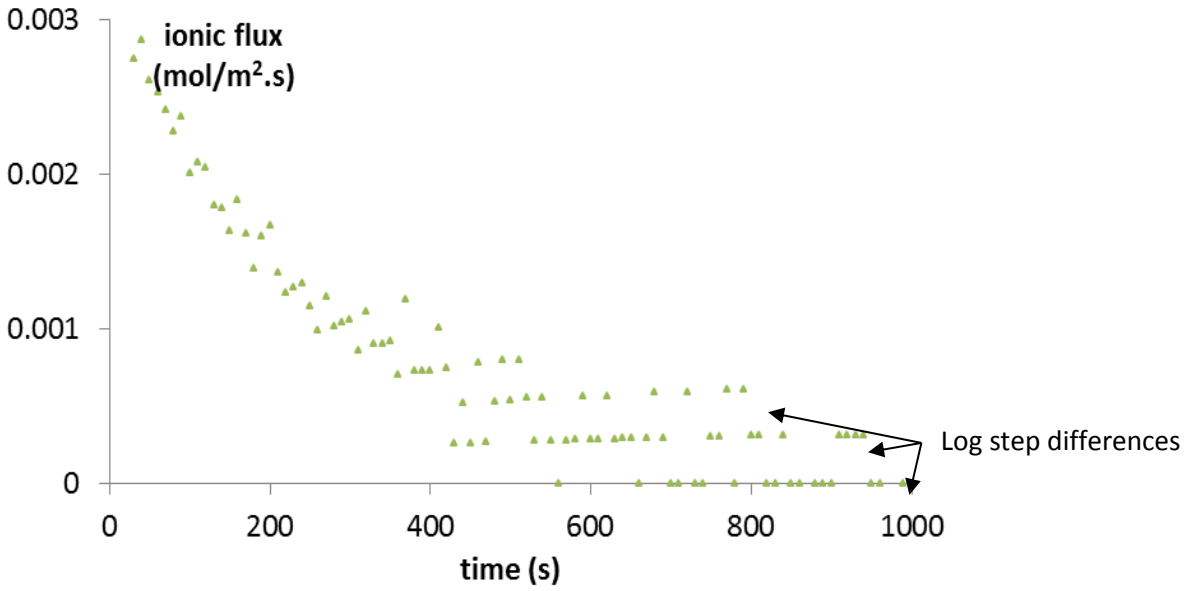

Fig.3-5 **Flux rate, calculated using Equ.3-9**.

As a pragmatic exercise, a further smoothing was achieved by fitting an adapted linearized form of a general first order decay function (Equ.3-10) to the averaged flux curve versus time. The result retuned unique values for K_1 and K_0 for each measured data set achieving excellent fits for all flux curves. Fig.3-6 shows the fitted curve and the raw flux data. Fig.3-7 is an example of a parity line fitted to model-generated flux data versus raw flux data.

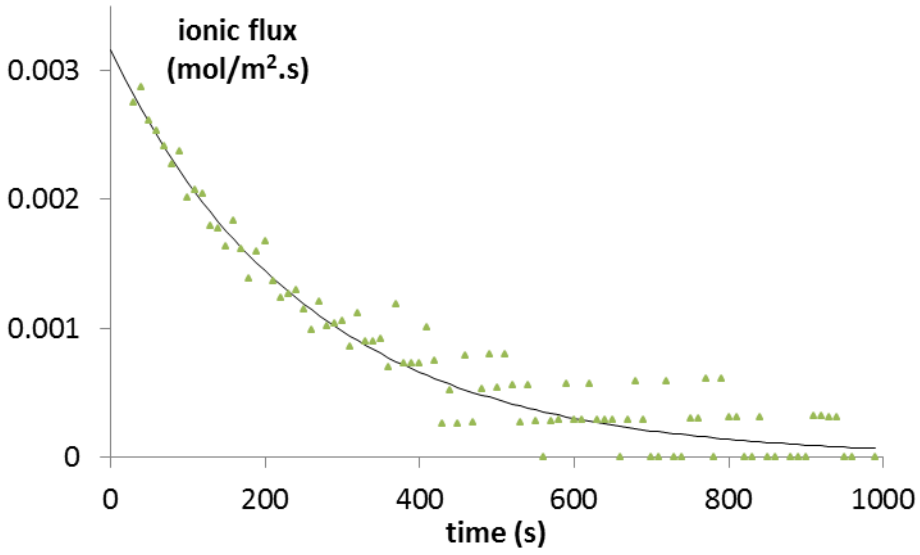

Fig.3-6 **Fitted first order model and raw flux data** $N_i^a = e^{K_0 + K_1 t}$

In addition to achieving a greatly smoothed curve it also gave a continuous function describing the rate of flux throughout the transient process (Equ.3-11) which was essential to ensure the smooth working of the simulator algorithm as a whole.

$$ln(N_i^a) = K_0 + K_1 t \qquad \textbf{3-10}$$

$$N_i^a = e^{K_0 + K_1 t} \qquad \textbf{3-11}$$

Where

K_0 Measured constant which can be equated to $Ln\left[N_i^a\right]_{t=0}$

K_1 Measured constant which can be equated to a rate constant

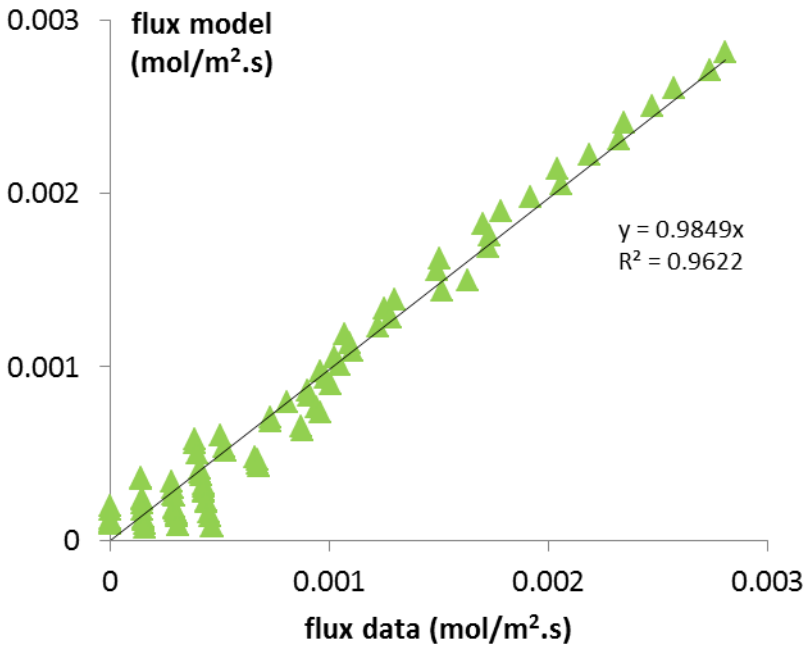

Fig.3-7 Flux data vs flux calculated from model

Finally, an accuracy check was undertaken by integrating the derived flux model over the entire time range (Equ.3-12) and then comparing it to the original bulk concentration data to ensure that it was still representative (Fig3-8).

$$\int_{C_{i,bulk(t=0)}}^{C_{i,bulk(t)}} dC_{i,bulk} = \int_{t=0}^{t=t} e^{K_0+K_1 t} dt$$

$$C_{i,bulk(t)} = C_{i,bulk(t=0)} - \left[e^{K_o+K_1 t} - e^{K_o}\right]\frac{1}{K_1} \qquad \textbf{3-12}$$

The goodness of fit in Fig.3-8 is seen as a final justification of the use of this convoluted numerical technique to elucidate the ion flux from the bulk solution into the resin, from bulk concentration data.

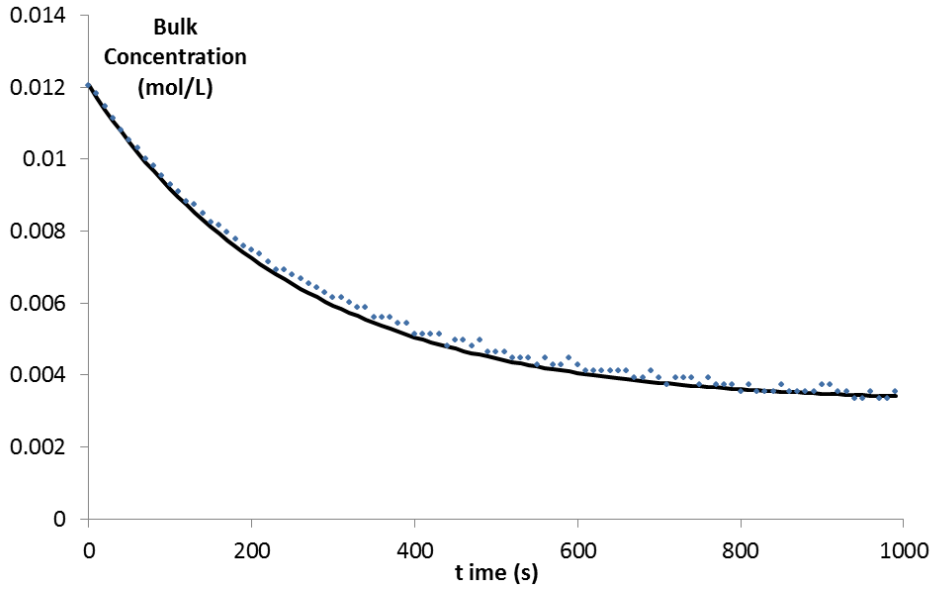

Fig.3-8 Integrated flux model fitted to raw bulk data

3.3.2. Surface concentration

With the establishment of a relationship that defines the flux across the laminar layer and into the resin bead it now becomes possible to simulate the mass transfer across both the laminar layer and into the resin. Both the bulk concentration and therefore the flux reduce during the adsorption transient, resulting in increasing surface concentration which ultimately equals bulk concentration once the no-net-flux condition is achieved. Fig.3-9 gives an indication of what might be expected for a specific mass transfer coefficient (K_L) and raw bulk data set ($C_{i,bulk} = f(t)$), the surface concentration being calculated from Equ.3-8&Equ.3-9.

Having established a model that determines the surface concentration from the derivative of bulk concentration the next challenge is to determine the concentration just inside the resin matrix, at the interface. The intra-particle diffusion process, it is postulated, will be entirely driven by this concentration making it necessary to establish a link between the surface concentration in the exterior liquid and the concentration in the outermost bounds of the resin matrix.

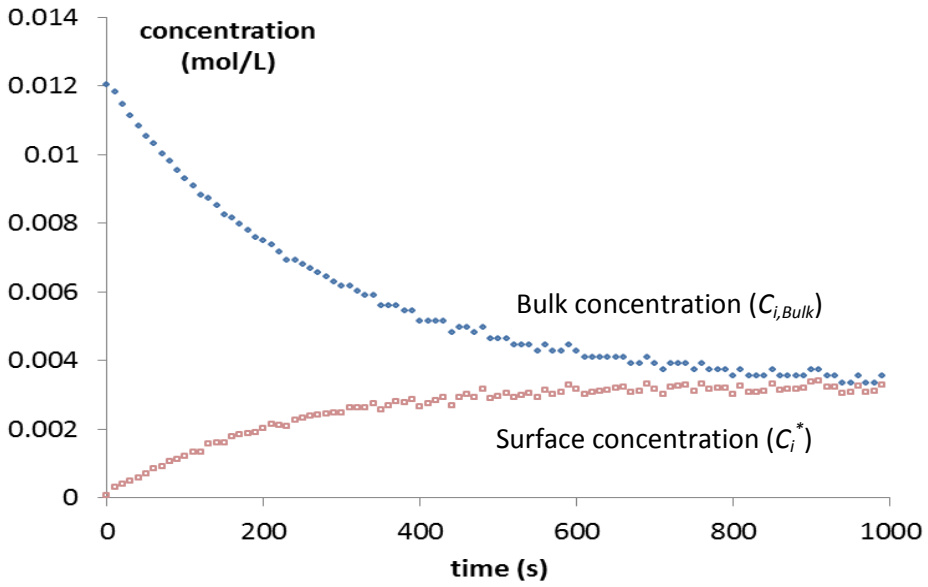

Fig.3-9 Simulation of surface concentration during transient (K_L = 0.275 m/s)

3.4. Equilibrium and the Mass-Action-Law

A reasonable assumption is that under all circumstances the concentration in the liquid at the surface and the concentration in the outer most bounds of the resin bead will always be at equilibrium as proximity ensures that any tendency for departure from equilibrium will rapidly be corrected and the equilibrium ion-distribution maintained/restored.

To link the surface concentration simulation to the outermost resin matrix concentration, the Mass-Action-Law equilibrium model (Equ.3-13) was used. This equilibrium model has a single parameter i.e. the equilibrium coefficient (α) to define the relationship and originates from the ratio of the forward and reverse rate equations (Equ.3.12) the two rates being assumed to be equal once equilibrium is reached.

$$C_i + \overline{C_D} \Leftrightarrow \overline{C_i} + C_D \qquad [C_i]\cdot[\overline{C_D}]k_f = [\overline{C_i}]\cdot[C_D]k_r \qquad \textbf{3-12}$$

$$\frac{\overline{C_i}}{C_i}\cdot\frac{C_D}{\overline{C_D}} = \frac{k_f}{k_r} = \alpha \qquad \textbf{3-13}$$

Where

$\overline{C_i}$, C_i	Concentrations of the adsorption ion in the resin and solution respectively at equilibrium (*mol/L*)
$\overline{C_D}$, C_D	Concentrations of the desorption ion in the resin and solution respectively at equilibrium (*mol/L*)
k_f, k_r	Forward and reverse rate constants respectively (*L/mol.s*)
α	Equilibrium constant for the Mass-Action-Law (*dimensionless*)

3.4.1. Calculating the equilibrium constant (α)

In an infinite medium system the release of desorbing ions into the bulk is of no consequence as these are immediately flushed out of the resin bed, likewise the concentration of the adsorbing ion adjacent to the resin will always be high and constant. However, if resin ion exchange is conducted in a finite medium there will be build-up of displaced desorbing ions in the finite bulk that will compete with the adsorbing ion for re-adsorption. In addition the total ions that can be accommodated on the resin are also finite. Under these circumstances the Mass-Action-Law model lends itself to resin equilibrium measurement as, unlike other common equilibrium models such as the Freundlich or Langmuir, it takes into account the concentrations of both competing ions in the finite system, in both the liquid and resin phases. The equilibrium constant (α) can be determined through dedicated equilibrium tests in a finite system in the laboratory, followed by the fitting of the Mass-Action-Law equilibrium model to the measured data a graphical output of which would be similar to Fig.3-10.

It is notable that the valence of the adsorbing ions will play an important role as capacity for a particular ionic species can only be measured in terms of equivalents i.e. ion molarity x valence. In the context of ion exchange resin the Mass-Action-Law equilibrium coefficient is the ratio of the product of the adsorbing ion equivalent fraction on the resin and the desorbing ion equivalent fraction in the bulk divided by the product of the equivalent fraction of the adsorbing ion in the bulk and the equivalent fraction desorbing ion in the resin all at the equilibrium condition. Both the finite bulk fluid and the resin copolymer mass have constant concentrations of ions - measured in equivalents – at all times during the transient hence the concentration of the competing ions in each phase can be measured in equivalent fractions. Equ.3-14 gives the appropriate equation providing both adsorbing and desorbing ions have identical valence.

$$\alpha = \frac{\dfrac{\overline{C_i}}{\overline{C_i}+\overline{C_D}} \times \dfrac{C_D}{C_i+C_D}}{\dfrac{C_i}{C_i+C_D} \times \dfrac{\overline{C_D}}{\overline{C_i}+\overline{C_D}}} \qquad \textbf{3-14}$$

Where

$\left[\dfrac{\overline{C_i}}{\overline{C_i}+\overline{C_D}}\right]$ Equilibrium fraction of adsorbing ion in resin (dimensionless)

$\left[\dfrac{C_i}{C_i+C_D}\right]$ Equilibrium fraction of adsorbing ion in bulk (dimensionless)

It's important to note that the equivalent fractions of the competing species in both the resin phase and the bulk solution are complementary and therefore it now becomes possible to remove the desorption ion from the equation. Hence Equ.3-14 can be re-written, to incorporate this complementarity, into Equ.3-15 assuming once again that the fraction is measured in equivalents or that both ions have the same valence.

$$\alpha = \frac{\left[\dfrac{\overline{C_i}}{\overline{C_i}+\overline{C_D}}\right]\left(1-\left[\dfrac{C_i}{C_i+C_D}\right]\right)}{\left[\dfrac{C_i}{C_i+C_D}\right]\left(1-\dfrac{\overline{C_i}}{\overline{C_i}+\overline{C_D}}\right)} \qquad \textbf{3-15}$$

Equ.3-15 can be reworked into Equ.3-16 for the purposes of conveniently demonstrating the entire range of equilibrium distribution for a finite system, as presented in Fig.3-10.

$$\left[\frac{\overline{C_i}}{\overline{C_i}+\overline{C_D}}\right]=\frac{\alpha\left(\dfrac{\dfrac{C_i}{C_i+C_D}}{1-\dfrac{C_i}{C_i+C_D}}\right)}{1+\alpha\left(\dfrac{\dfrac{C_i}{C_i+C_D}}{1-\dfrac{C_i}{C_i+C_D}}\right)} \qquad \textbf{3-16}$$

Essentially, the higher the equilibrium constant the greater the affinity the resin has for the adsorbing ion. An equilibrium coefficient of one (α =1) implies that there is no difference in affinity for the two ions between the bulk and the resin co-polymer matrix.

Fig.3-10 is a graphical output of the Mass-Action-Model, where α >1, taken from Helfferich (1962) page 152 and shows how the concentration relationship moves between there being both zero concentration on the resin and solution of the adsorption ion $\left[\overline{C_i}/\left(\overline{C_i}+\overline{C_D}\right)=0=C_i/(C_i+C_D)\right]$to an adsorption ion saturated resin matrix at full ion capacity $\left[\overline{C_i}/\left(\overline{C_i}+\overline{C_D}\right)=1=C_i/(C_i+C_D)\right]$ where the adsorption ion dominates the solution and the resin phases.

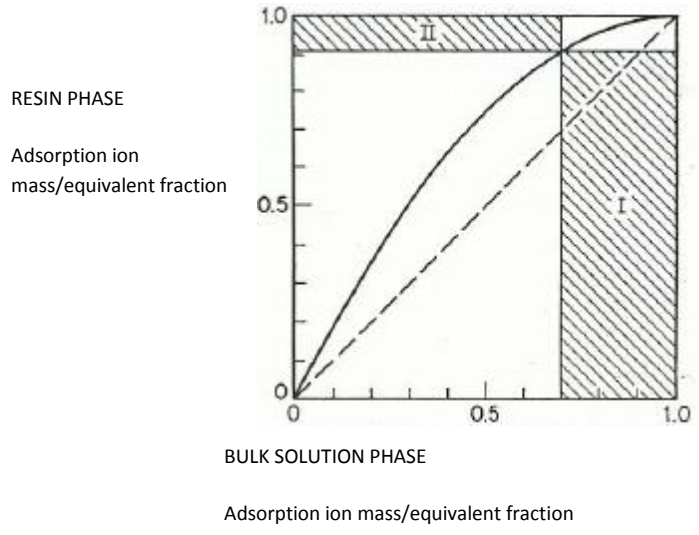

Fig.3-10 Mass-Action-Law equilibrium graph (Helfferich, 1962)

3.4.2. Mass-Action-Law for multi-valent ions

Multi-valent ions present a difficulty when applying the Mass-Action-Law. As we have already seen, the nature of the resin co-polymer matrix is such that it contains a finite number of active sites onto which the adsorbed ions can attach. A common assumption is that the total moles of ions attached to the resin matrix at any-time ***t*** during the transient are constant for adsorbing and desorbing ions that have the same valence. However for ions of different valence this will not be valid and this can easily be seen in Equ.3-17, which is generally assumed to hold true. This therefore requires the definition of two types of mass fraction occupying the resin matrix i.e. molar mass fraction or equivalent mass fraction.

$$z_i \overline{C_i} + z_D \overline{C_D} = \overline{C_T} \qquad 3\text{-}17$$

Where

$\overline{C_T}$ Total specific concentration of active sites in the resin (*equiv./L*)

z_i Valence of adsorbing ion on resin (*dimensionless*)

z_D Valence of desorbing ion on resin (*dimensionless*)

The relationship between molar mass fraction and equivalent mass fraction can be determined from fundamental principles. The concentration of the adsorbing ion in the resin medium in terms of equivalents (X_i) is given by Equ.3-18. Similarly the concentration of the desorbing ion in the resin medium in terms of equivalents ($1 - X_i$) is given by Equ.3-19.

$$\overline{C_i} = \frac{\overline{C_T} \times X_i}{z_i} \qquad \textbf{3-18}$$

$$\overline{C_D} = \frac{(1 - X_i) \times \overline{C_T}}{z_D} \qquad \textbf{3-19}$$

Where

X_i Equivalent mass fraction of species *i*, in resin medium (dimensionless)

To determine the molar fraction inside the resin matrix Equ.3-18 and Equ.3-19 are combined to give an equation based on molarity (Y_i) (Equ.3-20). Assuming that the desorbing ion has a valence of one, appropriate if the resin is in the H^+ form to begin with, Equ3-20 can be simplified to Equ3-21.

$$\frac{\frac{\overline{C_T} \times X_i}{z_i}}{\frac{\overline{C_T} \times X_i}{z_i} + \frac{(1 - X_i) \times \overline{C_T}}{z_D}} = Y_i \qquad \textbf{3-20}$$

$$\frac{X_i}{X_i + z_i - z_i \times X_i} = Y_i \qquad \textbf{3-21}$$

Where

Y_i molar mass fraction of ion species *i*, in the resin medium (dimensionless)

The relationship between the mass fractions based on equivalents versus mass fractions based on molarity, for an ion that has a valence of one, two, or three, when paired with an ion that has a valence of one, is displayed in Fig.3-11. This is an important relationship as the molar mass fraction in the bulk solution will be based on molar concentration and hence mol fraction. Through the Mass-Action-Law it becomes possible to determine the mole fraction concentration in the resin matrix. However, converting this to equivalents based mass fraction, because of the stricture of the active sites inside the resin, requires Equ.3-21.

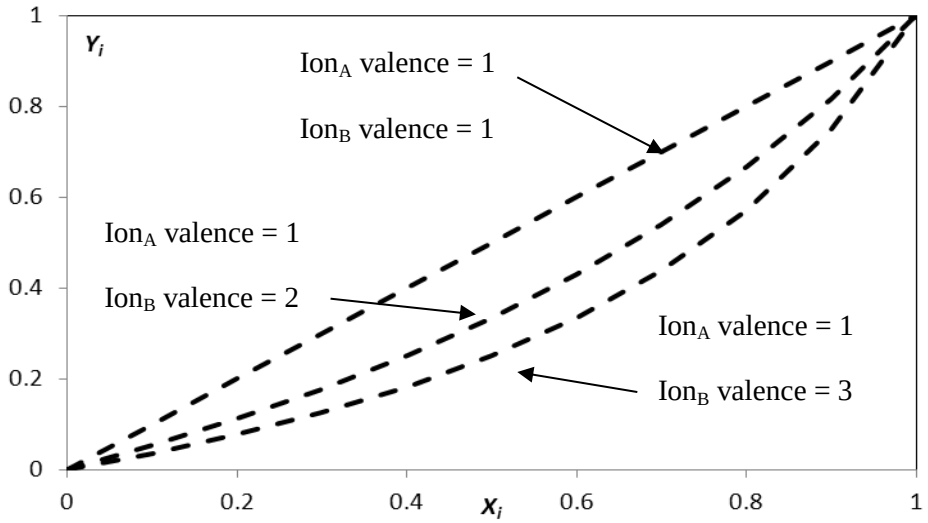

Fig.3-11 Mass fraction in resin medium, molar versus equivalent

For transient simulation purposes, when calculating the bulk and surface concentrations of the adsorbing ion it becomes necessary to link the quantities of both the desorbing and adsorbing ion in both the finite- bulk and resin phases. This is achieved by mass balances to ensure continuity between the two phases for each time step, during the entire transient. The concentration in the resin phase at the surface must be based on equivalents because of the stricture of the fixed number of resin active sites. As the equilibrium mass action model is the link between the concentration inside the resin and the surface concentration and it therefore becomes necessary to converted to mole mass fraction to determine the equilibrium situation in the liquid at the surface i.e. the surface concentration. In addition, the mass balances between the bulk and the resin phases need to take heed of the change in molar mass inside the resin applicable to having ions of different valence present.

3.5. Nernst-Plank equation

3.5.1. Application of Nernst-Plank on spherical coordinates.

With the concentration of ions present in the resin phase at the surface being established it now becomes possible to apply the Nernst Plank equation in a discrete manner to the internal environment of the resin.

The intra-particle diffusion of the de-sorption (D_i) and ad-sorption (D_D) ions is assumed to be intrinsically linked to the steric environment inside the resin bead which is considered homogeneous. Hence the state of the internal structure of the resin, it is hypothesised, will impact on the intrinsic intra-particle diffusion of the exchanging ions as they pass through the resin.

It was assumed in this study that ion diffusion inside the resin bead (J_i) and transient approach to total conversion is dictated by the Nernst-Plank diffusion equation for binary ionic systems that builds on Fick's Law i.e. Equ.3-22 and Equ.3-23. Fick's Law dictates that all atomic/molecular flux is due to concentration gradients. However, Nernst-Plank

incorporate the effect of charge clouds to Fick's Law which is highly applicable in an intra-particle environment such as that found in resin where the charge cloud present, generated by the migrating ions and the active sites, is bound to have an impact on ion diffusion.

For the ad-sorption ion

$$\boldsymbol{J_i = J_{diff.i} + J_{el.i} = -D_i\left(\nabla\overline{C_i} + z_i\overline{C_i}\frac{F}{RT}\nabla\varphi\right)} \qquad 3\text{-}22$$

For the de-sorption ion

$$\boldsymbol{J_D = J_{diff.D} + J_{el.D} = -D_D\left(\nabla\overline{C_D} + z_D\overline{C_D}\frac{F}{RT}\nabla\varphi\right)} \qquad 3\text{-}23$$

Where

J_D, J_i	Mol flux of the desorbing, adsorbing ion ($mol/dm^2.s$)
$J_{diff.i}$, $J_{diff.D}$	Mol flux resulting from concentration gradients for the adsorbing, desorbing ions ($mol/dm^2.s$)
$J_{el.i}$, $J_{el.D}$	Mol flux resulting from charge cloud forces for the adsorbing, desorbing ions ($mol/dm^2.s$)
D_i, D_D	Intrinsic diffusivity of adsorbing, desorbing ion (dm^2/s)
$\boldsymbol{\varphi}$	Charge cloud electrical potential (J/C)
$\boldsymbol{F}$	Faraday's constant (96 485 C/mol)
$\boldsymbol{R}$	Universal gas constant (8.314 $J/mol.K$)
$\boldsymbol{T}$	Temperature (K)

Combining these two equations on the grounds of assuming 'super position' in the electrical force field generated by the charge cloud (explained in Annexure I) gives a final equation (Equ.3-25) that resembles Fick's law but where the Fickian diffusivity is a variable and is a function of the concentration of the ionic species ($\overline{C_i}$,$\overline{C_D}$), their associated intrinsic diffusivities (D_i, D_D) and valences (z_i, z_D). Equ.3-25a defines it as being an apparent diffusivity (D_{app}). An additional assumption for the application of the Nernst-Plank model is the no-current condition within the resin described by Equ.3-24. This is a reasonable

assumption given that without it, excessive electrical charges would be allowed to build up within the resin matrix and hence it is used in the derivation of Equ.3-25.

$$z_i J_i + z_D J_D = 0 \qquad 3\text{-}24$$

$$J_i = -\left[\frac{D_i D_D \left(z_i^2 \overline{C_i} + z_D^2 \overline{C_D} \right)}{D_i z_i^2 \overline{C_i} + D_D z_D^2 \overline{C_D}} \right] \nabla \overline{C_i} \qquad 3\text{-}25$$

$$D_{app} = \left[\frac{D_i D_D \left(z_i^2 \overline{C_i} + z_D^2 \overline{C_D} \right)}{D_i z_i^2 \overline{C_i} + D_D z_D^2 \overline{C_D}} \right] \qquad 3\text{-}25a$$

Where

D_{app} Apparent diffusivity (m^2/s)

The simulation of intra-particle mass transfer has as its unconditional driving force the concentration of ad-sorption ions and de-sorption ions on the outer most edge of the resin, but inside the resin copolymer material. This value is obtained from the Mass-Action-Law equilibrium model that links to the concentration in the solution on external surface of the resin.

As this part of the simulation is contained inside the spherical-geometry resin particle, radial symmetry was assumed with respect to mass transport and the Nernst-Plank equation was therefore combined with the spherical geometry version of Fick's second law (Equ.3-26) for point mass balances,

$$\frac{\partial \overline{C_i}}{\partial t} = \frac{1}{r^2} \frac{\partial}{\partial r} \left(r^2 D_{app} \frac{\partial \overline{C_i}}{\partial r} \right) \qquad \mathbf{3\text{-}26}$$

Where

r Radial distance to the point where mass balance is applied (dm)

Fig.3-12 shows a simulation of the conversion of an ion exchange bead based on Equ3-25and Equ.3-26. The simulation is based on the bead being comprised of five consecutive concentric shells and shows the change in concentration in each. The resultant mass balance equation for each concentric shell was solved using a square matrix inversion technique and

the shells were solved implicitly for each second of the transient. It is notable that the inner most shell takes the longest to convert while the outer most shell converts the quickest which is to be expected.

Also important in the discrete application of the Nernst-Plank model is Equ.3-27 which calculates the overall conversion of the resin beads by integrating the concentrations of the adsorbing ions from the centre of the bead, along the radial line, to the external surface. Application of this equation at any point in time during the transient gives the overall conversion of the resin bead which is also presented in Fig.3-12.

$$\overline{C_{i,avg}} = \frac{\int_{r=0}^{r=R} \overline{C_i} dr}{\frac{4}{3}\pi R^3} \qquad \textbf{3-27}$$

Where

$\overline{C_{i,avg}}$ Average concentration of *i* throughout the bead (*mol/L*)

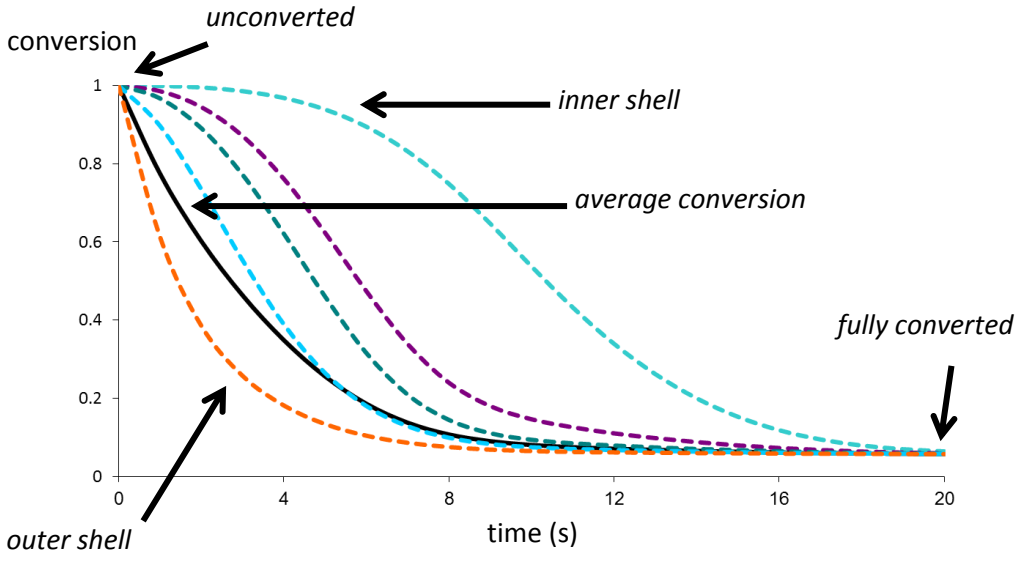

Fig.3-12 Simulation of Equ.3-25 on spherical co-ordinates (Equ.3-26), 5 shell system

3.6. Discrete application of the Nernst Plank equation

The easiest way of applying the Nernst Plank equation on spherical coordinates (Equ.3-29) is by using a discrete element method, effectively compartmentalising the resin bead into a number of concentric shells and ensuring that Equ.3-29 is adhered to in each.

$$\frac{\partial \overline{C_i}}{\partial t} = \frac{1}{r^2}\frac{\partial}{\partial r}\left(r^2 \left[\frac{D_i D_D \left(z_i^2 \overline{C_i} + z_D^2 \overline{C_D} \right)}{D_i z_i^2 \overline{C_i} + D_D z_D^2 \overline{C_D}} \right] \frac{\partial \overline{C_i}}{\partial r} \right) \qquad \textbf{3-29}$$

Boundary conditions for Equ.3-29 i.e. at $r = 0$ and $r =$ R, also need to be defined and they are as follows;

No ionic flux at the centre of the bead along the radial line of symmetry (Equ.3-29). The concentration of the adsorption ion at the outer most bound of resin polymer (r = R) at time t is defined as a function of the solution surface concentration of the adsorbing ion at time t, via the Mass-Action-Law (Equ.3-30).

$$r = 0, \quad \frac{\partial \overline{C_i}}{\partial r} = \frac{\partial \overline{C_D}}{\partial r} = 0 \qquad \textbf{3-29}$$

$$r = \mathrm{R}, \quad \overline{C_{i,sur}} = f(C_i^*) \qquad \textbf{3-30}$$

Where

$\overline{C_{i,sur}}$ Concentration of adsorbing ion in resin matrix at surface (*mol/L*)

To determine the apparent diffusivity (D_{app}), which is the combination of concentrations, intrinsic diffusivities and valences of the two ions present in the matrix, at any particular point r in the resin matrix (Equ.3-25a) it becomes necessary to calculate the concentration of

the desorbing ion at that particular point ***r***. Equ.3-31, which originates from Equ.3-17, is used for this.

$$\overline{C_D} = \frac{\overline{C_T} - z_i \overline{C_i}}{z_D} \qquad \textbf{3-31}$$

Although a number of numerical techniques could be employed to simulate Equ.3-29 discretely, it was decided to use the implicit method, where unique mass balancing equations, established for each discrete concentric shell, could be simultaneously rapidly solved by using matrices. Although more complicated than the explicit routine it is more stable and quicker which will be a necessity if it is to be part of a search algorithm requiring hundreds of simulations during one data fit. An alternate method is that of Crank-Nicolson but the minuscule increased accuracy was thought not to warrant the increased complication and computation time.

Determining the implicit discrete mass balance equation to be applied inside the resin matrix for the general case over a time increment Δt and across the boundaries of a discrete shell, can be achieved using Equ.3-32.

$$\left(\frac{\overline{C_{i,P}^{t+\Delta t}} - \overline{C_{i,P}^{t}}}{(t+\Delta t) - t} \right) = \frac{4\pi r_{ob}^2 D_{app,po} \dfrac{\overline{C_{i,O}^{t+\Delta t}} - \overline{C_{i,P}^{t+\Delta t}}}{r_{MO} - r_{MP}} - 4\pi r_{ib}^2 D_{app,pi} \dfrac{\overline{C_{i,P}^{t+\Delta t}} - \overline{C_{i,I}^{t+\Delta t}}}{r_{MP} - r_{MI}}}{4\pi r_{ib}^2 (r_{ob} - r_{ib})} \qquad \textbf{3-32}$$

Where

$\overline{C_{i,P}^{t+\Delta t}}$, $\overline{C_{i,P}^{t}}$ Conc. in the shell being balanced at $t + \Delta t$ and t respectively *(mol/L)*

$\overline{C_{i,O}^{t+\Delta t}}$ Conc. in outside shell of the shell being balanced at $t + \Delta t$ *(mol/L)*

$\overline{C_{i,I}^{t+\Delta t}}$ Conc. in inside shell of the shell being balanced at $t + \Delta t$ *(mol/L)*

t Time *(s)*

Δt Time increment *(s)*

r_{ob} Radial distance to the outer boundary of the shell being balanced *(dm)*

r_{ib} Radial distance to the inner boundary of the shell being balanced *(dm)*

r_{MP} Radial distance to the middle of shell being balanced *(dm)*

r_{MO} Radial distance to the middle of shell on the outside the shell being balanced *(dm)*

r_{MI} Radial distance to the middle of shell on the inside of shell being balanced *(dm)*

$D_{app,pi}$ Apparent diffusivity to inside shell from the shell being balanced *(dm^2/s)*

$D_{app,po}$ Apparent diffusivity to outside shell from the shell being balanced *(dm^2/s)*

When using discrete numerical methods to simulate a point dynamic equation it becomes imperative to study the accuracy and stability of the numerical method employed. If the size of the radial increment Δr is too large, an inaccuracy with respect to the volume of each concentric shell may become significant, in addition if the time increment chosen Δt is too large for the size of Δr chosen instability may also occur as the mass balance over any particular increment, if over too long a period, may cause the shell to run out of simulated ions before the next time increment, so to speak.

In addition, any volume inaccuracy with respect to the volume of the shell can easily be overcome by substituting Equ.3-33 into Equ.3-32 w.r.t. the volume term i.e. the denominator of the right hand term gives Equ.3-34 and Equ.3-35.

$$4\pi r_{ib}^2\left(r_{ob}-r_{ib}\right)\approx\frac{4}{3}\pi\left(r_{ob}^3-r_{ib}^3\right) \qquad \textbf{3-33}$$

$$\left(\frac{\overline{C_{i,P}^{t+\Delta t}}-\overline{C_{i,P}^{t}}}{(t+\Delta t)-t}\right)=\frac{4\pi r_{ob}^2 D_{app,po}\dfrac{\overline{C_{i,O}^{t+\Delta t}}-\overline{C_{i,P}^{t+\Delta t}}}{r_{MO}-r_{MP}}-4\pi r_{ib}^2 D_{app,pi}\dfrac{\overline{C_{i,P}^{t+\Delta t}}-\overline{C_{i,I}^{t+\Delta t}}}{r_{MP}-r_{MI}}}{4/3\pi\left(r_{ob}^3-r_{ib}^3\right)} \qquad \textbf{3-34}$$

Grouping concentration terms putting into a matrix friendly format we achieve Equ.3-35

$$-\frac{3r_{ib}^2\Delta tD_{app,pi}}{\left(r_{ob}^3-r_{ib}^3\right)\left(r_{MP}-r_{MI}\right)}\overline{C_I^{t+\Delta t}}+\left(1+\frac{3r_{ob}^2\Delta tD_{app,po}}{\left(r_{ob}^3-r_{ib}^3\right)\left(r_{MO}-r_{MP}\right)}+\frac{3r_{ib}^2\Delta tD_{app,pi}}{\left(r_{ob}^3-r_{ib}^3\right)\left(r_{MP}-r_{MI}\right)}\right)\overline{C_P^{t+\Delta t}} \\ -\frac{3r_{ob}^2\Delta tD_{app,po}}{\left(r_{ob}^3-r_{ib}^3\right)\left(r_{MO}-r_{MP}\right)}\overline{C_O^{t+\Delta t}}=\overline{C_P^{t}} \qquad \textbf{3-35}$$

The equation for the inner most shell takes into account that r_{ib} is equal to zero and that the inner most shell is essentially a sphere giving Equ.3-36;

$$\left(\frac{\overline{C_P^{t+\Delta t}}-\overline{C_P^{t}}}{\Delta t}\right)=\frac{4\pi r_{ob}^2D_{app,po}\dfrac{\overline{C_O^{t+\Delta t}}-\overline{C_P^{t+\Delta t}}}{\left(r_{MO}-r_{MP}\right)}}{4/3\pi r_{ob}^3}=\frac{D_{app,po}\dfrac{\overline{C_O^{t+\Delta t}}-\overline{C_P^{t+\Delta t}}}{\left(r_{MO}-r_{MP}\right)}}{1/3r_{ob}} \qquad \textbf{3-36}$$

Simplifying further and converting to a matrix friendly equation gives Equ.3-37;

$$\left(\frac{3r_{ob}}{\left(r_{MO}-r_{MP}\right)}+\frac{D_{app,po}}{\left(r_{MO}-r_{MP}\right)}\right)\overline{C_P^{t+\Delta t}}-\frac{D_{app,po}}{\left(r_{MO}-r_{MP}\right)}\overline{C_O^{t+\Delta t}}=\frac{3r_{ob}}{\left(r_{MO}-r_{MP}\right)}\overline{C_P^{t}} \qquad \textbf{3-37}$$

Establishing the boundary condition for the external surface of the resin presents a challenge in an implicit calculation as the main driving force the concentration of the adsorbing ion on the outer most limit of the resin matrix (i.e. r = R) is a function of the concentration on the external surface in the liquid phase, which varies. Therefore it was decided that the implicit calculation would have to incorporate the external bulk solution as an outer concentric shell. It was decided to split the resin up into twenty five concentric shells inside the resin matrix. A twenty sixth concentric shell was added to the implicit calculation which represented the bulk liquid, its volume being proportional to the portion of bulk liquid associated with each resin bead in the finite test circuit (Fig.3-13).

The full derivation of all discrete equations and their solving by matrix operation are described in Annexures II & V respectively.

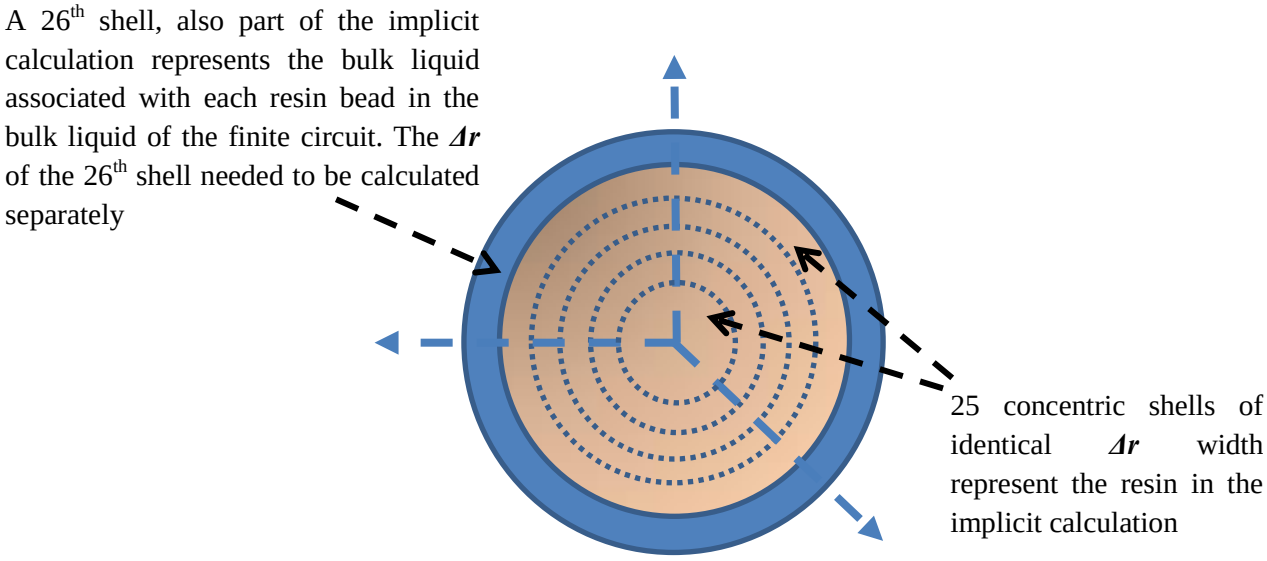

Fig.3-13 Implicit calculation has 25 shells for resin and a 26th for bulk liquid

3.7. Summary of overall model

In summation the model consists of three interconnected parts shown in Fig.3-14.

The first part concerns the extra-particle environment and is based on a form of Newton's Law of Cooling that attributes a mass transfer coefficient to describe the mass transport across the hydrodynamic laminar layer that is present on the external surface of the resin bead and that published empirical data would indicate constitutes a controlling mechanism for at least some of the earlier time data during the transient. This model requires as input, raw transient data from which a mass flux through the interface can be calculated in addition to a mass transfer coefficient (K_L) value.

The second part of the model is that described by the Nernst-Plank equation that reduces mass flux inside the resin matrix to an intra-particle diffusivity parameter defined for both the adsorbing and desorbing ions simultaneously taking into account the electrical forces present as a result of the ions present and the charge clouds associated with the active sites in

addition to the concentration gradients. This part of the model is applied in a radially discrete manner on what is assumed to be a homogeneous internal resin environment. It requires the intrinsic diffusivities (D_i, D_D) of both the desorbing and adsorbing ions.

Finally, for the purposes of total transient simulation the extra-particle and intra-particle parts of the model are linked by an equilibrium model based on the Mass-Action-Law that assumes that the outer most part of the resin matrix and the surface concentration in the bulk liquid are permanently at equilibrium with each other. This mode takes into account the change in concentration of both the adsorbing and desorbing ions in both the resin matrix and the finite external bulk solution. It requires a single equilibrium coefficient (**α**) to link the concentrations. Parallel to this equilibrium model is a mass balance that ensures continuity of both ad-sorption and de-sorption ions present in the finite system

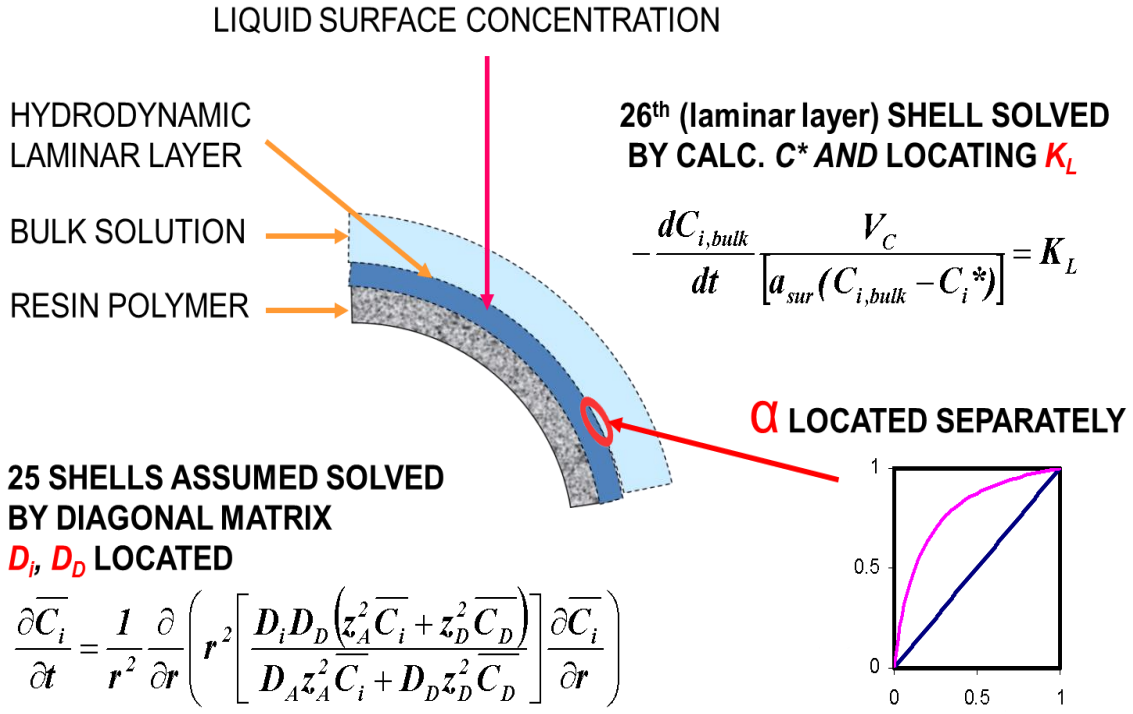

Fig.3-14 **Summary of the three model sections**

3.8. Numerical methods for simulation of developed model

The simulation of a transient adsorption via the model described in the previous section is a complex undertaking but was considered necessary as it was seen as being an integral part of calculating parameters of the system each of which would have to be calculated simultaneously i.e. the intra-particle diffusivities ($\boldsymbol{D_i}$, $\boldsymbol{D_D}$) and the mass transfer coefficient ($\boldsymbol{K_L}$).

The only manner in which accurate quantitative measurements can be determined is through observation of the behaviour of the bulk concentration during a transient adsorption. This infers that much needs to be deduced from this single variable and, as has already been shown in the literature survey, a complicated multi-mechanism adsorption process is envisaged. Comparison of the model simulation to the raw data is a traditional way of determining system parameters in the hopes that, should the model be rigorous enough, it may produce the same bulk concentration behaviour for the appropriately chosen parameters. All this necessitates the simultaneous simulation of the various parts of the model.

The investigative software written to elucidate the parameters of the system consisted of two main parts.

A simulator that simulates the three parts of the model described in the previous section with both the intra-particle and extra-particle parts running in series producing a kinetic curve of bulk concentration of the adsorbing ion versus time, as an output

A search algorithm that couples with the simulator effectively fitting simulated data to raw data measured in the laboratory by adjusting the system parameters such as intra-particle diffusivities and mass transfer coefficient. Fig.3-15 is a diagram of the overall structure of the software that combines both the simulator and the search algorithm.

3.8.1. The simulator

The simulator output is presented graphically in Fig.3-16. It consists of the bulk and surface concentration of the adsorption ion $\boldsymbol{t} = 0$ to $\boldsymbol{t} = \infty$, the measurement being in equivalents per litre. Also in the output for the purposes of studying mass flux inside the resin is the concentration versus time for each concentric shell, also measured in equivalents per litre. As can be seen from the list at the top of Fig.3-16, the required inputs are; the flux data versus time-array calculated from raw laboratory measured absorbing ion bulk concentration, an equilibrium constant, a mass transfer coefficient and the intrinsic diffusivities of the adsorbing and desorbing ions.

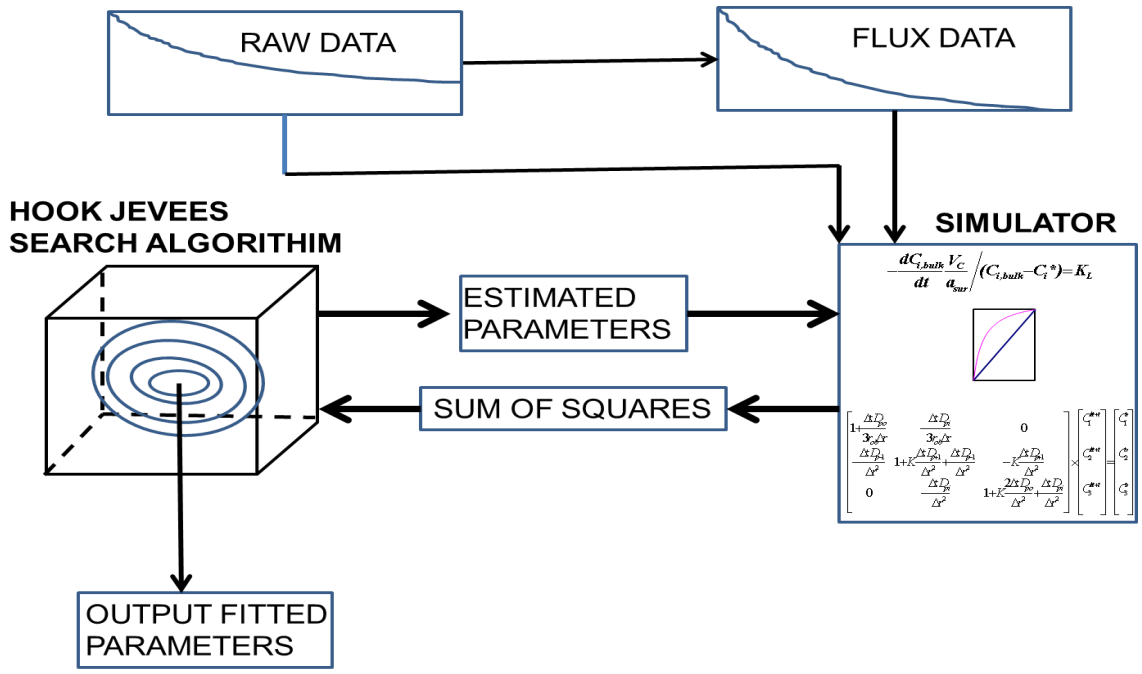

Fig.3-15 Overall structure of the simulator search algorithm software

3.8.2. The search algorithm

Estimated initial parameter values, of which generally there are either two or three ($\boldsymbol{D_i}$, $\boldsymbol{D_D}$, $\boldsymbol{\alpha}$) are giving to the search algorithm that then passes these to the simulator that then calculates a simulation as presented in Fig.3-16.

Initially in the study, the measure of goodness of fit between simulator and raw data was achieved by a simple sum of square fit of simulated to raw data (Fig.3-17), but this was considered to be inadequate as error was measured only in the vertical axis range (concentration) which meant that errors in steeper parts of the transient curve were given disproportionate prominence in the overall error measurement.

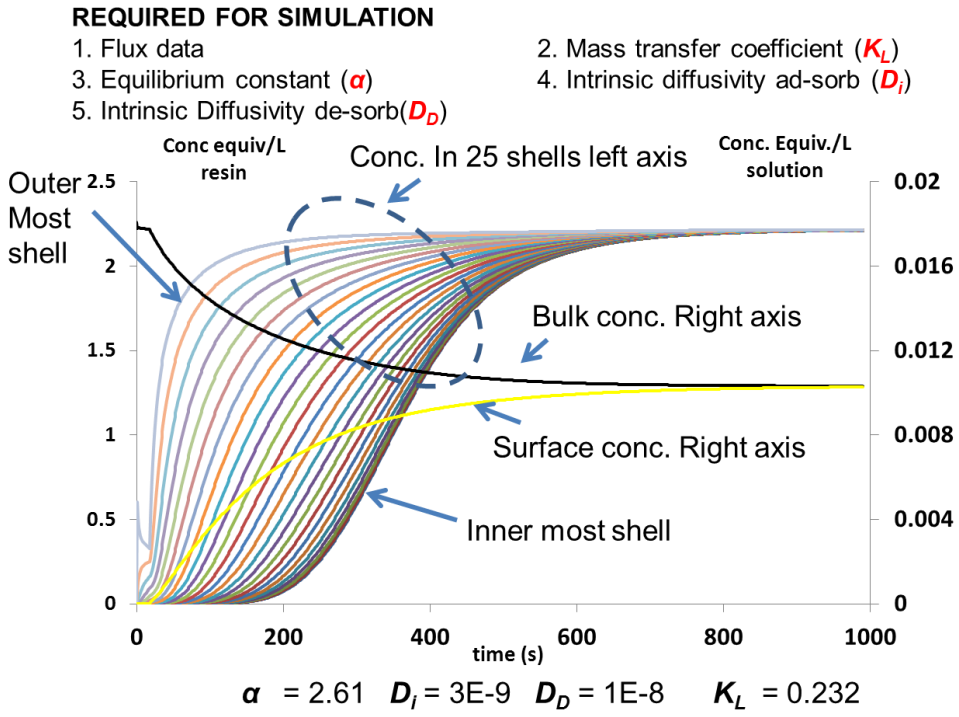

Fig.3-16 Graphical representation of simulator output

Later, an approach that achieved better results was to plot the concentrations of the raw data against the simulated concentrations for common times and then to perform linear regression calculating the PPMC i.e. the square of the Pearson product moment correlation coefficient (Fig.3-18a&b). This method also resulted in the minima being attained more quickly, a necessity as each simulation took approximately 11 seconds to compute.

Thereafter the PPMC is calculated between a particular measured bulk-adsorption-ion raw-data kinetic curve and the simulator generated bulk adsorption kinetic data effectively measuring the degree of discrepancy (0 = perfectly discrepant, 1 = perfectly non-discrepant).

In general the search algorithm then calculates incremental forays (increases and decreases) for each parameter causing the simulator to generate a new transient curve and calculating an associated PPMC correlation for each new combination of increments, evaluating the change in PPMC and deciding the best route to follow with respect to further altering the parameters and ultimately obtaining the maxima.

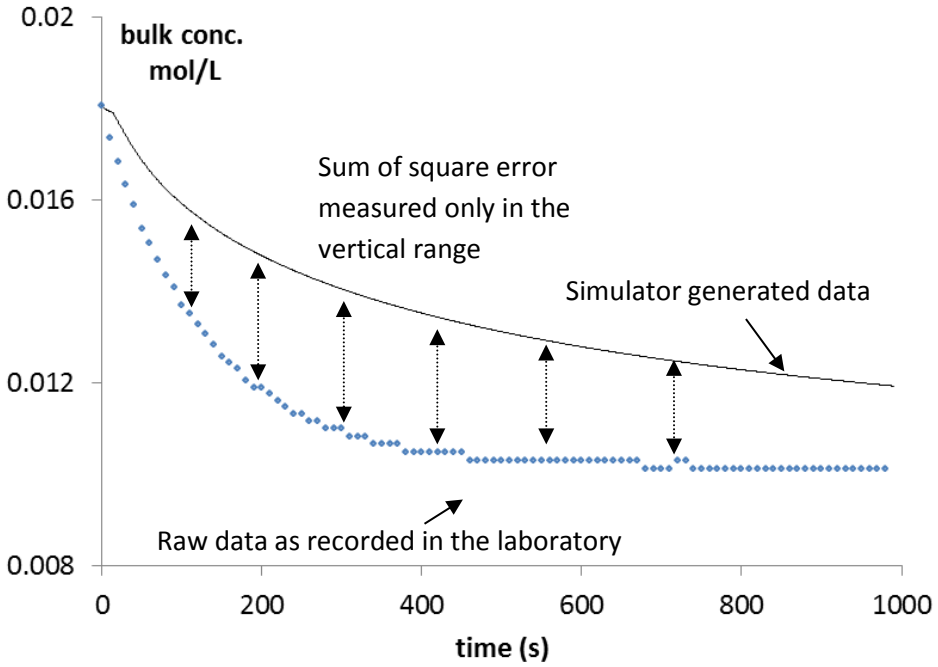

Fig.3-17 Simulation fit to raw data by sum of squares difference method

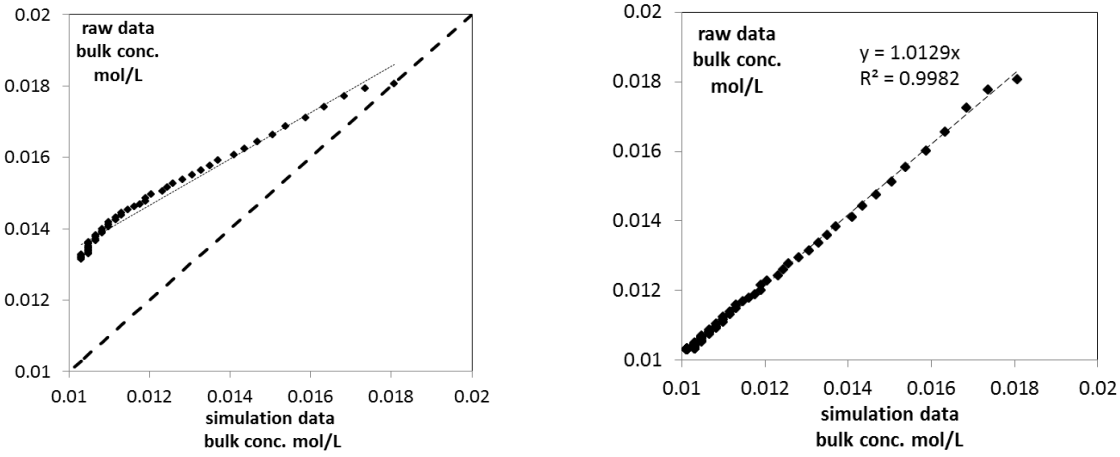

Fig.3-18a&b (a) Pre- and (b) post- model fit via PPMC method

3.8.3. Hooke-Jeeves optimisation

The process of fitting the simulated model to raw data requires a search method that obtains the overall maxima of the parameter/PPMC function in parameter coordinated space. The search algorithm employed follows the Hooke-Jeeves pattern search method while assuming a unimodal system.

The method consists of a sequence of exploratory moves in an n-dimensional Euclidian space (n = number of parameters) about a base point to try and understand the nature of the PPMC function contiguous to the point. At the beginning this base point will be the initial estimates of the parameters then each parameter in turn is given an increment in the positive and negative direction resulting in new sets of parameters each of which is passed onto the simulator that generates a transient curve for each set and the goodness of fit to the raw data measured by PPMC allowing for improvement trends to be identified.

From the PPMC determined at the point described by the coordinates of the initial parameter estimates and the PPMCs determined at the exploratory points, the general direction, in the Euclidean space toward the optimum, is identified. The algorithm then introduces a vector step change in the Euclidian space that incorporates changes in at least one if not all parameter values to locate a new point at which the PPMC is calculated again. A universal improvement promotes the new point as the next base point.

The optimisation algorithm also has sub-routines that either accelerate or attenuate the rate of approach along the located vector. Acceleration is undertaken if a repeated similar vector direction is observed, by introducing larger step changes to the parameters. Alternatively, attenuation is employed by decreasing step size if oscillatory type reversals in direction are observed, suggesting overshooting of the maxima and therefore proximity to the optimum point.

Although the nature of the Euclidean PPMC/parameter function generally appeared to be smooth and continuous, it was nevertheless complex and assumes a unimodal system. Therefore it was deemed necessary to begin the search algorithm from different starting coordinates to ensure the location of universal maxima. In all curve fitting activities a single universal maximum was located no matter from what direction it was approached. However, during the actual fitting exercise a number of trends and challenges were observed which elucidated on both the measured accuracy and the nature of the adsorption mechanisms. These are discussed in greater detail at the end of the methods (section *5.10/11*) and resulted in adjustments to the model.

3.9. Model sensitivity

Generally, during the model fitting process the mass transfer coefficient ($\boldsymbol{K_L}$) and the adsorption-ion intra-particle diffusivity ($\boldsymbol{D_i}$) were readily determined within approximately the initial half of the time it took the search algorithm to determine the optimum. However, the desorption-ion intra-particle diffusivity ($\boldsymbol{D_D}$) then took the balance of the time to be determined and then usually exceeded by four orders of magnitude the desorbing ion diffusivity. Its determination was slow with the optimum being approached in tiny increments, while only minimally improving the overall PPMC value.

To elucidate on this behaviour the sensitivity of the PPMC value to shifts in $\boldsymbol{K_L}$, $\boldsymbol{D_i}$, and $\boldsymbol{D_D}$ parameter value, close to the optimum point when fitting to raw data, was examined. After incorporating the 'tweaks' to the model, which are explained in detail in section *5.10* of the methods chapter, an exercise was undertaken using 12 raw data fits from the calibration data discussed in section *5.11* in which the behaviour of the three parameters, close to the optimum fit, was calculated.

Having determined the optimum fit for each set of data, each parameter was adjusted off the optimum in an exercise to test the resultant degree of error. Increments of 10% were applied up to a value of at least 50%. The percentage increase in error was then calculated using the determined PPMC values at the offset and Equ.3-38.

$$\left(O_{PPMC} - P_{PPMC}\right) \times \left(O_{PPMC} \times 100\right) = Err \qquad \textbf{3-38}$$

Where

O_{PPMC} Optimum point PPMC value (*dimensionless*)

P_{PPMC} PPMC value at offset increment (dimensionless)

Err Degree of error from optimum point (%)

3.9.1. Sensitivity of K_L in the vicinity of the optimum

Fig.3-19 presents graphically the errors determined for each perturbation exercise of twelve of the original eighteen optimisations undertaken in section *5.11*. The origin represents the optimum fit achieved via the Hook-Jeeves algorithm and it can be observed that a ±50% alternation in the parameter results in errors of up to 3% with very little in the way of ambivalence as to where the optimum value should be i.e. a clear semi-symmetrical distribution about the optimum value can be observed.

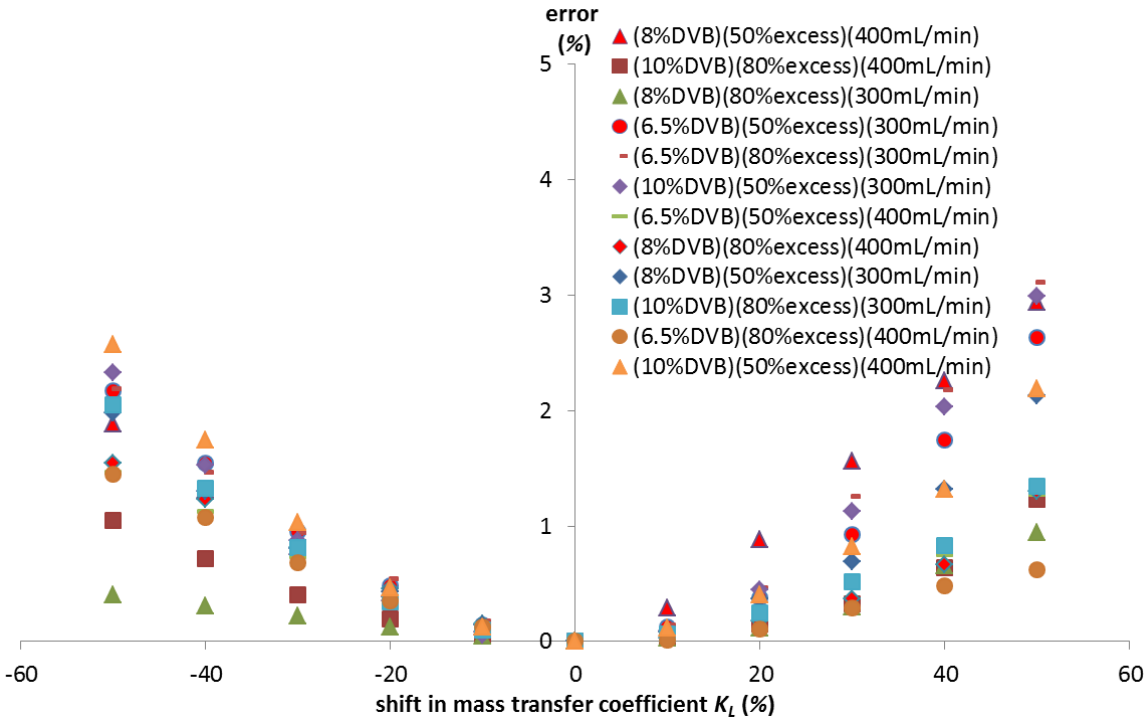

Fig.3-19 Degree of error of the mass transfer coefficient (K_L) about optimum

3.9.2. Sensitivity of D_i in the vicinity of the optimum

Fig.3-20 is the analogous graphical representation of Fig.3-19 for the adsorbing ion intra-particle diffusion and similarly shows a semi-symmetrical distribution about the optimum. However, a distinct drop in sensitivity, compared to the Fig.3-19, can also be observed with a perturbation of 50% returning between a 0.3% and 0.7% error. Once again a semi-symmetrical behaviour of the data about the origin can be observed with a clear indication of where the optimum is situated.

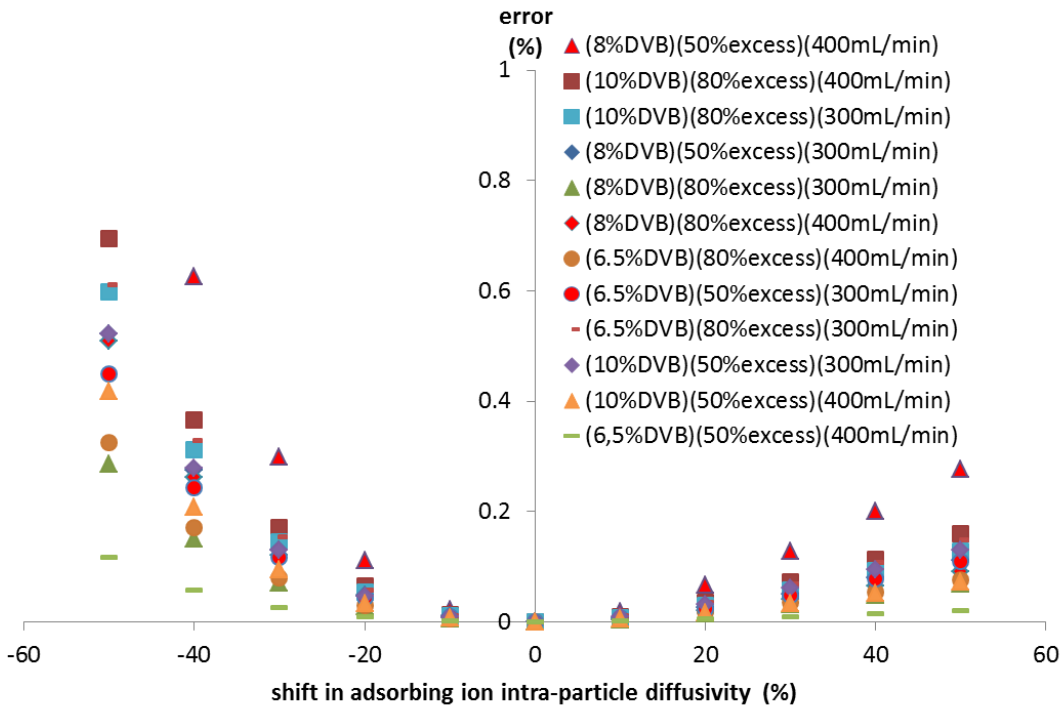

Fig.3-20 Degree of error of the intra-particle diffusivity (D_i) about optimum

3.9.3. Sensitivity of D_D in the vicinity of the optimum

In determining the error behaviour of the D_D parameter, the majority of curves followed the trend shown in Fig.3-21 indicating that a better PPMC value could be returned (negative error % = improved fit) if the Hook-Jeeves search algorithm continued to increase the desorbing ion intra-particle diffusion (D_D). The origin represents three orders of magnitude above (D_i). However, the curve to the right of the origin is exceedingly flat implying that the desorption-ion intra-particle diffusivity would have to be increased substantially to achieve any meaningful improvement in PPMC value while ultimately having little impact on the

appearance of the final curve fit which was already very good (PPMC > 0.99). In addition, during the search for this optimum value the Hook-Jeeves search algorithm altered the other two parameters very little.

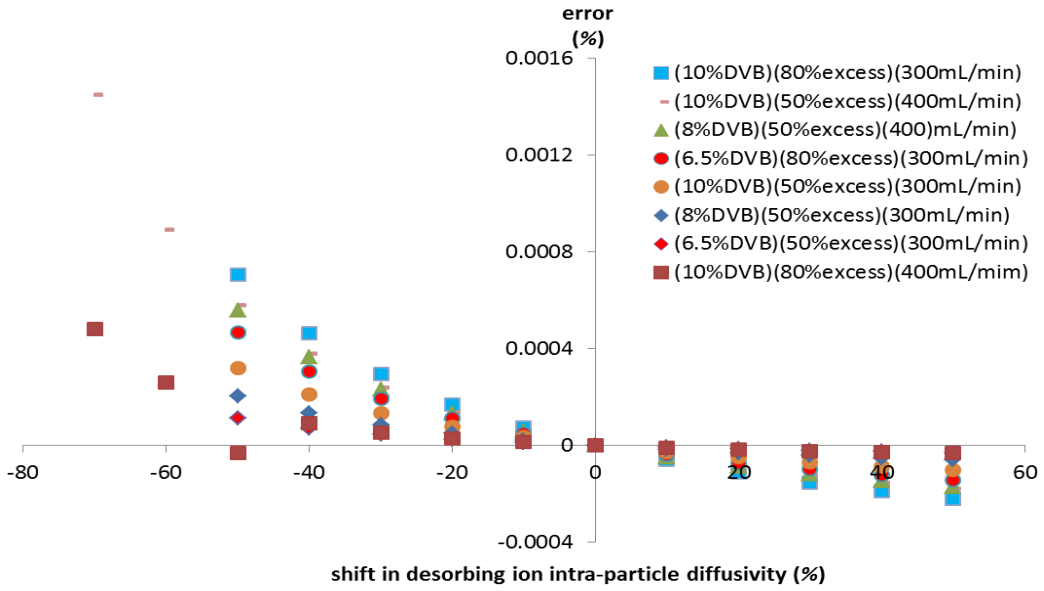

Fig.3-21 Desorption-ion Diffusivity (D_D) error at optimum

As increase in diffusivity inordinately implies that this parameter has little bearing on the rate of the overall adsorption process and given the fact that little improvement to the curve fit process is achieved, it was decided that a ceiling would be established for desorption-ion intra-particle diffusivity at approximately 3 orders of magnitude above adsorption-ion intra-particle diffusivity, effectively a null result.

The D_D error curves of two adsorptions of the twelve chosen in this group behaved differently to those displayed in Fig.3-21 and are shown in Fig.3-22. These indicated a decrease in error for decreasing diffusivity although once a single reduction in order is tested below the origin, error/diffusivity instability appears.

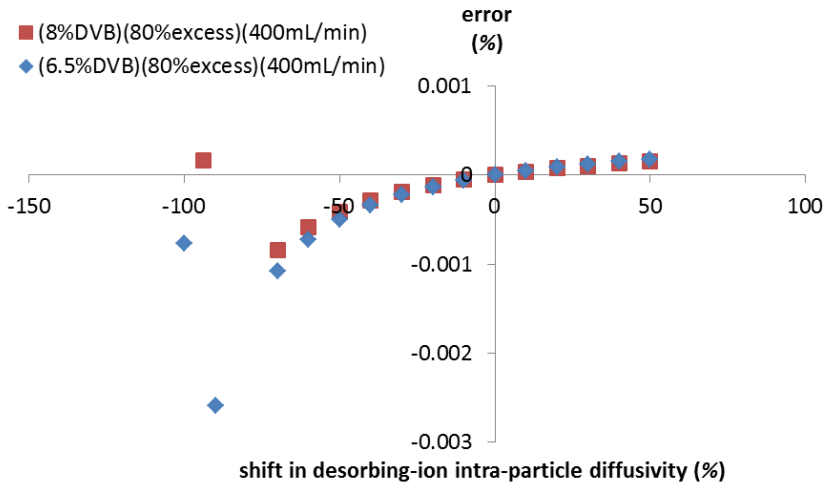

Fig.3-22 D_D errors show instability at a reduced order of magnitude

The remaining 2 data sets tested actually achieved optimum fit values and these are presented in Fig.3-23. It's notable that the attained values are very close to those achieved for the adsorption diffusivity (D_i) which is a reasonable outcome.

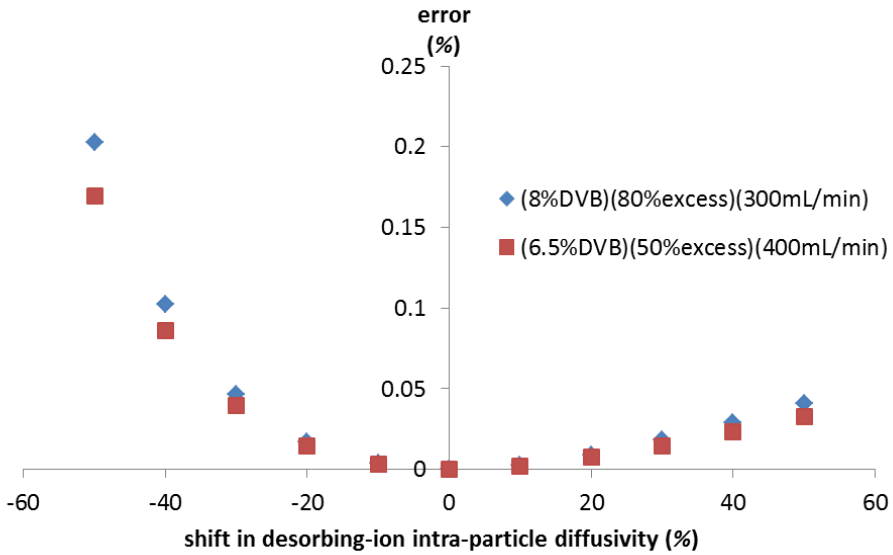

Fig.3-23 Two data sets achieve an optimum for desorption-ion diffusivity

Armed with a curve fitting algorithm that delivers good fits and confident that meaning full values of ***Di*** and K_L are attained in the process it was not considered possible to use this tool to measure actual ***Di*** and K_L values and most importantly how these values change as the resin ages. To fulfil this challenge the necessity to build dedicated equipment became apparent and this is dealt with in the following chapter.

4. EQUIPMENT

4.1. The necessity to manufacture equipment

The requirements of this study were such that equipment had to be designed and manufactured from scratch. Building a cycling machine that could automatically cycle resin through its various stages was a necessity. Such a machine would have to consist of solid state pinch valves and peristaltic pumps in addition to an electronic valve/pump control unit. Software would also need to be written that would then interact with the control unit to produce the cycling environment required for the resin being tested.

The original approach of testing the resin in a finite environment also required the design and construction of a customised Zero Length Column reactor (ZLC) and associated circuit and reservoir. An important capability of the ZLC should be its modularity i.e. the capability to move seamlessly between the aging machine, the kinetic testing unit, the capacity testing unit and the equilibrium testing unit.

4.2. Resin Decaying Machine

The degradation of ion exchange resin in normal cyclic duty is a natural process that occurs at either a slow or relatively fast pace depending on the environment in which the resin is being used. Hence, an important part of this thesis's investigation into the alteration in capacity and kinetics of ion exchange resin during decay is to be able to systematically degrade resin under constant/controlled conditions.

As it is chemical degradation that is investigated, the ion exchange resin needs to be continuously loaded and regenerated while monitoring its efficiency. If only fifty cycles were

to be manually performed this would constitute an arduous task at best and in addition care would have to be taken to ensure that each loading and regeneration is performed in exactly the same manner as the previous, to ensure scientific continuity. As it is envisioned that up to a five hundred cycles will have to be undertaken to observe significant alteration in resin performance, the automation of the cycling becomes all the more necessary, particularly if precision is required. This necessitates the building of a machine that systematically cycles resin through its loading and regeneration stages.

The machine that was built, to degrade the resin, continuously passes three solutions in succession through the resin bed with each cycle consisting of a load, regeneration, and a wash water stage. The wash water stage follows the regeneration stage and is important to make sure the entire excess regeneration electrolyte is washed away. Any of the highly concentrated extraneous electrolyte still present during the adsorption stage will push the equilibrium in the resin bed away from adsorption of the relatively low concentration adsorption species (ion), thus preventing a successful loading cycle. The amount of wash water required had to be carefully determined to ensure the wash objective is achieved.

Fig.4-1 is a schematic diagram of the machine which consists of a central unit that controls a number of peristaltic pumps in addition to a bank of pinch valves that control the flow of the various reagent solutions through the resin bed. Fig.4-2a, 4-2b, 4-2c are photographs of the unit in operation. The control unit receives the cycling program which is down loaded from a personal computer. The program is setup using software on the computer where the duration of each stage, the number of cycles and when the peristaltic pumps are required to be on or off, is established. As the control unit runs through the cycle program the point at which it is in the program is digitally passed back to the computer which then displays this on the monitor (Fig.4-3).

The envisaged overall cycle through which the resin is passed, approximately a thousand times consists of the following stages;

A loading stage in which a low concentration cationic solution is passed through the resin bed, during which it is envisaged that the cationic ions in solution are adsorbed by the resin displacing the hydrogen ions.

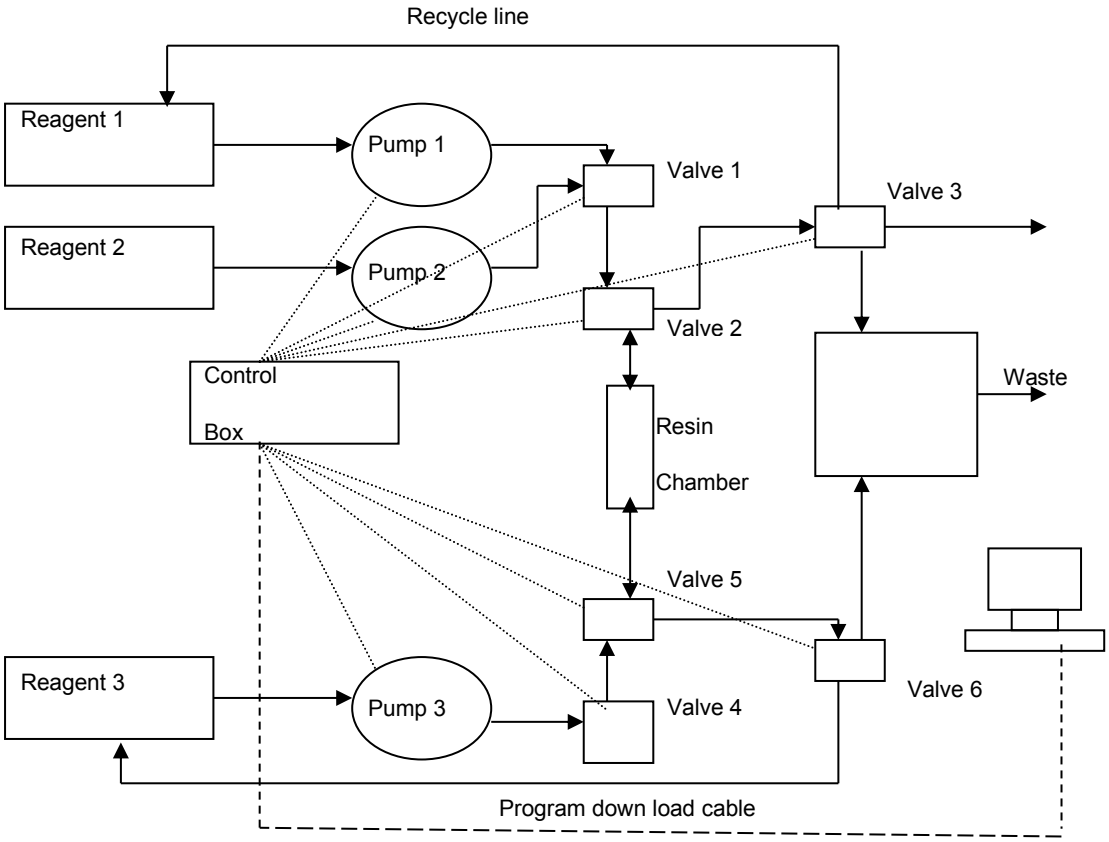

Fig.4-1 Schematic diagram of the cycling machine

A regeneration stage where a powerful electrolyte of an acid/peroxide mix, at a concentration of approximately one normal, is passed through the resin bed

A wash water stage where any excess regeneration electrolyte is removed by the passing of deionised water through the resin bed, ensuring the removal of the entire regeneration electrolyte before returning to the loading cycle.

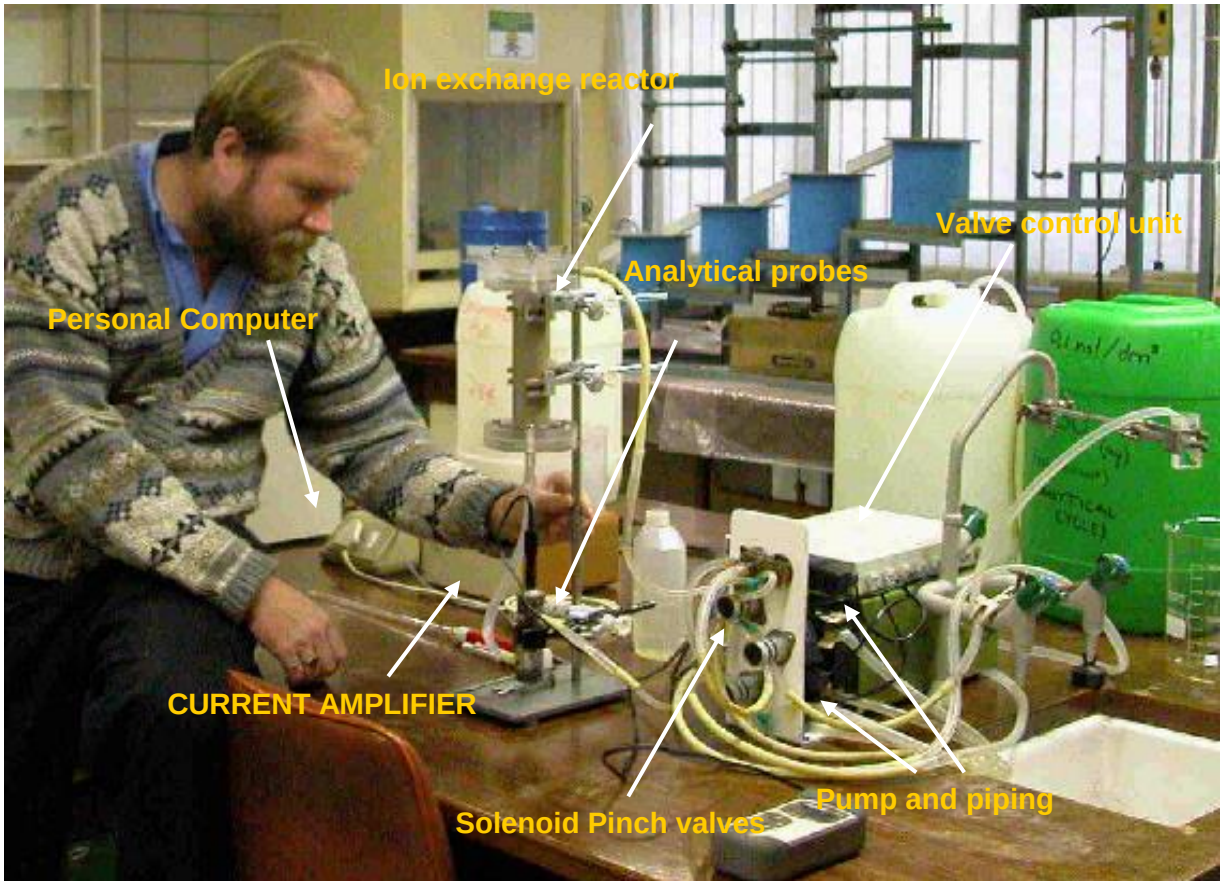

Fig.4-2a Cycling machine in operation with the original larger resin bed

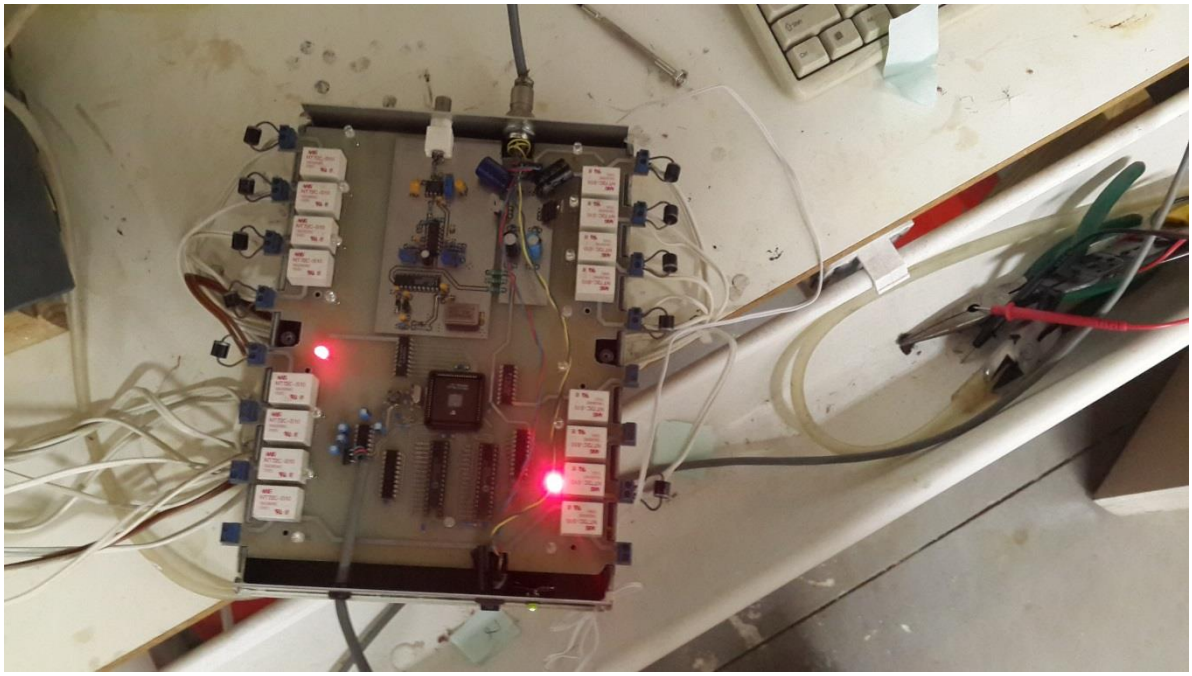

Fig.4-2b Valve control unit

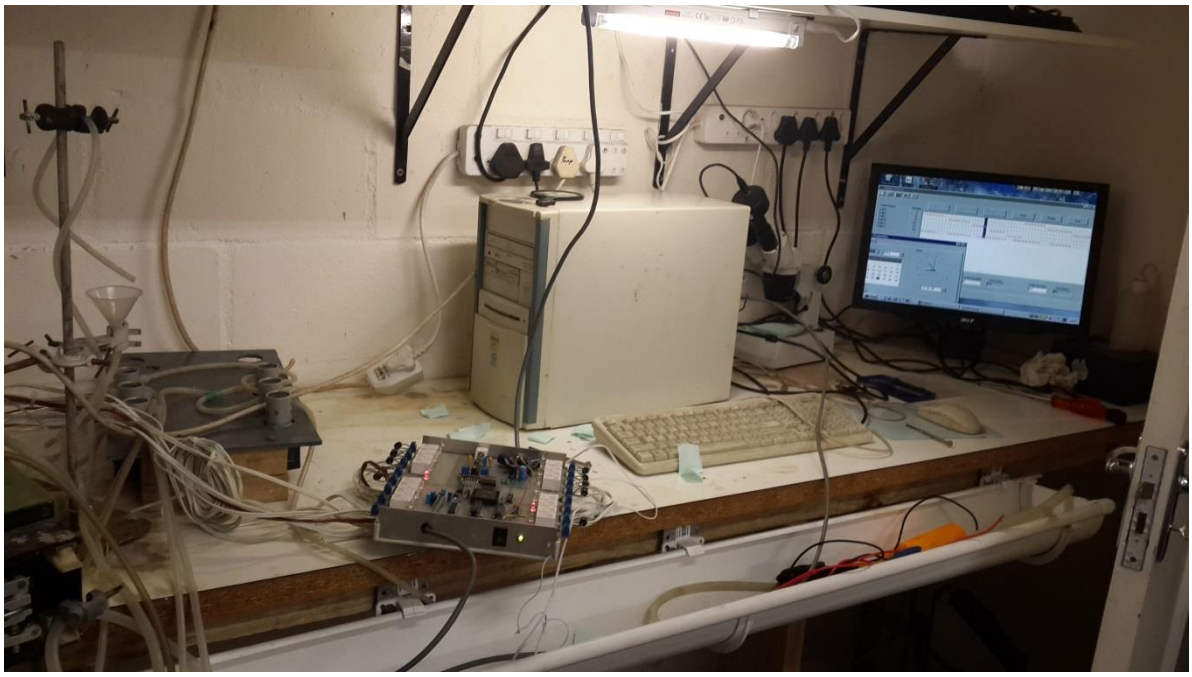

Fig.4-2c Control unit with computer and screen display

All solutions passing through the resin bed pass to effluent to ensure there is no contamination i.e. there is no re-circulation. The effluent highly-acidic regeneration solution is passed to a holding tank for further processing i.e. neutralisation. Gypsum is formed as lime is added manually to effect neutralisation. Finally, the excess wash water that is passed through the bed is also passed to a holding tank that is then neutralised - if necessary - and discarded. At a later stage in the test work the acid effluent was neutralised with NaOH which then resulted in neutralised brine and negated the necessity of having to discard any precipitate.

A full cycle is envisaged to last approximately thirty minutes with the loading to capacity taking approximately ten minutes, the regeneration eight minutes and the wash water stage twelve minutes. During the regeneration phase the peristaltic pump is stopped on two occasions for approximately two minutes. This is considered pertinent as the main driving force for the exchange during the regeneration is the very high concentration of the

regeneration electrolyte hence regeneration is likely to proceed even when the solution in the bed is stagnant. Stopping the peristaltic pump has the effect of limiting the consumption of acid

.

Paramount to the study is the systematic handling of the aging/decaying resin. It was envisaged that the ion exchange resin would need to undergo four main procedures during a normal test campaign i.e. be coupled to the cycling machine for extended periods of time, in addition to undergoing regular kinetic testing, capacity testing and equilibrium testing, while not allowing for the potential loss of any of the resin beads. As the resin undergoes more cycles its decayed state means that it will become more valuable to the project as a whole and any potential risk of loss has to be avoided.

To tackle this challenge a system needed to be developed in which the resin could be safely transported between separate apparatuses/procedures. To achieve this, a small container had to be designed that is able to hold and effectively immobilise about $5mL$ of ion exchange resin (Fig.4-4a & Fig.4-4b) through which reagents can be pumped. The resin container, which effectively amounts to a zero length column/reactor (ZLC) was manufactured from PVC piping and fittings and could be coupled into various apparatuses by means of a quick tube release mechanism that allowed for rapid disengagement and re-engagement without disturbing the resin.

Although the resin aging machine performs a robust process that does not require/perform any measurement on the resin, the far more precise kinetic, capacity and equilibrium measurements had to be carried out separately but could also be combined into a single device. As the most sophisticated measurement is kinetic data capture it was decided that the same device could be adapted to perform equilibrium and capacity measurements.

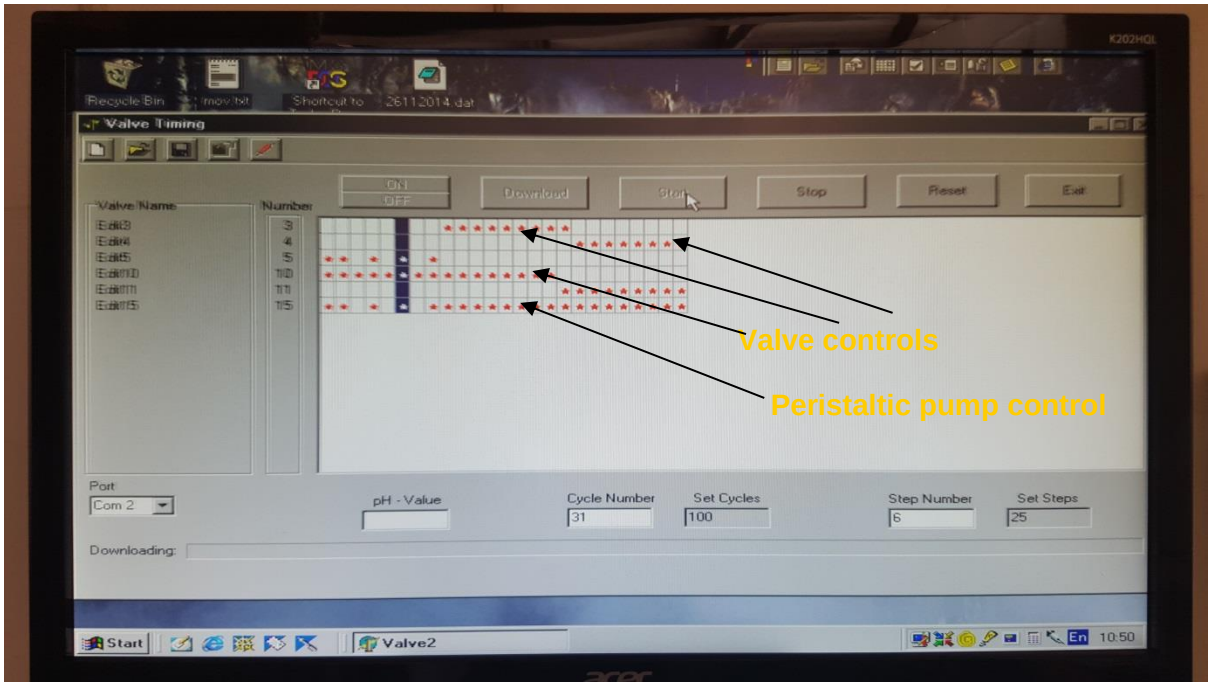

Fig.4-3 Cycle program display on the personal computer

Fig.4-4a Zero Length Column (ZLC) that holds 5*mL* of ion exchange resin

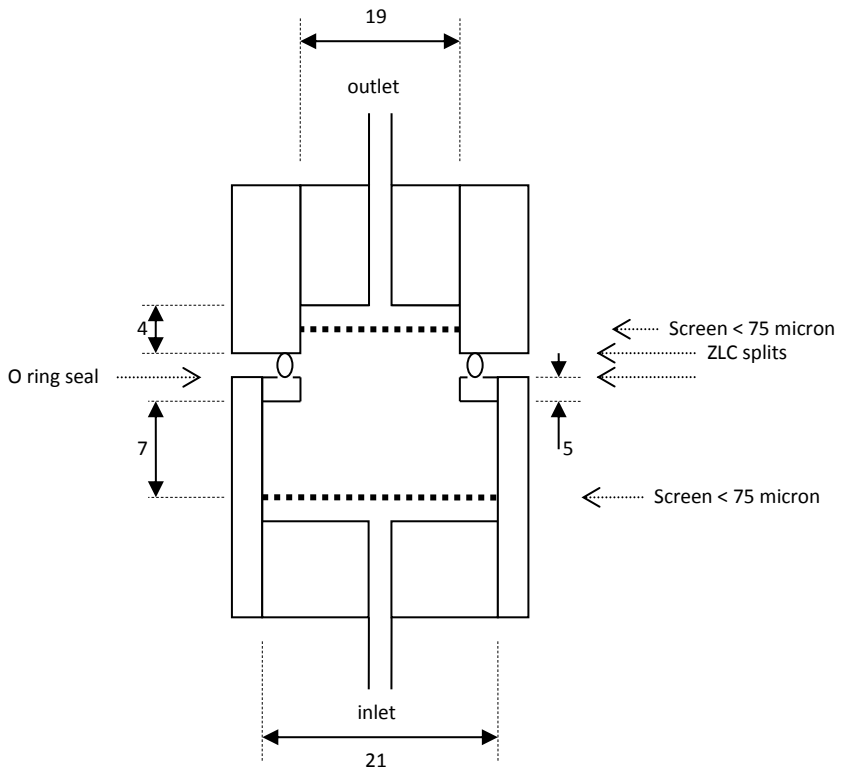

Fig.4-4b Engineering design of ZLC unit shown in the Fig.4-4a

4.3. Apparatus to measure resin stats

4.3.1. Kinetics apparatus

It was envisaged that the resin would be tested in a finite medium, and this means that the ZLC needs to be tied to a fixed quantity of bulk liquid that is intimately contacted with the resin in which the chemical matrix in solution is not at equilibrium with the ions on the resin. The result is the passing of ions for which the resin has an affinity from the solution into the resin matrix during the adsorption, causing a consequent drop in bulk concentration of the adsorbed ion. Simultaneously the ions loaded on the resin at the start of the transient - normally a hydrogen ion - desorbs from the resin causing a consequent increase in the concentration in the bulk i.e. the solution becomes more acidic. A diagram of the apparatus is shown in Fig.4-6.

The apparatus consists of the ZLC in a closed circuit with a variable speed peristaltic pump and a reservoir that is maintained in a highly mixed state by a Heidolph stirrer with a flat blade impeller causing a high turbulence radial flow pattern. The reservoir is an open-top baffled tank made of clear PVC and has a cooling jacket on the outside as the temperature of the system had to be kept constant for every kinetic test at below ambient temperature. The entire volume of the circuit is maintained accurately at one Litre. The circulating peristaltic pump is able to pump at flow rates of between 60 *mL/min* and 500 *mL/min*.

4.3.2. The pH probe and meter

Special attention had to be given to choosing a good quality pH probe and associated meter. The meter chosen was a Hanna Instruments HI4202. This meter has a dual pH measuring and temperature compensation capability. It also has a PC interface which allows for rapid downloading of data which was considered useful for this project. The pH probe uses a refillable glass body and has a double junction pH electrode. It also has three ceramic junctions in the outer reference cell to compensate for the increased flow rate of reference electrolyte and a rugged conical pH sensing tip. The pH meter and probe are shown in Fig.4-5.

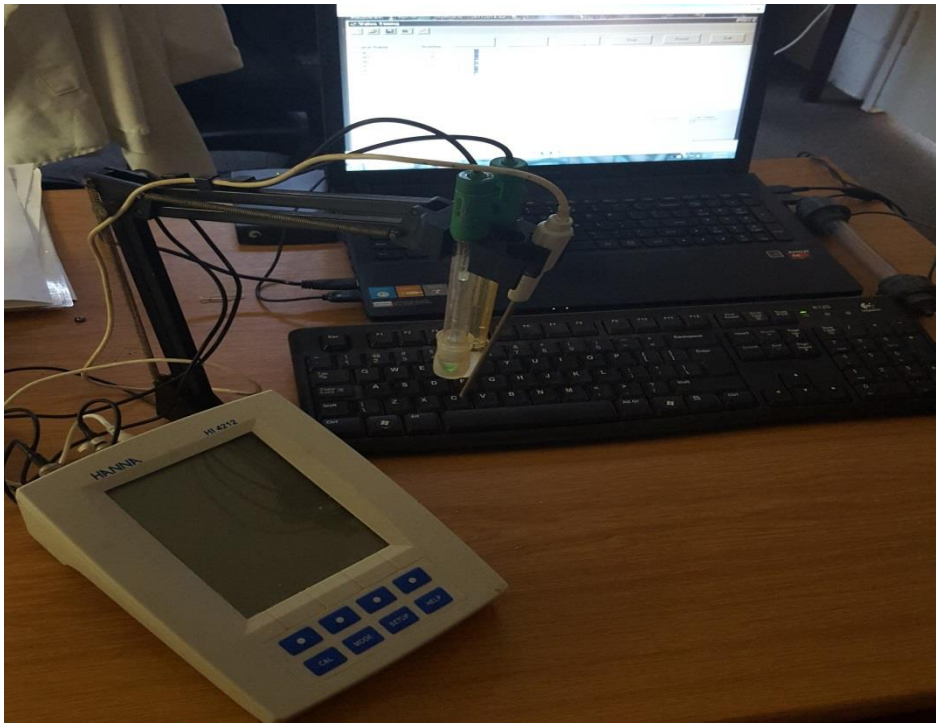

Fig.4-5 Hanna pH meter and probe

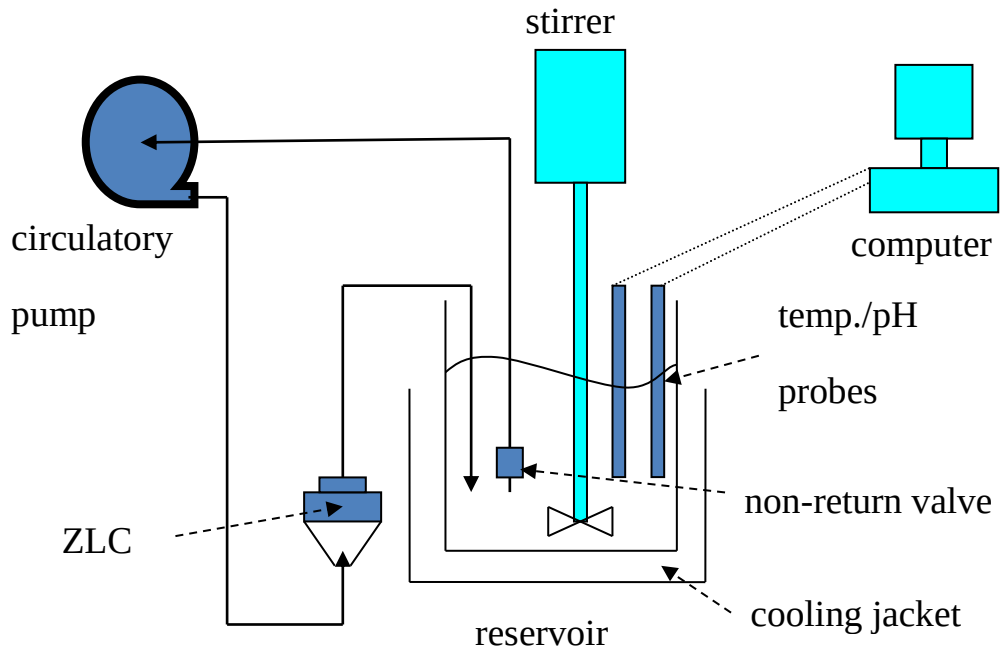

Fig.4-6 Closed circuit testing apparatus containing the Zero Length Column (ZLC)

While the peristaltic pump is switched off reagents can be added to the reservoir and are quickly dissolved by the action of the stirrer. The kinetic test begins when the peristaltic

pump is switched on although a small time lag of a few seconds is likely to be evident before a rapid change in the chemical matrix is detected in the reservoir. Any changes in the concentration in the bulk solution are monitored by either removing samples from the reservoir using a sampler pipette or by monitoring the change in ion concentration using an ion selective probe. The latter is more desirable as it does not intrude into the process by lessening the quantity of the bulk as the former would do. Another advantage of using a probe is that the end point of the transient can be easily observed i.e. change in chemical matrix in solution effectively ceases. In addition the probe measurements can be recorded electronically every ten seconds and providing the probe is well calibrated should give an excellent record of the transient process. Simultaneously small samples of solution – approximately 5 *mL* - can be withdrawn for wet chemical analysis to check the accuracy of the ion selective probe measurements. This removal of small quantities of liquid from the reservoir needs to be accounted for by using a rigorous mass balance algorithm, as this will likely impact on the overall ions present and hence the rate of ion concentration-change with time.

Starting concentrations can be varied and can be measured as a proportion of the capacity of the resin in addition the speed of the peristaltic pump would equate to the turbulence in effect around the resin.

4.3.3. Equilibrium apparatus (determination of $\boldsymbol{\alpha}$)

The equilibrium test can be conducted in exactly the same configuration (Fig4-5) as the kinetic test with the ultimate concentration being of the utmost importance. Suitable starting concentrations of the ion being adsorbed are chosen and are measured as a percentage of the capacity of the resin based in equivalents.

A fixed amount of each adsorption ion is added to the reservoir and the solution is circulated until no further alteration in the composition of the solution is detected. As the circuit is

entirely closed a mass balance concludes the quantity of ions on the resin and in the bulk at the point of equilibrium. From a number of determined equilibrium points the alpha value (α) can be calculated i.e. the equilibrium coefficient determined associated with the Mass-Action-Law.

4.4. Apparatus to measure resin capacity

The equipment required for this is a simple open circuit and the kinetic/ equilibrium testing equipment is easily adapted to this purpose. Fig.4-7 shows the configuration.

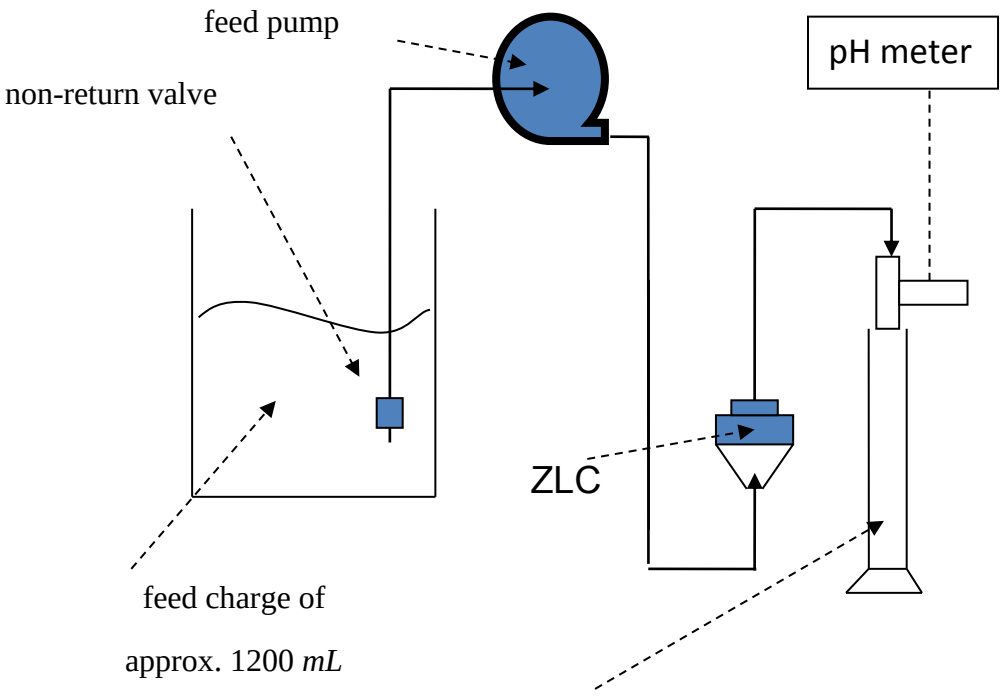

Fig.4-7, Open circuit apparatus for testing resin capacity of resin in the ZLC

An excess quantity of electrolyte is established as the feed which is passed directly through the ZLC. The cationic atoms in the electrolyte are adsorbed onto the resin in the ZLC which is in the hydrogen form. As the adsorption proceeds the hydrogen ions are desorbed and collected in the measuring flask. Once a finite quantity has been collected the quantity of

protons in the flask is determined by wet chemical analysis measured and equated with the capacity of the resin.

4.5. Microscope

For the visual examination of resin a microscope was used. It is a DCM310 microscope manufactured by CE. The microscope has a digital CMOS 3.2 mega pixel resolution camera that by the use of software ‘ScopePhoto, can take stills or videos through the microscope. Accurate measurements of items observed in the microscope can be made using associated software.

The camera attachment has the capability of linking electronically directly to a laptop through a 2.0 USB connection allowing for microscopic measurements and picture grabbing. A photo of the microscope, CMOS camera accessory and associated laptop computer is shown in Fig.4-8. For the purposes of measuring resin colour, light penetration and converting to grey scale image, a freeware software package called ‘imageJ’ was used.

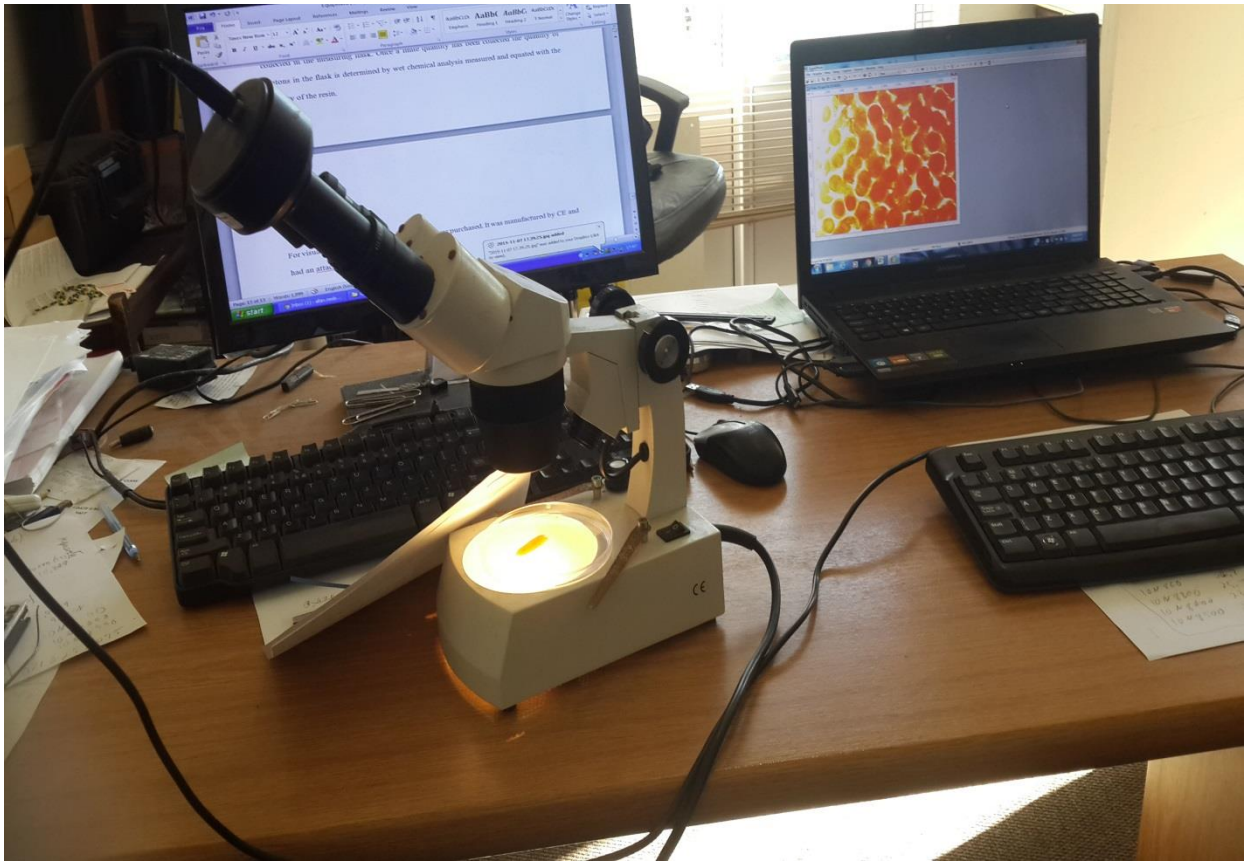

Fig.4-8 Microscope and picture grabber software on the laptop

5. METHODS

5.1. The Zero Length Column (ZLC)

For any particular campaign, approximately 5 *mL* of cationic resin was measured out in a measuring flask that was then filled to the brim with deionised water. The Free Wet Settled Volume of the resin (FWSV) is measured by suspending the contained quantity of ion exchange resin inside the measuring flask by methodically inverting the flask ensuring all beads are suspended. After all the resin has been suspended the flask is placed on a level surface allowing all beads to settle under the influence of gravity, for about one minute. The volume of resin is measured and is then recorded as the FWSV of the resin.

Once the desired resin volume was obtained, the resins were immobilised inside the ZLC reactor (Fig.4-4) and converted into the H^+ form with the passing of a one litre of a 2N HCl solution through the ZLC in open circuit (Fig.4-7) to ensure that nothing other than the H^+ is loaded on the resins active sites. The resin is then rinsed with deionised water until the effluent shows a pH ≈ 5 so as to exclude any excess acid. The ZLC can then be incorporated into either the closed circuit (Fig.4-6) for resin kinetics or equilibrium testing, or the open circuit (Fig.4-7) for capacity testing. It can also be incorporated into the rapid resin decaying unit, depending on what process/analysis is required. The flow through the ZLC is always upwards.

As the resin is immobilised, its volume/quantity is fixed and hence an actual capacity can be determined. This value, once accurately established, needs to be incorporated into both the equilibrium and the kinetic calculations. It was also an important value for estimating the required contact time for the repeated loading of the resin in the rapid decay unit.

5.2. Resins used in this test work

Four types of resins were tested in the ZLC. Three are Purolite manufactured resins; C100E, PPC100H and PPC100x10 and the fourth, Amberjet 1200H is a Rohm & Haas manufactured resin. All four resins are strong acid gel types with sulfonic acid functional-groups/active-sites.

The 1200H, PPC100H and PPC100x10 resins have narrow size distributions between 600 and 700 μm and therefore for the purposes of all tests an average diameter of 650 μm was assumed. The C100H resin is produced in a size distribution spanning from 300 to 1200 μm. For the purposes of the test work Purolite supplied a narrow size range spanning from 600 μm to 850 μm and hence an average size of 725 μm was assumed to be the representative resin diameter for this type.

All four resins are composed of styrene and DVB copolymers, the PPC100x10 has 10% DVB addition and the PPC100H and C100E have 8.0 % and 6.5% and DVB contents respectively. In the hydrogen form the PPC100x10 had a darker appearance the PPC100H has a lighter appearance and C100E the lightest. The DVB content of the 1200H is not given by the company but is estimated to be about 8% in line with a standard strong acid cation resin.

5.3. Kinetic test work method

This part of the analysis was considered to be the most sensitive measurement as up to three parameters would be determined through complicated numerical analysis of the generated data and hence had to be conducted as accurately as possible. A second, simpler algorithm is used to determine the early time data slope of the generated kinetic curve for the purposes of using a conventional method of determining the laminar layer mass transfer coefficient. Finally, a qualitative evaluation of each kinetic curve is also conducted by determining the

half-life of the entire decay curve as accurately as possible, by fitting a spline to the raw data and interpolating the time taken to achieve 50% conversion. This determination gave an estimate of the overall time taken to convert the resin and could be used as a qualitative global comparison against other similar kinetic curves.

5.3.1. Pre-kinetic test preparation

The modus operandi of the kinetic test is to begin by charging the reservoir, in the closed circuit, with the appropriate charge of ions that would constitute 120%, 150% or 180% of the actual capacity of the resin, measured in equivalents. The mass of the reservoir was noted prior to the charge being added to it. After the charge had been added (measured in grams to accuracy of three decimal places), 300 *mL* of cold deionised water, at approximately 6°C, is added to the reservoir. A further 600 *mL* is then added of ambient temperature deionised water after which the reservoir is topped up by the 6°C deionised water until the added liquid together with the salt charge, attained a mass of exactly 1000*g*. This final addition of water is undertaken so as to place the temperature of the reservoir at approximately 17°C. This then allowed for the cooling of the reservoir in the ice jacket to the required temperature of 15°C. With experience a technique was developed whereby the temperature could be controlled either by increasing the rate of mixing (upwards) or increasing the ice in the jacket (downwards). Temperature control maintained the temperature of the water between 14.7°C and 15.3°C as this was consistently below ambient temperature hence requiring only a cooling mechanism.

The mixer ensured that the reservoir is well mixed. At each of the concentrations established a kinetic test was conducted at six different circulation rates, of approximately 60 *mL/min*, 100 *ml/min*, 200 *mL/min*, 300 *mL/min*, 400 *mL/min* and 500 *mL/min*. During the early test work phase all six circulation rates were utilised. However, at a later stage, once the kinetic behaviour of the resin adsorption process was better understood, this test was reduced to three, generally the 300 *mL/min*, 400 *mL/min* and 500 *mL/min*. to ensure that intra-particle

control played a roll. To assist with control, the temperature in the cooling jacket is measured together with that in the reservoir.

5.3.2. Calibration of pH Probe

Prior to starting the kinetic test, the pH probe (Hanna Instruments HI1332 & HI1053) and meter (HI4212) would be rigorously calibrated to two decimal points (i.e. 0.01pH) using the meter's inherent three point calibration software. The high accuracy pH solutions supplied by Hanna Instruments for the purposes of calibration were pH 7.01, pH 4.01 and pH 1.01. Crosschecks are also regularly undertaken, by re-insertion of the probe into the calibration liquid, to confirm repeatable accuracy. Hence the process of calibrating the probe was laborious, but was undertaken frequently. Accuracy is considered important since ultimately the H^+ concentration that would be calculated from the pH measurement would constitute the antilog of the $[H^+]$ reading. Hence the slightest inaccuracy would be hugely amplified.

As has been stated before, the use of a probe allowed for the recording of high frequency data, a necessity given the curve fitting technique employed during kinetic test work. Probes are used that allowed for changing of the probe fluid regularly, (not solid state probes) which allowed for regular cleaning of the membrane and the removal of any crystal build up. To ensure rapid response times from the probe, the breather-hole situated at the top of the probe shaft, is regularly cleaned to ensure that there is always a good pressure head at the membrane on the inside of the probe. The reduction in internal electrolyte during normal use was not allowed to drop below the eighty percent mark approximately, ensuring that the internal meniscus was always substantially above that of the surface of the liquid being measured. This is done to ensure a rapid response in pH measurement.

With repeated tests the necessity for good data measurement and management became more apparent. The pH meter was connected to a personal computer that contains software (HI92000 4.2) that records the ion concentration/pH measurement every ten seconds, writing

a file that can be downloaded to a spread sheet or as a CSV (Comma Separated Variable) file for further processing.

5.3.3. Actual kinetic test

After ensuring that the mixture in the reservoir is homogenous, the switching on of the peristaltic pump in the closed circuit begun the kinetic test. After allowing for a short delay to fill the circuit and ZLC with circulatory fluid, (4.5 seconds to 7.5 seconds depending on the rate of circulatory flow) the measurement of the kinetic data began.

Right from the beginning, the change in concentration of the desorbing ion (i.e. H^+), monitored by pH probe and recorded every ten seconds by computer, became evident. The entire test was made to run for fifty minutes which, under all test conditions, resulted in equilibrium begin attained. During the course of the test, samples of approximately 5 *mL* liquid volume were removed from the reservoir at 0*s*, 30*s*, 60*s*, 90*s*, 150*s*, 240*s*, 420*s*, 660*s*, 1200*s*, 1800*s*, 2400*s*, and 3000*s*. This constituted the removal of approximately 60 *mL* from the one litre circuit which is significant and hence had to be incorporated into the calculation. These samples were removed for wet chemical analysis and the concentrations measured compared to those registered by probe. It is important that these two means of measurement coincided to ensure the accuracy of the kinetic test results. The wet chemical analysis that was carried out on each sample consisted of titrating it against a 0.003 mol/L solution, prepared from analytical NaOH, using phenolphthalein as an indicator. Coincidence between probe and wet chemical analysis is particularly important at the end of the kinetic test, to ensure that the equilibrium condition is correctly measured.

By measuring the pH of the closed circuit finite solution every 10 seconds throughout each kinetic test, a value for the concentration of the desorbing ion in solution ($\boldsymbol{C_D}$) can be calculated for every measurement. For the purposes of the initial slope method, a degree of conversion ($\boldsymbol{X_D}$) is also calculated from each $\boldsymbol{C_D}$ value calculated as described in section

3.2.2. Fig.5-1 is an example of the graph that is produced for each kinetic test, showing both the results measured by probe and wet chemical analysis.

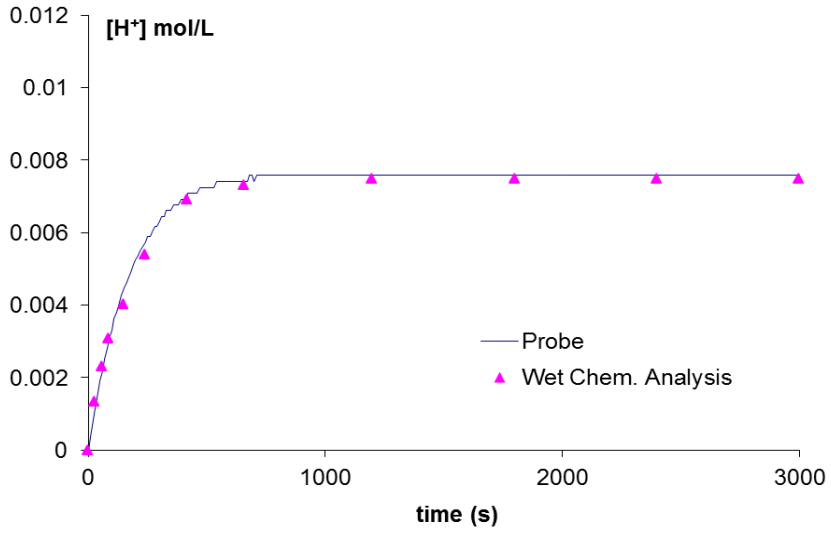

Fig.5-1 Typical kinetic test, data measured by probe & wet chemical analysis

Each kinetic test delivers 300 data points measured by the probe and twelve measured by wet chemical analysis. With a confirmed accurate and electronic measurement taken every ten seconds over a fifty minute period by the probe, a large amount of data is produced that could be used to number crunch the various posed mass transport parameters of the system. A 'comma-separated-variable' file is produced and processed for the main model fitting software. The nomenclature of the file naming procedure which is generally used throughout this thesis can be found in Annexure IX.

5.4. Preliminary study to verify the kinetic test method

The method of quantifying resin decay through the measurement of intra-particle diffusivity, as it is presented in this thesis, relies on a curve fitting procedure where three or fewer parameters, associated with different mechanisms, are determined simultaneously. The necessity of proceeding in this manner is due to documented evidence that during the

transient adsorption process (Petruzzelli *et al*, 1987a) different transport mechanisms control, as was discussed in section *2.8.2* of the Literature Review. The approach is original and requires a multi-parameter fit to what is essentially a simple kinetic curve, which is a product of a complex combination of mechanisms. Hence an experimental approach is required to ensure that the data obtained is meaningful and altered rationally with changing environments. This is all the more important as most authors that report measured parameters do so without any proof that their determined values are realistic and not just lumped parameters (Harries 1986; Gang-Choon Lee *et al*, 1997; Foutch & Chowdiah, 1992; Lee *et al*, 1997).

The data presented in the next five sections was either generated at an early stage in the study or gleaned from literature and gave qualitative insight on the impact the major system variables on the resin adsorption kinetics. These variables were deemed to be: impact of turbulence, impact of DVB cross-linking, impact of multiple controlling mechanisms, impact of infinite dilution diffusivity and impact of temperature. Another objective was to verify the initial assumptions regarding the validity of the kinetic test work method presented in the previous section.

5.4.1. Impact of turbulence on kinetics

Once the kinetic testing unit was developed, the effect of turbulence on mass transport onto the resin could be determined. It was assumed that there would be a marked increase in the rate of adsorption at higher turbulences due to the attenuating effect turbulence has on resistance to mass transfer by the laminar dynamic layer.

To establish the validity of this assumption and also to check if measured mass transport coefficients were in line with published data, a test was undertaken in which Na^+ ions were adsorbed onto a 6.5% DVB H^+ form resin in the closed circuit (Fig.4-6, finite environment) kinetic testing unit at different circulatory flowrates i.e. 60 *mL/min*, 100 *mL/min*, 200 *mL/min*,

300 *mL/min*, 400 *mL/min*, 500 *mL/min*. A relatively low internal-density steric-state of 6.5% DVB resin (C100E) was chosen so as to lessen the impact of intra-particle diffusion on mass transport, thereby promoting the impact of laminar layer resistance.

The volume of resin placed into the ZLC was 5 *mL* which had a measured capacity of 1.8 *equiv./L*. The starting concentration of Na^+ ions in solution in the 1 *L* circuit load was originated from the dissociation of $NaNO_3$ crystals and was set at a concentration 0.0135 *mol/L*. This amount corresponded to 50% excess of the resin capacity. During each kinetic test, the concentration of the desorbing ion H^+ was measured by a probe and complimented by the regular extraction of samples for wet chemical analysis. The determined concentrations in both cases are shown in a graphical representation of the results (Fig.5-2). An explanation of the nomenclature can be found in Annexure IX. It can clearly be seen from Fig.5-2 that, as expected, the rate of mass transfer, shown as accumulation of desorbed ions in the liquid circuit, increases as the circulatory flowrate and thus turbulence is increased.

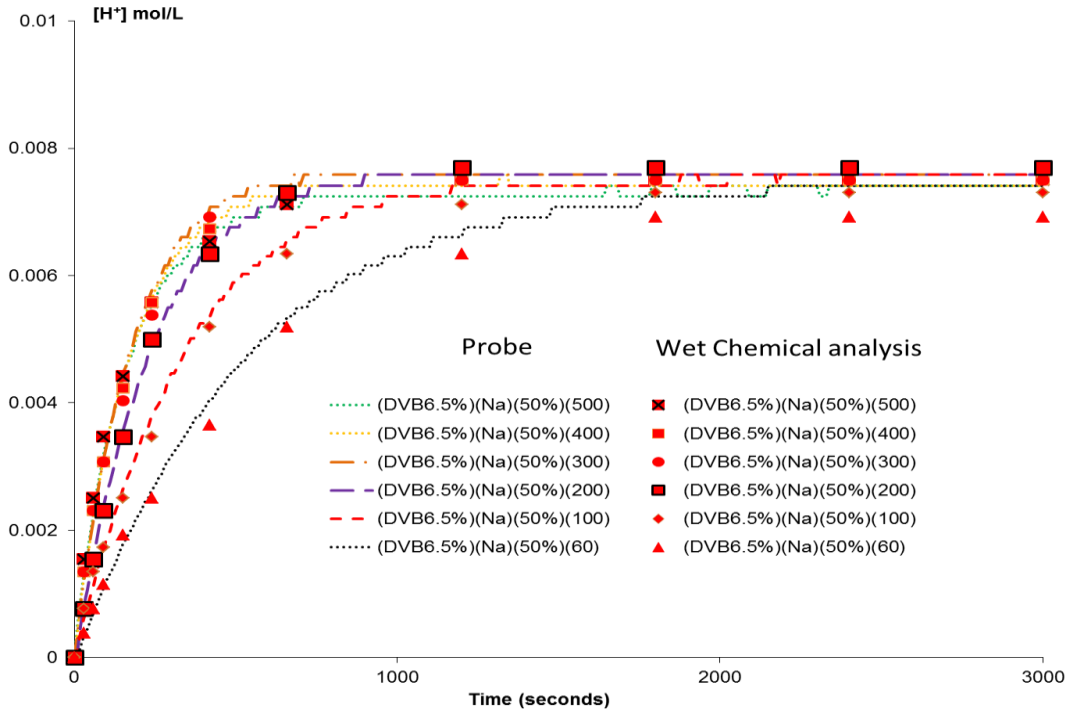

Fig.5-2, Desorbed $[H^+]$ in solution at various flowrates as Na^+ is adsorbed

The lower flowrates, i.e. 60 *mL/min*, 100 *mL/min*, 200 *mL/min*, show a progressive increase in the rate of mass transfer, however the 300 *mL/min*, 400 *mL/min*, 500 *mL/min* kinetic curves are seen to be virtually on top of each other. This can be seen as an indication that during the three highest flowrates the laminar layer resistance is sufficiently supressed and that at this point intra-particle diffusion plays a more dominant role in resistance to mass transport.

Approximately 85% of the H^+ is desorbed at equilibrium, achieving an average pH of 2.1. Also noticeable is the congruency between the probe measurements and that of the wet chemical analysis, an important aspect given probe calibration is more difficult to achieve than carrying out accurate wet chemical analysis, and it is the high frequency probe measurements that will be used during the curve fitting process to determine the parameters of the system.

More of a challenge to achieve but equally important is ensuring that the final concentration/equilibrium point for each test falls on similar concentration values. This can only be achieved by ensuring accuracy in all measurements and that all the starting bulk concentrations and all the regenerated/starting resin states are identical for each test. In the present set of tests the final concentrations are seen to all fall appropriately within a narrow margin between 0.0074 *mol/L* and 0.0076 *mol/L*, with the exception of the 60 *mL/min* test which is slightly lower at 0.0069 *mol/L*.

5.4.2. Impact of DVB content and ion diffusivity on kinetics

In addition to a qualitative study of effect of turbulence on kinetics, it was also necessary to observe the impact of the resin DVB content and ion diffusivity on kinetics of adsorption. It was decided to undertake preliminary tests using both Na^+ and Mg^{2+} to ensure that the impact of varying DVB content could be observed in both ions as all resin manufactures indicate that higher valence ions have a greater affinity for resin and both have quite different free diffusivities (section *5.4.4*).

Na^+ and Mg^{2+} ions were adsorbed, separately, onto resin in the H^+ form in the closed-circuit kinetic testing unit, using six different circulatory flowrates 60 *mL/min*, 100 *mL/min*, 200 *mL/min* , 300 *mL/min*, 400 *mL/min*, 500 *mL/min*. In addition, two resins of different DVB content were used (10%, 6.5%), generating a total of twenty four kinetic curves.

The kinetic tests were conducted in a similar manner to that described in section *5.3*, however, to lessen the impact of laminar layer control, the starting concentration of adsorbent ion in the circuit was set at a higher level of 0.0162 *equiv./L* for both the Na^+ and Mg^{2+}, which corresponds to 0.0081 *mol/L* in the case of the divalent Mg^{2+}. This amounted to a starting mass of adsorbent in the circuit at approximately 80% in excess of the capacity of the ion exchange resin.

To characterise the nature of each transient, its half-life was determined as outlined in section *5.3.* This was an easy task given the high frequency recording rate of the probe data. It was envisaged that the adsorption process of the slower diffusing Mg^{2+} ions, as concluded from published infinite dilution diffusivities (Li&Gregory, 1974) for Mg^{2+}, would take longer to reach equilibrium and hence its kinetic curves should display longer half-lives compared to the Na^+ curves. Theoretically, this phenomenon should then be enhanced in the higher 10% DVB content resin (higher internal steric-state environment) when compared to the 6.5% DVB resin. Fig.5-3 shows the four families of curves generated from the systematic adsorption of each ion onto each resin type in terms of the conversion of the resin based on bulk concentration of the adsorbing ion.

Fig.5-4 shows a composite of the half-lives of every kinetic curve presented in Fig.5-3. From Fig.5-4 a number of observations can be made. Firstly, the kinetic curves displaying the adsorption of the slower diffusing Mg^{2+} ions do indeed display longer half-lives in both the 10% and 6.5% DVB resins compared to that of the Na^+ ion. This is good evidence that resin ion adsorption is diffusion driven in the intra-particle zone.

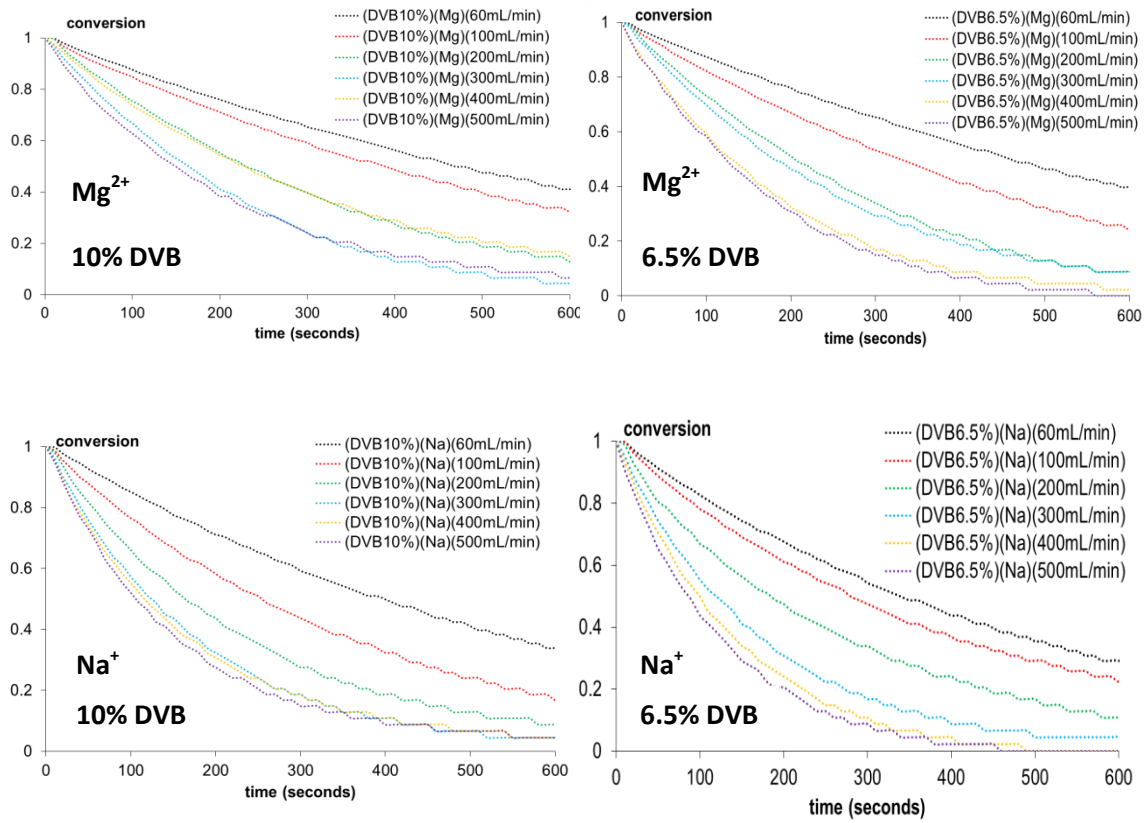

Fig.5-3 Adsorption of Na^+ & Mg^{2+} on 10% & 6.5% DVB resin

Secondly, for constant flowrate (turbulence) the half-lives of most of the kinetic curves show an increase for both the Na^+ and the Mg^{2+} ions when adsorbed onto the 10% DVB higher internal steric-state environment resin compared to the 6.5% DVB lower steric- state environment resin. Although this trend is not universal throughout the data it certainly appears to be the average, and it is also notable that this trend is well established especially for the higher flowrates (400 *mL/min* & 500 *mL/min*). This is significant, as this is the region where the turbulence is at its highest, minimising the impact of laminar layer control on mass transport and respectively passing greater primacy to intra-particle control.

5.4.3. Impact of multiple controlling mechanisms

In an attempt to replicate the findings of Petruzzelli *et al* (1987a), the probable existence of mixed mechanism control during the transient was investigated. This was attempted by

assuming that laminar layer control was in effect over the entire duration of the experiment, with the rate of mass transport being only impacted upon by a change in turbulence, all else being equal.

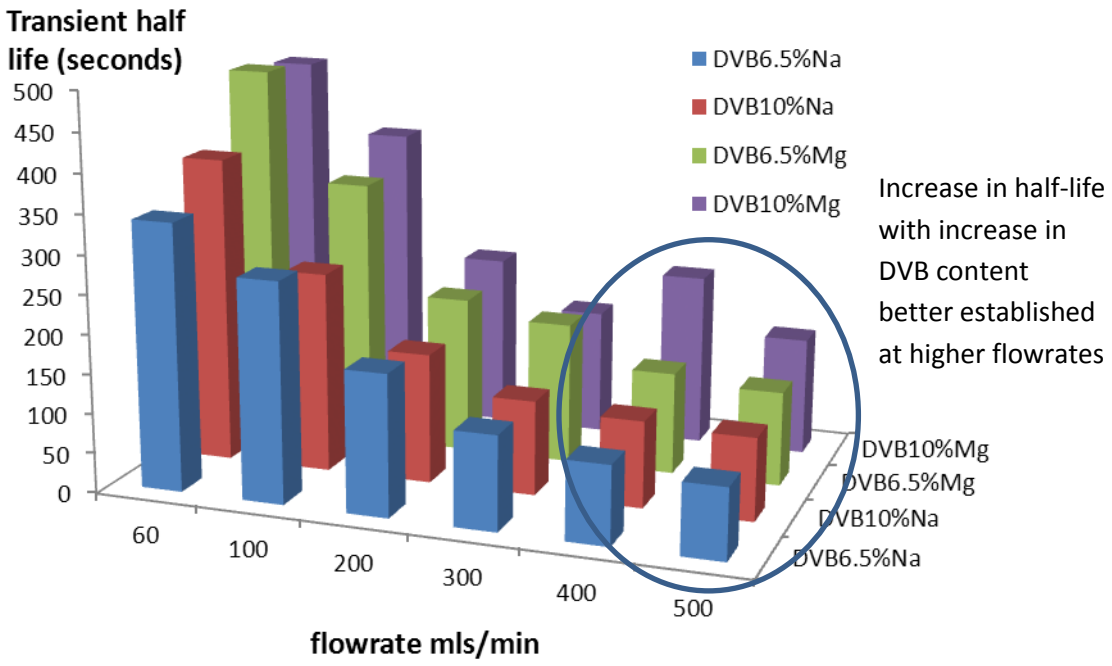

Fig.5-4, Impact of half-life adsorption kinetics for different DVB contents, Na^+ & Mg^{2+} onto 10% & 6.5% DVB resin

If the mass transfer coefficient (K_L) could be determined and an adsorption test performed where the turbulence is maintained constant, divergence from laminar layer control would be indicative of a change in control mechanism. A prediction, calculated from a model based on laminar layer control would indicate expected behaviour, any deviation from which would constitute an indication of a shift to another controlling mechanism.

The main challenge is to determine the mass transfer coefficient (K_L) and this can be achieved by generating a family of kinetic curves, each at a different turbulence, which can then be analysed by using the standard technique of determining the mass transfer coefficient from the initial slope of the kinetic curve. This assumes that laminar layer control is dominant in early time data, the probability of which would be enhanced by using low starting concentrations of adsorbing ion together with using resin with a low internal steric-state

density. The method assumes that the concentration on the surface of the resin is equal to zero and therefore the driving force across the laminar dynamic layer is the bulk concentration. In the context of determining the mass transfer coefficient for the laminar layer alone, i.e. ignoring the rate of intra-particle diffusion, this assumption is reasonable as any ions reaching the resin will thereafter not be constrained and will then quickly recede into the resin, negating any possibility of build-up. Under these circumstances control will be along the lines of Newton's Law of cooling. See Equ.3-1 to 3-6 in the model development section.

The study was conducted as described in section *5.3*, by adsorbing Mg^{2+} ions onto 5 *mL* of a 6.5% DVB acid resin contained in the ZLC as part of the closed circuit system for kinetic measurements as described in 'equipment' section *4.3.1*. The 6.5% DVB (C100E) resin was chosen as it has a relatively low density steric state environment inside its copolymer matrix which would present lower resistance to intra-particle diffusion. The concentration of the adsorbing ion in the bulk was carefully set at 80% excess to the capacity of the resin for all five tests to ensure the same final concentration will be arrived at once equilibrium has been attained in each test. The adsorption achieved was left to proceed to equilibrium and can be represented chemically by Equ.5-1. Fig.5-5 gives the conversion curves for the resin at different flowrates based on the change in desorbing ion concentration.

$$\boldsymbol{2R - H + Mg^{2+} \Rightarrow R - Mg + 2H^{2+}} \qquad \textbf{5-1}$$

Finally, a proportionality coefficient (Equ.3-4) could be determined via linear regression from the early time data for each kinetic curve measured, from which the mass transfer coefficient could be calculated (Equ.3-4) by mathematically removing the measurable parameters of the system i.e. $\boldsymbol{N_R}$, R, $\boldsymbol{V_c}$. The data points used and considered to be part of 'early time data' were discerned visually as can be seen in Fig.5-5.

The study proceeded to use the mass transfer coefficient to predict each conversion-derivative curve versus conversion to $X_D = 0$ (completion). The conversion-derivative versus conversion of the lab data was then superimposed. The results are shown in Fig.5-6.

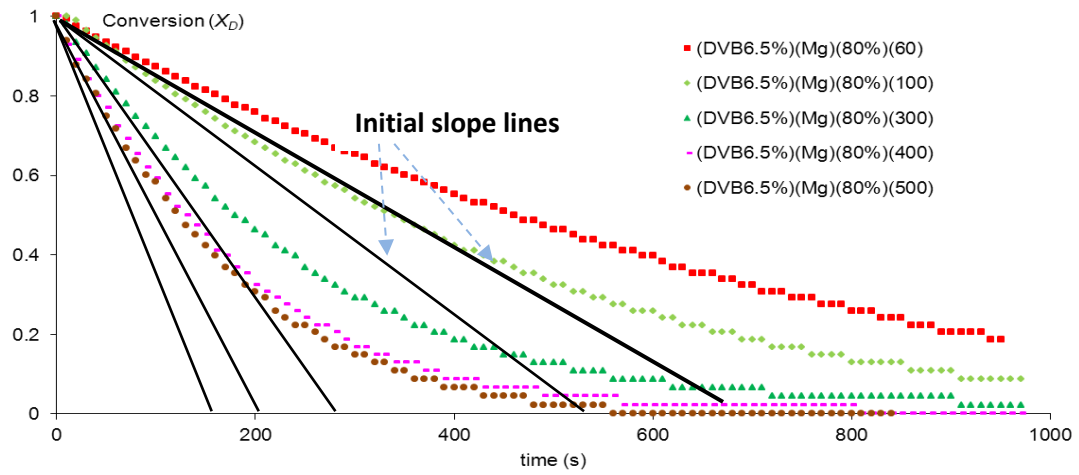

Fig.5-5 Desorption data for five flowrates, Mg^{2+}/H^{+} system onto 6.5DVB resin

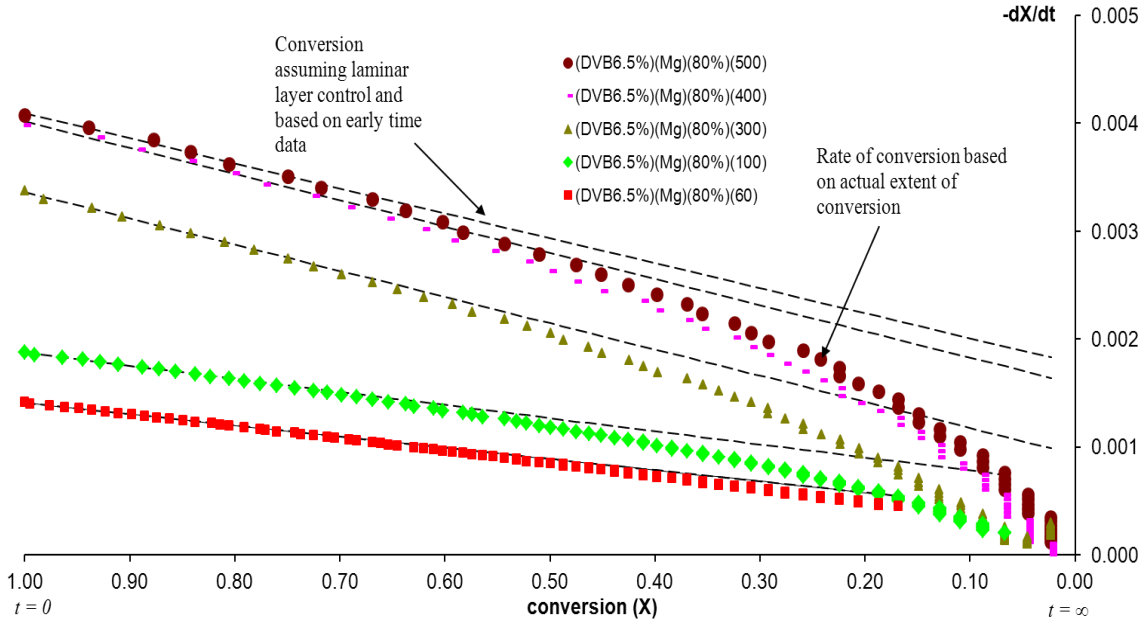

Fig.5-6, Comparison of predicted laminar layer curve against measured data.

As can be seen from the Fig.5-6, the model derived from the initial slope of the kinetic curve gives a straight line on these axes, which is to be expected given the proportionality relationship presented in Equ.3-4. When superimposing the raw data on top of the model curve, perfect congruency can be observed at higher rates of change i.e. earlier stages of the kinetic test. This is to be expected as the model is based on early time data. However, as the kinetic test proceeds towards equilibrium, the raw data begins to move off the proportional model, earlier for higher turbulence kinetic tests, and later for lower turbulence kinetic tests.

In every case the rate of change of the derivative of conversion against conversion of the lab data began to decrease more rapidly compared to the model prediction. These results are not unexpected as they are indicative that at some point in the transient, another controlling mechanism steps in and significantly slows the adsorption rate below that permitted by the controlling laminar layer mechanism. This other mechanism can only be intra-particle diffusion, and predictably it impacts the process earlier for the higher turbulent transients, where the calculated proportionality constant (Equ.3-4) mass transfer coefficient is higher i.e. the resistance of the laminar layer is less. These results confirm conclusively the findings of Petruzzelli *et al* (1986), of the existence of multiple controlling mechanisms during the transient and are also in agreement that during the early time data it is laminar layer control that generally controls under appropriate circumstances.

In the process of attempting to locate both the laminar layer mass transfer coefficient and the intra-particle diffusivity it is important to ensure that both mechanisms control at some stage during the transient. We can see from Fig.5-6 that for very low turbulences it appears that the laminar layer controls for almost the entire duration of the transient and this would then imply the lesser likelihood of locating intra-particle diffusivity under these conditions.

Although it was assumed that for early time data the surface concentration of the adsorbing ion in the liquid was zero, at higher flowrates it is possible that it might not have been so. Whatever the value of the surface concentration during early time data, as the transient proceeds, it is only likely to rise as the resin becomes saturated with the adsorbing ion. This confirms the difficulty of rigorously modelling transient adsorption behaviour onto ion exchange resin and the challenge to elucidate meaningful parameters from what could principally be lumped parameters.

5.4.4. Free aqueous solution diffusivities and the impact of temperature

As the ion exchange adsorption process is considered to be dominated by diffusion mechanisms, an important parameter of each system is the free aqueous solution diffusivities

(D_L) for Na^+, Mg^{2+}, Ba^{2+}. These were taken from Li & Gregory (1974), which gives values for 25°C, 18°C, 0°C and compared to calculated values using the 'Method of Wilke-Chang' (Wilke & Chang, 1955) all of which are displayed in Fig.5-7. The congruency is apparent. It is therefore necessary to use these correlations as there is a substantial change in diffusivity even over this relatively narrow temperature range. It is observed that the infinite dilution diffusivity of Na^+ increases by as much as 37% over the relatively minor temperature increase of 10°C to 20°C.

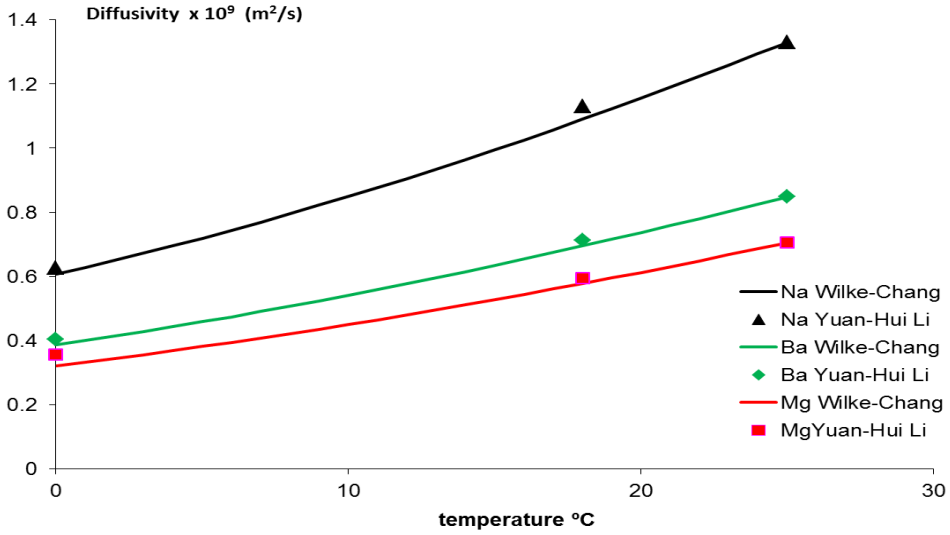

Fig.5-7 Free diffusivities for Na^+, Ba^{2+} and Mg^{2+}

5.4.5. Impact of temperature change on kinetics

It is well documented that temperature has an impact on diffusion, a phenomenon also shown in section *5.4.4.* Therefore it is not unreasonable to assume that a change in temperature will affect both the mass transfer coefficient and the intra-particle diffusion rates. Accurate measurement of this diffusion could require precise control of the temperature of the system. As a preliminary check on the effect of temperature, an exercise was undertaken to determine its impact on kinetics of adsorption and equilibrium.

A 5*mL* sample of 10DVB resin was loaded with Mg^{2+} ions from a one litre $Mg(NO_3)_2$ solution, at a concentration that equated to 20% excess of the capacity of the resin, in the closed circuit unit, described in the Equipment chapter (Fig.4-6). The test was undertaken at four different temperatures and the kinetic curve for each measured separately.

Fig.5-8a displays the resultant four kinetic curves of different temperatures. Fig.5-8b shows the equilibrium coefficient values calculated from the ultimate values achieved in each kinetic test.

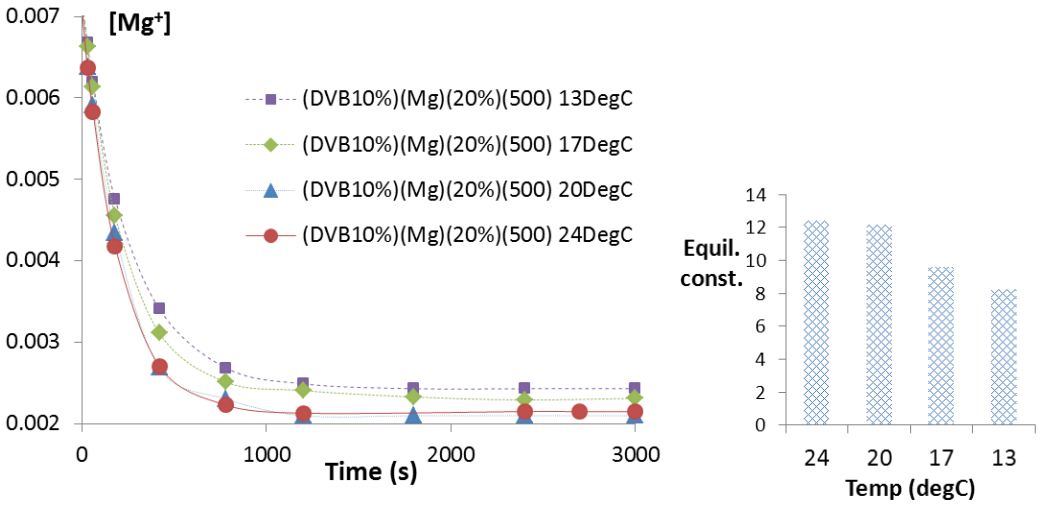

Fig.5-8a, Kinetic adsorption of Mg^{2+} onto 10DVB resin at four temperatures

b, Calculated equilibrium coefficients at each temperature

Fig.5-8a shows clearly that there is a shift in the kinetic curve with change in temperature. The lower temperatures appear to slow the adsorption process down as the initial slopes of the curves appear flatter. This would agree with the general trend of lower temperatures slowing down diffusion shown in section *5.4.4.* Notable also is the change in calculated equilibrium coefficient. The necessity to control the temperature of the system when proceeding with a kinetic test is thus clearly apparent.

5.5. Capacity Test work method

The capacity of resin, based on available active sites, needs to be measured regularly and accurately. A standard analytical measurement is available in the literature published by Rohm and Haas: MTM0230 (Master Test Method): Cation salt splitting method and it is this method that is used to determine the capacity of the strong acid cationic resin. The method requires an open circuit, as displayed in Fig.4-7, and requires a $NaNO_3$ solution as influent. As the resin is confined to the ZLC the capacity of the specific resin present could be determined at any stage in the test work using this method.

The ZLC reactor is removed from the aging/decaying machine and placed in an open circuit system. One litre of one normal solution of hydrochloric acid is passed through the ZLC at a rate of 25 *mL/min*. Thereafter one litre of deionised water is passed through the ZLC to ensure that all the excess acid is removed. This can be checked by confirming that the pH coming out of the ZLC is above five.

Thereafter one litre of 0.5 mol $NaNO_3$ analytical solution (approximately fifty times the capacity of the bed) is passed through the ZLC at a rate of 25 *mL/min*, carefully catching exactly one litre of effluent. This one litre of solution, it was discovered, has to be very thoroughly mixed as the greater acid portion leaves the bed at the beginning of the loading process and therefore congregates at the bottom of the flask resulting in stratification.

From the one litre of effluent 100 *mL* of solution is removed and titrated against an analytical solution of NaOH at a concentration prepared to the following level of accuracy 0.1000 *mol/L*. Synthetic solutions of acid are made up to check that the NaOH solution is at the correct concentration. A blank 100 mL of solution is also taken from the feed solutions and titrated against the NaOH and subtracted from the final acid measured in the effluent.

Equ.5-2 is the calculation that is carried out on the titration results to determine the capacity of the resin bed inside the ZLC.

$$\boldsymbol{Q} = \frac{10 \times [\boldsymbol{V}_{NaOH} - \boldsymbol{V}_{blank}] \times \boldsymbol{N}_{NaOH}}{\boldsymbol{FWSR}} \qquad \textbf{5-2}$$

Where

$\boldsymbol{Q}$	Capacity of the resin (*equiv./L*)
$\boldsymbol{V_{NaOH}}$	Volume of NaOH added to neutralise the sample (*mL*)
$\boldsymbol{V_{blank}}$	Volume of NaOH added to neutralise the blank (*mL*)
$\boldsymbol{FWSR}$	Volume of Free Wet Settled Resin in the bed. (*L*)
$\boldsymbol{N_{NaOH}}$	Concentration of NaOH titrant (*mol/mL*)

If the capacity determining method is carried out, in exactly the same manner, using either $Mg(NO_3)_2$ or $Ba(NO_3)_2$, very similar results are achieved in the case of the $Mg(NO_3)_2$. However, there is a marginal difference of approximately 10% when using $Ba(NO_3)_2$, which could be attributed to the far slower diffusion of the Ba^{2+} ion implying that the adsorption process might not have been completed once all the feed solution had been used up, see Tab.5-1. Repeatability with the Barium test also proved difficult, and this could be attributed to the greater affinity that the resin has for the Ba^{+} ion, making its removal by acid less efficient.

Tab. 5-1 Fresh resin equivalent ion capacity using different reagents

Capacity using $NaNO_3$	1.938 *Equiv./L* (***FWSV***)
Capacity using $Mg(NO_3)_2$	1.942 *Equiv./L* (***FWSV***)
Capacity using $Ba(NO_3)_2$	1.715 *Equiv./L* (***FWSV***)

5.6. Equilibrium Test work method

Equilibrium test work has as its objective the measurement of concentrations at dynamic equilibrium from which is calculated the equilibrium coefficient as dictated by the Mass-Action-Law. In this study this was carried out in two ways; 1) through dedicated laboratory test work and 2) by recording/calculating all concentrations at the end of any kinetic test.

5.6.1. Equilibrium coefficient calculated from dedicated laboratory work

The dedicated laboratory test was conducted in the following manner. The ZLC reactor was placed in a closed circuit with the reservoir and peristaltic pump similar to the kinetic testing apparatus in Fig.4-6 shown in the Equipment section.

After the capacity of the resin has been determined (section *5.5*), the ZLC containing the carefully measured volume of resin, has one litre of one normal solution HCl passed through it to ensure that the resin is in the H^+ form, as at the start of the capacity (section *5.5*) and kinetic tests (section *5.3*). This part of the exercise is conducted in open circuit to ensure that the resin is exposed to an infinite solution, i.e. adsorbed cationic ions that are released are not allowed to re-adsorb onto the resin.

Thereafter, also in open circuit, the ZLC is flushed with an excess of deionised water until effluent rises to a pH >5, to ensure that all excess acid has been removed from the resin, as any remaining excess acid will hamper the adsorption process. The open circuit is then closed so that the effluent from the ZLC reports back to the reservoir.

Although either chloride or nitrate salts could be used for this test work, it was decided to standardise using nitrate salts. Initial charges of either $NaNO_3$, $Mg(NO_3)_2$ or $Ba(NO_3)_2$ are placed in the reservoir, with the mass equating to one of the following percentages of the capacity of the resin bed in the ZLC all measured in equivalents; 10%, 50%, 80%, 120%, 150%, 180%, 210%, 250%. Each test is allowed to proceed until the pH probe detects zero movement in the pH, i.e. dynamic equilibrium has been reached. The pH, which would by then have dropped considerably, is noted, and a wet chemical sample is taken and its concentration determined by titration against a NaOH solution at a concentration of 0.00300 *mol/L*. Once a number of tests have been completed all with different starting concentrations, the results can be portrayed graphically as in Fig.5-9, which is the equilibrium curve for the adsorption of Na^+ onto the 10 DVB resin (PPC100x10).

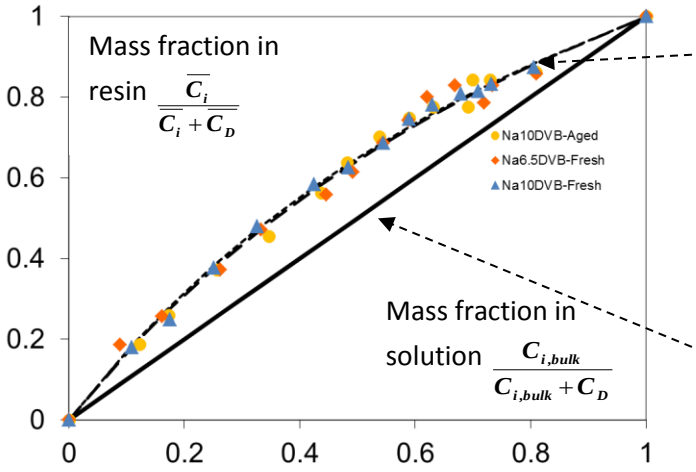

The fitted curve gives a parameter equilibrium coefficient (α) of 1.81, which is close to the published value of 1.7.

Parity line i.e. no affinity for either the solution or the resin

Fig.5-9 Na^+/H^+ equilibrium for fresh 6.5%DVB, 10%DVB, aged 10DVB resins

A single empirical parameter known as the equilibrium coefficient (α), describes the curve dictated by the Mass-Action-Law equilibrium model. This value can be calculated by fitting the appropriate form of the Mass-Action-Model Equ.5-3. This is covered in greater detail in the model section *3.4.*

$$\frac{\dfrac{\overline{C_i}}{\overline{C_i}+\overline{C_D}}}{\dfrac{\dfrac{C_i}{C_i+C_D}}{1-\dfrac{C_i}{C_i+C_D}}\left(1-\dfrac{\overline{C_i}}{\overline{C_i}+\overline{C_D}}\right)}=\alpha \qquad \textbf{5-3}$$

Where

$\frac{\overline{C_i}}{\overline{C_i}+\overline{C_D}}$ Equilibrium molar fraction of adsorbing ion in resin (dimensionless)

$\frac{C_i}{C_i+C_D}$ Equilibrium molar fraction of adsorbing ion in bulk (dimensionless)

5.6.2. Determining the base case equilibrium coefficients

In a kinetic test the final ratios between the concentrations on the resin and in solution should match up to the (α) value for the system. Measuring the equilibrium value achieved in a kinetic test and finding it not to concur with that calculated using the laboratory measured equilibrium coefficient, would amount to circumstantial evidence that the kinetic test results are poor and this would be an important cross check of each kinetic test

Therefore knowledge of the likely values of equilibrium coefficients for the different ions adsorbed, and the resins used, was considered necessary, and this required dedicated tests to be undertaken for each of the three ions used in the test work (Na^{+}, Mg^{2+}, Ba^{2+}).

A study was conducted in which the equilibrium coefficient for the Na^{+}, Mg^{2+} and Ba^{2+} adsorbed onto fresh 10%DVB (PPC100x10) and 6.5%DVB (C100E) resin was determined. The testing method is described in section *5.6.1*. Fig.5-10 shows the results of these experiments.

As is generally the case with equilibrium test work, there is a degree of scatter of data. To overcome this, the Mass-Action-Law equilibrium model was fitted to the equilibrium data points for each ion and the result are the dashed lines in Fig.5-10. The functional form of the Mass-Action-Law used to fit the model to the data is described in more detail in the model section *3.4.1*.

From Fig.5-10a&b it can be seen that the affinities for the three ions are as follows; $Na^{+} < Mg^{2+} < Ba^{2+}$. This is perfectly in keeping with the literature and shows that the increase in resin affinity for cations is due to a combination of larger ion size and valence. The equilibrium coefficients determined were; $Na^{+} = 1.8$, $Mg^{2+} = 10$, $Ba^{2+} = 25$. It can also be seen that the affinities for the cations are virtually the same for both resins types. This is to be expected as the difference between the resins is purely structural and should not affect the chemical equilibrium conditions. The raw data for these equilibrium tests are presented in Annexure VIII.

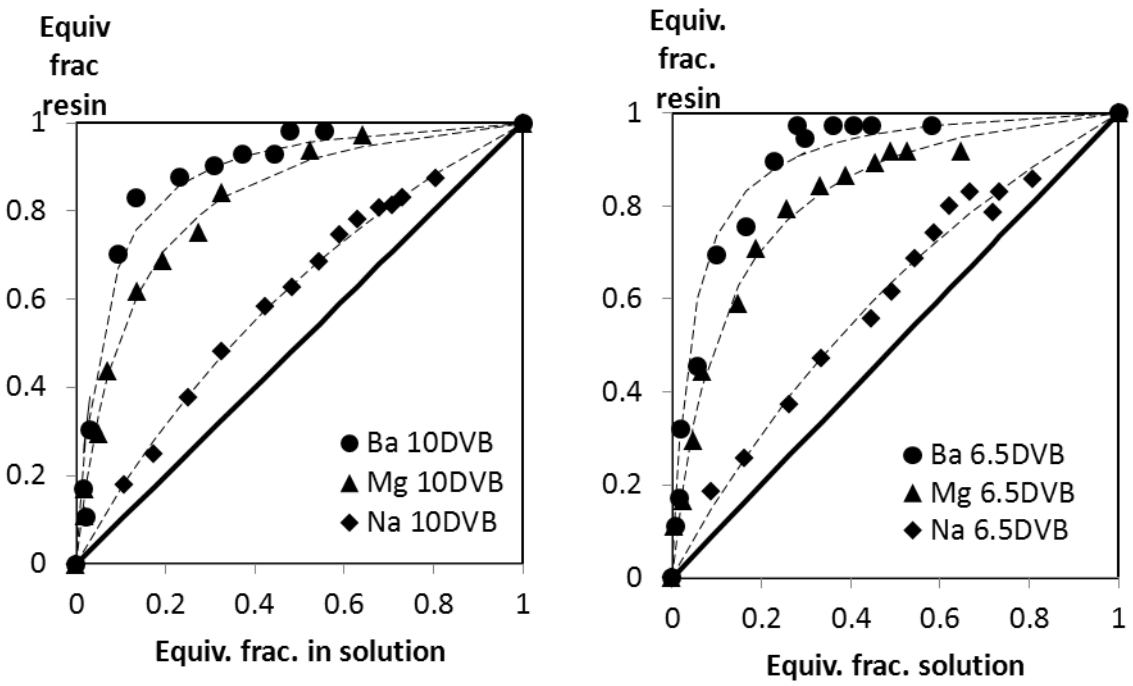

Fig.5-10a&b, Equilibrium curves for Na^{+}, Mg^{2+}, Ba^{2+}ions (a)10DVB (b)6.5DVB

5.6.3. Equilibrium coefficient calculated from kinetic test asymptote

Equilibrium tests carried out in the laboratory are likely to produce a more accurate equilibrium constant (α) as it will be calculated by the fitting of the Mass-Action-Law model to an entire data set. However, the asymptotic value of a kinetic curve is also indicative of the equilibrium value and hence can also be used to forward-calculate the equilibrium constant (α) albeit from a single equilibrium condition. This fact becomes attractive as it lowers the amount of test work to be undertaken and will result in attaining an equilibrium coefficient value appropriate to the particular kinetic test. In addition, the kinetic model simulation algorithm requires an equilibrium coefficient. Using the equilibrium coefficient calculated from the final kinetic point was considered reasonable, providing the value was realistically close to that obtained in the dedicated equilibrium test work.

Primarily, an equilibrium coefficient (α) based on the Mass-Action-Law is calculated using an altered form of Equ.5-3 that uses the starting ($t = 0$) and final values ($t = \infty$) of the kinetic curve. More detail in the method of calculation can be found in Annexure IV. For all kinetic test work data the equilibrium coefficient was calculated directly from the asymptotic value

achieved and checked for reasonableness against dedicated laboratory equilibrium test work before being used in the fitting of the transient simulation algorithm to the kinetic data.

5.7. Wet chemical analysis method

As we have already seen, the wet chemical analysis of the samples consisted of titrating against a 0.1 *mol/L,* or 0.003 *mol/L* solution of NaOH. The higher concentration required for the capacity tests the lower for the kinetic and equilibrium tests. The indicator used in the tests was phenolphthalein.

As was stated in the test work section, to ensure accuracy, wet chemical analyses were performed. The challenge was that in a reservoir of one liter volume being fed hydrogen ions from a resin bed of only 5 *mL* volume, the degree of increase in acid level was, predictably, very small being of the order of 0.005 *mol* at full conversion.

However, to limit the reduction in volume of the circuit the quantity of solution removed from the reservoir was limited to approximately 5 *mL* per sample taken, the exact volume being measured for each sample. This meant that in a typical kinetic test the quantity of released acid that required measurement in the sample varied between 2.5 *µmol* and 25 *µmol*.

This required the setting up of a standard solution for titration purposes of NaOH at a concentration of 0.003 *mol/L* with only as little as two mL being consumed for some of the critically important early time data samples in the lower turbulence kinetic tests. This required the analyst to develop a keen sense of indicator hues and to consistently employ the thirty second rule (ensuring the indicator colour change is maintained for thirty seconds) to be sure that the end point of the titration has been genuinely obtained. Although difficult, with some experience the end point was eventually reliably obtained.

In the case of sodium adsorption onto the resin this was a straightforward analysis, although it had to be confirmed that the acid dissociation between the H^+ and the anionic element associated with the original sodium salt was as high as possible. As the anionic element used

in all cases was nitrate, the dissociation was considered to be high enough not to cause there to be a discrepancy between the probe and wet chemical analysis.

In the case of the sodium adsorption test work the solubility product (K_{sp}) of NaOH is extremely high and there is no chance of hydroxide precipitate forming. However, in the case of Mg^{2+} and Ba^{2+} both metals could precipitate as hydroxides and therefore assurance was needed that this tendency did not interfere with the analytical process as the formation of the hydroxide complex which would lead to inaccurate results. Both metal hydroxides have relatively low solubility products (K_{sp}) i.e.

$Mg(OH)_2$ @25DegC $1.5x10^{-11}$ $Ba(OH)_2$ @25DegC $5.0x10^{-3}$

However, as the solutions are generally in the acidic range i.e. pH < 5 the calculations displayed in Annexure XII prove that neither during test work nor during the titration is it likely that these metal hydroxides will precipitate. The resultant equations for Mg^{2+} and Ba^{2+} hydroxide precipitation are presented in Equ.5-4 and Equ.5-5 respectively.

$$\log[Mg^{2+}] = -2\,pH + 17.18 \qquad \textbf{5-4}$$

$$\log[Ba^{2+}] = -2\,pH + 25.70 \qquad \textbf{5-5}$$

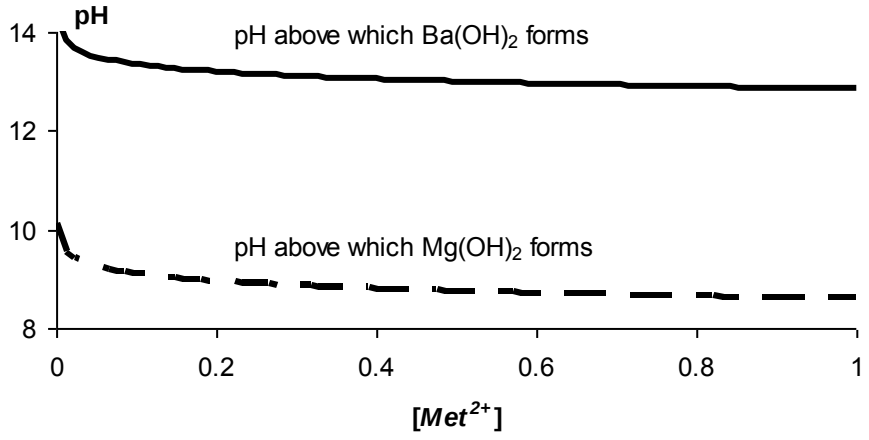

Fig.5-11 Graphical representation of Equ.5-4 & Equ.5-5

5.8. Difficulties with the regeneration of resins after Mg^{2+} and Ba^{2+} adsorption

From Fig.5-10 its possible to see the difference in the equilibrium between the Ba^{2+}, Mg^{2+} and Na^{+} ions. The Na^{+} appears to be held least strongly and the Mg^{2+} and Ba^{2+} ions consecutively more strongly. The regeneration of the resin after Na^{+} adsorption was achieved relatively easily by passing a half litre of 1 *mol/L* HCl through the circuit with the capacity of the resin always returning to the original starting capacity. To achieve the same regeneration after adsorbing Mg^{2+} the concentration of the regeneration solution needed to be closer to 2 *mol/L* HCl. Finally, to achieve total regeneration of the resin after Ba^{2+} loading a regeneration concentration of at least 2 *mol/L* was required and then the resin needed to be soaked in this solution for a few hours and even after this it could not be assured that the all the Ba^{2+} had been removed. Hence Ba^{2+} was not considered to be an ideal ion for repetitive equilibrium/kinetic tests where it was required that the resin, at the start of a kinetic test, have as full a capacity as possible available.

Therefore it was decided that for the resin aging test work only Na^{+} ion would be used to determine the mass transport parameters of the system.

5.9. Resin aging method

This test work was performed using the Resin Decaying Machine described in section *4.1*. The ZLC is filled with approximately 5 *mL* of fresh 10 DVB (PPC100x10) resin that is in the Na^{+} form, as supplied by the manufacturer. It is then regenerated by passing a half litre of 1 molar HCl solution through the ZLC at a flow rate of < 20 *mL/min*. Thereafter the resin is removed and its volume measured to confirm its H^{+} form volume. Generally, the resin bed expands from the Na^{+} form to the H^{+} by approximately 14% on a volume bases. After completing the expanded volume measurement the resin is returned to the ZLC and a standard capacity (section *5.5*) test is performed followed by a triple kinetic test (section *5.3.1*) to determine the zero-cycle laminar layer mass transfer coefficient and intra-particle diffusivities.

The ZLC is then put into the open circuit Resin Decaying Machine and undergoes the three stages of Loading, Regeneration and Washing cyclically one hundred times with each cycle taking exactly 30 minutes to complete.

The loading stage is a 0.05 *mol* $CuSO_4$ solution. Approximately 530 *mL* of solution is passed through the ZLC during each loading, effectively 265% in excess of the resin bed capacity. The loading process is carried out at a flow rate of 50 *mL/min* and therefore takes 9.6 minutes. This duration was considered sufficient to load the resin with Cu^{2+} ions.

The regeneration stage has a 2N (1.0 *mol/L*) H_2SO_4 and 0.135 *mol/L* H_2O_2 solution mixture passing through the ZLC at a flow of 50 *mL/min* over a period of 6 minutes. The flow is stopped on three occasions for 1.2 minutes during the regeneration thus the regeneration stage takes 9.6 minutes in total time. The routine stoppage is undertaken to save reagent as it is in great excess to what is required by the resin i.e. approximately 2900% .

The entire cycle takes 30 minutes and hence the washing stage proceeds for 10.8 minutes and consists of tap water being passed through the ZLC at 50 *mL/min*. Analysis of the effluent showed that there was sufficient volume to reduce the acid content to a pH above that of 5, ensuring there would be no impact on the adsorption in the following cycle.

5.10. Resin aging test work and model tweaking

The presence of Cu^{2+} and H_2O_2 in solution during the regeneration phase causes Fenton's reaction (*Geameay et al.*, 2004) that leads to the accelerated breakdown of the resin active sites and structure. After every 100 cycles, the ZLC is removed from the aging machine and placed into the capacity testing apparatus described in section *4.3* and the capacity

determined as described in section *5.5.* Thereafter the ZLC is passed to the kinetic testing unit described in section *4.2.1* and kinetic tests conducted.

From Fig.5-6 it is possible to conclude that for the lower flowrates of 60mL/min and 100mL/min through the ZLC the laminar layer control is dominant for virtually 50% to 70% of the duration of the test and hence it is unreasonable to assume that reliable intra-particle diffusivities can be measured from kinetic test work conducted at these lower flowrates using a combined-model fitting method. It was therefore decided to only undertake kinetic test work during the resin aging process at higher ZLC through-put flowrates i.e. 300 *mL/min*, 400 *mL/min* and 500 *mL/min*. This would also lessen the amount of test work required for each 100 cycles by half. The tests were conducted using the Na^+ ion, and at a starting concentration of 80% in excess of the resin capacity. After completion of the three kinetic tests, the ZLC is returned to the resin decaying machine for the next 100 cycles.

The resin decay experiment was continued for 800 cycles (taking approximately a month) thereafter the raw kinetic data recorded through each test was then processed by the computer program that is described in detail under model development in section *3.7* and in Annexure III. This program computes the mass transfer coefficient associated with the laminar dynamic layer and the intra-particle diffusivities of both the desorbing and adsorbing ions present in the system by means of fitting a transient adsorption simulation to the raw data.

5.10.1. Curve fitting (optimisation) difficulties

The process of fitting the model to the data was a substantial task that initially took between one and four hours per set, depending on the data. With some experience this time was shortened as better initial estimates of parameter values could be passed to the search algorithm. However, with continued fitting campaigns some trends were observed with respect to how the algorithm determined the $\boldsymbol{K_L}$ value and the relationship between the intrinsic diffusivities of the adsorbing and desorbing ions.

5.10.2. Search algorithm appears to obtain K_L value in early time data

From an early stage in the curve fitting exercises it become apparent that the mass transfer coefficient (K_L) was important in the simulation algorithm. In model development (section *3.3.2.*) it can be seen that the surface concentration is calculated directly from the estimated K_L value which is one of the parameters sought by the search algorithm and is therefore sought iteratively.

It has already been established that it is at the start of the adsorption transient where the bulk adsorbing ion concentration and therefore flux are at their highest and surface concentration at its lowest and hence where the K_L value is likely to dictate that the laminar layer will be the controlling mechanism for mass transfer. This implies that the lowest possible mass transfer coefficient could theoretically be calculated from the earliest time data, where the highest driving force is present. If the proposed value of K_L is too low, it causes the simulator to generate surface concentrations that are negative during early time data, which is of course meaningless.

However, as the K_L value plays a role to a greater or lesser extent throughout the transient no bound was placed on its posed iterative value while a lower bound was set on the surface concentration, directing that it could not drop below zero. Fig.3-16 is an example of a simulation that used this approach.

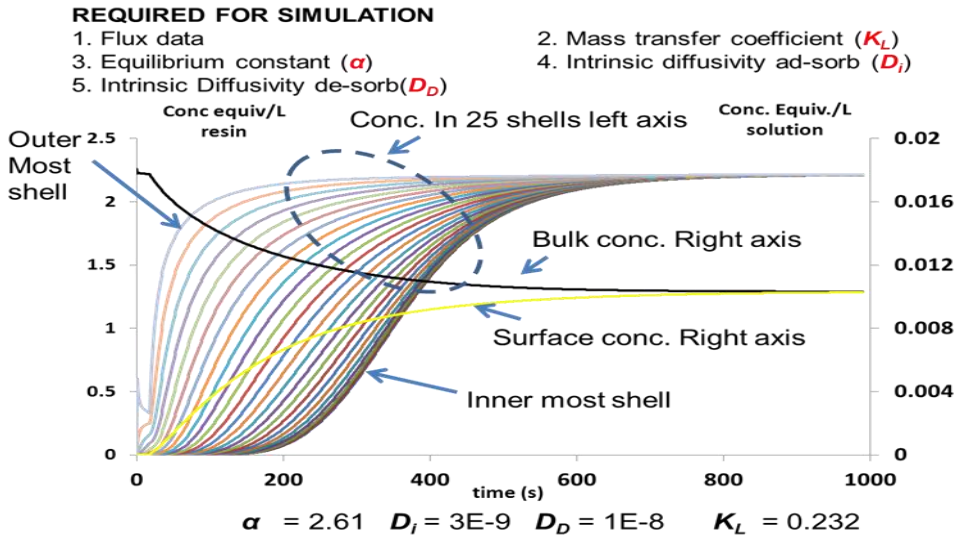

Fig 3-16 Graphical representation of simulator output

5.10.3. Simulation presents a discrepancy in the first 200 seconds

As adsorption advances, the ions build up in the resin and an increase in concentration at the surface, dictated by equilibrium, is inevitable, with the surface and bulk concentration slowly approaching parity. Ultimately laminar layer mass transfer control (the $\boldsymbol{K_L}$ is assumed constant throughout) will reduce to nothing as the bulk and surface concentrations narrow asymptotically towards each other.

Invariably, the search algorithm obtained best fit $\boldsymbol{K_L}$ values that were similar to those that could be located from early time data assuming zero concentration at the surface (see model development section *3.2.2.*), which was good circumstantial evidence that the obtained $\boldsymbol{K_L}$ value was meaningful. However, due to set surface concentration boundary ($C_i^* \geq 0$) (as explained in section *5.10.2*) the final fits obtained $\boldsymbol{K_L}$ values causing the simulator to calculate zero surface concentrations for very early time data up to 200 seconds, which is a significant length of time.

This had the effect of holding back the ion flux onto the resin – from a simulation perspective – and causing an unrealistic decaying-oscillatory effect of concentration in the outer resin shell once simulated flux into the resin was permitted i.e. as the simulated surface concentration rises above zero. The reason for this is that after the unrealistic zero concentration/flux phase the simulator sought to ensure mass balance continuity hence causing over-corrections which then decayed back to realistic values via oscillation. This trend is seen clearly in Fig.5-12a&b which is a simulation fitted to the bulk concentration of Na^+ being adsorbed onto 10DVB resin and flowrate of 400 *mL/min* at 20% excess.

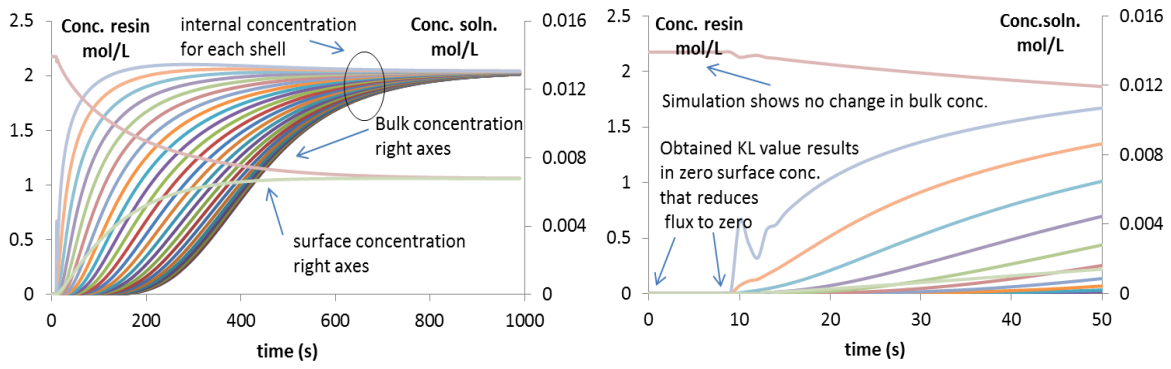

Fig.5-12a&b Simulated zero-surface concentration phenomenon (PPMC = 0.9974)

The zero surface concentration results in the simulator calculating a zero concentration inside the resin bead at the surface through the Mass-Action-Law equilibrium model. In a concentration driving-force based model (Nernst-Plank) which is assumed to be in effect in the resin at the liquid boundary, the zero concentration at the outer boundary of the resin di-polymer matrix, translates into an unrealistic zero flux into the resin proper. This results in the mass balance algorithm, causing the early time simulated bulk concentration to flat-line, which the early time lab measured data clearly does not do.

The effect of this was that for all early time data the simulation fitted poorly to the lab data. Since it is from this data that the mass transfer coefficient is derived, the likelihood of there being inaccuracies in the obtained $\boldsymbol{K_L}$ value was high. Fig.5-13 shows the early time model fit for the data presented in Fig.5-12 under these circumstances where it is clear that the slope of the data and the simulator are not congruent in early time data and this must have a negative impact on the correct determination of the $\boldsymbol{K_L}$ value.

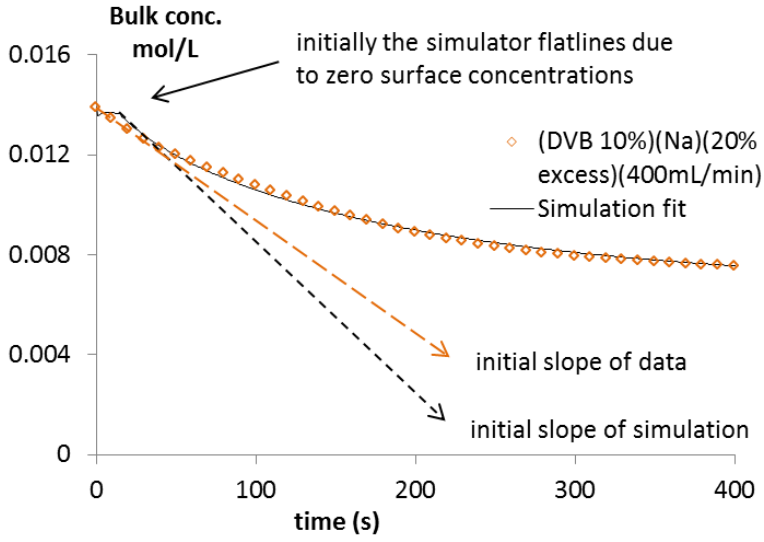

Fig.5-13 Non-congruency between simulator and early time data

5.10.4. Refined simulation

The rapid drop in bulk concentration of the adsorbing ion in early time data infers a high flux through the laminar layer and into the resin. It is unreasonable to assume that equilibrium is present across the phase boundary during very-high-flux, early-time data and although the

surface concentration was deemed to be zero, a buildup of concentration inside the resin has to be occurring.

Therefore it was decided that under these circumstances a non-equilibrium state would be assumed at the interface. In addition it was also assumed that the ions were entering into the resin and becoming evenly distributed throughout the internal resin matrix. This is a reasonable assumption given that laminar layer controls under these circumstances and the ion adsorption and desorption ions inside the resin are left to distribute dictated by their intrinsic intra-particle diffusivity. With no means to measure the distribution of ions in the resin during this early phase, even ion distribution remains the assumption, until the technology becomes available to do this. Fig.5-14 is a simulation fit to the same data presented in Fig.5-12 using these new assumptions. It is notable that the finally fitted $\boldsymbol{K_L}$ value causes the simulator to calculate a period of uniform increase in the shell concentration of approximately 60 seconds. Although this is far longer than the original flat line period shown in Fig.5-12, the PPMC achieved is 0.9985, which is a subtle improvement on the former simulation (Fig.5-12) that gave a PPMC of 0.9974.

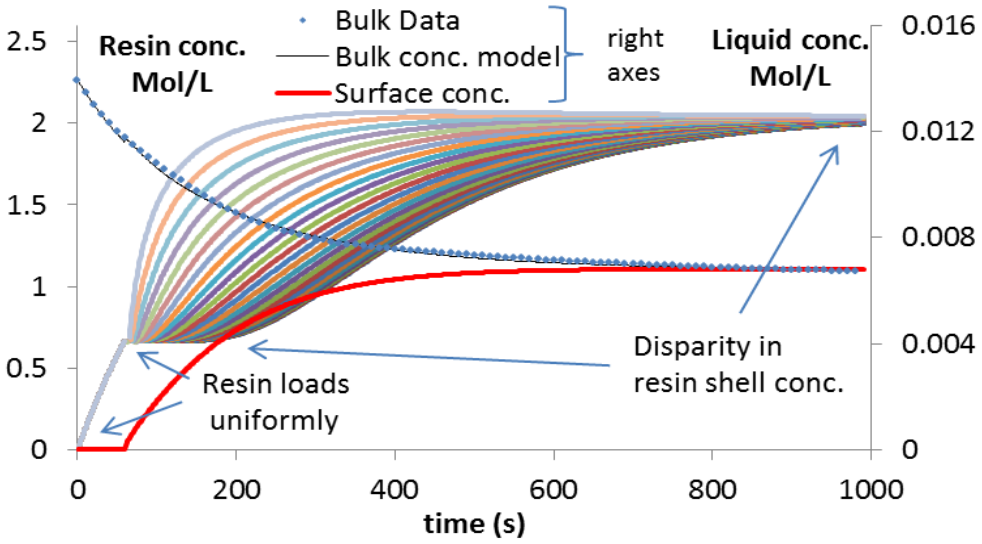

Fig.5-14 Sodium adsorption and fitted simulation (PPMC = 0.9985)

Fig.5-15&Fig.5-16 show the data and fitted simulation that incorporate these new assumptions for the adsorption of Mg^{2+} and Ba^{2+} respectively, onto a 10DVB resin with a starting concentration of 20% in excess of resin capacity at a circulatory flowrate of 400mL/min and includes; the bulk concentration, fitted model to bulk concentration, surface concentration (model) and the concentration in the internal shells of the resin.

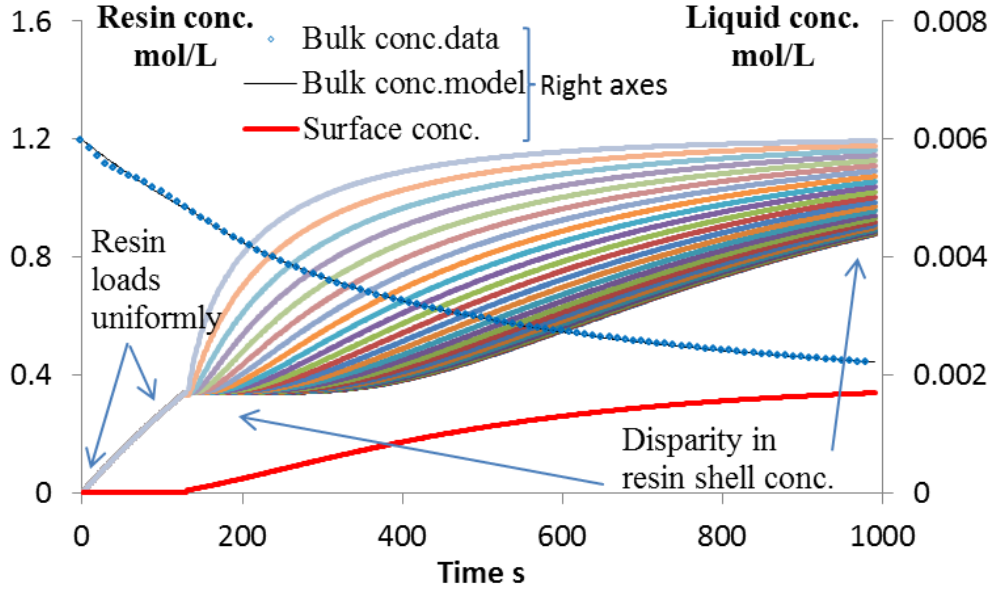

Fig.5-15 Magnesium adsorption and fitted simulation (PPMC = 0.9996)

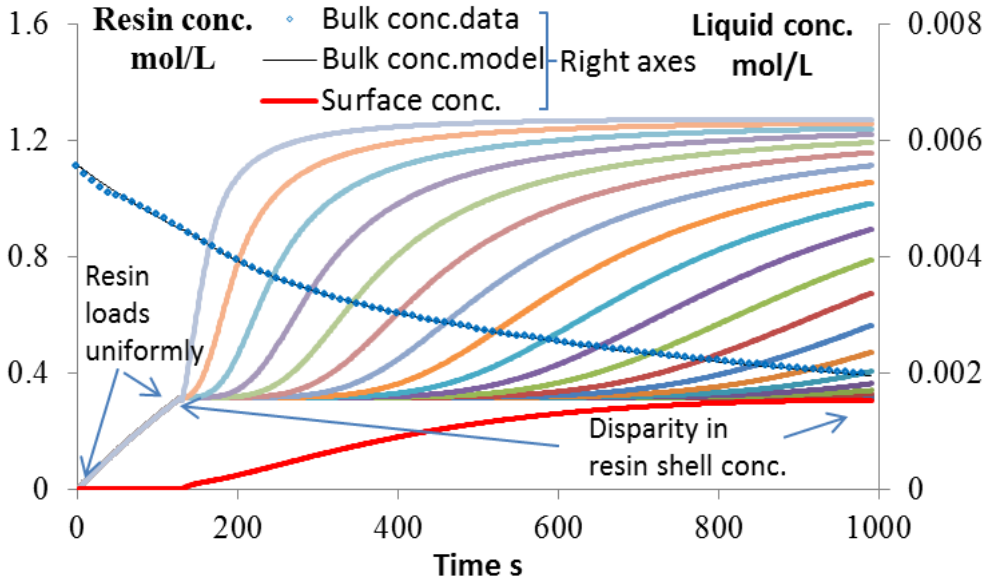

Fig.5-16 Barium adsorption and fitted simulation (PPMC = 0.9996)

From Fig.5-14, 5-15, 5-16 certain traits can be distinguished. The first is the similarity in the early time data implying that the rate of mass transfer in the laminar layer is similar for the Mg^{2+} and the Ba^{2+}. Given the similarity in the open water diffusivities of these two atoms (Mg^{2+} = 7.1x10^{-10} m^2/s, Ba^{2+} = 8.48x10^{-10} m^2/s) and that the turbulence is identical in both

cases, this is to be expected. The actual mass transfer coefficient ($\boldsymbol{K_L}$) returned by the fitting algorithm was 4.98x10^{-5} *m/s* and 4.93x10^{-5} *m/s* for the Mg^{2+} and Ba^{2+} respectively.

In the case of the Na^{+} (Fig.5-14) the early time data shows a far steeper curve implying a higher rate of flux. This is to be expected given the higher open water diffusivity - compared to Ba^{2+} and Mg^{2+} - for Na^{+} (Na^{+} = 1.33x10^{-9} m^2/s). The $\boldsymbol{K_L}$ value achieved in the Na^{+} test was 8.45x10^{-5} m/s.

The second observation is that the substantial difference in intrinsic intra-particle diffusivity. 2.7x10^{-11} m^2/s and 1.35x10^{-12} m^2/s for Mg^{2+} and Ba^{2+}, respectively, as determined by the search algorithm with the Ba^{2+} displaying intra-particle diffusion which is approximately 20 times slower than that of the Mg^{2+}. The simulation returned an intra-particle diffusivity for Na^{+} of 4.13x10^{-11} m^2/s.

A third observation is what appears to be an inflection point in the laboratory recorded data, visible in both Fig.5-15&Fig5-16 shortly before the 100 second point in the data that was also observed in other kinetic data but not in all sets.

It was noted from the data that the diffusivity of the desorbing ion (H^{+}), which was calculated during the curve fitting process, often came out at a value of approximately three orders of magnitude higher and sometimes drifted to the uppermost bound, set for the search algorithm. Further investigation showed that changing the intrinsic diffusivity value of the H^{+} ultimately had little effect on the overall simulation kinetic curve. This is a reasonable observation as it is likely that the slower diffusivity of the far larger adsorbing ion will likely control the entire mass transfer process. This is also indicated by the mathematics. From Equ.3-29 (presented in the model development section) it is possible to see that in the presence of the adsorbing ion tending to zero ($\overline{C_i} \rightarrow 0$) the diffusivity reduces to that of the adsorbing ion ($Dapp = D_i$). This essentially presents a situation where the minority ion dominates the diffusion. As the mobility of all the absorbing ions are likely to be far less than that of the H^{+}, which is only a proton, it makes sense that the intrinsic H^{+} diffusivity should have little impact on the overall process.

$$\frac{\partial \overline{C_i}}{\partial t} = \frac{1}{r^2}\frac{\partial}{\partial r}\left(r^2 \left[\frac{D_i D_D \left(z_i^2 \overline{C_i} + z_D^2 \overline{C_D} \right)}{D_i z_i^2 \overline{C_i} + D_D z_D^2 \overline{C_D}} \right] \frac{\partial \overline{C_i}}{\partial r} \right) \qquad 3\text{-}29$$

5.11. Accurate measurement of transport parameters in fresh resin

Studies indicating an inverse relationship between intra-particle diffusivity and the internal steric state of the resin have been reported (Yoshida&Kataoka, 1988; Kataoka *et al*, 1974). If the breakdown of internal structure leads to a less dense steric state, it is hypothesized that a possible increase in intra-particle diffusivity is to be expected as the resin ages. Therefore, a grasp of the intra-particle diffusivity inside fresh resins of different steric state (DVB content) will be a useful indicator of what to expect in aging resin.

To accurately measure the likely domain of the mass transfer coefficient and intra-particle diffusivity parameters during the aging test work, measured by means of the model presented in this study, a campaign was undertaken using 6.5% DVB, 8% DVB and 10% DVB resins, using the test method described in section *5.3.* Only the Na^+ ion was used in the test work because of the relative ease of removal during resin regeneration. Two starting concentrations were used i.e. 50% and 80% in excess of the capacity of the resin in the ZLC and three flow rates i.e. 500 *mL/min*, 400 *mL/min* and 300 *mL/min*, resulting in eighteen tests. All tests were conducted at a temperature of 15°C ±0.2°C.

The results of this campaign are presented in Table 5-2, and indicate that the mass transfer coefficients determined for all tests were between $1x10^{-4} > (\boldsymbol{K_L}) > 1x10^{-5}$ *m/s* while the intra-particle diffusivities of the adsorbing ion (Na^+) were between $8x10^{-11} > (\boldsymbol{D_i}) > 3x10^{-11}$ m^2/s. In the determination of the intra-particle diffusivity of the desorbing (H^+) ion, the search algorithm tended to drift to the highest set boundary for this parameter i.e. $1.00x10^{-8}$ m^2/s.

In all adsorption tests the fits achieved were reasonable with all PPMCs (Pearson Product moment correlation, section *3.7.2.*) being >0.99. The average Mass-Action-Law equilibrium coefficient achieved was 1.78 and for every test was situated $1.61 < \alpha < 2.14$. In the case of the 50% excess starting concentration the average conversion achieved was 68.5 % and that of the 80% excess achieved and average of 72.7 %. Fig.5-17 is a sample of the results

showing three kinetic curves achieved for the 8% DVB content resin with starting concentrations that amounted to the quantity of ions present being at 80% excess of resin capacity.

Tab 5-2 Transport parameters determined in fresh resins

Tests commenced at 80% excess of resin capacity Na^+ in solution

	u mL/min	K_L m/s	D_i m^2/s	D_D m^2/s	R^2 fit	α	conversion. %
6.5DVB	300	$5.45x10^{-5}$	$4.53x10^{-11}$	$1.00x10^{-8}$	0.9978	1.69	71.9
	400	$6.00x10^{-5}$	$4.90x10^{-11}$	$1.00x10^{-8}$	0.9991	1.70	71.9
	500	$7.02x10^{-5}$	$7.24x10^{-11}$	$1.41x10^{-10}$	0.993	1.76	72.3
8.0DVB	300	$6.05x10^{-5}$	$3.03x10^{-11}$	$5.10x10^{-11}$	0.9995	1.88	73.1
	400	$6.80x10^{-5}$	$4.90x10^{-11}$	$1.00x10^{-8}$	0.9995	1.63	71.6
	500	$9.42x10^{-5}$	$6.29x10^{-11}$	$1.00x10^{-8}$	0.9998	1.66	71.6
10DVB	300	$6.49x10^{-5}$	$3.83x10^{-11}$	$1.00x10^{-8}$	0.9970	1.65	72.9
	400	$7.55x10^{-5}$	$3.66x10^{-11}$	$1.00x10^{-8}$	0.9988	1.88	74.6
	500	$9.50x10^{-5}$	$4.20x10^{-11}$	$1.00x10^{-8}$	0.9981	1.88	74.6

Tests commenced at 50% excess of resin capacity Na^+ in solution

	u mL/min	K_L m/s	D_i m^2/s	D_D m^2/s	R^2 fit	α	conversion. %
6.5DVB	300	$6.10x10^{-5}$	$4.57x10^{-11}$	$1.00x10^{-8}$	0.9993	1.70	68.5
	400	$6.12x10^{-5}$	$8.70x10^{-11}$	$7.08x10^{-11}$	0.9996	1.65	68.0
	500	$7.08x10^{-5}$	$6.00x10^{-11}$	$1.00x10^{-8}$	0.9982	1.82	69.5
8.0DVB	300	$6.54x10^{-5}$	$3.82x10^{-11}$	$1.00x10^{-8}$	0.9981	1.61	66.8
	400	$7.83x10^{-5}$	$3.52x10^{-11}$	$1.00x10^{-8}$	0.9987	2.14	70.6
	500	$1.02x10^{-4}$	$4.53x10^{-11}$	$1.00x10^{-8}$	0.9980	1.65	68.6
10.0 DVB	300	$6.62x10^{-5}$	$3.80x10^{-11}$	$1.00x10^{-8}$	0.9982	1.78	65.8
	400	$7.70x10^{-5}$	$6.15x10^{-11}$	$1.00x10^{-8}$	0.9987	1.89	68.9
	500	$9.11x10^{-5}$	$4.65x10^{-11}$	$2.28x10^{-9}$	0.9995	2.01	69.8

The graphical representation of all the kinetic curves and full simulations achieved in each test presented in Table 5-2 can be found in Annexure XI.

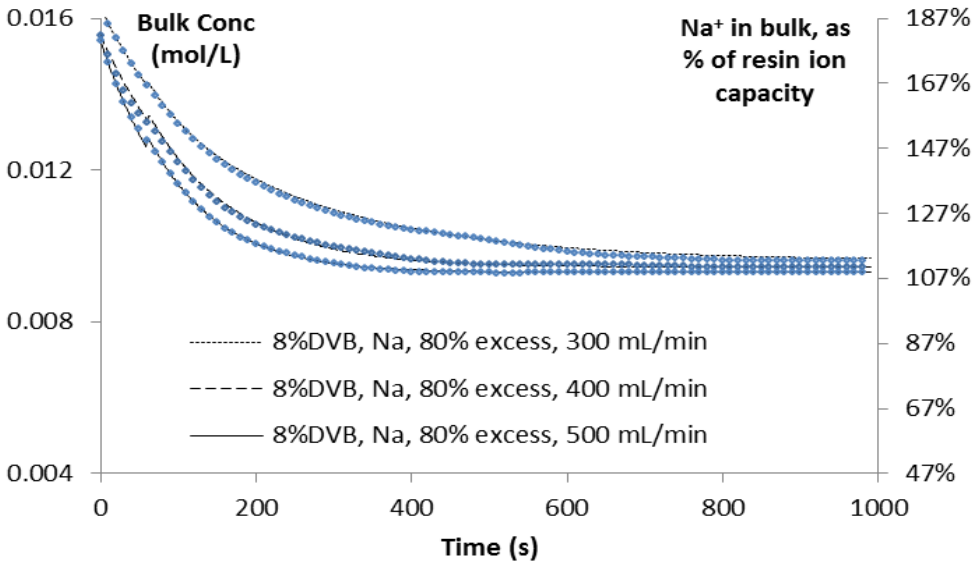

Fig.5-17 Measured data and fitted simulations for Na onto fresh 8DVB resin

Fig.5-18 is a graphical representation of the average intra-particle diffusivity of the Na^+ ion which clearly shows the average decrease in intra-particle diffusivity with increasing DVB content and includes variance. The little difference between the 8% and 10% DVB in the case of the 50% excess data could be attributed to the dominance of the laminar layer at this lower bulk concentration.

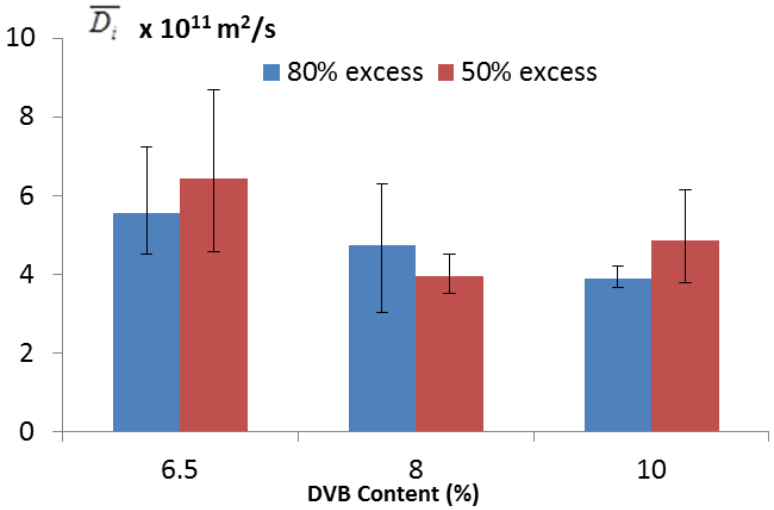

Fig.5-18 Intra-particle diffusivities in, fresh resins, of varying DVB content

Confident that a set of mass transfer/diffusivity values had been measured for the base case situation and that all the possible parameters that might impact on the system had been identified, it was now possible to embark on a test program to measure the change in kinetic behaviour of resin as it is systematically degraded. As the transport values achieved are similar to other published data and this is shown in the results & discussion (section *6.4.3* and *6.4.4*) it was also determined that the numerical technique used to attain these values was reliable and could meaningfully separate the different parameters by applying the rigorous model presented in this thesis.

6. RESULTS & DISCUSSION

6.1. Mass transfer coefficient (K_L) measurement by conventional means

The empirical approach is an essential tool in the modelling of transient systems for practical purposes, although, from a scientific perspective, when applied to ion exchange resin the method gives little understanding of the mechanism of adsorption. Paradoxically, for a standard exercise in empiricism a single control mechanism is assumed to be present and values of a coefficient, assumed to be associated with that mechanism, are recorded against measured descriptions of the environment. To formulate a composite relationship, copious amounts of transient data are required that will mandate a comprehensive matrix of tests in an attempt to cover as broad a spectrum of environments as possible. Structure in the relationship is then achieved by the incorporation of the data into dimensionless numbers such as the Sherwood number (***Sh***), a ratio that measures the mass transfer coefficient against physical dimensions and infinite dilution diffusivity.

Generally, in the case of ion-exchange-resin empirical modelling laminar layer resistance is assumed to be controlling, and hence the main objective is the determination of the surface mass transfer coefficient. Via dimensionless number analysis this is correlated to the temperature dependent physical properties of the solution encompassed in the Schmidt number (***Sc***) and the fluid turbulence of the system described by the Reynolds number (***Re***).

Although the literature shows a vast list of empirical dimensionless relationships for transient ion exchange resin systems, Equ.6-1a postulated by Kataoka *et al* (1973) has been used by many researchers in attempt to estimate the laminar layer mass transfer coefficient (Jones & Carta, 1993; Lee *et al*, 1997; Rodriguez *et al*, 1998; Valverde *et al*, 2004; Valverde *et al*, 2005),. Equ.6-1b is an adapted version of 6-1a that makes the Sherwood number the subject of the model for comparative purposes.

$$K_L = \frac{V}{\varepsilon} 1.85 Re^{-0.66} Sc^{-0.66} \left(\frac{1-\varepsilon}{\varepsilon} \right)^{-0.33} \qquad \textbf{6-1a}$$

$$\boldsymbol{Sh} = \frac{2\mathrm{R}}{\boldsymbol{D_L}}\frac{\boldsymbol{V}}{\boldsymbol{\varepsilon}}1.85\boldsymbol{Re}^{-0.66}\boldsymbol{Sc}^{-0.66}\left(\frac{1-\boldsymbol{\varepsilon}}{\boldsymbol{\varepsilon}}\right)^{-0.33} \qquad \textbf{6-1b}$$

where

$\boldsymbol{\varepsilon}$ Bed voidage assumed to be 0.3 (dimensionless)

$\boldsymbol{\rho}$ Fluid density (kg/m^3)

$\boldsymbol{\mu}$ Fluid viscosity ($kg/m.s$)

$\boldsymbol{V}$ Superficial liquid velocity (m/s)

R Resin radius *(m)*

$\boldsymbol{D_L}$ Free aqueous solution diffusivity (m^2/s)

$\boldsymbol{K_L}$ Mass transfer coefficient (m/s)

$\boldsymbol{Re}$ Reynolds No. $\left[\rho(2\mathrm{R})\boldsymbol{V}\right]/\left[\mu(1-\boldsymbol{\varepsilon})\right]$(dimensionless)

$\boldsymbol{Sc}$ Schmidt No. $\mu/\rho\boldsymbol{D_L}$ (dimensionless)

$\boldsymbol{Sh}$ Sherwood No. $\boldsymbol{K_L}2\mathrm{R}/\boldsymbol{D_L}$ (dimensionless)

Another correlation, first proposed by Dwivedi & Upadhyay (1977) (Equ.6-2), had been determined as being the most appropriate correlation for mixed bed ion exchange by Chowdiah *et al* (2003) and is valid over a wide range of particle Reynolds numbers (0.01 < Re < 15000).

$$\boldsymbol{Sh} = \boldsymbol{Sc}^{0.33}\,\boldsymbol{Re}\left(\frac{\boldsymbol{0.765}}{\boldsymbol{Re}^{0.82}} + \frac{\boldsymbol{0.365}}{\boldsymbol{Re}^{0.386}}\right) \qquad \textbf{6-2}$$

6.1.1. Testing the Kataoka *et al*, and Dwivedi & Upadhyay models

As a first attempt to validate laboratory measured kinetic data it was thought necessary to match it to the models presented here that have been used by other authors in their study of ion exchange kinetics. Calculation of the mass transfer coefficient ($\boldsymbol{K_L}$) was undertaken by using the early time data method described in section *5.4.3.*

Congruency of the measured data to the predictions of Equ.6-1b and Equ.6-2 could easily be checked and would be an important exercise for validating the measured data. In addition it allows for the determination of the lower boundary of the range of values of the mass transfer

coefficient. Assuming zero concentration on the resin surface, the system is exposed to the highest possible concentration differential as driving force ($C_{i,bulk} - C_i^*$, where $C_i^* = 0$) for a measured mass transfer rate.

The test work proceeded by measuring early-time-data adsorption rates for all three ions being tested (Na^+, Mg^{2+}, Ba^{2+}). Kinetic curves were measured in the kinetic testing unit (Fig.4-6 'Equipment') at three different concentrations set at 20%, 50% and 80% excess of the capacity of the resin present in the ZLC and at six circulatory flowrates (60, 100, 200, 300, 400, 500 *mL/min*). Finally, all the tests were repeated for two different resin DVB contents (6.5% DVB resin type C100E and 10% DVB resin type PPC100x10), producing a total of 108 kinetic curves. Details of these resins are given in section *5.2*. All tests were carried out at a temperature as close to 25ºC as possible.

The initial slope was measured from each kinetic test so it could be inserted into Equ.3-3 to determine a laminar layer mass transfer coefficient (K_L) (described in more detail in section *3.2.1*) from which a Sherwood number was calculated. Reynolds numbers were calculated from the flowrate passing through the ZLC and a Schmidt number from the temperature-corrected physical properties of the bulk solution. Fig.5-5 is an example of one of the data sets, with the remainder shown in Annexure VII.

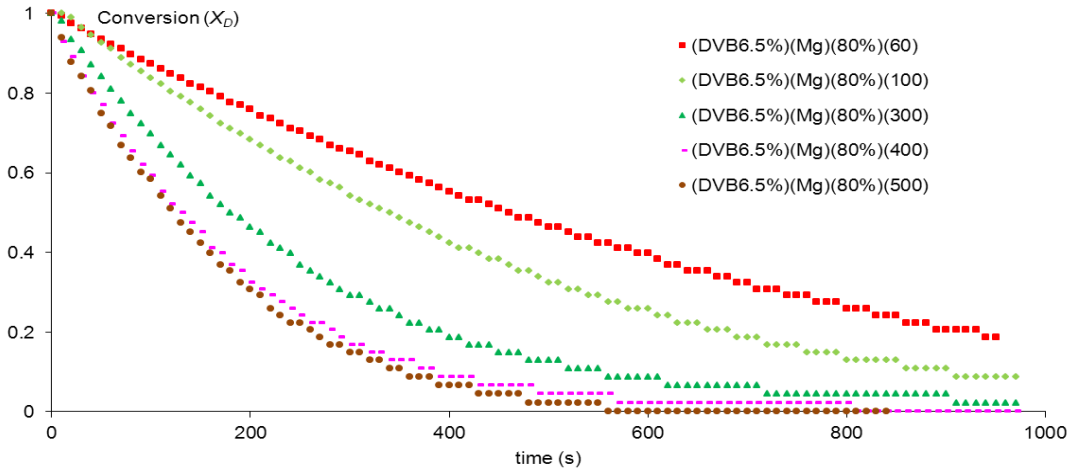

Fig.5-5, Desorption data for five flowrates, Mg^{2+}/H^+ system onto 6.5DVB resin

Finally, in the context of this study, it was thought prudent to test some aged resin in the same manner as the fresh resin, the objective being to determine whether the mass transfer

coefficient for the aged resin, determined using early time data, displays significant differences in value compared to that of fresh resin. The aged resin had been prepared from fresh 10DVB resin (type PPC100x10), in the manner described in section *5.7* and had lost approximately half of its capacity and showed signs of altered kinetic behaviour compared to its fresh state.

Tab.6-1 gives the results achieved for the kinetic curves presented in Fig.5-5 where the Reynolds No. is calculated using the superficial tube velocity, and the mass transfer coefficient (K_L) by using the initial slope method. The first column of Sherwood No. is calculated from the laboratory data and the following two are from the models presented in section *6.1.1*. The final column is from that of the Nesbitt & Maloka model described in detail in section *6.1.2*. The value used for the resin diameter (2R) was 725 μm and the free aqueous solution diffusivity 7.10 x 10^{-10} m^2/s.

Tab.6-1, Data and model values of Sherwood Nos. for data shown in Fig.5-5

V (*dm/s*)	*Re.* Data	K_L (*m/s*)	*Sc.* Data	*Sh.* Data	*Sh.* Kataoka	*Sh.* Div&Up	*Sh.* N&M
4.94x10^{-2}	4.0	2.68x10^{-5}	1295	27.9	50.3	24.3	24.0
8.58x10^{-2}	6.7	3.89x10^{-5}	1370	41.7	61.1	32.6	33.6
1.78x10^{-1}	14.4	5.79x10^{-5}	1275	59.8	76.9	49.7	48.2
2.70x10^{-1}	22.2	7.47x10^{-5}	1231	75.7	87.8	64.7	59.5
3.63x10^{-1}	30.5	9.70x10^{-5}	1177	95.9	96.1	78.6	68.3
4.60x10^{-1}	36.7	11.0x10^{-5}	1315	115.4	106.1	92.4	82.8

Kataoka (Kataoka *et al*.,1973),

Div&Up (Dwivedi & Upadhyay, 1977),

N&M (Nesbitt & Maloka, publication pending).

Fig.6-1a&b show the model-predicted Sherwood No. for the Kataoka *et al* (a) and Dwivedi & Upadhyay (b) models versus the Sherwood No. calculated from early time data for all the kinetic tests performed in the laboratory. Theoretically, the results should be fairly close to the parity line and in the case of the Dwivedi & Upadhyay model a linear regression fit does indeed produce a correlation that is close to the parity line, albeit with significant scatter. However, in the case of the Kataoka *et al* model, although a correlation of sorts is achieved, linear regression results in a correlation further from the parity line, with the average model

prediction being higher than that calculated from laboratory test work. In both models the scatter is considered to be substantial, which is, however, not uncommon for an empirical exercise of this nature.

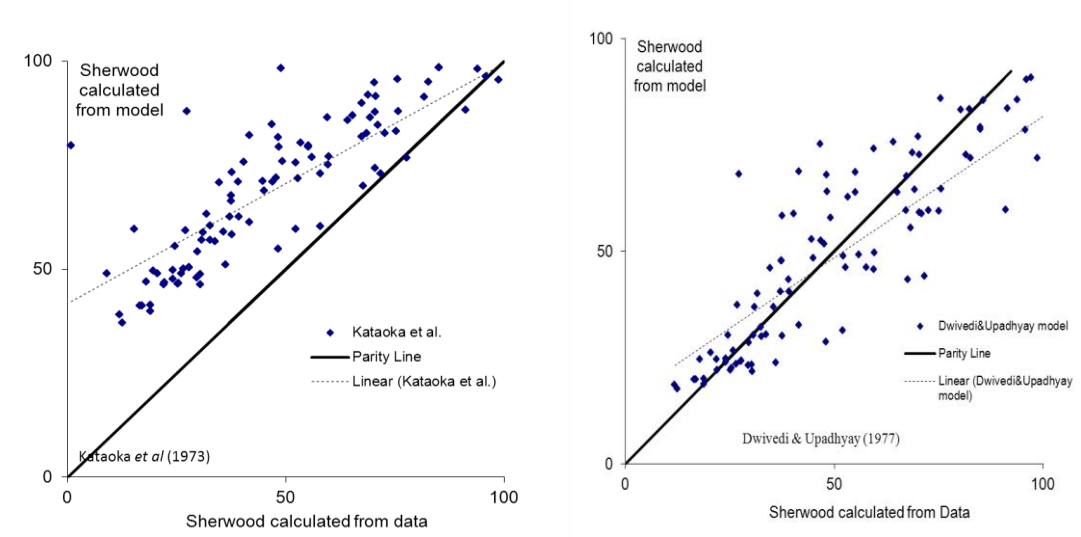

Fig.6-1a&b Correlations for the Kataoka *et al* and Diwivedi & Upadhyay models

6.1.2. Developing the Nesbitt & Maloka model

As the data presented in Fig.6-1a&b is from a narrow range of Sherwood numbers ($0 < Sh < 100$) it was thought that a simplified model developed from the data generated in this study alone might give a better correlation and hence the Nesbitt & Maloka model was developed. It was based on seeking linear relationships between the logs of the calculated Reynolds, Schmidt and Sherwood numbers. Linear relationships were determined between log of the Sherwood and Reynolds numbers for different values of Schmidt number with a gradient equal to 0.5. The log of each intercept determined was then plotted against the log of the associated Schmidt number with the gradient being 0.8 and the intercept 0.05.

The final model is presented in Equ.6-3 and the results of the fit are presented in Fig.6-2. The linear regression produces a line that is virtually congruent with the parity line, and arguably produces a better fit than the other two published models presented in the previous section.

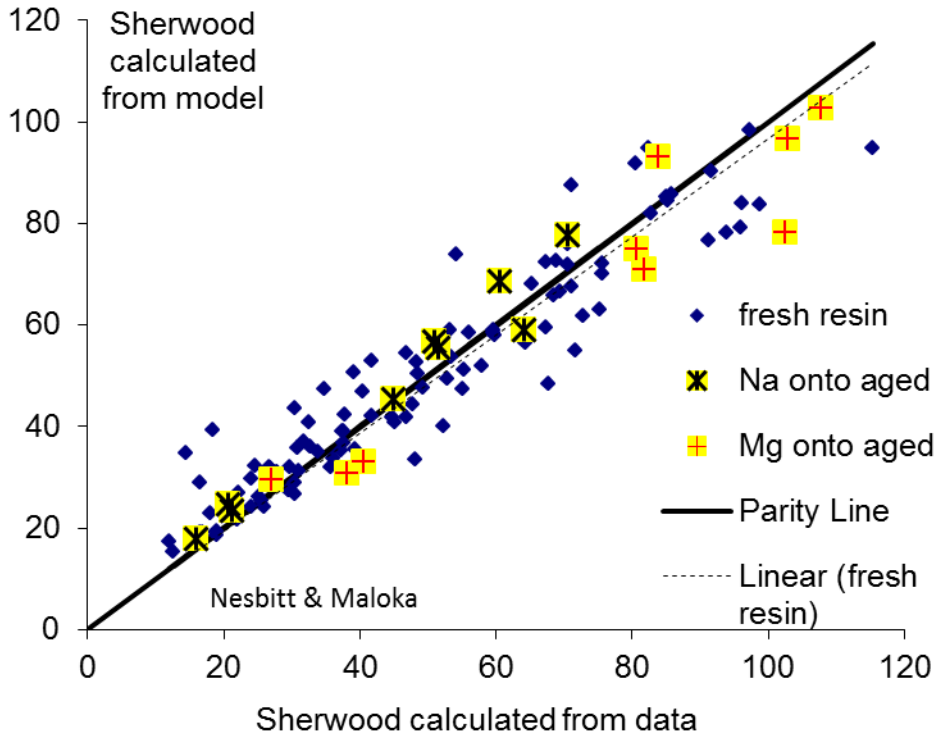

Fig.6-2, Nesbitt & Maloka model incorporating aged resin

$$Sh = 0.05\, Re^{0.5}\, Sc^{0.8} \qquad \textbf{6-3}$$

In the context of the broader objective of this study it was hypothesised that resin aging is unlikely to have any major impact on the laminar layer mass transfer coefficient. For the purposes of proving this, an exercise was undertaken in which the Sherwood numbers calculated from the aged resin, determined by initial slope measurement, were compared to the predictions of the Nesbitt & Maloka model, the calibration being based on fresh resin data alone.

To generate the aged resin, a 10DVB strong acid resin (PPC100x10) was used that had been artificially aged through repetitive cycling in which Cu^{2+} was adsorbed and desorbed for 1000 cycles, with regeneration being undertaken each time using a one molar sulphuric acid solution mixed with a 0.1 molar concentration of H_2O_2. This caused the resin to reduce capacity by approximately 40%, in addition to there being a marked increase in the rate of kinetic adsorption. The Na^+ and Mg^{2+} were both adsorbed onto the this aged resin separately

at circulatory flow rates of 60, 300 and 500 *mL/min* and starting concentrations of 20%, 50% and 80% of the reduced capacity of the resin resulting in eighteen kinetic curves from which eighteen Sherwood numbers were calculated. The results of these tests are superimposed on Fig.6-2. The calculated dimensionless numbers and model predictions are shown in Annexure VII.

It is observed that the Sherwood numbers achieved during the early time data of the adsorption of the Na^{+} and Mg^{2+} onto the older resin compare very well with those achieved by the fresh resin. This is a strong indication that the laminar layer diffusion resistance is unaffected by resin decay. It's also notable that higher Sherwood numbers were achieved in the aged resin tests compared to the fresh resin tests, probably as a result of the higher rate of mass transfer due to higher intra-particle diffusion rates.

6.2. Qualitative/visual study of resin break-down

There are a number of visually discernible physical contortions resins pass through as they undergo a cyclical conversion transient, some of which could be considered temporary and others permanent. Anecdotal evidence suggests that resins tend to undergo permanent macro-structural breakdown during ageing. Partially-spherical fragments of beads are often found in resin beds that have been exposed to high numbers of cycles, with gel type resins being particularly susceptible to this kind of physical breakdown. If continuous cycling has the effect of causing gradual structural damage to the resin matrix, the question has to be asked: what impact does this have on the internal steric environment in the context of internal mass transport? It has already been indicated qualitatively (section *5.4.2.*) that a reduction in the steric state inside the resin does indeed have an impact on the rate of internal mass transport and further on in this results section numbers are put to this phenomenon (section *6.4.4*).

There is also the phenomenon of osmotic shock that results in a permanent change in which exposure to extreme electrolyte concentrations results in the instant cracking and potential breakup of resin beads. The instantaneous nature of osmotic shock places it in a different category from that of resin degradation which is supposed to happen over a duty-related time period. However, it is important for test work purposes to know at what electrolyte concentrations osmotic shock is likely to occur.

Another important, visually discernible characteristic of resin, that results in temporary change as it proceeds through its loading cycles, is the swelling/shrinking phenomenon. It is not unreasonable to assume that if circumstances cause swelling/shrinking to occur too rapidly, osmotic shock and particle breakup may occur.

Finally, a further question that has to be asked is if there is a discernible link between the aging of the resin and changes in the degree of swelling/shrinking. It is reasonable to assume that during the aging process, as the resins' internal structure breaks down resulting in decreasing rigidity, there could be an impact on the degree to which the resin matrix is allowed to shrink, all circumstances being equal.

A study was initiated to determine the following;

- Does higher DVB content show improved resistance to osmotic shock?
- What is the degree of swelling for different DVB percentages, and ionic concentrations?
- Does the degree of swelling/shrinking alter as the resin ages?

An understanding of these phenomena was deemed to be imperative for the transient modelling of the adsorption process in aging resin, as any increased shrinking during the adsorption process reduces the radial distances through which the ions need to diffuse and is hence an important variable in the measurement of diffusivity.

6.2.1. Osmotic shock.

Osmotic shock is a phenomenon that results in cracking and ultimately structural break-up of the resin and stems from powerful forces within the resin matrix triggered by extremely high concentration gradients. This can occur if the resin is exposed to a particularly concentrated electrolyte.

As has already been reported in the literature review, the higher the DVB content the stronger the resin structure and supposedly less susceptible to osmotic shock. In an attempt to verify this, a study was carried out in which three resins of different DVB content (6.5% 8% and 10%) were exposed batch-wise to three different ions (Ba^{2+}, Mg^{2+} and Na^{+}) at different electrolyte concentrations, varying from 0.07 mol/L to 3 mol/L. After twelve hours of exposure each batch of resin was examined under a microscope and pictures taken.

In every batch in which 6.5 DVB resin was tested evidence of osmatic shock could be detected. Fig.6-3 shows before and after pictures of 6.5 DVB exposed to various electrolytes, and it is clear that in each case the resin has taken on serious structural damage and this occurs even at the lowest of the high electrolyte concentrations. In contrast Fig.6-4 shows the effect of high electrolyte exposure to 8%DVB resin and we see that there appears to be less evidence of osmotic shock. Only the larger resin bead in the case of the adsorption of Mg^{2+} appears to show some cracking, indicating that the increase in DVB content has made a difference to the resilience of the resin at these same electrolyte concentrations.

Fresh resin After loading
6.5% DVB in Mg^{2+} at 0.5 *mol/L*

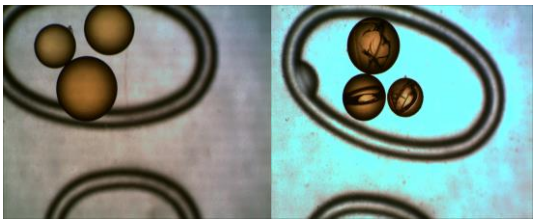

Fresh resin After loading
6.5% DVB in Ba^{2+} at 0.07 *mol/L*

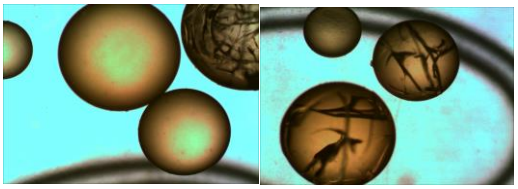

Fresh resin After loading
6.5% DVB in Na^{+} at 0.5 *mol/L*

Fig.6-3 6.5% DVB resin exposed to various electrolytes

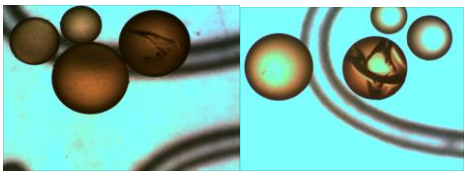

Fresh resin After loading
8% DVB in Mg^{2+} at 0.5 *mol/L*

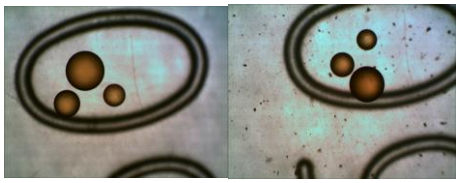

Fresh resin After loading
8% DVB in Ba^{2+} at 0.07 *mol/L*

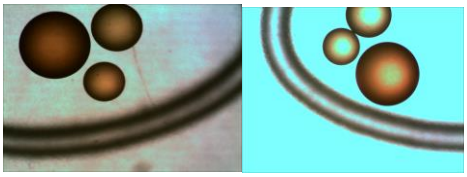

Fresh resin After loading
8% DVB in Na^{+} at 0.5 *mol/L*

Fig.6-4, 8% DVB resin exposed lowest range of electrolyte concentrations

Fig.6-5 shows the concentrations of Na^{+} and Ba^{2+} at which the 8% DVB resin first showed symptoms of osmotic shock and these are 0.11mol/L for Ba^{2+} and 3mol/L for Na^{+}

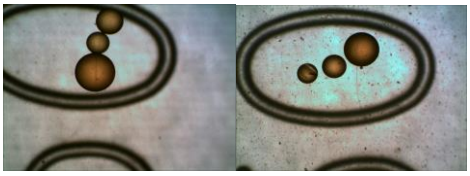

Fresh resin After loading
8% DVB in Ba^{2+} at 0.11 *mol/L*

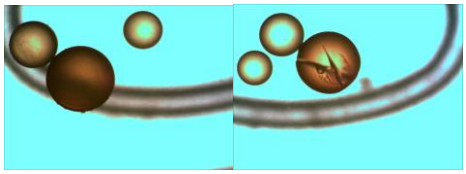

Fresh resin After loading
8% DVB in Na^{+} at 3 *mol/L*

Fig.6-5, 8% DVB resin exposed to osmotic shock electrolyte concentrations

Even at excessively high concentrations osmotic shock could not be observed in 10% DVB resins and this can be seen in Fig.6-6.

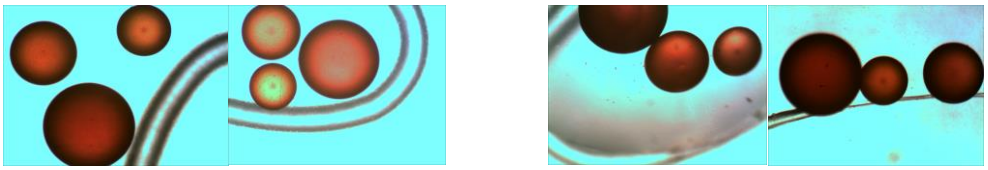

Fresh resin After loading
10% DVB in Mg^{2+} at 3 *mol/L*

Fresh resin After loading
10% DVB in Na^{+} at 3 *mol/L*

Fig.6-6, 10% DVB resin exposed to extremely high electrolyte concentrations

A challenge in this test work was adding the stronger electrolyte solution to the existing solution containing the resin beads nominated for observation. The approximately 500 μm to 700 μm resin beads under the microscope tended to move no matter how subtly the solution was added – this explains why resins tended to move between 'before' and 'after' pictures.

An attempt was made to observe the metamorphosis of a resin bead through the osmotic shock phenomenon, which proved to be extremely difficult. A successful series is shown in Fig.6-7.

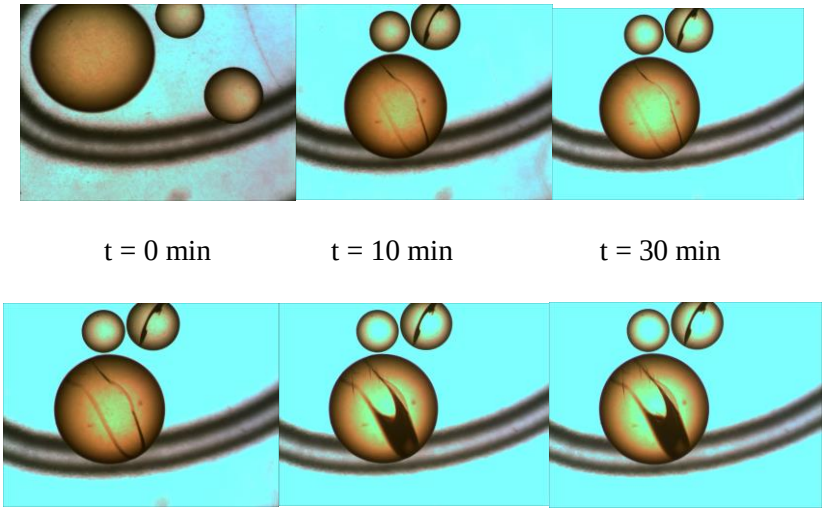

t = 0 min t = 10 min t = 30 min

t = 60 min t = 120 min t = 240 min

Fig.6-7 A time sequence of resin undergoing osmotic shock
(6.5% DVB exposed to Mg^{2+} at 3 mol/L)

At t = 0 minutes, the resin beads show no sign of any osmotic shock. At t = 10 minutes the resin starts to show fault lines which are faint but quite distinguishable against the translucent

back ground of the resin. The lines grow into increasing cracks through t = 60 minutes and by t = 120 minutes a portion of resin has detached itself and a hole can now be seen. At t = 240 minutes a final crack can be observed on the tip of the jagged section remaining.

6.2.2. The impact of DVB content on degree of swelling/shrinking

Hypothetically, the generation of resin bead debris can be linked to the impact of forces that derive directly from the contortion of the resin matrix as it is exposed to cycles of alternating electrolytes of different concentration, which is part of the loading/regeneration process. The swelling and contraction phenomenon of the cationic resin bead is an explicit part of the loading/regeneration cycle, with the swelling occurring as the bead is exposed to a strong concentration of acid solution, generally during the regeneration stage, and the contraction during the adsorption stage. The variance in resin size from one form to the other can be substantial with volumes changing as much as 30%

It was considered important to have a measure of the extent of contraction/swelling in different electrolyte concentrations of beads of different DVB content, so as to ensure that the correct diameters could be determined for the model fitting process and ultimately the determination of the intra-particle diffusion. Resin in the H^+ form is generally at its most swollen, but when the resin is exposed to a cation for which it has a greater affinity, the adsorption thereof causes it to contract as the H^+ ion attracts water molecules that fill the resin matrix causing it to swell. However, any larger atom/molecule with associated negative charges attracts less water molecules leading to a contraction of the resin. The degree of contraction appears to be a function of the type of ion and the concentration of the ion in the electrolyte.

A test program was undertaken that had the three fresh resins of different DVB content (6.5%, 8%, 10%) contacted with electrolytes containing the three ions (Na^+, Mg^{2+}, Ba^{2+}) at five different concentrations; 0.5, 1.0, 1.5, 2.0, 3.0 mol/L for Na^+ & $Mg^{2+}$and 0.12, 0.08, 0.06, 0.04, 0.02 *mol/L* for Ba^{2+}. The lower concentrations for Ba^{2+} were to accommodate its lower solubility. Measurements were made of the size of the resin beads, before and after, exposure to the electrolytes using the microscope described in section *4.4* of 'Equipment' and associated software 'ScopePhoto'. The diameters were measured of all the beads found in

three frames containing up to nine beads per frame. The electrolyte was added as carefully as possible to ensure minimal disturbance of the beads.

Fig.6-8 shows typical transient contraction behaviour that the resin follows as it adsorbs Mg^{2+} and Na^{+} ions, with 100% equating to the volume of the resin in the H^{+} form. The starting concentrations in each test were vastly in excess of the capacity of the resin, and therefore the tests can be considered have been conducted in an unchanging environment. There was virtually no reduction in the bulk concentration throughout the test.

It can be seen that the degree of contraction is a function of the concentration of the electrolyte and also that the rate of shrinkage is extremely rapid, with the final volume being approached within 30 seconds of the start of the adsorption.

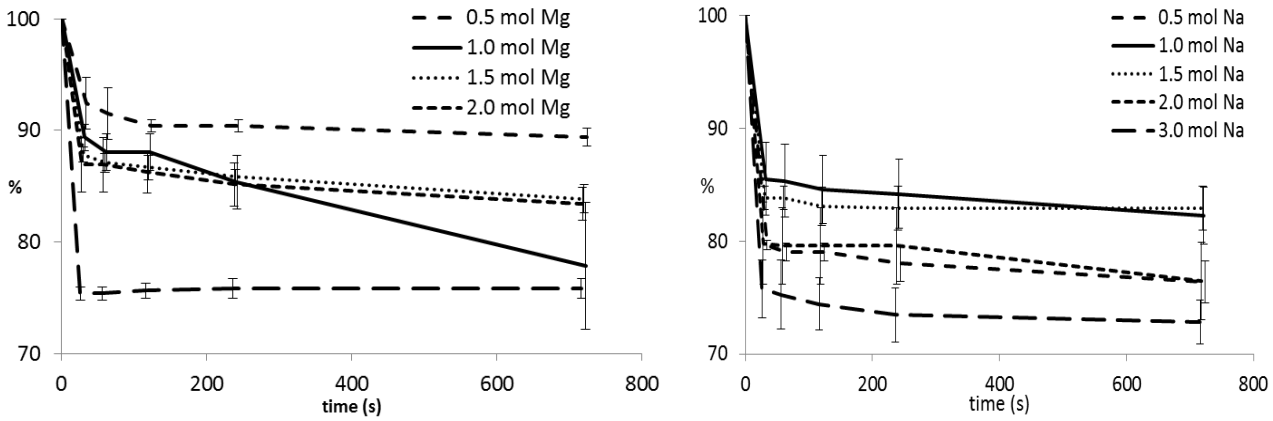

Fig.6-8a&b, Volume-contraction for (a) Mg^{+} on 10%, (b) Na^{+} on 6.5%, DVB resins

Tab.6-2,3,4 show the extent to which the volume of the resin contracts at equilibrium for all three DVB resins types for all three ions at various concentrations. These results confirm that the higher DVB content (more rigid structure) the less the contraction will be, all else being equal. The relationship between resin contraction, DVB content and electrolyte concentration can be seen more clearly in Fig.6-9. Knowing the potential changes in resin diameter is important for determination of the intra-particle diffusion inside the aged resin.

Tab.6-2 Resin % vol. reduction

10% DVB

Conc.	Na	Mg	Conc.	Ba
3.0mol	76%	76%	*0.12mol*	78%
2.0mol	86%	83%	*0.08mol*	78%
1.5mol	83%	84%	*0.06mol*	80%
1.0mol	84%	78%	*0.04mol*	80%
0.5mol	91%	89%	*0.02mol*	79%

Tab.6-3 Resin % vol. reduction

8% DVB

Conc.	Na	Mg	Conc.	Ba
3.0mol	75%	75%	*0.12mol*	68%
2.0mol	80%	78%	*0.08mol*	67 %
1.5mol	84%	79%	*0.06mol*	68 %
1.0mol	82%	88%	*0.04mol*	69%
0.5mol	87%	88%	*0.02mol*	70%

(H^+ form is 100%)

Tab.6-4, Resin % vol. reduction

6.5% DVB

Conc.	Na	Mg	Conc.	Ba
3.0mol	73%	70%	*0.12mol*	70%
2.0mol	76%	76%	*0.08mol*	69%
1.5mol	83%	82%	*0.06mol*	68%
1.0mol	82%	85%	*0.04mol*	67%
0.5mol	76%	87%	*0.02mol*	69%

(H^+ form is 100%)

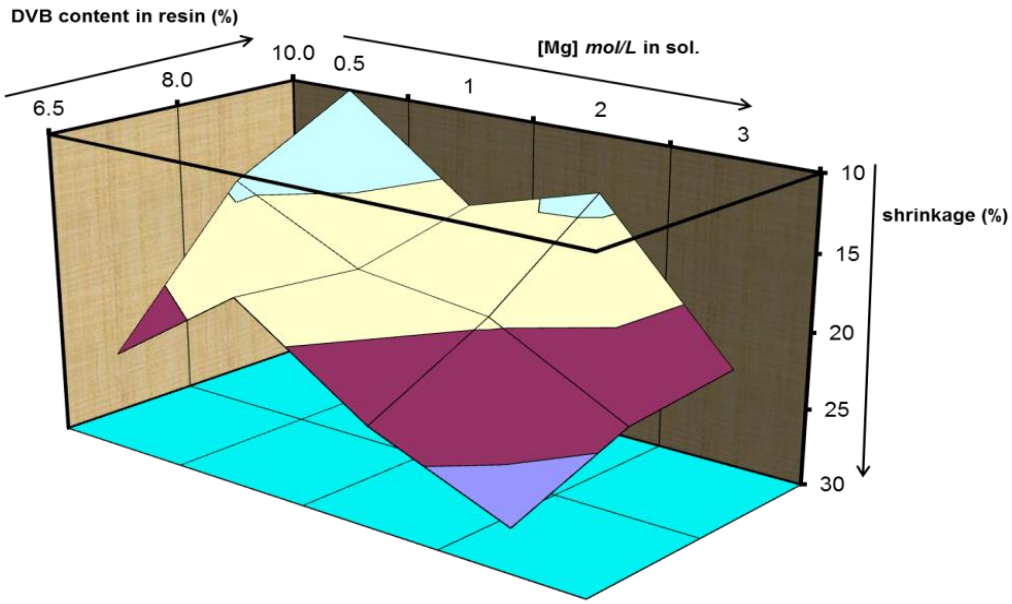

Fig.6-9, Relationship between contraction, DVB content and concentration for Na^+

6.2.3. Swelling characteristics of aged resin

Using the aging machine described in the section *4.1* 'Equipment', a small quantity of 7% DVB resin (Rohm & Haas) was aged by loading and regenerating it 1200 times, using a 0.02 *mol* Cu^{2+} solution and a regeneration solution of one normal sulphuric acid. The resin's capacity was found to be approximately 1.8 *equiv./L* when fresh. However, after it had been exposed to 1200 cycles its capacity had dropped to approximately 1.2 *equiv./L*

Fig.6-10 shows both the old and new resin beads together. It's notable that the colour of the aged resin appears to be lighter than that of the fresh 7% DVB resin, which is an indication of loss of internal structure. It had been observed that the higher the DVB content in the resin the darker its appearance.

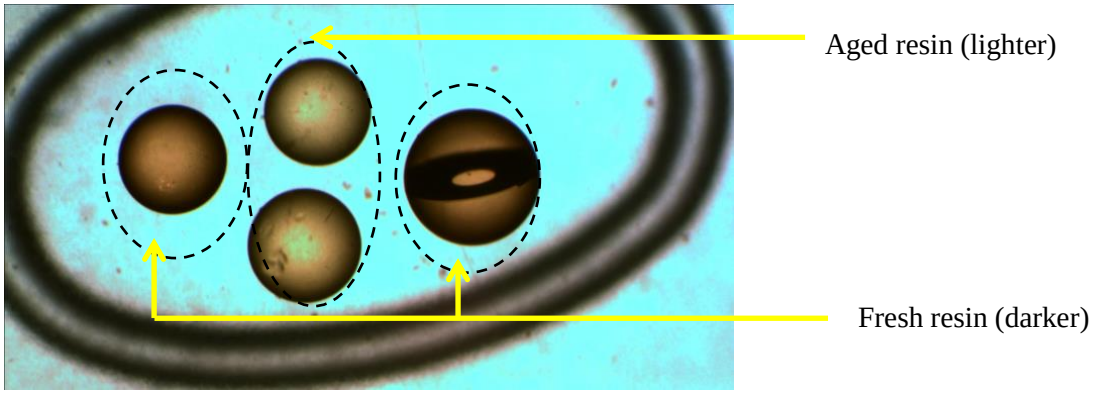

Fig.6-10 10% DVB resin before and after aging by 1200 cycles

The expansion/contraction of the aged resin generated in this study using a 3.0 *mol* Na^{+} electrolyte was measured in exactly the same manner as described in the previous section, and the results are presented in Fig.6-11. Also shown in Fig.6-11 are the results of contraction at the same 3.0 *mol* Na^{+} electrolyte concentration for the three fresh DVB content resins (10%, 8%, 6.5%) shown in black.

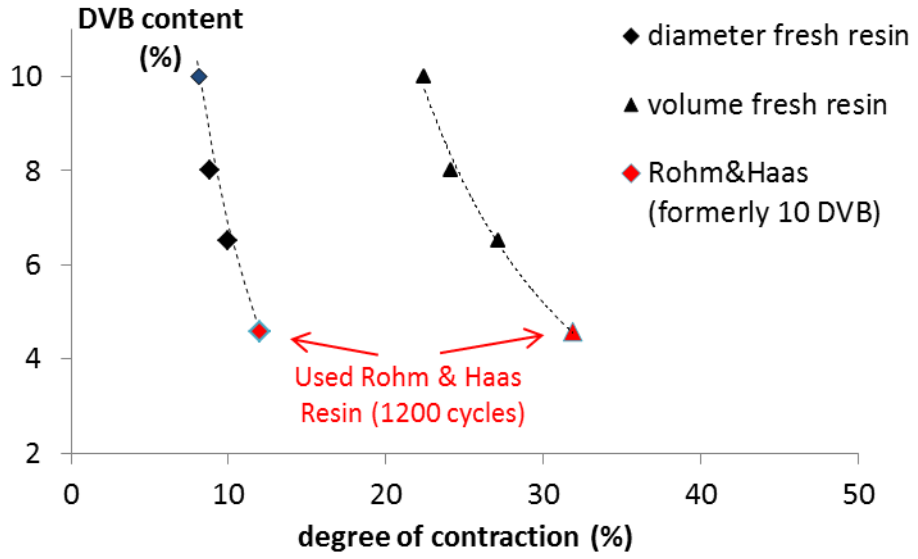

Fig.6-11, Degree of contraction versus DVB content including used resin

Also shown in Fig.6-11 is an extrapolation of the contraction/DVB content function of the fresh resin. A simple two parameter power-law function was found to best represent the fresh resin data and hence was chosen and is presented in Equ.6-4;

$$\boldsymbol{DVB}(\%) = 720 \cdot [contraction(\%)]^{-0.2} \qquad \textbf{6-4}$$

By placing the percentage degree of contraction of the aged resin on the extrapolated line it is possible to determine that the aged resin manufactured by Rohm & Haas, which underwent 1200 cycles and had lost 32% capacity, displays the same contraction characteristics as 4.6% DVB resin, which is entirely possible as this would imply a reduction in rigidity due to a decrease in internal structure through attrition.

Its notable that the differential of the power law function used (Fig.6-4) to extrapolate the contraction trend of the fresh resins is very (negatively) steep and hence minor adjustment to the parameters makes a large difference to the determined DVB for the decayed Rohm & Haas resin. This implies that although contraction measurement can be used as a measure of resin internal steric state, achieving high accuracy may be elusive.

6.3. Quantitative study of ageing ion exchange resin

6.3.1. Effectiveness of the cyclic aging machine in degrading resin

The rapid aging machine was used to accelerate the decay of resin by cyclically passing a loading solution ($CuSO_4$ electrolyte), a regeneration solution (H_2SO_4 + H_2O_2) and wash water through the ZLC containing 5 *mL* of resin as described in section *5.9&5.10* of 'Methods'.

Fig.6-12a shows the reduction in resin capacity with successive cycles in two early campaigns that used a Rohm & Haas manufactured resin (1200H) that had a starting DVB content estimated to be 8%. The analysis used is described in the methods section *5.4.* Fig.6-12a and shows that a more or less linear reduction in capacity with successive cycles is achieved, a useful trend which is also shown to be repeatable.

Fig.6-12b shows the reduction in resin capacity for two further campaigns that were undertaken both of which used the 10% DVB Purolite manufactured resin (PCC100x10). It's notable that in the identical environment the Purolite resins appear to have decayed marginally less i.e. to an average of approximately 72% of the original fresh capacity, while the Rohm and Haas resins decayed to 68%

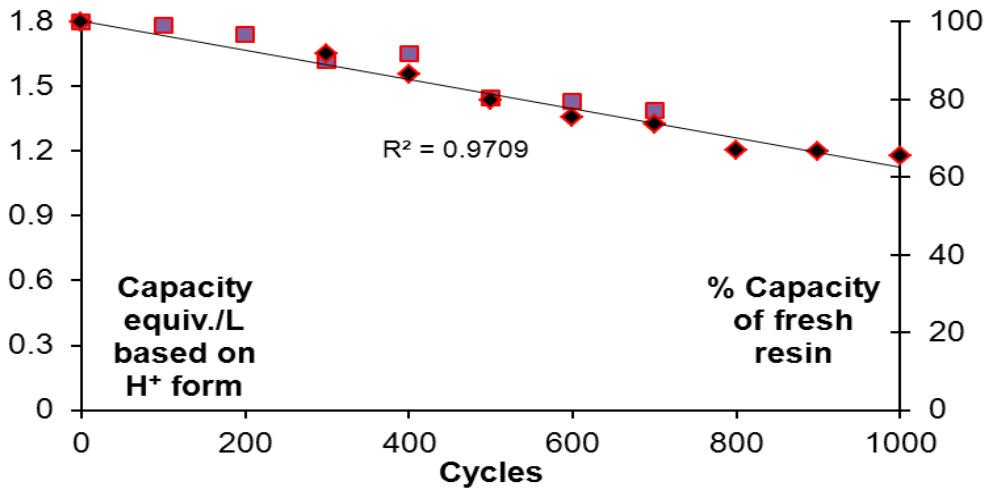

Fig.6-12a, Ion exchange capacity with successive cycles, 1200H Rohm & Haas

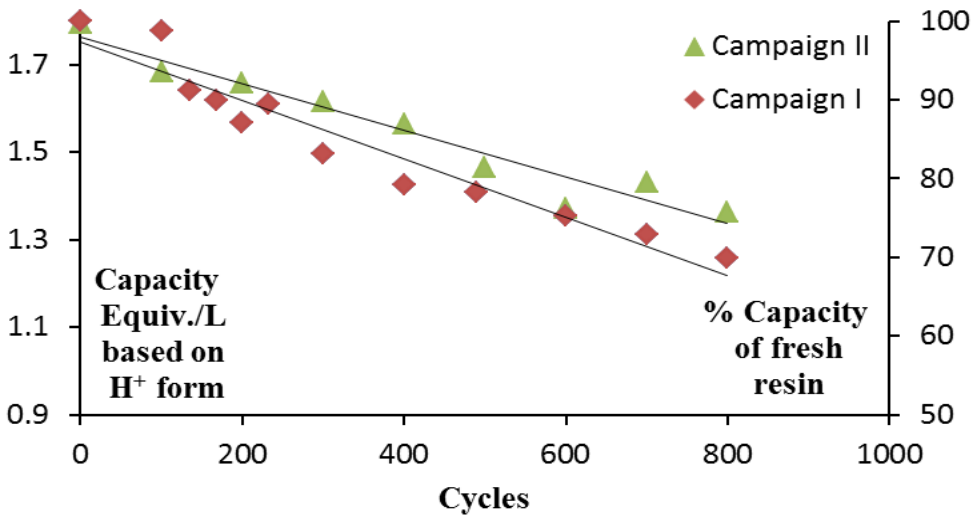

Fig.6-12b Ion exchange capacity with successive cycles, PPC100x10 Purolite®

The ability to degrade resin in this manner proved to be useful for the purposes of 'manufacturing' degraded cation exchange resin that had experienced some oxidation and was now mimicking resin that had been exposed to many multiple cycles. A cycle took approximately thirty minutes which meant 100 cycles would take about fifty hours i.e. two days. This degrading process allowed for the examination of the change in kinetics through test work carried out at discrete numbers of cycles.

During the initial attempts to find the parameters of the system by fitting the simulator to the data (as described in greater detail in section *5.10*) the fits were considered to be reasonable. However, one of the challenges was the difficulty of accommodating a zero concentration on the resin surface during the early time data. In addition to this being untenable, there was also a spike followed by oscillation in the concentration of the adsorbing ion in the outer shell of the resin due to the inevitable disparity in the mass balance. This difficulty was overcome by assuming that during the 'zero' concentration at the surface phase, the concentration in the resin is assumed to rise uniformly until the concentration moves above zero at which point diffusion gradients in the resin start to cause a disparity in concentration between the various shells. This is explained in greater detail in section *5.10.4*. and in Fig.5-14&15.

6.4. Two campaigns to measure the impact of resin ageing on transport phenomena

Two separate samples of 10% DVB Purolite resin were each systematically degraded over a period of two successive months with the objective of;

- Measuring the change in laminar layer mass transfer coefficient, if any.

- Measuring intra-particle diffusivity of the adsorbing and desorbing ions to determine if realistic values for these parameters are achieved and to observing any change therein with aging.

- Proving the feasibility of using a multiple mechanism modelling approach to characterise resin decay.

- The undertaking of two campaigns was to ensure repeatability of the results.

The test work consisted of using the resin aging machine (*4.1*) in the resin aging procedure described in more detail in section *5.9*, and systematically conducting the capacity test (*5.4*), equilibrium test (*5.5.3*) and the kinetic test (*5.2*) at discrete numbers of cycles, normally every 100 cycles.

The simulator that systematically generates bulk concentration data of the adsorbing ion for different values of mass transfer coefficient ($\boldsymbol{K_L}$), adsorbing ($\boldsymbol{D_i}$) and desorbing ($\boldsymbol{D_D}$) ion intrinsic diffusivities, combines the models of Newton's law of cooling (section *3.2*), the Mass-Action-Law (section *3.4*) and Nernst-Plank (section *3.5*) for the laminar layer, interface and intra-particle transport parts, respectively. The model is described in greater detail in the model chapter and further developed in the method chapter (section *5.10*) of this thesis. The simulator predicts the bulk and surface concentration against time and while these transient variables differ greatly, the laminar layer transport tends to dominate. As their values narrow as equilibrium is approached i.e. bulk concentration reduces and surface increases, control gradually passes from laminar layer to intra-particle diffusion.

6.4.1. Campaign I

The main outputs of the campaign were the mass transfer coefficient ($\boldsymbol{K_L}$) and the intra-particle diffusivity ($\overline{D_i}$) of the adsorbing ion which were obtained by fitting the simulator produced kinetic curves to the laboratory obtained kinetic curve for each test while searching for these parameters. A capacity test (section *5.5*) and three standard kinetic tests (sections *5.9 & 5.3.1*) were performed at through flow rates of 300 *ml/min*, 400 *mL/min*, and 500 *mL/min* after each 100 cycles.

6.4.1.1. The laminar mass transfer coefficient ($\boldsymbol{K_L}$)

All kinetic measurements performed throughout the duration of the aging test produced mass transfer coefficient ($\boldsymbol{K_L}$) values determined by the multi-model simulator fitting process. These are displayed in Fig.6-13a,b,c. The kinetic tests were conducted at three different ZLC throughput flowrates as explained in section *5.10* i.e. a) 300 *mL/min* , b) 400 *mL/min* , c) 500 *mL/min*. For comparative purposes the average $\boldsymbol{K_L}$ determined for each of the three of the flowrates are indicated in Fig.6-13a,b,c. The raw kinetic data are presented in Annexure X

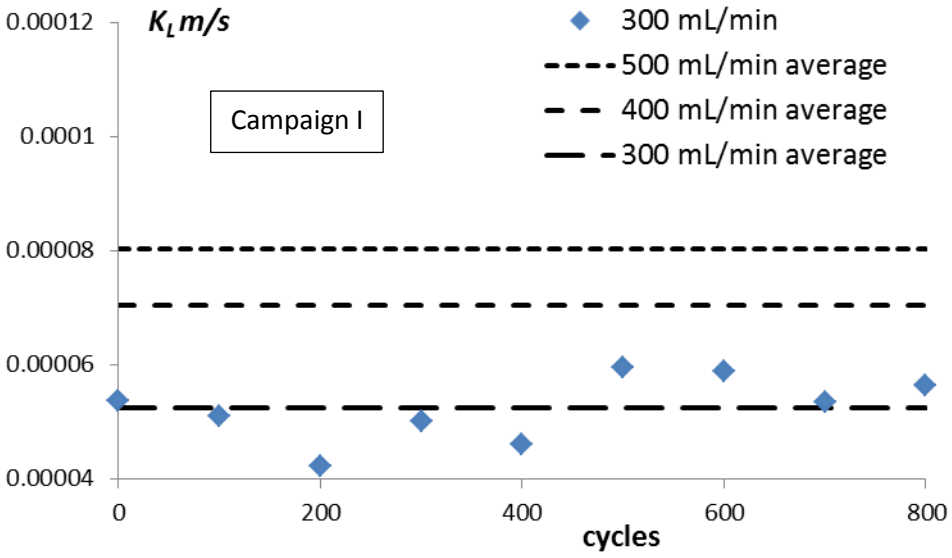

Fig6-13a K_L values calculated through simulation fit, as resin ages 300 mL/min

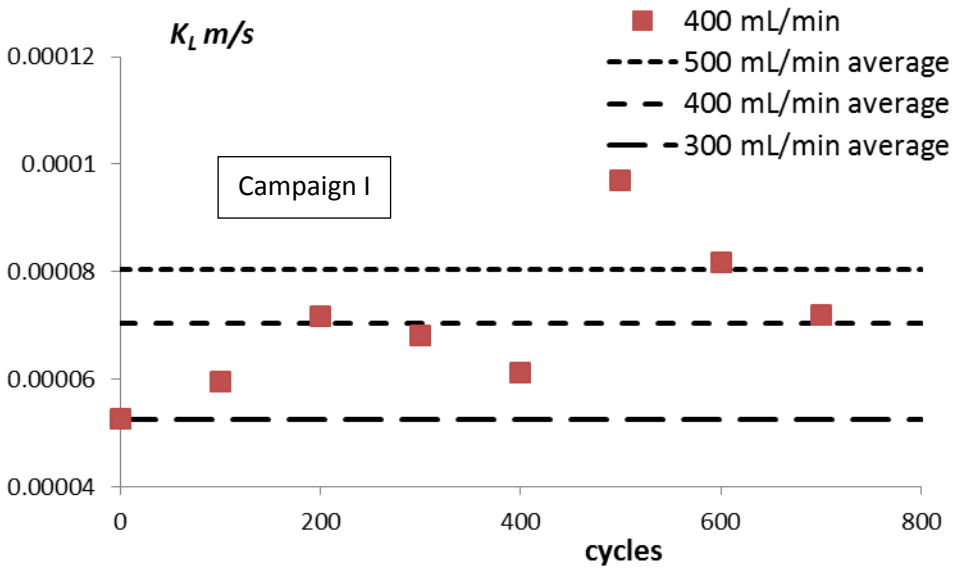

Fig6-13b K_L values calculated through simulation fit, as resin ages.

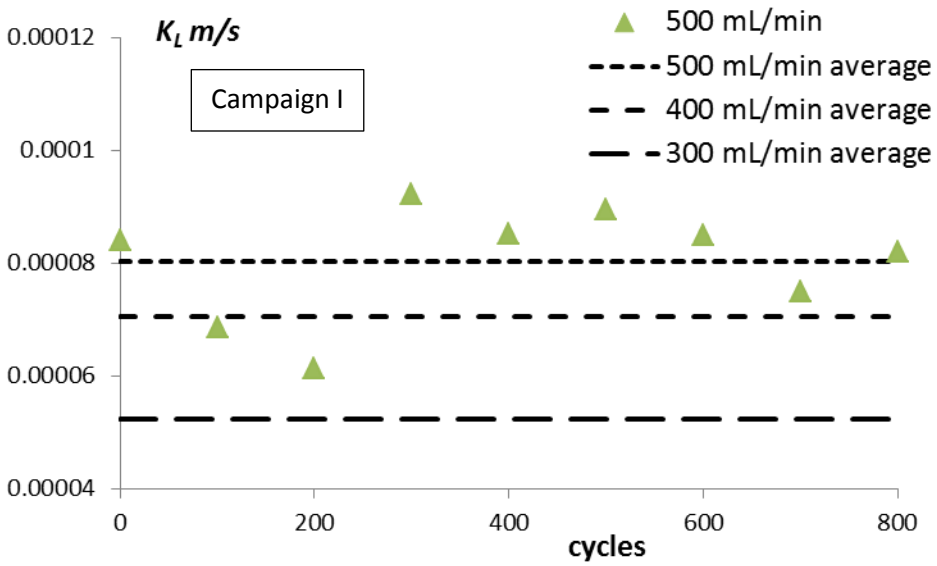

Fig6-13c K_L values calculated through simulation fit, as resin ages.

Although the 500 *mL/min* and 300 *mL/min* flowrate data show reasonably constant values throughout the campaign the 400 *mL/min* data show a fair amount of scatter. Fig.6-14 is a composite of all the campaign I mass transfer coefficient results and shows the average $\boldsymbol{K_L}$ values obtained for each flowrate. These average values are also presented in Tab.6-5. It can clearly be observed in Fig.6-14 that there is a systematic increase in $\boldsymbol{K_L}$ value with increase in volumetric flowrate which is to be expected as the greater turbulence is likely to improve ionic transport rate. Another observation is that there appears to be a very slight increase in

K_L values as the resin ages which might be due to the change in resin physical characteristics as the resin ages.

In Fig.6-14 it can be seen that the average variation (excluding the 500th cycle of the 400 *mL/min*) is of the order of ±22.5 % and from Fig.3-19 in section *3.8* that discusses model sensitivity, it can be seen that at this variance the residual error on the curve fitting varies by less than 1%. Therefore the variations can be assumed due entirely to the relative insensitivity of the model to the value of K_L and not poor experimentation.

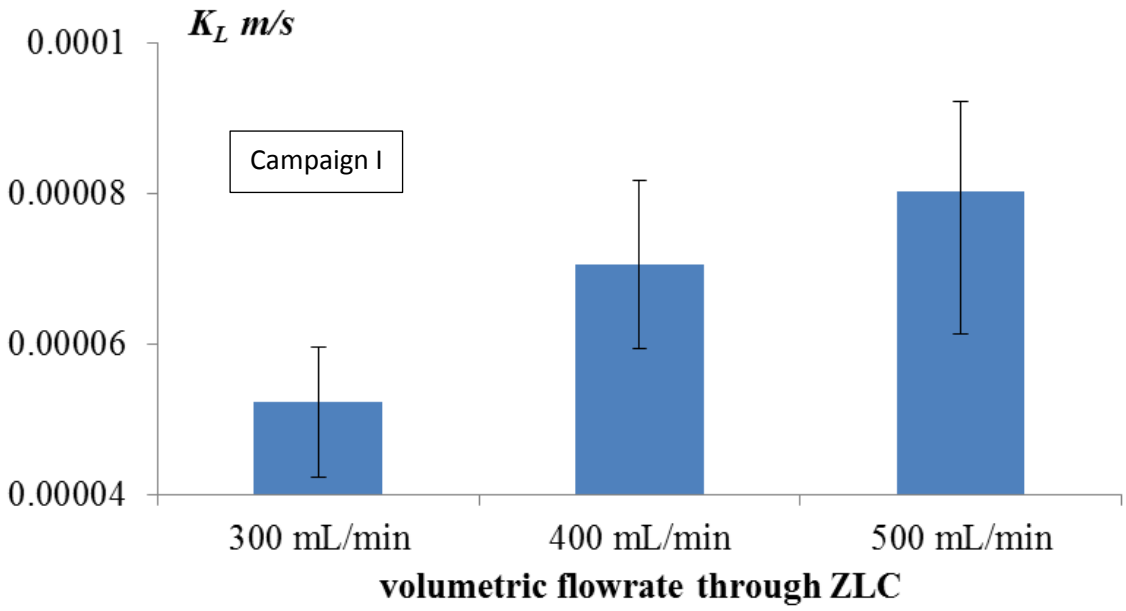

Fig.6-14 Average K_L value for each volumetric flowrate, fitted data

6.4.1.2. Intra-particle diffusion values ($\overline{D_i}$)

Three values of adsorption-ion intra-particle diffusion ($\overline{D_i}$) was calculated by the simulator fitting process for each 100 cycles of the aging process, one for each of the three ZLC throughput flowrates (300, 400, 500 *mL/min*) which are shown graphically in Fig.6-15.

From Fig.6-15 it can be seen that six of the measured inter-particle diffusivities appear to have been located on the boundary that was set in the search algorithm i.e. 10x10^{-11} m^2/s.

These values tended to be spread equally throughout the aging process with three being from the 400 *mL/min* data, two from the 300 *mL/min* and one from the 500 *mL/min*. This constituted 22% of the data points and might be attributed to inherent procedural inaccuracies during the campaign.

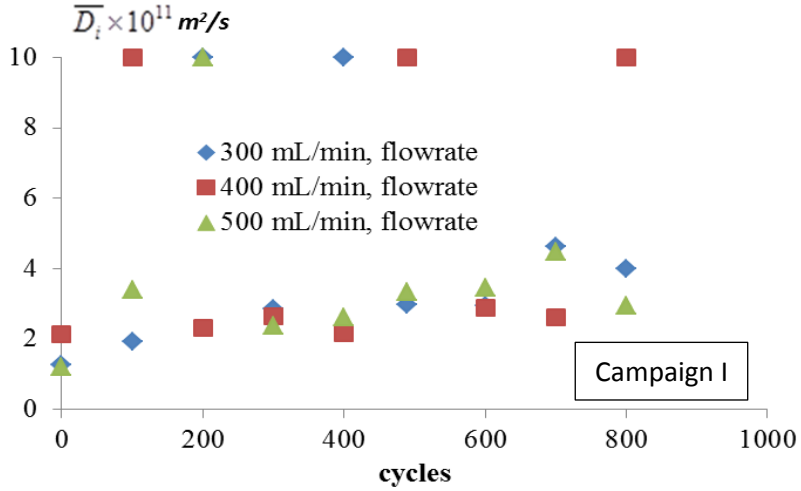

Fig.6-15 Calculated Inter-particle diffusion $(\overline{D_i})$ (simulator fitting)

An explanation for the lowest number of erratic measurements being from the 500 *mL/min* could be that at the highest velocity flow the intra-particle diffusion control is likely to dominate. There was a similar phenomenon observed for the intra-particle diffusion of the desorbing H^+ ions during the calibration tests using fresh resin, the results of which are presented in section *5.11*.

Aside from these boundary values, it can clearly be seen that for the balance of the measured intra-particle diffusivities very similar values are determined for each of the three volumetric flowrates for any given aged state and that the intra-particle diffusion substantially increases during the course of the aging, approximately doubling in value from $2x10^{-11}$ m^2/s to $4x10^{-11}$ m^2/s, from zero to 800 cycles, respectively.

Fig.6-16 is identical to Fig.6-15 however the erratic boundary values have been removed and the three separate legends have now been combined and a linear regression line incorporated to assist with the observation of the trend. The presented data points in Fig.6-16 shows a maximum variance from the linear regression line of 50% (@100 cycles) where there is very

low sensitivity of the curve fitting error (Fig.3-20 less than 0.7%) to this variation and hence is an artefact of the modelling rather than poor experimentation.

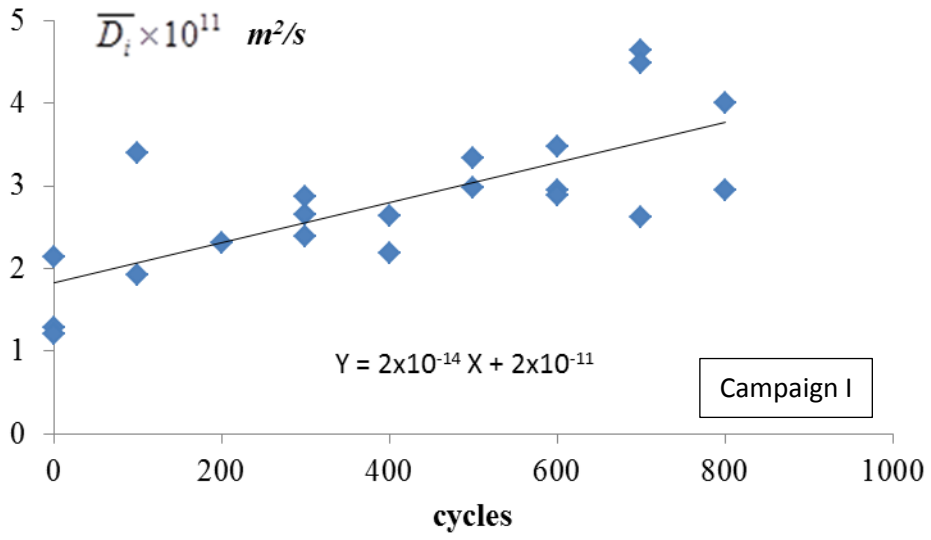

Fig.6-16 Simulator calculated intra-particle diffusions for all kinetic tests $\overline{D_i}$

6.4.2. Campaign II

As mentioned before, undertaking a second campaign to check for the repeatability of these results was considered necessary. The second campaign was undertaken in the identical manner to the first, and like the first took approximately one month to complete.

6.4.2.1. The laminar mass transfer coefficient ($\boldsymbol{K_L}$)

Fig.6-17a, b, c, show the calculated mass transfer coefficients ($\boldsymbol{K_L}$) throughout the aging process in each of the kinetic tests i.e. three at each 100 cycles. Just as in campaign I a fair scatter in the data is observed, but if the values are presented as averages with distributions as shown in Fig.6-18, the systematic increase in average $\boldsymbol{K_L}$ value with increase in volumetric flow through the ZLC is apparent.

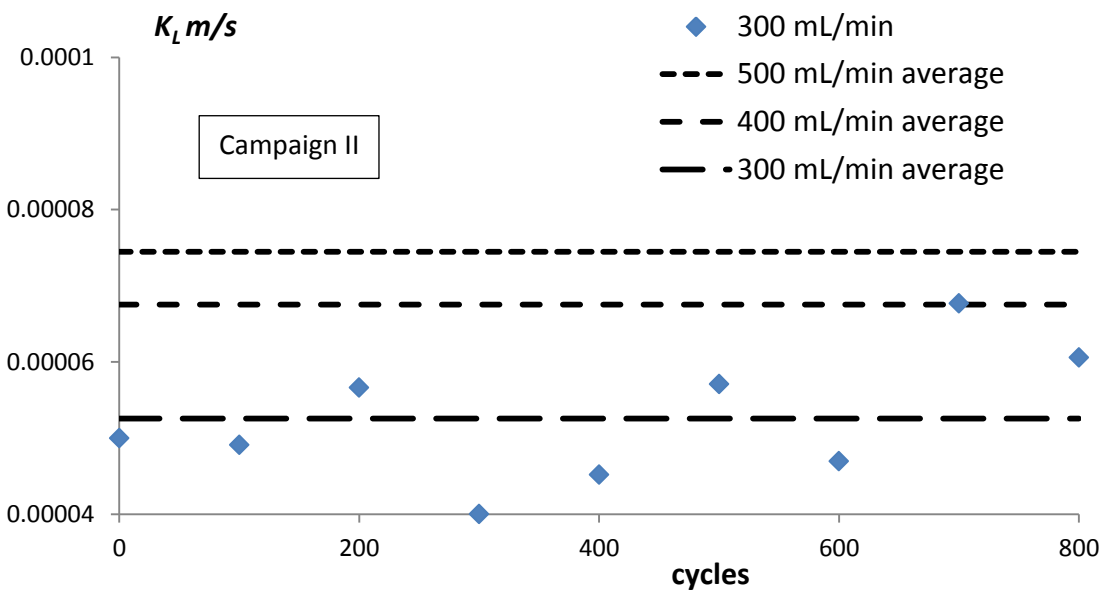

Fig.6-17a K_L values calculated through simulation fit, as resin ages.

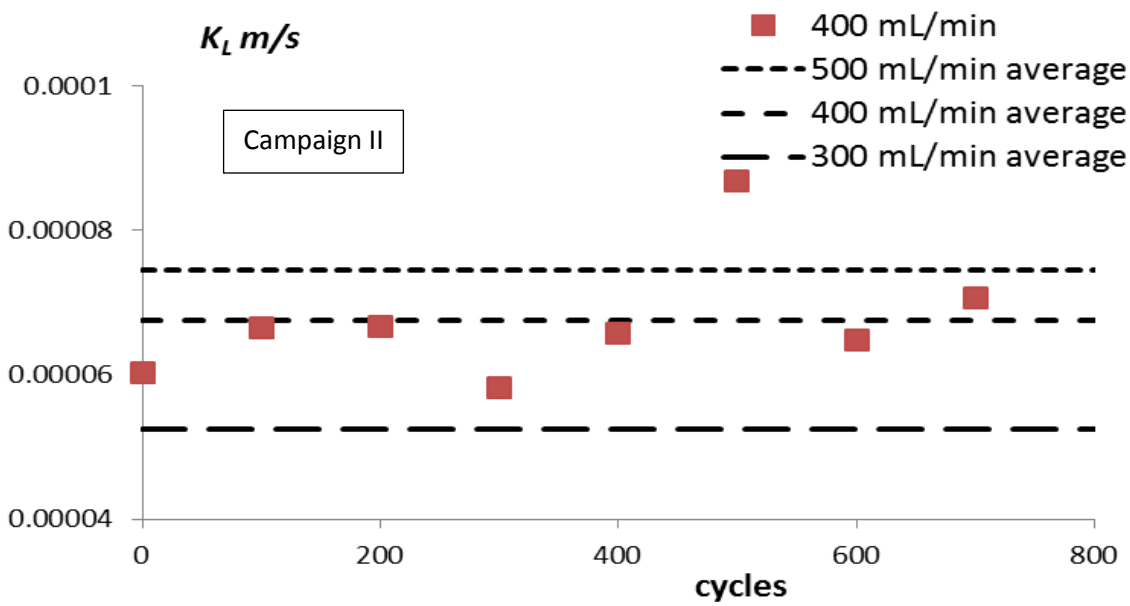

Fig.6-17b K_L values calculated through simulation fit, as resin ages.

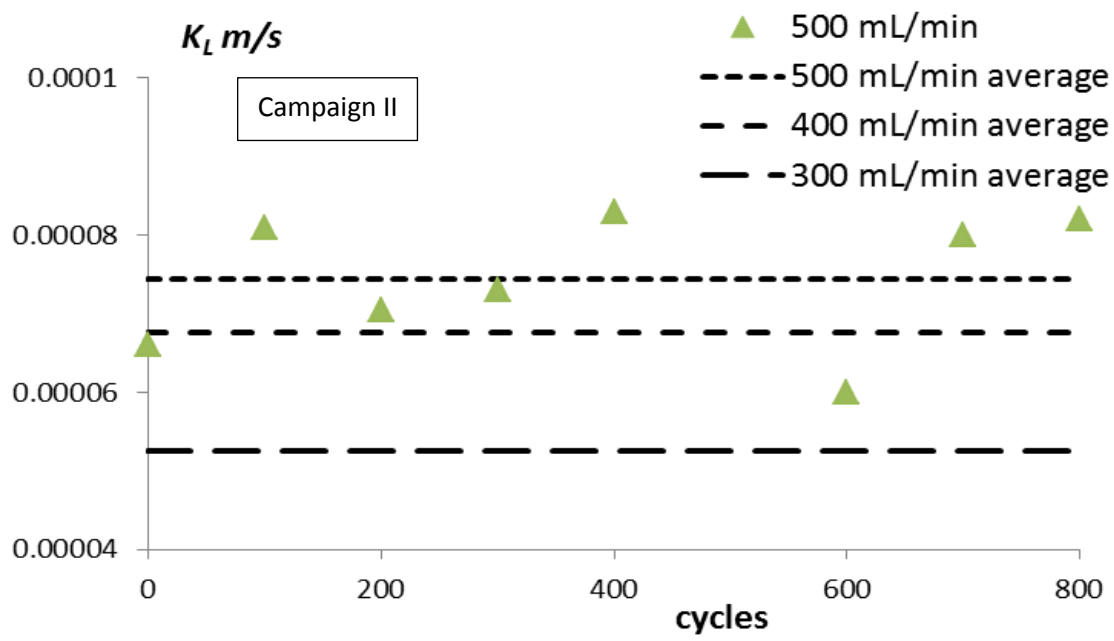

Fig.6-17c K_L values calculated through simulation fit, as resin ages.

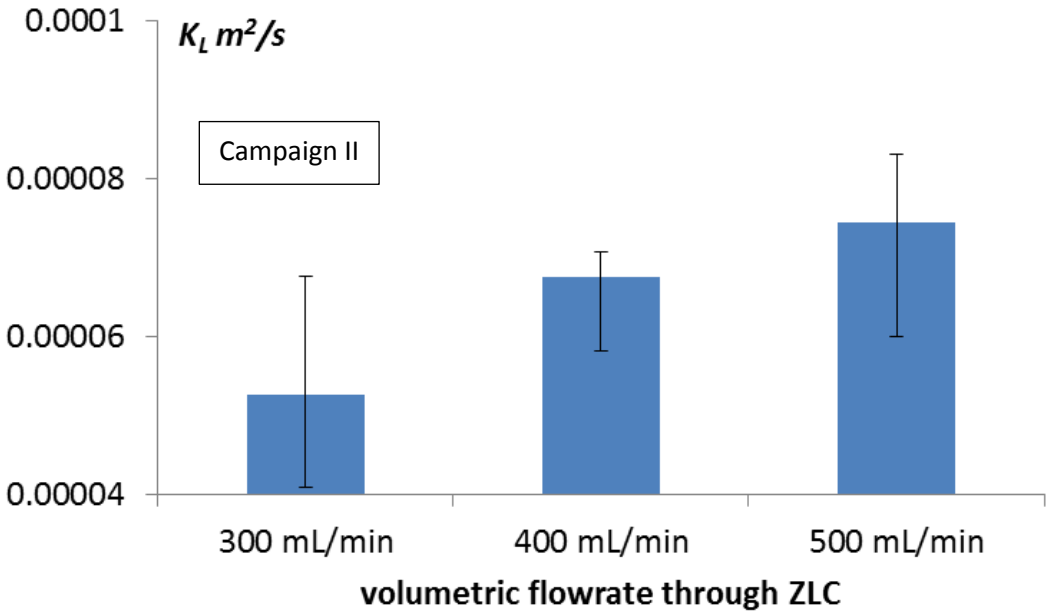

Fig.6-18 Average K_L value for each volumetric flowrate, fitted data

The values achieved in campaign II are seen to very similar to those achieved in campaign I. As can be seen in Fig.6-17c, a single data point moved to the upper boundary and was excluded in the calculation of the average and distribution of the 500 *mL/min* flowrate

calculation. Just as in campaign I, in Fig.6-18 it can calculate that the average variation is of the order of ±17 % and from Fig.3-19 in section *3.8* that discusses model sensitivity it can be seen that at this variance the residual error on the curve fitting varies by less than 1%. Once again a conclusion can be drawn that the variations can be assumed to be due entirely to the relative insensitivity of the model to the value of $\boldsymbol{K_L}$ rather than poor experimentation.

6.4.2.2. Intra-particle diffusion values ($\overline{D_i}$)

Fig.6-19 shows the simulator determined intra-particle diffusions for the adsorbing ion measured off each of the kinetic curves produced, at each of the three volumetric flowrates for every 100 cycles. Similarly to campaign I, data points (three) are seen to move to the upper boundary of the search area and were considered to be erratic. Just as in campaign I a discernible trend of increase in intra-particle diffusion with age is apparent although the scatter appears to be greater in campaign II.

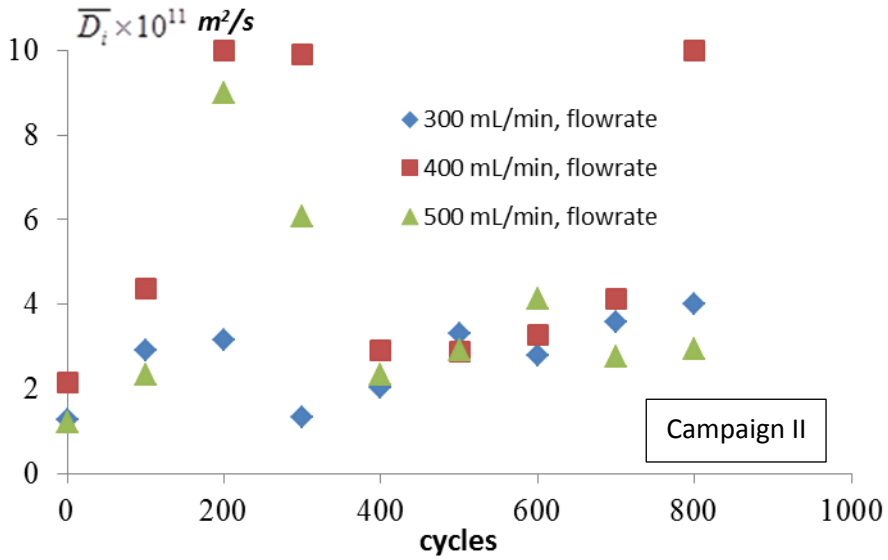

Fig.6-19 Calculated Inter-particle diffusion ($\overline{D_i}$) (simulator fitting)

Although some of the values in Fig.6-19 overshoot the mean by as much as 300% the extremely low sensitivity of the model to the variance i.e. < 1% (Fig.3-20) implies that this could be justified.

6.4.3. Combining Campaign I&II data and model comparison

An important exercise is to compare the $\boldsymbol{K_L}$ values achieved by this multiple-model simulator fitting technique to those obtained via the initial slope of the early time data method described in more detail in section *3.2.1.* Congruency would be strong evidence of the validity of the multi-model fit technique.

Having recorded all the variables of the system it now becomes possible to calculate a Reynolds No. and Schmidt No. for every kinetic test that was carried out on the ZLC during both aging campaigns. From these calculated dimensionless numbers and by using the Nesbitt & Matukela model an associated Sherwood No can be calculated for each throughput flowrate and from this Sherwood No. a mass transfer coefficient can be back-calculated for each of the three flowrates used in the kinetic test work. The $\boldsymbol{K_L}$ values obtained in this manner are presented on Tab.6-5 where they are compared to those obtained by the multi-model simulator fitting method applied to the data of each of the campaigns separately. The relative standard deviation about the mean of the data measured at each flowrate is included and these vary between 10% and 18% off the mean. These values can be explained by the curve fitting sensitivities shown in Fig.3-19.

Tab.6-5 Mass transfer coefficients determined by model and by simulation fit

Vol. flowrate ($\boldsymbol{u}$)	300mL/min	400mL/min	500mL/min
Campaign I ($\boldsymbol{K_L}$) Standard deviation	$5.24\text{x}10^{-5}$ m/s $5.37\text{x}10^{-6}$	$7.05\text{x}10^{-5}$ m/s $1.30\text{x}10^{-5}$	$8.04\text{x}10^{-5}$ m/s $9.50\text{x}10^{-6}$
Campaign II ($\boldsymbol{K_L}$) Standard deviation	$5.26\text{x}10^{-5}$ m/s $8.11\text{x}10^{-6}$	$6.75\text{x}10^{-5}$ m/s $8.19\text{x}10^{-6}$	$7.44\text{x}10^{-5}$ m/s $7.91\text{x}10^{-6}$
N&M model ($\boldsymbol{K_L}$)	$8.08\text{x}10^{-5}$ m/s	$9.46\text{x}10^{-5}$ m/s	$1.07\text{x}10^{-4}$ m/s

When comparing the simulator/model calculated mass transfer coefficient values presented in Tab.6-5 it can be seen that they are approximately all of the same order of magnitude. The values attained in each of the two campaigns are seen to be very similar. However, the model calculated coefficients are significantly higher.

A possible explanation for the Nesbitt & Maloka model estimating slightly higher K_L values could lie in the nature of the dimensionless-number modelling technique. The nature of empiricism is to reduce a plethora of complicated variables of a system to a relationship between fewer dimensionless variables and in the process inaccuracies are absorbed. These inaccuracies are likely amplified when calculating in the opposite direction i.e. using the Nesbitt & Maloka model to back calculate a mass transfer coefficient, as is undertaken in this exercise.

Notwithstanding that the means of K_L measurement is quite different in these two methods, another possible explanation for this difference could be that during the early time data it is for an extended period (at least one hundred seconds) that the surface concentration appears to be zero before starting to climb. Simultaneously the gradient of the bulk solution $\left(dC_{i,bulk}/dt\right)$ concentration against time has reduced, implying a lower rate of flux onto the resin at the end of this period. Hence a significantly lower mass transfer coefficient would be determined (as calculated by the simulator) for the same rate of mass transport at the lower concentration differential at the end of the period, everything else being constant.

Fig.6-20 is a collective of intra-particle diffusivities for both campaigns and gives an overall representation if the erratic data points are excluded. The results for campaigns I&II appear to be very similar from the perspective of overall values and overall trends, which would constitute strong evidence of the repeatability of the test work. The above average scatter in the early cycles is repeated in both campaigns, but is more apparent in campaign II and this might be an indication of the presence of a settling down period. Initially, the matrix may have a combination of weaker and stronger links and it could be that the weaker links deteriorate initially, eventually leading to a more uniform structure at which point the opening up of the steric environment proceeds more uniformly.

It can be seen from Fig.6-20 that during the resin aging metamorphosis the measured intra-particle diffusivity effectively increases by 50% to 100%. Despite the high scatter of results this change can be considered significant when considering the exercise conducted in section *3.8* of the model chapter which indicates significant and obvious variation in PPMC error of 3% and 0.3% for the K_L and D_i parameters at 50% deviation from optimum.

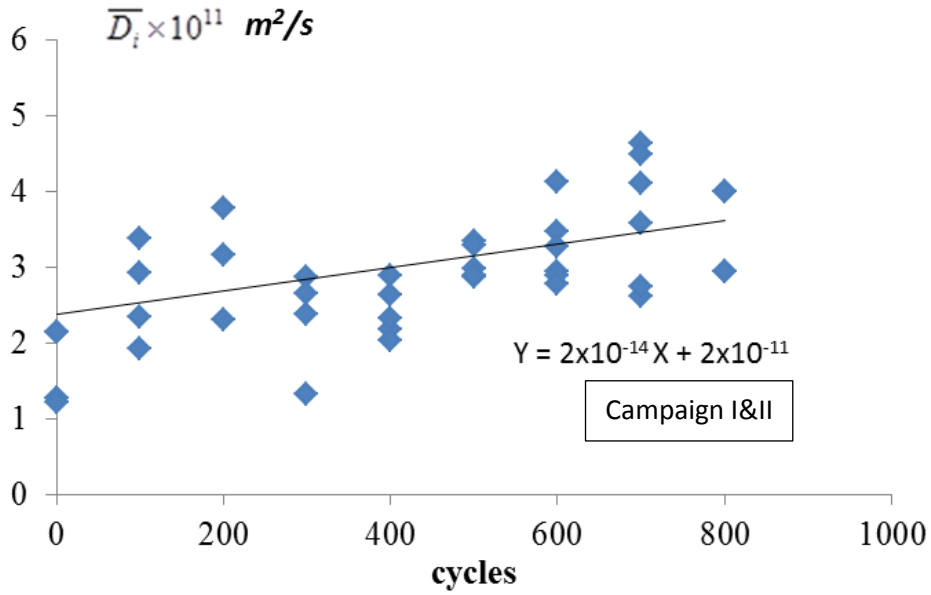

Fig.6-20 Intra-Particle diffusivity ($\overline{D_i}$) (simulator fitting)

6.4.4. Comparing measured intra-particle diffusion to other published data

The intra-particle diffusion value calculated using the simulator is compared with those in the literature obtained by other authors and these comparisons are shown in Tab.6-6. The intra-particle diffusivities obtained in this study are seen to be in agreement with that of Melis *et al*. (1996). However, those measured in older studies appear to be approximately four times higher.

An explanation for this is that the method used in this study is unique and, unlike the other studies, does not rely on existing empirical relationships to describe the laminar layer mass transfer coefficient. It is noted that in these older studies determination of the intra-particle diffusion was seen as a scientific endeavour, with the measurement itself being the sole objective, not unreasonable given the complexity of the challenge. There was no intention of comparing it to any environmental/steric change inside the resin, although the DVB content of the resin tested was always reported along with the particular ion being adsorbed.

Another key aspect of this study is the more complicated, calculation-intensive method. Earlier studies adopted the easier route of ignoring Nernst-Plank, while others used Nernst-

Plank but assumed intra-particle diffusion control throughout and performed tests in the practically more complex infinite environment.

Tab.6-6 Reported intra-particle diffusivities for Na^+ in 10 DVB resin

Authors	$\overline{D_i}$ **(m^2/s)**
This study (taken as average)	$3x10^{-11}$
Melis *et al*. (1996)	$5x10^{-11}$
Yoshida & Kataoka (1987)	$1.10x10^{-10}$
Graham & Dranoff (1982)	$1.57x10^{-10}$
Kataoka *et al*. (1973)	$1.35x10^{-10}$
Turner *et al*. (1966)	$1.21x10^{-10}$

Although there are a number of differences between the experimental methods and models used by each researcher, the main two differences between other studies and that described in this work are;

1) All test work described in this study was performed in a finite environment while ensuring that both laminar layer and intra-particle diffusion were controlling at some stage in the transient. In most other studies an infinite system was used, where it was assumed that intra-particle diffusion was controlling.

2) The laminar mass transfer coefficient obtained in this study is calculated by using the multi-model simulator fitting process, which includes the in-series laminar layer controlling mechanism. In the other studies either a single mass transfer coefficient value is used, calculated from existing empirically determined models, as dictated by the turbulence of the system and other physical characteristics. This was normally calculated from dimensionless empirical relationships, which by nature may incorporate inaccuracies making them unsuitable for such an application.

Although accuracy in intra-particle diffusion measurement is always desirable in all scientific studies, the main objective of this research was to detect changes in this parameter of the

system for the purposes of developing practical tools to study resin degradation. Therefore the intra-particle diffusivities, determined using the method described in this study, can be considered reasonable if evaluated in the context of the change in the physical state of the resin which goes hand in hand with the diffusivity study and is discussed in the following section.

6.5. Qualitative evaluation of decayed resin used in Campaign I&II

Prior to commencing the degradation of the 10DVB resin, in each campaign an evaluation of the resin was made with respect to capacity, swelling/shrinking and general appearance. Linking the change in intra-particle diffusivity to the change in the steric state inside the ion exchange resin was considered to be an important validation of this resin degradation study. Hence two non-intrusive techniques were developed, both of which gave similar results. These were the method of observing the degree of contraction in a powerful electrolyte and the observation of degree of translucence.

6.5.1. Contraction of fresh and spent-resin

The technique of measuring the contraction of the resin and relating this to the internal steric state of the resin (measured in DVB addition), as displayed in Fig.6-11 and described in section *6.2.3*, was also carried out on the decayed resins used in campaigns I&II. The spent resin from the two campaigns were regenerated and then contacted with 3 mol Na^+ solution as $NaNO_3$ and the contraction in resin diameter measured using the microscope described in section *4.5* of the 'Equipment' chapter. The resin from each campaign was measured separately and the contraction determined for each under these specific conditions was found to be virtually identical. Campaign I & II resins both contracted by an average of 8.6% which was marginally more than that of the fresh 10% DVB resin which contracted by 7.0%, all measurements based on resin bead diameter.

Having measured the shrinkage of the spent campaign I&II resins and then interpolating a DVB content by means of using Equ.6-4 indicated that both resins' contraction behaviour

could be equated to that of a fresh resin having a DVB content of approximately 9.0% indicating that a reduction in steric state must have occurred due to loss of internal matrix structure. Fig.6-21 shows the result of this test.

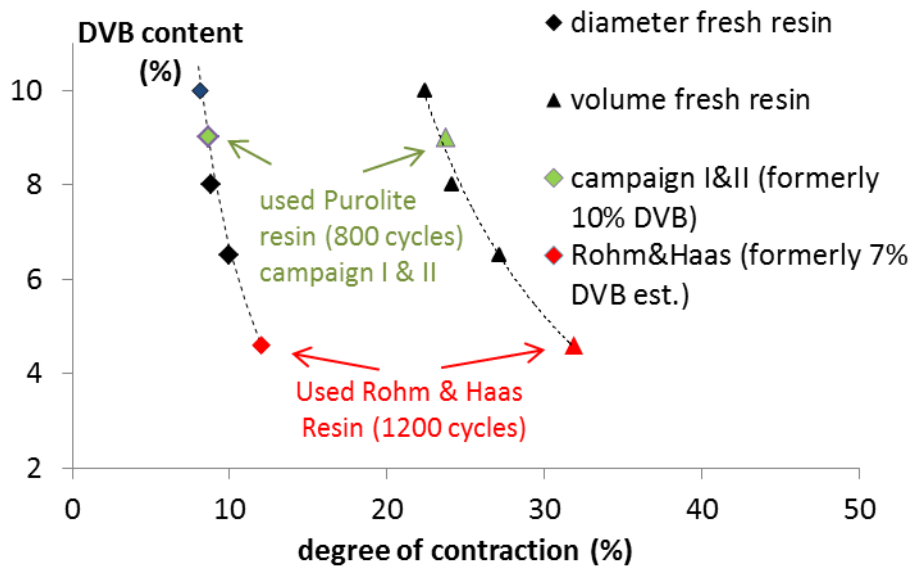

Fig.6-21 Degree of contraction versus DVB, fresh and old resins

6.5.2. Translucence of fresh and spent resin

Qualitative observation of the various resins of different DVB content during the test work indicated that there may be a relationship between resin internal steric state and the degree of translucence. Fig.6-10 is an indication of the difference in translucence between fresh and used resin. The degraded resin was shown to have a lower steric state by contraction compared to the fresh resin, which displays a darker colour.

With the objective of quantitatively evaluating this relationship, photos were taken of all the resins used in the test work. The translucent/steric state environment phenomenon can be clearly seen in Fig.6-22a/b/c which shows fourteen-fold magnified images of the three fresh resins of varying steric state (10% DVB, 8% DVB and 6.5% DVB) all taken with the DCM310 microscope described in more detail in Equipment section *4.5.*
Fig.6-23a/b/c are similarly magnified images of the Rohm&Haas resin (post 1200 cycles) as described in section *6.2.3* and the campaign I & II resins (post 800 cycles) respectively.

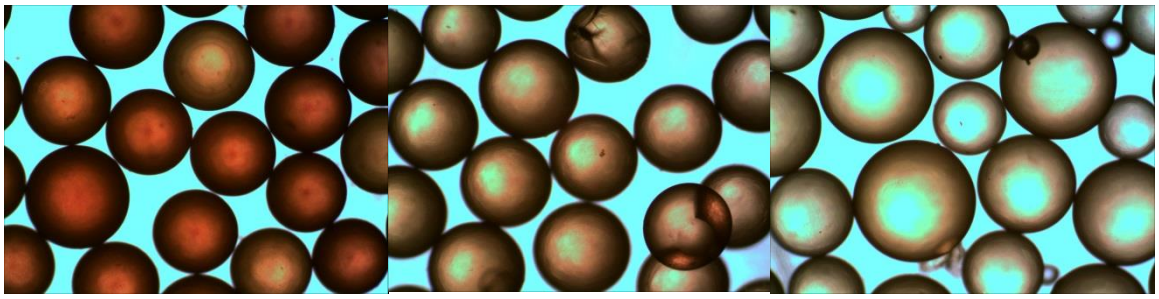

Fig.6-22a/b/c Magnified images of 10%, 8% and 6.5% DVB content respectively

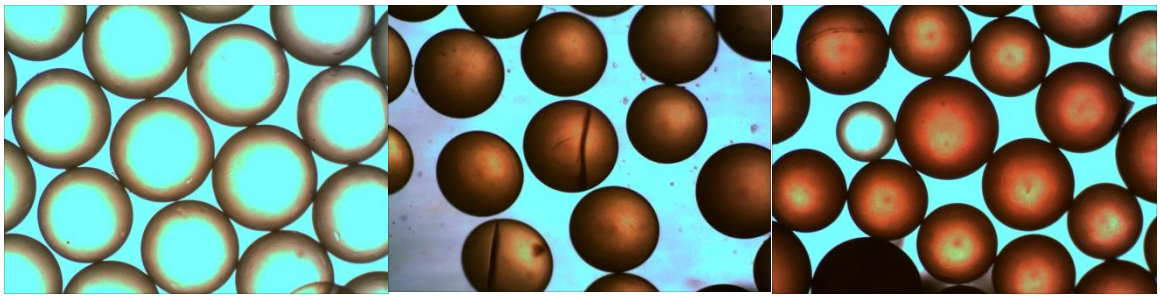

Fig.6-23a/b/c Decayed magnified resin a) Rohm&Haas and b), c) campaign I&II

In an attempt to standardise the image environment the images were converted to a Grey Scale according to the method described by the 'Consultative Committee for International Radio' (CCIR). This formula requires the measurement of the intensity of colours i.e. 'Red', 'Green' and 'Blue' on an 8 bit scale (2^8 or 0 - 255 degrees), with 0 being black and 255 the full intensity of the colour. Grey Scale intensity i.e. a value from 0 – 214 can then be calculated using Equ.6-5 where 214 is equated with white and 0 with black. Performing this calculation for every pixel in a colour image, results in a Grey Scale image. Fig.6-24a/b/c and Fig6-25a/b/c are Grey scale equivalents of Fig.6-22a/b/c and Fig6-23a/b/c calculated in this manner using 'ImageJ' freeware software.

$$0.266(\boldsymbol{red}) + 0.587(\boldsymbol{green}) + 0.1144(\boldsymbol{blue}) = \boldsymbol{Y}(\boldsymbol{grey}) \qquad \textbf{6-5}$$

Where

$\boldsymbol{Y}$ is the calculated grey scale intensity value (*0 – 214)*

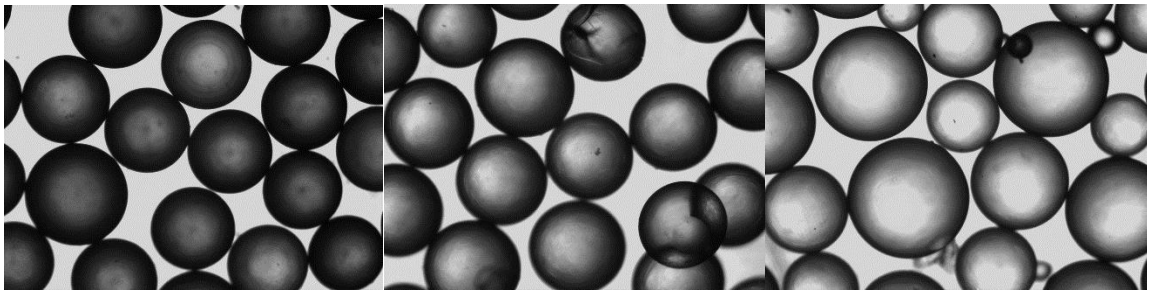

Fig.6-24a/b/c Grey scale of Fig.6-22a/b/c

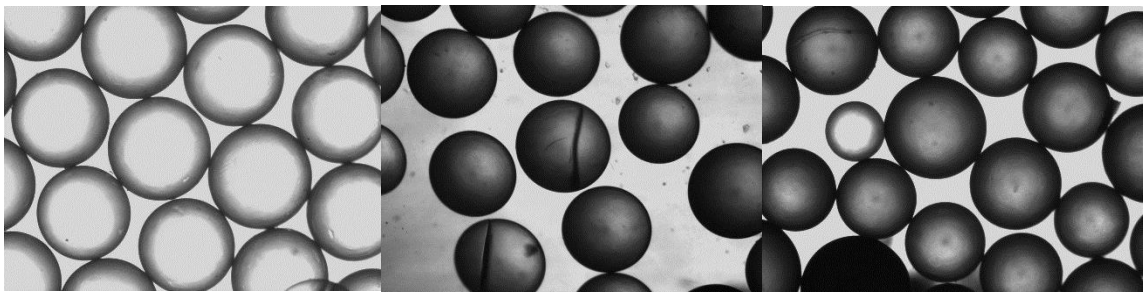

Fig.6-25a/b/c Grey scale of Fig.6-23a/b/c

For each resin group Grey Scale measurements were carried out on numerous resin beads and at a number of predefined distances from the middle of each bead, ultimately giving an overall average result. A linear relationship between the fresh resin DVB's and the average Grey Scale values appeared to give the best fit that serendipitously, from the perspective of predicting changes in DVB content, shows a far flatter gradient compared to the DVB/contraction relationship.

Interpolation and extrapolation are used to determine the apparent DVB content of the decayed campaign I&II resins. The Rohm & Haas resin is also included however the Grey Scale test on the fresh resin interpolated off the model returned a DVB content of 7.1%. The graphical results are shown in Fig. 6.26. The numeric results of these tests are presented in Table.6-7 and Fig.6-27.

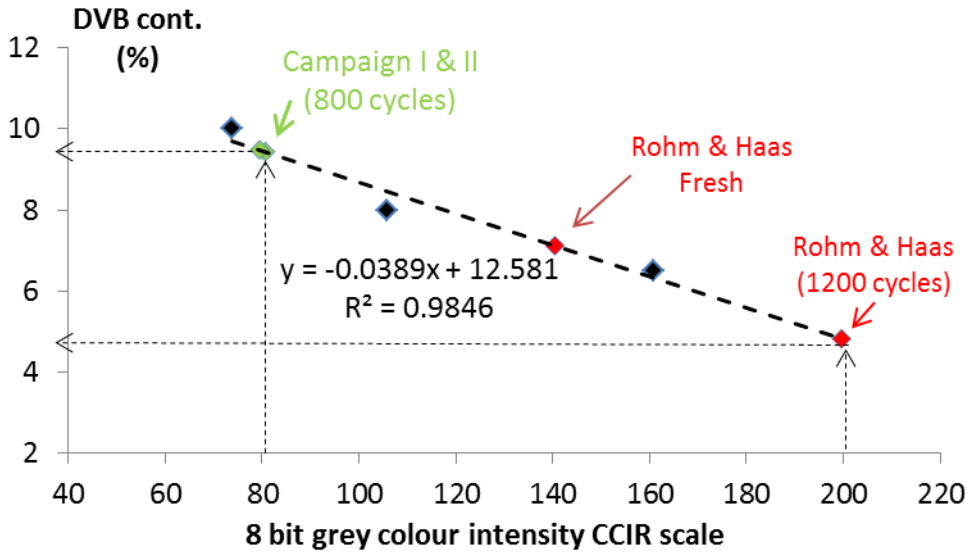

Fig.6-26 DVB content vs Grey Scale calibration curve

Tab.6-7 Grey Scale (GS) values achieved for each resin group

	10.0 DVB % (fresh)	8.0 DVB % (fresh)	6.5 DVB % (fresh)	Campaign I (800 cycles)	Champaign II (800 cycles)	Rohm&Haas (0 cycles)	Rohm&Haas (1200 cycles)
Ave.	73.88	105.88	160.75	80.7	79.5	140.4	199.6
Std.Dev	30.93	53.37	52.99	38.4	29.5	62.7	51.5
Low GS	43	47	83	38	40	40	133
High GS	133	182	212	147	137	215	215
DVB %	10.0	8.0	6.5	9.4	9.5*	7.1*	4.8*
* interpolated							

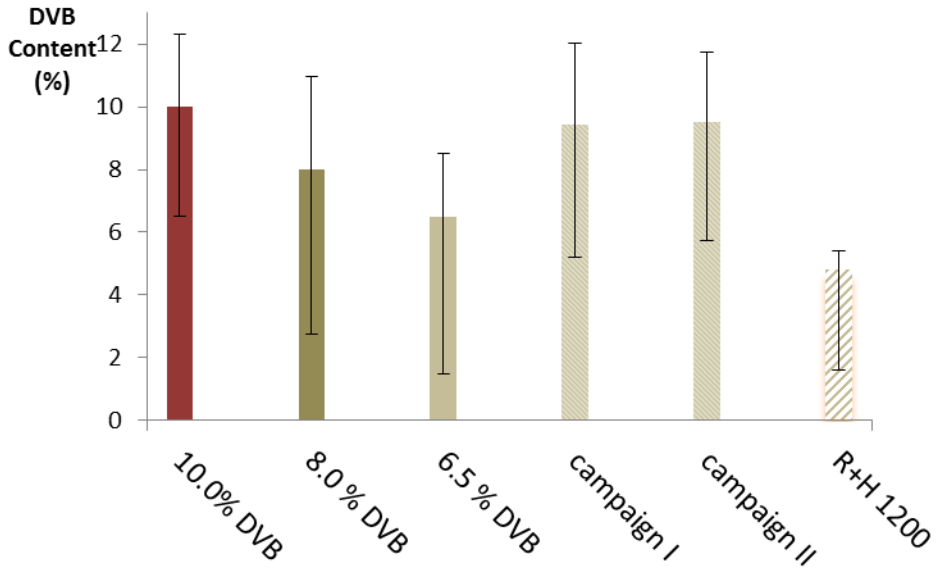

Fig.6-27 Graphical representation of Tab.6-7

Using translucence to determine the steric state inside a resin bead could be developed into a more accurate method than the contraction method. It is simpler and does not require a challenging before-after chemical addition measurement as described in section *6.2.1*. However, basing our model on only three points will need to be improved upon.
Although the translucent method could be developed further for the purposes of achieving even more accurate results, for the purposes of this study this outcome was considered to be reasonable.

6.5.3. Comparing the results of the contraction/translucent methods

The results achieved for both the contraction and translucent methods for the final DVB values measured in each test were not identical but are nevertheless reasonably close and these are presented in Tab.6-8.

Tab.6-8 Comparison of Contraction/translucence methods

	campaign I	campaign II	Rohm & Haas
contraction method	9.0	9.0	4.6
translucence method	9.4	9.5	4.8

From the results achieved it is clear that the internal environment of the resin has changed due to decay and this is easily measurable using either the contraction or translucence method. This is an important observation as it neatly gives foundation to the observed change in intra-particle diffusivity during the decay metamorphosis of the resin and could be further developed in the study of resin decay.

The results presented in this chapter show that developing a quantitative relationship between the loss in DVB content and intra-particle diffusivity is possible. From the intra-particle diffusivities determined in the calibration section *5.11* it is possible to see a gradual shift from 3.5 - 4 x10^{-11}(m^2/s) for (10%DVB) to 6 x 10^{-11}(m^2/s) for (6.5%DVB) resin. The same analysis on the artificially decayed resin roughly shows a change from 2 – 3.5 x 10^{-11}(m^2/s) for (fresh resin) to 3.5 – 4.5 x 10^{-11}(m^2/s) for estimated (9.5 – 9 DVB). Hardening up on this

relationship should be achievable and with multiple ways of measuring DVB content, getting a grip on resin performance/decay can become a quantitative reality.

7. CONCLUSION

7.1. From general question to system parameters

In an attempt to answer the general question; *how often does the inventory of a particular resin, in a particular duty, need to be replaced,* a generalised approach to the characterisation of resin decay-state is required, particularly with respect to the efficient performance of the resin. With the attainment of a proficient resin characterisation method, based on measurable parameters, a link to contactor simulation and ultimately design modelling can be created. This would augment resin performance simulation by incorporating the phenomenon of resin decay and would allow the contactor-design engineer to introduce contingency with a view to compensating for the resin's decrease in performance/efficiency as it ages.

To answer the specific question; *how does one model the decay of resin performance so as to give the design engineer a practical tool with which to design the resin contactor,* the development of a tool to model resin decay-state is necessitated. In this study the approach was to prove that resin transport parameters could be linked to resin decay. Initially, this involved the development of an algorithm that separated lumped parameters into individual component parameters i.e. the development of a rigorous mathematical transient model, and then proving that the component parameters do indeed represent meaningful constants of the system, particularly with respect to resin decay.

One of these component parameters is intra-particle diffusivity. As a key hypothesis of this study was that the internal steric-state of resin alters with the degree of resin decay, the linking of intra-particle diffusivity to resin steric-state would proffer the dual return of elucidating the state of resin decay in addition to providing an important transient modelling parameter that could be incorporated into a larger design simulator.

7.2. Postulated algorithm and model

The model simulation postulated in this thesis requires an external laminar dynamic-layer mass transport coefficient ($\boldsymbol{K_L}$) and two intra-particle diffusivities ($\boldsymbol{D_i}$, $\boldsymbol{D_D}$) i.e. of the adsorbing and desorbing ions to simulate any particular transient. To measure these parameters from transient data, a simulator generated curve is fitted to laboratory generated data using a suitable search mechanism. By conducting kinetic test work in which the environment inside and outside the resin beads was altered independently, and observing the appropriate change in these measured parameters, it was then possible to conclude that the postulated mathematical model does indeed appropriately represent the transient diffusion mechanism. A change in turbulence by varying flow velocity through the resin bed was used to alter the external environment, and fresh resins of varying DVB content were used to alter the resin internal environment.

Obtained intra-particle diffusivities ($\boldsymbol{D_i}$) were smaller than those attained by other researchers, although only slightly less than those more recently published. More traditional methods were used by these other researchers which are described in more detail in section *6.4.4.* It can be concluded that the proximity achieved in this study, despite the novel method used, is a vindication of the method presented here.

However, obtaining intra-particle diffusivity for the desorbing ion proved challenging and it was concluded that at no stage during the transients encountered in the present study did the diffusion of the desorbing ion (H^+) constitute a constraint on mass transport, precluding it from mechanism control. Model sensitivity to the value of this parameter was negligible and hence did not affect the determination of the other two. Simultaneously measurement of the mass transfer coefficient ($\boldsymbol{K_L}$) gave results slightly higher than those achieved by the traditional method of measuring it off the initial slope; however this is not unreasonable given the novel method proposed. The variability of $\boldsymbol{K_L}$ is also well within the range of model sensitivity to optimal fit (section *3.8*)

It could further be concluded that the steric-state/internal-structure of the ion exchange resins had indeed altered through ageing shown by physical measurement, by testing resin structure using two original methods i.e. observation of changes in swelling/contraction and resin translucence. Resins of varying states of decay and fresh resins of decreasing DVB content could be presented on a continuum that had resin rigidity weaken and translucence increase with reduction in DVB content, which is commensurate with a weakening structure.

7.3. Two decay campaigns

In an attempt to prove reliability and repeatability of the results, two completely independent resin decay campaigns were conducted, in each of which a charge of resin was cyclically loaded and stripped over 800 cycles. Regular parameter measurements were conducted as the resin aged, by the fitting of kinetic test data conducted at three different turbulences with the help of the proposed model simulator, at regular cycle intervals. The measurements indicated the expected change in mass transfer coefficient with respect to change in turbulence but not with resin aging, from which it can be concluded that this parameter measurement was true. Simultaneously, the determined adsorbing ion diffusivity was seen to remain constant with turbulence but altered significantly as the resin aged, from which it can be concluded that the value obtained was not only realistic but that it could be used to characterise the state of resin decay.

During this study it became apparent that in the application of the proposed model the mass transfer coefficient is essentially derived from early time data and intra-particle diffusivity from a later part of the curve. This is entirely in keeping with the literature that acknowledges the dominance of the laminar layer in mechanistic control during the early stages of resin conversion and intra-particle diffusion during the final stages of conversion.

All conclusions regarding the measurement of resin decay were further bolstered by the observation that the change in the specific values of the intra-particle diffusivity, the change

in resin swelling/contraction and translucence all showed congruency in their individual degrees of change with respect to resin aging/DVB-change. From this it could be concluded that, the linking of DVB to intra-particle-diffusion quantitatively for the purposes of deriving a convenient model for resin decay, is possible as postulated in section *6.5*. It might be pertinent at this point to mute the term 'apparent DVB content' as there is the distinct concept of 'added DVB content' as in resin manufacture which gives structure and rigidity and then the weakening of the this structure during aging that could then be measured in 'apparent DVB content'.

7.4. Model sensitivity, analysis and stability

The model proposed in this study is complicated not only mathematically but also in the manner of application. The sensitivity analysis (section *3.8*) of the model inputs to the PPMC output indicates that the model is mildly sensitive to variation of the mass transfer coefficient at approximately 3% change for a 50% variance in parameter input. The model is less sensitive to variance in adsorbing ion diffusivity at approximately 0.3% for a 50% variance in input and is extremely insensitive to the desorbing ion diffusivity to the point of insignificance. The semi-symmetrical sensitivity curves achieved in the analysis of section *3.8* prove the stability of the fitting process with little ambivalence as to where the optimum point is located.

It can be concluded that there is little challenge in the procedure of fitting the simulator to raw kinetic data, as the model approach presented in this study appears to be relatively stable and the Hook-Jeeves optimum search process proceeds smoothly with the algorithm achieving the objective relatively rapidly. However, occasionally instability was observed when the desorbing ion attained certain thresholds, but this was rectified by limiting its possible search domain, and in most fitting procedures the value climbed to an insignificant value three orders of magnitude above that of the adsorbing ion diffusivity.

Finally it can be concluded that the results of work completed in this study adds weight to laminar layer transport theory, albeit it through more experimental means. The excellent fits achieved by the Hook-Jeeves search algorithm (0.999 > PPMC > 0.99) is evidence thereof.

7.5. Study limitations and further work

An exhaustive search of the literature showed almost no quantitative study of resin degradation, making this one of the first rigorous studies on the subject. Therefore discovering a link between resin internal steric state and intra-particle diffusivity, which is an important transport parameter, constitutes a success. However, it has been applied only to acid resin in an environment of decreasing steric state.

Further studies should be undertaken on observing the impact of densification of the resin steric state on mass transport parameters, where there is a buildup of foreign matter, although this is unlikely to happen slowly as in the case of the resin degradation in this study. Intuitively, a reduction in intra-particle diffusivity could be expected. Likewise, this entire study should also be carried out on base resin, which is known to be chemically more sensitive. Further, the study of macro-porous resins adds an order of magnitude of complication due to the heterogeneous environment of the resin. However, the basic concept of linking intra-particle diffusivity to resin decay state is still likely to be important as it allows for quantitative insertion of the decay metamorphosis into bigger algorithms.

The development of two tools i.e. translucence and degree of resin swelling to measure resin structural changes are novel and proved most useful in this study. However, their further development for the purposes of further resin decay studies is a necessity, in addition to developing into a diagnostic tool for assessing in-service resin decay. Aside from these two methods, and the obvious technique of measuring resin capacity, there is no other way of independently determining resin state.

For the purpose of functionality all computer based work in this study was conducted using a combination of Excel and Turbo Pascal version 7. For the purposes of research work requiring the application of fundamental mass transport models and sophisticated search algorithms this arrangement was considered pertinent especially being part of a fundamental

PhD study. However, for the purposes of conducting further studies the development of more elegant user friendly software that can be standardized and more widely used is a necessity.

The development of the resin aging machine proved to be necessary as the aging process was laborious and had to be automated to ensure repetitive testing. Despite being a rugged tool developed over many years by a mechanical/electronic amateur the necessity to further develop this machinery, for wide spread use and ultimately offering a resin testing service to industry, would be pertinent.

8. REFERENCES

Boyd, G. E., Adamson, A. W., Myers, L. S., 1947. The Exchange Adsorption of Ions from Aqueous Solutions by Organic Zeolites: II. Kinetic, J. Am. Chem. Soc., 60

Chowdia, V., N., Lee, G., C., Foutch, G., L., 2003, Binary liquid-phase mass transport in mixed-bed ion-exchange at low solute concentration, Ind. Eng. Chem. Res., **42,** (7) 1485-1494.

De Dardel. F., Arden. T., 1989, Ion exchange Principles and Applications, Rohm and Haas separation technologies.

Fernando, K., Lucien, F., Tran, T., Carter, M. L., 2008, Ion Exchange resin for the treatment of cyanidation tailings Part 3 – Resin deterioration under oxidative acid conditions. Minerals Engineering **21,** (10) 683-690

Fernando, K., Tran, T., Laing, S., Kim, M. J., 2002, The use of ion exchange resin for the treatment of cyanidation tailings. Part 1 – process development of selective base metal elution. Minerals Engineering **15,** (12), 1163-1171

Fleming, C., Hancock, R., 1979. The mechanism in the poisoning of anion-exchange resins by cobalt cyanide *J. SAIMM* **79**, 334

Foutch, G. L., Chowdiah, V., 1992, Resin degradation effects in mixed-bed ion exchange. Ultra-pure water J. **9**, (2) 29-32

Gemeay, A.H., Mansour, I.A., El-shardawy, R.G., Zaki, A.B., 2004. Kinetics of the oxidative degradation of thionine dye by hydrogen peroxide catalysed by supported transition metal ions complexes. Journal of Chemical Technology and Biotechnology **79**, (1), 85-96

Glaski, F. A., Dranoff, J. S., 1963, Ion Exchange Kinetics: A comparison of Models, *AIChE J.*, 9, (3),427

Gomez-Vaillard, R., Kershenbaum, L., S., Streat, M., 1980, The Performance of Continuous, Cyclic Ion- Exchange Reactors – I, Chem. Eng. Sci. **36,** 307 – 319

Gomez-Vaillard, R., Kershenbaum, L., S., 1980, The Performance of Continuous, Cyclic Ion-Exchange Reactors – II, Chem. Eng. Sci. **36**, 319 – 326

Graham, E., Dranoff, J., 1982, Application of the Stefan-Maxwell Equations to the diffusion in Ion Exchange. 2. Experimental Results. *Ind. Eng. Chem. Fundam*. **4**, 365.

Grossman, J., Adamson, A., 1952, The Diffusion Process for Organolite Exchangers, J. Phys. Chem., **56**, 97.

Harries, R. R., P.h.D. dissertation, 1986, Loughborough University of Technology, Loughborough.

Hasnat, A., Juvekar, V. A, 1996. Ion-Exchange Kinetics: Heterogeneous Resin-Phase Model. *AIChE J.,* **42**, (1) 161

Helfferich, F., G., Ion Exchange, McGraw-Hill, New York, 1962

Holl, W., Sontheimer, H., 1977, Ion Exchange Kinetics of the Protonation of Weak Acid Ion Exchange resin, Chem. Eng. Sci., **32,** 7 755-762

Hwang, Y., L., Helfferich, F., G., 1987, Generalized model for multi-species ion-exchange kinetics including fast reversible reactions, Reactive Polymers, **5**, 237-253

Jones, I., L., Carta, G., 1993, Ion Exchange of Amino Acids and Dipeptides on Cation Resins with Varying Degree of Cross-Linking. 2. Intra-particle Transport, Ind. Eng. Chem. Res. **32,** 117-125

Kataoka, T., Yoshida, H., 1981, Intra-particle Mass Transfer in Weak Acid Ion-Exchanger. Can. J. Chem. Eng., **59**, 475-482

Kataoka, T., Yoshida, H., Sanada, H., 1974, Estimation of the resin phase diffusivity in isotopic ion exchange, Chem. Eng. Japan, **7**, (2) 105-109

Kataoka, T., Yoshida, H., Yamada, T., 1973, Liquid-Phase Mass Transfer in Ion Exchange Based on the Hydraulic Radius Model. J. Chem. Eng. Jpn., **2**, 172.

Kressman, T., Kitchener, J., 1949, Cation exchange with a synthetic phenol-sulfonate resin V. Kinetics. Discuss. Faraday Soc., **7,** 90.

Lee, G., Foutch, G., L., Arunachalam, A., 1997, An evaluation of mass-transfer coefficients for new and used ion-exchange resins. Reactive Polymers **35,** 55 -73

Li, Y., H., Gregory, S., 1974, Diffusion of ions in sea water an in the deep-sea sediments, Geochim. et Cosmochim. Acta **38,** 703-714

Melis, S., Markos, J. Cao, G., Morbidelli, M., 1996, Separation between Amino Acids and Inorganic Ions through Ion Exchange De-velopment of a Lumped Model. *Ind. Eng. Chem. Res*., **35**, 3629

Nesbitt A., 2010, Study of the Deterioration of Acid Resins in Cyclic Duty, Minerals Engineering, **23**, (6) 478-485

Nesbitt, A., Abrahams, J., 2005, Computational power and ion-exchange modelling, Computational Analysis in Hydrometallurgy 35th Annual Hydrometallurgy Meeting, Calgary, Canada.

Perry's Chemical Engineers' Handbook, R H Perry, D W Green, Seventh addition, McGraw & Hill, New York, 1997

Petruzzelli, D., Helfferich, F., G., Liberti, L., Millar, J., B., Passino, R., 1987b, Kinetics of ion Exchange with Intra-particle Rate Control; Models Accounting for Interactions in the Solid Phase **7**, 1 – 13

Petruzzelli. D., Liberti. L., Passino. R., Helfferich. Hwang. Y., 1987a, Chloride/sulphate exchange kinetics: solution for combined film and particle diffusion control, Reactive polymers, **5**, 219-226

Reichenberg, D., J., 1953. Properties of Ion-Exchange Resins in Relation to Their Structure. III Kinetics of Exchange, *J. Amer. Chem. Soc.*, **75**, 589

Rodriquez, J., F., de Lucas, A., Leal, J. R., Valverda, J., L., 2002, Determination of Intra-particle Diffusivities of Na^+/K^+ in water and water/Alcohol Mixed Solvents on a Strong Acid Cation Exchanger, Ind. Eng. Chem. Res., **41,** 3019-3027

Rodriquez, J., F., Valverde, J., J., Rodriques, A., E., 1998, Measurements of Effective Self-diffusion Coefficients in a Gel-Type Cation Exchanger by the Zero-Length-Column Method, Ind. Eng. Chem. Res. **37**, 2020-2028.

Streat M., 1984, Kinetics of slow diffusion species in ion exchangers, Reactive polymers **2**, 79 – 91

Turner, J. C. R., Church, M. R., Johnson, A. S. W., Snowdon, C. B., 1966. An experimental verification of the Nernst-Plank model for diffusion in an ion-exchange resin *Chem. Eng. Sci.*, **21,** 317

Valverde, J., L., De Lucas, A., Carmona, M., Gonzalez, M., Rodriquez, F., 2004, A generalized model for the measurement of effective diffusion coefficients of hetero-valent ions in ion exchangers by the zero-length column method, Chem. Eng. Sci. **59,** 71-79

Valverde, J., L., De Lucas, A., Carmona, M., Gonzalez, M., Rodriquez, F., 2005, Model for the determination of diffusion coefficients of hetero-valent ions in macroporous ion exchange resins by the zero-length column method. 60, 5836-5844

Wilke, C., R., Chang, P., 1955, Correlation of diffusion coefficients in dilute solutions, University of California, Berkeley, California.

Yahorava, V., Scheepers, J., Kotze, M., Auerswald., 2009, Impact of Silica on Hydrometallurgical properties of RIP Grad Resins for Uranium Recovery, Mintek 75th Anniversary Conference.

Yoshida, H., Kataoka, T., 1987, Intra-particle ion-exchange mass transfer in a ternary system., Ind. Eng. Chem. Res., **26,** 1179-1184

ANNEXURE I NERNST-PLANK EQUATION

Incorporation of Nernst-Plank equation into the diffusive term of Fick's law for the purposes of solving the equation by finite element method

There are two sections the first deals with binary-ion systems and the second with multi-ion systems.

Binary-ion systems

The theory of coupled Diffusivity was developed in the late 1950's and normally begins by stating the Nernst-Plank equation which takes into account all the forces that an ion might experience i.e. diffusion forces (Fick's law) and electrostatic forces due to charges. When ignoring the electrostatic forces and disparities in ion activity, the system reverts to Fick's law. However, in an ion exchange bead it is a gross assumption to exclude the effect of the charge cloud that can produce powerful forces which will then be exerted on the ions. The concept of superposition is assumed to be in effect where at any point a force will arise from the charge cloud that will be exerted on any particular ion present irrespective of the source or sources of the charge cloud.

To determine the function for coupled diffusivity in a binary ion system, the starting point will be Equ.AI-1 & AI-2 that are the flux equations for the adsorbing and desorbing ions respectively.

$$J_i = J_{diff.i} + J_{el.i} = -D_i\left(\nabla\overline{C_i} + z_A\overline{C_i}\frac{F}{RT}\nabla\varphi\right) \quad \text{AI-1}$$

$$J_D = J_{diff.D} + J_{el.D} = -D_D\left(\nabla\overline{C_D} + z_D\overline{C_D}\frac{F}{RT}\nabla\varphi\right) \quad \text{AI-2}$$

Equ.AI-3 and Equ.AI-4 are the standard assumptions for flux inside a resin bead. Equ.AI-3 exists because of the finite number of active sites on the resin bead and Equ.AI-4 is the no current condition assumption.

$$z_i\overline{C_i} + z_D\overline{C_D} = -w\overline{C_T} \quad \text{AI-3}$$

$$z_iJ_i + z_DJ_D = 0 \quad \text{AI-4}$$

Where

$\overline{C_{i,D}}$	Concentration of components ***i*** and ***D*** respectively (*mo/L*)
$\overline{C_T}$	Total No. of equivalents on resin medium (*equiv./L*)
D_i, D_D	Diffusivity specific to ***i*** and ***D*** respectively (m^2/s)
F	Faradays constant (96 485 *C/mol*)
J_i, J_D	Flux of ions ***i*** and ***D*** respectively ($mol/dm^2.s$)
$J_{diff,i}, J_{diff,D}$	Flux due to ion diffusion for species ***i*** and ***D*** respectively ($mol/dm^2.s$)
$J_{el,i,}J_{el,D}$	Flux due to elec. charge for species ***i*** and ***D*** respectively ($mol/dm^2.s$)
R	Ideal gas constant 8.314 (*J/mol.K*)
T	Temperature (*K*)
w	Sign (±) of the immovable charges (*dimensionless*)
z_i, z_D	Valence of ions ***i*** and ***D*** respectively (*dimensionless*)
φ	Charge cloud electrical potential in the vicinity of the ion (*J/C*)

As the common term in both equations is the charge cloud and super position is assumed, it is made the subject and substituted giving Equ.AI-5.

$$\frac{\frac{\boldsymbol{J}_{\boldsymbol{D}}}{-\boldsymbol{D}_{\boldsymbol{D}}}-\nabla\overline{\boldsymbol{C}_{\boldsymbol{D}}}}{\boldsymbol{z}_{\boldsymbol{D}}\overline{\boldsymbol{C}_{\boldsymbol{D}}}\frac{\boldsymbol{F}}{\mathrm{R}\boldsymbol{T}}}=\nabla\boldsymbol{\varphi}$$

Substituting

$$\boldsymbol{J}_{\boldsymbol{i}}=-\boldsymbol{D}_{\boldsymbol{i}}\left[\frac{\boldsymbol{z}_{\boldsymbol{D}}\nabla\overline{\boldsymbol{C}_{\boldsymbol{i}}}\,\overline{\boldsymbol{C}_{\boldsymbol{D}}}+\boldsymbol{z}_{\boldsymbol{i}}\overline{\boldsymbol{C}_{\boldsymbol{i}}}\left(\frac{\boldsymbol{J}_{\boldsymbol{D}}}{-\boldsymbol{D}_{\boldsymbol{D}}}-\nabla\overline{\boldsymbol{C}_{\boldsymbol{D}}}\right)}{\boldsymbol{z}_{\boldsymbol{D}}\overline{\boldsymbol{C}_{\boldsymbol{D}}}}\right] \qquad \text{AI-5}$$

Incorporating the no current condition Equ.AI-4 gives Equ.AI-6;

$$\boldsymbol{J}_{\boldsymbol{D}}=\frac{-\boldsymbol{z}_{\boldsymbol{i}}\boldsymbol{J}_{\boldsymbol{i}}}{\boldsymbol{z}_{\boldsymbol{D}}}$$

$$\boldsymbol{J}_{\boldsymbol{i}}=-\boldsymbol{D}_{\boldsymbol{i}}\left[\frac{\boldsymbol{z}_{\boldsymbol{D}}\nabla\overline{\boldsymbol{C}_{\boldsymbol{i}}}\,\overline{\boldsymbol{C}_{\boldsymbol{D}}}+\boldsymbol{z}_{\boldsymbol{i}}\overline{\boldsymbol{C}_{\boldsymbol{i}}}\left(\frac{\boldsymbol{J}_{\boldsymbol{i}}\boldsymbol{z}_{\boldsymbol{i}}}{\boldsymbol{D}_{\boldsymbol{D}}\boldsymbol{z}_{\boldsymbol{D}}}-\nabla\overline{\boldsymbol{C}_{\boldsymbol{D}}}\right)}{\boldsymbol{z}_{\boldsymbol{D}}\overline{\boldsymbol{C}_{\boldsymbol{D}}}}\right]$$

$$\boldsymbol{J}_{\boldsymbol{i}}=-\boldsymbol{D}_{\boldsymbol{i}}\left[\frac{\boldsymbol{z}_{\boldsymbol{D}}\nabla\overline{\boldsymbol{C}_{\boldsymbol{i}}}\,\overline{\boldsymbol{C}_{\boldsymbol{D}}}+\frac{\boldsymbol{J}_{\boldsymbol{i}}\boldsymbol{z}_{\boldsymbol{i}}^{2}\overline{\boldsymbol{C}_{\boldsymbol{i}}}}{\boldsymbol{D}_{\boldsymbol{D}}\boldsymbol{z}_{\boldsymbol{D}}}-\boldsymbol{z}_{\boldsymbol{i}}\overline{\boldsymbol{C}_{\boldsymbol{i}}}\nabla\overline{\boldsymbol{C}_{\boldsymbol{D}}}}{\boldsymbol{z}_{\boldsymbol{D}}\overline{\boldsymbol{C}_{\boldsymbol{D}}}}\right] \qquad \text{AI-6}$$

Moving the denominator out to recombine the terms;

$$J_i z_D \overline{C_D} = -D_i \left[\frac{D_D z_D^2 \nabla \overline{C_i}\,\overline{C_D} + J_i z_i^2 \overline{C_i} - z_i z_D D_D \overline{C_i} \nabla \overline{C_D}}{D_D z_D} \right]$$

And making J_i the subject;

$$\frac{J_i z_D \overline{C_D}}{1} + \frac{J_i D_i z_i^2 \overline{C_i}}{D_D z_D} = \frac{D_i z_i z_D D_D \overline{C_i} \nabla \overline{C_D}}{D_D z_D} - \frac{D_i z_D^2 B \nabla \overline{C_i}\,\overline{C_D}}{D_D z_D}$$

$$J_i \frac{\left(D_D z_D^2 \overline{C_D} + D_i z_i^2 \overline{C_i}\right)}{D_D z_D} = \frac{D_i z_i z_D D_D \overline{C_i} \nabla \overline{C_D} - D_i z_D^2 D_D \nabla \overline{C_i}\,\overline{C_D}}{D_D z_d}$$

$$J_i = \frac{D_i z_i z_D D_D \overline{C_i} \nabla \overline{C_D} - D_i z_D^2 D_D \nabla \overline{C_i}\,\overline{C_D}}{D_D z_D} \frac{D_D z_D}{D_D z_D^2 \overline{C_D} + D_i z_i^2 \overline{C_i}}$$

$$J_i = \frac{D_i z_i z_D D_D \overline{C_i} \nabla \overline{C_D} - D_i z_D^2 D_D \nabla \overline{C_i}\,\overline{C_D}}{D_D z_D^2 \overline{C_D} + D_i z_i^2 \overline{C_i}}$$

Finally giving us Equ.AI-7;

$$J_i = \frac{D_i D_D \left(z_i z_D \overline{C_i} \nabla \overline{C_D} - z_D^2 \overline{C_D} \nabla \overline{C_i}\right)}{D_i z_i^2 \overline{C_i} + D_D z_D^2 \overline{C_D}} \qquad \text{AI-7}$$

This can also be split into two terms effectively separating the two Del operators for the desorbing and adsorbing ions, Equ.AI-8.

$$J_i = \frac{D_i D_D z_i z_D \overline{C_i}}{D_i z_i^2 \overline{C_i} + D_D z_D^2 \overline{C_D}} \nabla \overline{C_D} - \frac{D_i D_D z_D^2 \overline{C_D}}{D_i z_i^2 \overline{C_i} + D_D z_D^2 \overline{C_D}} \nabla \overline{C_i} \qquad \text{AI-8}$$

Equ.AI-8 now present two terms the first containing the del operator of the desorbing ion and the second the del operator of the adsorbing ion. As Equ.AI-3 links the concentrations and

hence the rate of change of concentrations of the desorbing and adsorbing ion we can use this to determine the relationship between them i.e. $\nabla\overline{C_i} = f(\nabla\overline{C_D})$.

From Equ.AI-3, which accounts for the finite number of charges, it's possible to show the del operator in long notation of $\overline{C_i}$ to $\overline{C_D}$. Finding the grad of both $\nabla\overline{C_D}, \nabla\overline{C_i}$ and finding the ratio of one to the other by division;

$$\nabla\overline{C_i} = \frac{\partial\overline{C_i}}{\partial x} + \frac{\partial\overline{C_i}}{\partial y} + \frac{\partial\overline{C_i}}{\partial z} = \frac{\partial\left(\frac{-w\overline{C_T}}{z_i} - \frac{z_D}{z_i}\overline{C_D}\right)}{\partial x} + \frac{\partial\left(\frac{-w\overline{C_T}}{z_i} - \frac{z_D}{z_i}\overline{C_D}\right)}{\partial y} + \frac{\partial\left(\frac{-w\overline{C_T}}{z_i} - \frac{z_D}{z_i}\overline{C_D}\right)}{\partial z}$$

$$\nabla\overline{C_D} = \frac{\partial\overline{C_D}}{\partial x} + \frac{\partial\overline{C_D}}{\partial y} + \frac{\partial\overline{C_D}}{\partial z}$$

$$\frac{\nabla\overline{C_D}}{\nabla\overline{C_i}} = \frac{\frac{\partial\overline{C_D}}{\partial x} + \frac{\partial\overline{C_D}}{\partial y} + \frac{\partial\overline{C_D}}{\partial z}}{\frac{\partial\left(\frac{-w\overline{C_T}}{z_i} - \frac{z_D}{z_i}\overline{C_D}\right)}{\partial x} + \frac{\partial\left(\frac{-w\overline{C_T}}{z_i} - \frac{z_D}{z_i}\overline{C_D}\right)}{\partial y} + \frac{\partial\left(\frac{-w\overline{C_T}}{z_i} - \frac{z_D}{z_i}\overline{C_D}\right)}{\partial z}}$$

Simplifying

$$\frac{\nabla\overline{C_D}}{\nabla\overline{C_i}} = \frac{\frac{\partial y\partial z\partial\overline{C_D} + \partial x\partial z\overline{C_D} + \partial x\partial y\overline{C_D}}{\partial x\partial y\partial z}}{\frac{\partial y\partial z\partial\left(\frac{-w\overline{C_T}}{z_i} - \frac{z_D}{z_i}\overline{C_D}\right) + \partial x\partial z\partial\left(\frac{-w\overline{C_T}}{z_i} - \frac{z_D}{z_i}\overline{C_D}\right) + \partial x\partial y\partial\left(\frac{-w\overline{C_T}}{z_i} - \frac{z_D}{z_i}\overline{C_D}\right)}{\partial x\partial y\partial z}}$$

Simplifying

$$\frac{\nabla\overline{C_D}}{\nabla\overline{C_i}} = \frac{\partial y\partial z\partial\overline{C_D} + \partial x\partial z\overline{C_D} + \partial x\partial y\overline{C_D}}{\partial y\partial z\partial\left(\frac{-w\overline{C_T}}{z_i} - \frac{z_D}{z_i}\overline{C_D}\right) + \partial x\partial z\partial\left(\frac{-w\overline{C_T}}{z_i} - \frac{z_D}{z_i}\overline{C_D}\right) + \partial x\partial y\partial\left(\frac{-w\overline{C_T}}{z_i} - \frac{z_D}{z_i}\overline{C_D}\right)}$$

Removing common factors and dividing throughout

$$\frac{\nabla\overline{C_D}}{\nabla\overline{C_i}} = \frac{\partial\overline{C_D}\left(\partial y\partial z + \partial x\partial z + \partial x\partial y\right)}{\partial\left(\frac{-w\overline{C_T}}{z_i} - \frac{z_D}{z_i}\overline{C_D}\right)\left(\partial y\partial z + \partial x\partial z + \partial x\partial y\right)} = \frac{\partial C_D}{\partial\left(\frac{-w\overline{C_T}}{z_i} - \frac{z_D}{z_i}\overline{C_D}\right)}$$

Fortunately inside our resin bead the assumption is that flux will only be along the radial dimension. Therefore with all ***dr*** cancelling the following can be concluded.

$$\frac{\nabla\overline{C_D}}{\nabla\overline{C_i}} = \frac{d\overline{C_D}}{dr}\frac{dr}{d\overline{C_i}} = \frac{d\overline{C_D}}{d\overline{C_i}} = \frac{d\overline{C_D}}{d\left(\frac{-w\overline{C_T}}{z_i} - \frac{z_D}{z_i}\overline{C_D}\right)}$$

Determining $d\overline{C_i}/d\overline{C_D}$ from Equ.AI-3 gives

$$\frac{\nabla\overline{C_i}}{\nabla\overline{C_D}} = \frac{d\overline{C_i}}{d\overline{C_D}} = -\frac{z_D}{z_i}$$

Making z_D the subject

$$z_D = -\frac{z_i\nabla\overline{C_i}}{\nabla\overline{C_D}}$$

Substituting into the EquAI-8 achieves the following

$$J_i = -\frac{D_i D_D z_i \overline{C_i}}{D_i z_i^2 \overline{C_i} + D_D z_D^2 \overline{C_D}} \frac{z_i \nabla \overline{C_i}}{\nabla \overline{C_D}} \nabla \overline{C_D} - \frac{D_i D_D z_D^2 \overline{C_D}}{D_i z_i^2 \overline{C_i} + D_D z_D^2 \overline{C_D}} \nabla \overline{C_i}$$

Simplifying

$$J_i = -\frac{D_i D_D z_i^2 \overline{C_i}}{D_i z_i^2 \overline{C_i} + D_D z_D^2 \overline{C_D}} \nabla \overline{C_i} - \frac{D_i D_D z_D^2 \overline{C_D}}{D_i z_i^2 \overline{C_i} + D_D z_D^2 \overline{C_D}} \nabla \overline{C_i}$$

Finally, this gives us the equation that resembles Fick's law but the concentration term is now for two ions in the same system incorporating flux due to diffusion and electrical charge.

$$J_i = -\left[\frac{D_i D_D \left(z_i^2 \overline{C_i} + z_D^2 \overline{C_D} \right)}{D_i z_i^2 \overline{C_i} + D_D z_D^2 \overline{C_D}} \right] \nabla \overline{C_i} \qquad \text{AI-9}$$

The combined diffusivity can be expressed as follows

$$D_{app} = \frac{D_i D_D \left(z_i^2 \overline{C_i} + z_D^2 \overline{C_D} \right)}{D_i z_i^2 \overline{C_i} + D_D z_D^2 \overline{C_D}}$$

The following form of the radial flux equation will have to be used as D_{app} is not a constant

$$\frac{\partial \overline{C_i}}{\partial t} = \frac{1}{r^2} \frac{\partial}{\partial r} \left(r^2 D_{app} \frac{\partial \overline{C_i}}{\partial r} \right)$$

Finally, giving the Equ.AI-10 that governs the radial flux of both the adsorbing and desorbing ions simultaneously.

$$\frac{\partial \overline{C_i}}{\partial t} = \frac{1}{r^2}\frac{\partial}{\partial r}\left(r^2 \left[\frac{D_i D_D \left(z_i^2 \overline{C_i} + z_D^2 \overline{C_D} \right)}{D_i z_i^2 \overline{C_i} + D_D z_D^2 \overline{C_D}} \right] \frac{\partial \overline{C_i}}{\partial r} \right) \qquad \text{AI-10}$$

Multi-ion systems

In some systems there are tertiary, quaternary and multi- species of ions all of which can be said to interact. For the purposes of clarity and continuity, the following is a derivation for a multi ion system that describes how the mass transport equations for such systems can be developed from the Nernst Plank theory (Yoshida & Kataoka, 1987). Although papers that refer to this model normally only present the final equation the derivation could not be found anywhere. Assuming constant active site density throughout the resin, electro neutrality, Equ.AI-11 and the no current condition, Equ.AI-12 gives the basic Nernst plank, Equ.AI-1, holds true for any ion flux and combining it with Equ.AI-12 gives Equ.AI-13.

$$z_A \overline{C_A} + z_B \overline{C_B} + z_C \overline{C_C} = \overline{C_T} \qquad \text{AI-11}$$

$$z_A J_A + z_B J_B + z_C J_c = 0 \qquad \text{AI-12}$$

$$0 = -D_A z_A \left[\frac{\partial \overline{C_A}}{\partial r} + \frac{z_A \overline{C_A} F}{RT} \frac{\partial \varphi}{\partial r} \right] - D_B z_B \left[\frac{\partial \overline{C_B}}{\partial r} + \frac{z_B \overline{C_B} F}{RT} \frac{\partial \varphi}{\partial r} \right] - D_C z_C \left[\frac{\partial \overline{C_C}}{\partial r} + \frac{z_C \overline{C_C} F}{RT} \frac{\partial \varphi}{\partial r} \right] \qquad \text{AI-13}$$

where

z_A, z_B, z_C Are the valences of the A, B, and C ions respectively (*dimensionless*)

$\overline{C_A}, \overline{C_B}, \overline{C_C}$ Are the concentrations of species A, B and C respectively (*mol/L*)

J_A, J_B, J_C Are the fluxes of species A, B, C respectively (*mol/dm^2.s*)

Making the electric potential differential the subject

$$0 = -D_A z_A \frac{\partial \overline{C_A}}{\partial r} - D_A z_A \frac{z_A \overline{C_A} F}{RT} \frac{\partial \varphi}{\partial r} - D_B z_B \frac{\partial \overline{C_B}}{\partial r} - D_B z_B \frac{z_B \overline{C_B} F}{RT} \frac{\partial \varphi}{\partial r} - D_C z_C \frac{\partial \overline{C_C}}{\partial r} - D_C z_C \frac{z_C \overline{C_C} F}{RT} \frac{\partial \varphi}{\partial r}$$

$$D_A z_A \frac{\partial \overline{C_A}}{\partial r} + D_B z_B \frac{\partial \overline{C_B}}{\partial r} + D_C z_C \frac{\partial \overline{C_C}}{\partial r} = -D_A z_A \frac{z_A \overline{C_A} F}{RT} \frac{\partial \varphi}{\partial r} - D_B z_B \frac{z_B \overline{C_B} F}{RT} \frac{\partial \varphi}{\partial r} - D_C z_C \frac{z_C \overline{C_C} F}{RT} \frac{\partial \varphi}{\partial r}$$

$$\left(D_A z_A \frac{\partial \overline{C_A}}{\partial r} + D_B z_B \frac{\partial \overline{C_B}}{\partial r} + D_C z_C \frac{\partial \overline{C_C}}{\partial r} \right) \frac{RT}{F} = -D_A z_A z_A \overline{C_A} \frac{\partial \varphi}{\partial r} - D_B z_B z_B \overline{C_B} \frac{\partial \varphi}{\partial r} - D_C z_C z_C \overline{C_C} \frac{\partial \varphi}{\partial r}$$

$$\left(D_A z_A \frac{\partial \overline{C_A}}{\partial r} + D_B z_B \frac{\partial \overline{C_B}}{\partial r} + D_C z_C \frac{\partial \overline{C_C}}{\partial r} \right) \frac{RT}{F} = \frac{\partial \varphi}{\partial r} \left(- D_A z_A^2 \overline{C_A} - D_B z_B^2 \overline{C_B} - D_C z_C^2 \overline{C_C} \right)$$

Simplifying gives Equ.AI-14 that neatly combines all three individual Nernst-Plank equations for each of the three species.

$$\frac{\left(- D_A z_A \frac{\partial \overline{C_A}}{\partial r} - D_B z_B \frac{\partial \overline{C_B}}{\partial r} - D_C z_C \frac{\partial \overline{C_C}}{\partial r} \right)}{D_A z_A^2 \overline{C_A} + D_B z_B^2 \overline{C_B} + D_C z_C^2 \overline{C_C}} \frac{RT}{F} = \frac{\partial \varphi}{\partial r} \qquad \text{AI-14}$$

The differential of the active site concentration (Equ.AI-15), which effectively equals zero, is added to the numerator of the first fraction on the left. This is assuming that active site density in the resin bead is constant throughout and therefore does not change with radial distance.

$$D_B \frac{\partial C_T}{\partial r} = D_B \frac{\partial}{\partial r} \left(z_A \overline{C_A} + z_B \overline{C_B} + z_C \overline{C_C} \right) = 0 \qquad \text{AI-15}$$

In this case the diffusivity of B has been chosen and thereby makes ion B the reference ion.

$$\frac{\left[D_B \frac{\partial}{\partial r}\left(z_A \overline{C_A} + z_B \overline{C_B} + z_C \overline{C_C}\right)\right] - D_A z_A \frac{\partial \overline{C_A}}{\partial r} - D_B z_B \frac{\partial \overline{C_B}}{\partial r} - D_C z_C \frac{\partial \overline{C_C}}{\partial r}}{D_A z_A^2 \overline{C_A} + D_B z_B^2 \overline{C_B} + D_C z_C^2 \overline{C_C}} \frac{RT}{F} = \frac{\partial \varphi}{\partial r}$$

Simplifying

$$\frac{D_B z_A \frac{\partial \overline{C_A}}{\partial r} + D_B z_B \frac{\partial \overline{C_B}}{\partial r} + D_B z_C \frac{\partial \overline{C_C}}{\partial r} - D_A z_A \frac{\partial \overline{C_A}}{\partial r} - D_B z_B \frac{\partial \overline{C_B}}{\partial r} - D_C z_C \frac{\partial \overline{C_C}}{\partial r}}{D_A z_A^2 \overline{C_A} + D_B z_B^2 \overline{C_B} + D_C z_C^2 \overline{C_C}} \frac{RT}{F} = \frac{\partial \varphi}{\partial r}$$

$$\frac{\left(D_B - D_A\right) z_A \frac{\partial \overline{C_A}}{\partial r} + \left(D_B - D_C\right) z_C \frac{\partial \overline{C_C}}{\partial r}}{D_A z_A^2 \overline{C_A} + D_B z_B^2 \overline{C_B} + D_C z_C^2 \overline{C_C}} \frac{RT}{F} = \frac{\partial \varphi}{\partial r}$$

This gives the equation for charge intensity change with radial distance as a function of ion concentration and specific diffusivities, which can then be substituted into individual Nernst-Plank equations for the various ions. For ion A it will be Equ.AI-16.

$$J_A = -D_A \left[\frac{\partial \overline{C_A}}{\partial r} + \frac{z_A \overline{C_A} F}{RT} \frac{\left(D_B - D_A\right) z_A \frac{\partial \overline{C_A}}{\partial r} + \left(D_B - D_C\right) z_C \frac{\partial \overline{C_C}}{\partial r}}{D_A z_A^2 \overline{C_A} + D_B z_B^2 \overline{C_B} + D_C z_C^2 \overline{C_C}} \frac{RT}{F} \right] =$$

$$- D_A \left[\frac{\partial \overline{C_A}}{\partial r} + \frac{\left(D_B - D_A\right) z_A \frac{\partial \overline{C_A}}{\partial r} z_A \overline{C_A} + \left(D_B - D_C\right) z_C \frac{\partial \overline{C_C}}{\partial r} z_A \overline{C_A}}{D_A z_A^2 \overline{C_A} + D_B z_B^2 \overline{C_B} + D_C z_C^2 \overline{C_C}} \right] \quad \text{AI-16}$$

For the purposes of simplifying into a series the ineffectual term ($D_B - D_B$) which is in effect present is added.

$$J_A = -D_A \left[\frac{\partial \overline{C_A}}{\partial r} + \frac{(D_B - D_A) z_A \frac{\partial \overline{C_A}}{\partial r} z_A \overline{C_A} + \left((D_B - D_B) z_B \frac{\partial \overline{C_B}}{\partial r} z_A \overline{C_A} \right) + (D_B - D_C) z_C \frac{\partial \overline{C_C}}{\partial r} z_A \overline{C_A}}{D_A z_A^2 \overline{C_A} + D_B z_B^2 \overline{C_B} + D_C z_C^2 \overline{C_C}} \right]$$

Divide the terms into individual fractions and take out the common differential through by the Diffusivity of D_A and reduce the denominator of the right fraction to the summation that it is.

$$D_A z_A^2 \overline{C_A} + D_B z_B^2 \overline{C_B} + D_C z_C^2 \overline{C_C} = \sum_{i=A}^{C} D_i z_i^2 \overline{C_i}$$

Dividing into different factors

$$J_A = -D_A \left[1 + \frac{(D_B - D_A) z_A z_A \overline{C_A}}{\sum_{x=A}^{C} D_i z_i^2 \overline{C_x}} + \frac{(D_B - D_B) z_B z_A \overline{C_A}}{\sum_{x=A}^{C} D_i z_i^2 \overline{C_x}} + \frac{(D_B - D_C) z_C z_A \overline{C_A}}{\sum_{x=A}^{C} D_i z_i^2 \overline{C_x}} \right] \frac{\partial \overline{C_A}}{\partial r}$$

Multiply all terms by z_A

$$J_A = -D_A \frac{1}{z_A} \left[z_A + \frac{(D_B - D_A) z_A z_A z_A \overline{C_A}}{\sum_{X=A}^{C} D_i z_i^2 \overline{C_x}} + \frac{(D_B - D_B) z_B z_A z_A \overline{C_A}}{\sum_{x=A}^{C} D_i z_i^2 \overline{C_x}} + \frac{(D_B - D_C) z_C z_A z_A \overline{C_A}}{\sum_{x=A}^{C} D_i z_i^2 \overline{C_x}} \right] \frac{\partial \overline{C_A}}{\partial r}$$

Grouping the first two terms in brackets removing z_A, z_B, z_C etc..

$$J_A = -D_A \frac{1}{z_A}\left[z_A\left(1+\frac{(D_B - D_A)z_A z_A \overline{C_A}}{\sum_{x=A}^{C} D_i z_i^2 \overline{C_x}} \right) + z_B \frac{(D_B - D_B)z_A z_A \overline{C_A}}{\sum_{x=A}^{C} D_i z_i^2 \overline{C_x}} + z_C \frac{(D_B - D_C)z_A z_A \overline{C_A}}{\sum_{x=A}^{C} D_i z_i^2 \overline{C_x}} \right] \frac{\partial \overline{C_A}}{\partial r}$$

Finally, changing the signs around in the curved brackets

$$J_A = -D_A \frac{1}{z_A}\left[z_A\left(1-\frac{(D_A - D_B)z_A^2 \overline{C_A}}{\sum_{x=A}^{C} D_i z_i^2 \overline{C_x}} \right) - z_B \frac{(D_B - D_B)z_A^2 \overline{C_A}}{\sum_{x=A}^{C} D_i z_i^2 \overline{C_x}} - z_C \frac{(D_C - D_B)z_A^2 \overline{C_A}}{\sum_{x=A}^{C} D_i z_i^2 \overline{C_x}} \right] \frac{\partial \overline{C_A}}{\partial r}$$

Multiplying the D_A through all the brackets gives Equ.AI-17.

Finally presenting a form of Fick's law that incorporates mass flux due to electrical potential for multiple ions.

$$J_A = -\frac{1}{z_A}\left[z_A\left(D_A - \frac{D_A(D_A - D_B)z_A^2 \overline{C_A}}{\sum_{x=A}^{C} D_i z_i^2 \overline{C_x}} \right) - z_B \frac{D_A(D_B - D_B)z_A^2 \overline{C_A}}{\sum_{x=A}^{C} D_i z_i^2 \overline{C_x}} - z_C \frac{D_A(D_C - D_B)z_A^2 \overline{C_A}}{\sum_{x=A}^{C} D_i z_i^2 \overline{C_x}} \right] \frac{\partial \overline{C_A}}{\partial r} \qquad \text{AI-17}$$

ANNEXURE II FINITE ELEMENT EQUATIONS

Starting with the equation of state this annexure then presents Fick's first and second law and then proceeds to present these in a finite state on radial coordinates. Initially developing an explicit and thereafter presenting the implicit approach as used in this thesis.

The general finite equation for each shell is determined which is then followed by special equations for the surface and for the inner most shell both of which need to incorporate boundary conditions.

Equation of state

Generally, in mass transport systems there are four terms that need to be brought into any dynamic mass balance at any point in Cartesian space; accumulation, convection, conduction, generation and in the case of a fluid element the following links these terms for the purpose of achieving a balance.

Accumulation of ions in fluid element	+	Convection flow of ions out of fluid element	=	Increase of ions due to diffusion into fluid element	+	Appearance of ions due to Chemical Generation inside fluid element

Inside a resin bead our element is static (i.e. no bulk flow) and ions are neither destroyed nor generated which immediately allows for the removal of the convection and chemical generation terms. In mathematical expression the remaining terms give us our mass balance or conservation equation and can be presented as Equ.AII-1;

$$\frac{\partial}{\partial t}\overline{C}_i = \nabla\left(-D_i \nabla\overline{C}_i\right) \qquad \text{AII-1}$$

Where

$\overline{C}_i$ Point measurement of the property (*mol/L*)

D_i Diffusivity term (m^2/s)

t Time (*s*)

This neatly equates the accumulation of ions with the diffusivity of ions and resembles Fick's second law.

For the purpose of developing the finite element equations, Fick's first law gives the point relationship between the gradient of a concentration and the rate of flux.

$$J_i = -D_i \nabla \overline{C_i} \qquad \text{AII-2}$$

Where

J_i Flux of $\overline{C_i}$ ($mol/m^2.s$)

In long notation, Cartesian coordinates

$$J_i = -D\left(\frac{\partial \overline{C_i}}{\partial x}\hat{i} + \frac{\partial \overline{C_i}}{\partial y}\hat{j} + \frac{\partial \overline{C_i}}{\partial z}\hat{k} \right) \qquad \text{AII-3}$$

Where

x, y, z	Constitute the three dimensions
$\hat{i}, \hat{j}, \hat{k}$	Represent the vector length in the associated dimension

The geometry of a resin bead and hence the type of system we have, makes the use of spherical coordinates, convenient. Application of Fick's law in spherical coordinates gives us the following;

$$\boldsymbol{J_i = D_i \nabla \overline{C}_i = D\left(\frac{\partial \overline{C}_i}{\partial r}\hat{r} + \frac{1}{r}\frac{\partial \overline{C}_i}{\partial \theta}\hat{\theta} + \frac{1}{r\sin\theta}\frac{\partial \overline{C}_i}{\partial \phi}\hat{\phi} \right)} \qquad \text{AII-4}$$

Where

$\hat{r}, \hat{\theta}, \hat{\phi}$ Represent the vector lengths (spherical coordinates)

Fick's second law

In the un-steady state system, which would be applicable during any transient mass transport inside a resin bead, the diffusion term will be equal to the accumulation term which essentially gives us our conservation Equ.AII-5 that is identical to Equ.AII-1.

$$\frac{\partial \overline{C}_i}{\partial t} = \nabla\left(-D_i \nabla \overline{C}_i\right) \qquad \text{AII-5}$$

More simply put, the term on the right hand side will be the Laplacian of the concentration scalar value, assuming that the diffusivity is constant throughout. This gives us Equ.AII-6 which is the Laplacian equivalent in spherical coordinates;

$$\frac{\partial \overline{C}_i}{\partial t} = D\nabla^2 \overline{C}_i = D_i\left[\frac{1}{r^2}\frac{\partial}{\partial r}\left(r^2 \frac{\partial \overline{C}_i}{\partial r} \right) + \frac{1}{r^2 \sin\theta}\frac{\partial}{\partial \theta}\left(\sin\theta \frac{\partial \overline{C}_i}{\partial \theta} \right) + \frac{1}{r^2 \sin^2\theta}\frac{\partial^2 \overline{C}_i}{\partial \phi^2} \right]$$

AII-6

Fortunately, given the resin bead geometry, we will consider our flux to move along radially symmetrical lines only i.e. only along the $\boldsymbol{r}$ axis, allowing us to drop the two tangential curvy terms/dimensions phi $\boldsymbol{\phi}$ and theta $\boldsymbol{\theta}$ and simplifying to the following;

$$\frac{\partial \overline{\boldsymbol{C}_i}}{\partial \boldsymbol{t}} = \boldsymbol{D}_i \frac{1}{\boldsymbol{r}^2} \frac{\partial}{\partial \boldsymbol{r}} \left(\boldsymbol{r}^2 \frac{\partial \overline{\boldsymbol{C}_i}}{\partial \boldsymbol{r}} \right) \qquad \text{AII-7}$$

This can be taken one step further as the *product of two functions rule* in differentiation that can be applied to the brackets on the right leaving us with Equ.AII-8 the commonly quoted mass balance for radically diffusing systems;

$$\frac{\partial \overline{\boldsymbol{C}_i}}{\partial \boldsymbol{t}} = \boldsymbol{D}_i \left(\frac{\partial^2 \overline{\boldsymbol{C}_i}}{\partial \boldsymbol{r}^2} + \frac{2}{\boldsymbol{r}} \frac{\partial \overline{\boldsymbol{C}_i}}{\partial \boldsymbol{r}} \right) \qquad \text{AII-8}$$

It is notable that the important assumption – constant diffusivity throughout – has to be adhered to for this relationship to hold.

As prudence requires the use of the Nernst-Plank equation to determine the diffusivity which is a function of the concentration of the diffusing elements, we conclude that diffusivity may be different at different radial distances from the centre of the bead. It was therefore thought necessary to use a finite element method allowing for a variance in diffusivity that would have to be calculated separately for each element as dictated by the Nernst-Plank equation.

The finite element on radial coordinates

If we apply Fick's first law at two distinct distances from the centre of the bead at the boundaries of a shell i.e. r_{ob} and r_{ib} and apply a mass balance across the shell, in effect giving the Laplacian we achieve the following for outgoing flux;

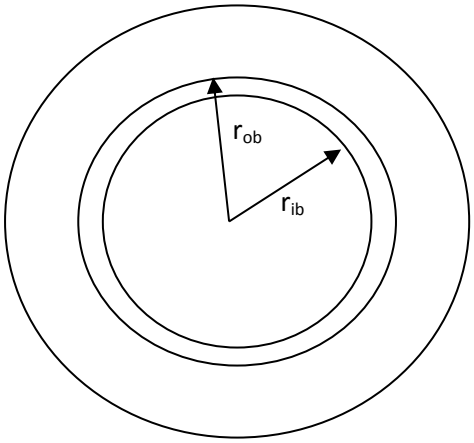

$$\textbf{\textit{Shell volume}} = \frac{4}{3}\pi\left(r_{ob}^3 - r_{ib}^3\right)$$

$$\textbf{\textit{accum. in shell}} = \frac{\partial \overline{C}_i}{\partial t} = \frac{\left(4\pi r_{ib}^2\right)D\frac{\partial \overline{C}_i}{\partial r_{ib}} - \left(4\pi r_{ob}^2\right)D\frac{\partial \overline{C}_i}{\partial r_{ob}}}{\frac{4}{3}\pi\left(r_{ob}^3 - r_{ib}^3\right)}$$

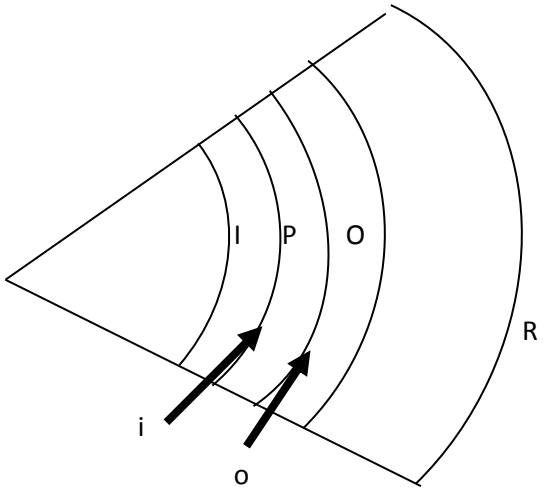

I = Inner shell

P = in Point

O = Outer shell

R = outer surface

i = inner boundary

o = outer boundary

With reference to the diagram above a mass balance can be set up across the control element shell of this sphere designated P.

$$Accumulation = flux\ in - flux\ out$$ AII-9

Using the **explicit** method of differences we begin with Fick's first law being applied along the radial line of the bead at two arbitrarily chosen, adjacent boundaries i and o.

$$J_i = D_i \frac{d\overline{C_i}}{dr} \qquad \text{AII-10}$$

Finding the difference in flux into and out of the shell by multiplying by the boundary area and dividing the difference by the volume of the element gives us accumulation in terms of a finite difference of time Δt as shown in Equ.AII-11a;

$$\left(\frac{\overline{C_{i,P}^{\,t+\Delta t}} - \overline{C_{i,P}^{\,t}}}{(t+\Delta t) - t} \right) = \frac{4\pi r_{ob}^2 D_{app,po} \dfrac{\overline{C_{i,O}^{\,t}} - \overline{C_{iP}^{\,t}}}{r_{MO} - r_{MP}} - 4\pi r_{ib}^2 D_{app,pi} \dfrac{\overline{C_{i,P}^{\,t}} - \overline{C_{i,I}^{\,t}}}{r_{MP} - r_{MI}}}{4\pi r_{ib}^2 \left(r_{ob} - r_{ib} \right)} \qquad \text{AII-11a}$$

Where

$\overline{C_{i,P}^{t+\Delta t}}$	**C**oncentration in the shell being balanced at $t + \Delta t$ *(mol/m^3)*
$\overline{C_P^t}$	**C**oncentration in the shell being balanced at t *(mol/m^3)*
$\overline{C_I^t}$	**C**oncentration in the inner shell at previous time *(mol/m^3)*
$\overline{C_O^t}$	Concentration in the outer shell at previous time *(mol/m^3)*
t	Time *(s)*
Δt	Time increment *(s)*
r_{ob}	Radial distance to outer boundary of the shell being balanced *(m)*
r_{ib}	Radial distance to inner boundary of the shell being balanced *(m)*
r_{MP}	Radial distance to middle of the shell being balanced *(m)*

r_{MO} Radial distance to middle of the outer shell *(m)*

r_{MI} Radial distance to middle of the inner shell *(m)*

$D_{app,po}$ Apparent diffusivity to inner shell from the shell being balanced *(m^2/s)*

$D_{app,pi}$ Apparent diffusivity to outer shell from the shell being balanced *(m^2/s)*

It is notable that Equ.AII-11a could become inaccurate for coarser/lower numbers of concentric shells. i.e. $4/3\pi(r_{ob}^3 - r_{ib}^3) \neq 4\pi r_{ib}^2(r_{ob} - r_{ib})$ and therefore Equ.AII-11a can be corrected to Equ.AII-11b;

$$\left(\frac{\overline{C_{i,P}^{t+\Delta t}} - \overline{C_{i,P}^{t}}}{(t+\Delta t)-t}\right) = \frac{4\pi r_{ob}^2 D_{app,po}\dfrac{\overline{C_{i,O}^{t}} - \overline{C_{i,P}^{t}}}{r_{MO} - r_{MP}} - 4\pi r_{ib}^2 D_{app,pi}\dfrac{\overline{C_{i,P}^{t}} - \overline{C_{i,I}^{t}}}{r_{MP} - r_{MI}}}{\dfrac{4}{3}\pi\left(r_{ob}^3 - r_{ib}^3\right)} \qquad \text{AII-11b}$$

However, for an infinite number of shells Equ.AII-11 is sufficient and can be used to check that we genuinely can achieve an equation for diffusive flux of mass on spherical coordinates. For all further analytical calculation Equ.AII-11a is used while Equ.AII-11b is used in all practical/computer calculations involving data.

Seeking the limits as shell No. → ∞, the volume of the shell is reduced to zero, ultimately form a point differential function. Cancelling out the constants associated with the surface area of a sphere gives Equ.AII-12;

$$\left(\frac{\overline{C_{i,p}^{t+\Delta t}} - \overline{C_{i,P}^{t}}}{\Delta t}\right) = \frac{r_{ob}^2 D_{app,po}\dfrac{\overline{C_{i,O}^{t}} - \overline{C_{i,P}^{t}}}{\Delta r} - r_{ib}^2 D_{app,pi}\dfrac{\overline{C_{i,P}^{t}} - \overline{C_{i,I}^{t}}}{\Delta r}}{r_{ib}^2 \Delta r} \qquad \text{AII-12}$$

As the volume of the shell reduces all the radiuses start to approach r thus;

$r_{ob} \approx r_{ib} \approx r_{MO} \approx r_{MI} \approx r_{MP} \rightarrow r$. Its then possible to describe the radial differences in the form of Δr, giving Equ.AII-13;

$$\left(\frac{\overline{C_{i,p}^{t+\Delta t}} - \overline{C_{i,P}^{t}}}{\Delta t} \right) = \frac{1}{r^2} \frac{r^2 D_{app,po} \frac{\overline{C_{i,O}^{t}} - \overline{C_{i,P}^{t}}}{\Delta r} - r^2 D_{app,pi} \frac{\overline{C_{i,P}^{t}} - \overline{C_{i,I}^{t}}}{\Delta r}}{\Delta r} \qquad \text{AII-13}$$

Seeking the limits i.e. $\Delta t \rightarrow 0$, and $\Delta r \rightarrow 0$, this discrete equation reverts to the correct spherical co-ordinate flux Equ.AII-14;

$$\left(\frac{d\overline{C_{i,P}^{t}}}{dt} \right) = \frac{1}{r^2} \frac{r^2 D_{app,po} \frac{d\overline{C_{i,O}}}{dr} - r^2 D_{app,pi} \frac{d\overline{C_{i,I}}}{dr}}{dr} \qquad \text{AII-14}$$

Getting the equation into the form of derivatives gives Equ.AII-15

$$\left(\frac{d\overline{C_{i,P}^{t}}}{dt} \right) = \frac{1}{r^2} \frac{\partial}{\partial r} \left[r^2 D_{app} \left(\frac{d\overline{C_{i,O}}}{dr} - \frac{d\overline{C_{i,I}}}{dr} \right) \right] \qquad \text{AII-15}$$

Finally, Equ.AII-7 results and should be held true at all radial distances from the centre of the bead proving the effectiveness of Equ.AII-11a&b as a discrete form of the Equ.AII-7.

$$\frac{\partial \overline{C_{i,P}}}{\partial t} = \frac{1}{r^2} \frac{\partial}{\partial r} \left(r^2 D_{app} \frac{d\overline{C_{i,P}}}{dr} \right) \qquad \text{AII-7}$$

Discrete equation for each shell (explicit approach)

General equation

Equ.AII-16 is the general discrete form of Equ.AII-7 derived from Equ.AII-13, providing $r_{ib} - r_{ob} = r_{mo} - r_{mp} = r_{mp} - r_{mi} = \Delta r$

$$\left(\frac{\overline{C_{i,P}^{t+\Delta t}} - \overline{C_{i,P}^{t}}}{\Delta t}\right) r_{ib}^2 \Delta r = r_{ob}^2 D_{app,po} \frac{\overline{C_{i,O}^{t}} - \overline{C_{i,P}^{t}}}{\Delta r} - r_{ib}^2 D_{app,pi} \frac{\overline{C_{i,P}^{t}} - \overline{C_{i,I}^{t}}}{\Delta r} \qquad \text{AII-16}$$

Getting Equ.AII-16 into the form of discrete differences gives Equ.AII-17;

$$\frac{\Delta r}{\Delta t}\left(\overline{C_{i,P}^{t+\Delta t}} - \overline{C_{i,P}^{t}}\right) = \frac{r_{ob}^2}{r_{ib}^2} \frac{D_{app,po}}{\Delta r}\left(\overline{C_{iO}^{t}} - \overline{C_{iP}^{t}}\right) - \frac{D_{app,pi}}{\Delta r}\left(\overline{C_{i,P}^{t}} - \overline{C_{i,I}^{t}}\right) \qquad \text{AII-17}$$

Simplifying Equ.AII-17 by dividing all along by r^2_{ib} gives Equ.AII-18;

$$r_{ib}^2 \frac{\Delta r}{\Delta t}\left(\overline{C_{i,P}^{t+\Delta t}} - \overline{C_{i,P}^{t}}\right) = r_{ob}^2 \frac{D_{app,po}}{\Delta r}\left(\overline{C_{i,O}^{t}} - \overline{C_{i,P}^{t}}\right) - r_{ib}^2 \frac{D_{app,pi}}{\Delta r}\left(\overline{C_{i,P}^{t}} - \overline{C_{i,I}^{t}}\right) \qquad \text{AII-18}$$

The ratio/factor $(r_{ob}/r_{ib})^2$ will depend on the value of Δr providing there is uniformity from shell to shell. From spherical geometry, it can be proved algebraically that the Equ.AII-19 holds true which conveniently disposes of r^2_{ob} on the right hand side and gives us a function for this factor based on a single radial distance.

$$\frac{r_{ob}^2}{r_{ib}^2} = \left(\frac{\Delta r}{r_{ib}}\right)^2 + 2\left(\frac{\Delta r}{r_{ib}}\right) + 1 = K \qquad \text{AII-19}$$

Assuming that our Δr is equal at all r, by definition the factor in Equ.AII-19 is at its highest when it is close to the centre of the sphere. This is because the ratio of inner area to outer area increases to infinity at $r \to 0$ and decays to one at $r \to \infty$. If the inner most shell chosen has a radial dimension equal to Δr, and the inner sphere, with its external surface being synonymous with r_{ib} has a radius also equal to Δr, then the factor $(r_{ob}/r_{ib})^2$ will be equal to 4 for any chosen value of Δr.

For the first shell the equation simplifies to Equ.AII-20;

$$\frac{\Delta r}{\Delta t}\left(\overline{C_{i,P}^{t+\Delta t}} - \overline{C_{i,P}^{t}}\right) = 4\frac{D_{app,po}}{\Delta r}\left(\overline{C_{i,O}^{t}} - \overline{C_{i,P}^{t}}\right) - \frac{D_{app,pi}}{\Delta r}\left(\overline{C_{i,P}^{t}} - \overline{C_{i,I}^{t}}\right) \qquad \text{AII-20}$$

The factor (Equ.AII-19) is a function of the chosen gap width and the r_{ib} value. It is fairly high when r_{ib} is low and then tails off asymptotically to 1 as we get further away from the centre of the sphere. Therefore Equ.AII-21 can be assumed applicable;

$$\frac{\Delta r}{\Delta t}\left(\overline{C_{i,P}^{t+\Delta t}} - \overline{C_{i,P}^{t}}\right) = \left[\left(\frac{\Delta r}{r_{ib}}\right)^2 + 2\left(\frac{\Delta r}{r_{ib}}\right) + 1\right]\frac{D_{app,po}}{\Delta r}\left(\overline{C_{i,O}^{t}} - \overline{C_{i,P}^{t}}\right) - \frac{D_{app,pi}}{\Delta r}\left(\overline{C_{i,P}^{t}} - \overline{C_{i,I}^{t}}\right) \qquad \text{AII-20}$$

Solving for $\overline{C_{i,P}^{t+\Delta t}}$ and reverting back to the shorter form of the factor equation gives Equ.AII-21;

$$\overline{C_{i,P}^{t+\Delta t}} = \frac{\frac{r_{ob}^2}{r_{ib}^2}\frac{D_{app,po}}{\Delta r}\overline{C_{iO}^{t}} - \frac{r_{ob}^2}{r_{ib}^2}\frac{D_{app,po}}{\Delta r}\overline{C_{i,P}^{t}} - \frac{D_{app,pi}}{\Delta r}\overline{C_{i,P}^{t}} + \frac{D_{app,pi}}{\Delta r}\overline{C_{i,I}^{t}} + \frac{\Delta r}{\Delta t}\overline{C_{i,P}^{t}}}{\frac{\Delta r}{\Delta t}} \qquad \text{AII-21}$$

Simplifying further and grouping like terms about $\overline{C_{i,P}^{t}}$ gives Equ.AII-22;

$$\overline{C_{i,P}^{t+\Delta t}} = \frac{\frac{r_{ob}^2}{r_{ib}^2}\frac{D_{app,po}}{\Delta r}\overline{C_{i,O}^{t}} + \frac{D_{app,pi}}{\Delta r}\overline{C_{i,I}^{t}} + \overline{C_{i,P}^{t}}\left(\frac{\Delta r}{\Delta t} - \frac{r_{ob}^2}{r_{ib}^2}\frac{D_{app,po}}{\Delta r} - \frac{D_{app,pi}}{\Delta r}\right)}{\frac{\Delta r}{\Delta t}} \qquad \text{AII-22}$$

Finally, further simplification gives Equ.AII-23 which is now in a form that makes it conducive to solving multiple equations of this type using a matrix operation, as each term on the right hand side is consecutively associated with consecutive shell numbers.

$$\overline{C_{i,P}^{t+\Delta t}} = \frac{D_{app,pi}\Delta t}{\Delta r^2}\overline{C_{i,I}^{t}} + \left(1 - K\frac{D_{app,po}\Delta t}{\Delta r^2} - \frac{D_{app,pi}\Delta t}{\Delta r^2}\right)\overline{C_{i,P}^{t}} + K\frac{D_{app,po}\Delta t}{\Delta r^2}\overline{C_{i,O}^{t}} \qquad \text{AII-23}$$

The explicit Finite Element method has an inherent stability fault, which is related to the ratio of Δt to Δr. We investigate this matter in the following manner.

Equ.AII-23 can be written in the manner of Equ.AII-24 where ***A, B, C*** represent constants.

$$A\overline{C_{i,P}^{t+\Delta t}} = C\overline{C_{i,I}^{t}} + \left[A - (B + C)\right]\overline{C_{i,P}^{t}} + B\overline{C_{i,O}^{t}} \qquad \text{AII-24}$$

To investigating the time increment that should be used to solve this equation, Equ.AII-25 should hold;

$$A - B - C > 0 \qquad \frac{\Delta r}{\Delta t} - \frac{r_{ob}^2}{r_{ib}^2}\frac{D_{app,po}}{\Delta r} - \frac{D_{app,pi}}{\Delta r} > 0$$

$$or$$

$$\frac{\Delta r}{\Delta t} - \left[\left(\frac{\Delta r}{r_{ib}}\right)^2 + 2\frac{\Delta r}{r_{ib}} + 1\right]\frac{D_{app,po}}{\Delta r} - \frac{D_{app,pi}}{\Delta r} > 0 \qquad \text{AII-25}$$

If the coefficient of $\overline{C_{i,P}^t}$ is not greater than zero, the time increment chosen would be too large for the physical size of the finite element. This is tantamount to the diffusion process being allowed to proceed - time wise - beyond what the mass balance constraints i.e. by choosing an insufficient number of shells.

For the inner most shell, where the coefficient of the second term will be at its highest (= 4) Equ.AII-26 should hold;

$$\frac{\Delta r}{\Delta t} - 4\frac{D_{app,po}}{\Delta r} - \frac{D_{app,pi}}{\Delta r} > 0 \qquad \text{AII-26}$$

Making Δt the subject we get Equ.AII-27 that effectively gives us the relationship between Δt and Δr and defines a required maximum value for Δr.

$$\Delta t > \frac{\Delta r^2}{4D_{app,po} + D_{app,pi}} \qquad \text{AII-27}$$

Spherical shell at the centre of the bead

The central part of any resin bead will be a sphere that requires a look at the finite element equation in terms of the boundary condition we set. Equ.AII-28 is a boundary condition for the centre of the resin bead and is a standard assumption implying no flux across the boundary that is the very centre of the resin

$$\left.\frac{\partial \overline{C_i}}{\partial r}\right|_{r=0} = 0 \qquad \text{AII-28}$$

This means that the general Equ.AII-20 can be changed to Equ.AII-29;

$$\frac{\Delta r}{\Delta t}\left(\overline{C_{i,P}^{t+\Delta t}} - \overline{C_{i,P}^{t}}\right) = \left[\left(\frac{\Delta r}{r_{ib}}\right)^2 + 2\left(\frac{\Delta r}{r_{ib}}\right) + 1\right]\frac{D_{app,po}}{\Delta r}\left(\overline{C_{i,O}^{t}} - \overline{C_{i,P}^{t}}\right) - 0 \qquad \text{AII-29}$$

The geometric factor (***K***) however incorporates r_{ib}^2 which is equal to zero making K = ∞, Equ.AII-30.

$$\left[\left(\frac{\Delta r}{0}\right)^2 + 2\frac{\Delta r}{0} + 1\right] = K = \infty + \infty + 1 \qquad \text{AII-30}$$

This makes it necessary to go back to fundamentals giving us Equ.AII-31. The term describing flux inwards is equated to zero;

$$\left(\frac{\overline{C_{i,P}^{t+\Delta t}} - \overline{C_{i,P}^{t}}}{(t+\Delta t) - t}\right) = \frac{4\pi r_{ob}^2 D_{app,po}\dfrac{\overline{C_{i,O}^{t}} - \overline{C_{i,P}^{t}}}{r_{MO} - r_{MP}}}{4\pi r_{ib}^2\left(r_{ob} - r_{ib}\right)} \qquad \text{AII-31}$$

The denominator on the right is the volume of the inner most shell, but the inner most shell is effectively a sphere and so we can change Equ.AII-31 to 32;

$$\left(\frac{\overline{C_{i,P}^{t+\Delta t}}-\overline{C_{i,P}^{t}}}{\Delta t}\right)=\frac{4\pi r_{ob}^{2}D_{app,po}\dfrac{\overline{C_{i,O}^{t}}-\overline{C_{i,P}^{t}}}{\Delta r}}{4/3\,\pi r_{ob}^{3}}=\frac{D_{app,po}\dfrac{\overline{C_{i,O}^{t}}-\overline{C_{i,P}^{t}}}{\Delta r}}{1/3\,r_{ob}} \qquad \text{AII-32}$$

Simplifying further gives Equ.AI-33;

$$\frac{3r_{ob}}{\Delta t}\overline{C_{i,P}^{t+\Delta t}}-\frac{3r_{ob}}{\Delta t}\overline{C_{i,P}^{t}}=\frac{D_{app,po}}{\Delta r}\overline{C_{i,O}^{t}}-\frac{D_{app,po}}{\Delta r}\overline{C_{i,P}^{t}} \qquad \text{AII-33}$$

Making $C_P^{t+\Delta t}$ the subject gives Equ.AII-34;

$$\overline{C_{i,P}^{t+\Delta t}}=\frac{\dfrac{3r_{ob}}{\Delta t}\overline{C_{i,P}^{t}}+\dfrac{D_{app,po}}{\Delta r}\overline{C_{i,O}^{t}}-\dfrac{D_{app,po}}{\Delta r}\overline{C_{i,P}^{t}}}{\dfrac{3r_{ob}}{\Delta t}} \qquad \text{AII-34}$$

Providing the distance from the middle of the bead to the first concentration point is equal the Δr, and getting it into the form of equation that allows for incorporation into a matrix calculation results in Equ.AII-35,

$$\overline{C_{i,P}^{t+\Delta t}}=\left(1-\frac{\Delta t D_{app,po}}{3r_{ob}\Delta r}\right)\overline{C_{i,P}^{t}}+\frac{\Delta t D_{app,po}}{3r_{ob}\Delta r}\overline{C_{i,O}^{t}} \qquad \text{AII-35}$$

Equ.AII-47 effectively gives us the discrete equation in for mass transport in the centre of the resin bead.

Outer shell of the bead

This requires some knowledge of the system in which the resin is experiencing the transient ion exchange. A changing boundary condition may exist here, depending on the circumstances. If the resin is in an infinite solution the concentration of the adsorbing ion can be considered constant and there will be no build-up of released counter ion in the solution thus a constant boundary condition can be assumed. However, if the resin is in a finite solution where the adsorbing ion is likely to reduce in concentration and the desorbing ions will likely increase in concentration, in the bulk solution, it will be necessary to take this into account as it means that the boundary condition will not be constant. The equilibrium concentration levels, towards which the system is decaying, will move during the transient process and this reality has to be included in the simulation equations.

In addition an equilibrium relationship has to be determined. For these systems it is reasonable to assume equilibrium conditions between solid and liquid phase, at the surface of the resin bead and stems from the rigid adherence to the theory of Donnan exclusion. The equilibrium relationship followed in this study was that of Mass-Action-Law which is useful as the equilibrium relationship is defined by a single constant (α). Equ.AII-36 is this function which is a explained in greater detail in the model chapter section and the difficulty with multi valence ions explained in Annexure IV. Equ.AII-37 is the form of the Mass-Action-Law we assume to be in effect during the transient process.

$$\alpha = \left[\frac{\overline{C^t_{i,(R)}}}{C^t_{D,(R)}}\right] \bullet \left[\frac{C^t_D}{C^{*,t}_i}\right] \qquad \text{AII-36}$$

where

α Equilibrium constant *(dimensionless)*

$\overline{C^t_{i,(R)}}$ Concentration of adsorption ion in resin phase at surface at time *t (mol/L)*

$\overline{C^t_{D,(R)}}$ Concentration of desorption ion in resin phase at surface at time *t (mol/L)*

$C^{*,t}_i$ Concentration of adsorption ion in solution at surface at time *t (mol/L)*

C^t_D Concentration of desorption ion in solution at surface at time *t (mol/L)*

R Radius to the external surface of the bead (*m*)

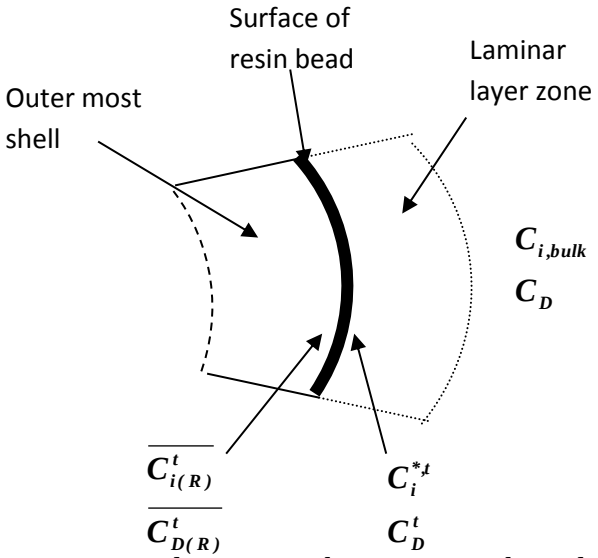

Another important consideration with respect to the solid liquid interface is the boundary layer. In effect the situation could be such that this laminar layer may be controlling, not necessarily for the entire transient process, but if for the majority of time its effect will be felt. The following diagram shows graphically the various zones and interfaces.

Our boundary condition will be a concentration in the resin phase, at the outer boundary of the outermost shell.

$$\overline{C^t_{i,(R)}} = \frac{\alpha \times \overline{C^t_{D,(R)}} \times C^{*,t}_i}{C^t_D} \qquad \text{AII-37}$$

Where C_D^t can be measured directly and $C_i^{*,t}$ can be calculated through a mass balance and $\overline{C_{i,(R)}^t}$ can be determined as the fraction of active sites that are not occupied by desorbing ions ($\overline{C_{D,(R)}^t}$).

The mass balance for the outer most shell is therefore Equ.AII-38 which incorporates the concentration term $\overline{C_{i,(R)}^t}$ at the furthest extent of the resin matrix;

$$\frac{\Delta r}{\Delta t}\left(C_{i,P}^{t+\Delta t}-C_{i,P}^{t}\right)=-\frac{D_{app,pi}}{\Delta r}\left(C_{i,P}^{t}-C_{i,I}^{t}\right)+\left[\left(\frac{\Delta r}{r_{ib}}\right)^2+2\left(\frac{\Delta r}{r_{ib}}\right)+1\right]\frac{D_{app,po}}{\Delta r/2}\left(\overline{C_{i,(R)}^t}-C_{i,P}^{t}\right) \quad \text{AII-38}$$

Grouping we achieve Equ.AII-39;

$$\overline{C_{i,P}^{t+\Delta t}}=+\overline{C_{i,I}^t}\frac{\Delta t D_{app,pi}}{\Delta r^2}+\overline{C_{i,P}^t}\left(1-K\frac{2D_{app,po}\Delta t}{\Delta r^2}-\frac{\Delta t D_{app,pi}}{\Delta r^2}\right)+K\frac{2D_{app,po}\Delta t}{\Delta r^2}\overline{C_{i,(R)}^t} \quad \text{AII-39}$$

Summary of Explicit finite element equations

The main equation;

$$\overline{C_{i,P}^{t+\Delta t}}=+\frac{D_{app,pi}\Delta t}{\Delta r^2}\overline{C_{i,I}^t}+\overline{C_{i,P}^t}\left(1-K\frac{D_{app,po}\Delta t}{\Delta r^2}-\frac{D_{app,pi}\Delta t}{\Delta r^2}\right)+K\frac{D_{app,po}\Delta t}{\Delta r^2}\overline{C_{i,O}^t} \quad \text{AII-23}$$

The boundary equation at the center of the resin bead;

$$\overline{C_{i,P}^{t+\Delta t}} = \overline{C_{i,P}^{t}} + \frac{\Delta t D_{app,po}}{3 r_{ob} \Delta r} \overline{C_{i,O}^{t}} - \frac{\Delta t D_{app,po}}{3 r_{ob} \Delta r} \overline{C_{i,P}^{t}} \qquad \text{AII-35}$$

The boundary equation at the surface of the resin bead;

$$\overline{C_{i,P}^{t+\Delta t}} = +\overline{C_{i,I}^{t}} \frac{\Delta t D_{app,pi}}{\Delta r^2} + \overline{C_{i,P}^{t}} \left(1 - K \frac{2 D_{app,po} \Delta t}{\Delta r^2} - \frac{\Delta t D_{app,pi}}{\Delta r^2} \right) + K \frac{2 D_{app,po} \Delta t}{\Delta r^2} \overline{C_{i(R)}^{t}} \qquad \text{AII-39}$$

Discrete equation for each shell (implicit approach)

Ultimately, using the implicit approach to solve multiple equations will always be more efficient. In addition to being more accurate there is less chance of instability unlike in the case of the explicit approach. The difficulty with using the implicit approach for simulating a transient for resin in a finite medium is that implicitness requires encapsulation of the continuous medium into the matrix of equations for mass balance purposes, in addition to the shells inside the resin. In this exercise it was thought pertinent to include an extra ‘shell’ positioned on the outside of the resin that represents the bulk fluid.

General equation

Based on Equ.AII-11b, Equ.AII-40 is the equivalent discrete general equation for simulating the transient, implicitly.

$$\left(\frac{\overline{C_{i,P}^{t+\Delta t}}-\overline{C_{i,P}^{t}}}{(t+\Delta t)-t}\right)=\frac{4\pi r_{ob}^{2}D_{app,po}\dfrac{\overline{C_{i,O}^{t+\Delta t}}-\overline{C_{i,P}^{t+\Delta t}}}{r_{MO}-r_{MP}}-4\pi r_{ib}^{2}D_{app,pi}\dfrac{\overline{C_{i,P}^{t+\Delta t}}-\overline{C_{i,I}^{t+\Delta t}}}{r_{MP}-r_{MI}}}{\frac{4}{3}\pi\left(r_{ob}^{3}-r_{ib}^{3}\right)} \qquad \text{AII-40}$$

In the implicit scheme the equation is based on the situation at time $t + \Delta t$ unlike in the explicit scheme where the concentration for the shell was worked out at t, i.e. the previous time frame. We make the changes and interchange all the concentrations on the right hand side of the equation, associated with diffusion term, with concentrations of the following time frame. To improve on the accuracy we determine the actual volume of the discrete element in the denominator i.e. $4/3\pi(r_{ob}^{3}-r_{ib}^{3})\neq 4\pi r_{ib}^{2}(r_{ob}-r_{ib})$.

Simplifying and putting the equation into a form for solving by matrix gives Equ.AII-41.

$$\begin{aligned}&-\frac{3r_{ib}^{2}\Delta tD_{app,pi}}{\left(r_{ob}^{3}-r_{ib}^{3}\right)(r_{MP}-r_{MI})}\overline{C_{i,I}^{t+\Delta t}}+\left(1+\frac{3r_{ob}^{2}\Delta tD_{app,po}}{\left(r_{ob}^{3}-r_{ib}^{3}\right)(r_{MO}-r_{MP})}+\frac{3r_{ib}^{2}\Delta tD_{app,pi}}{\left(r_{ob}^{3}-r_{ib}^{3}\right)(r_{MP}-r_{MI})}\right)\overline{C_{i,P}^{t+\Delta t}}\\&-\frac{3r_{ob}^{2}\Delta tD_{app,po}}{\left(r_{ob}^{3}-r_{ib}^{3}\right)(r_{MO}-r_{MP})}\overline{C_{i,O}^{t+\Delta t}}=\overline{C_{i,P}^{t}}\end{aligned} \qquad \text{AII-41}$$

This gives us the finite element equation that will be effective at any shell in the resin bead using the implicit scheme of solving the equation of state.

Spherical shell at the centre of the bead

The boundary conditions at the centre of the resin bead are as follows i.e. there is no flux across the boundary at the middle of the sphere (Equ.AII-8);

$$\left.\frac{\partial C_i}{\partial r}\right|_{r=0} = 0 \qquad \text{AII-28}$$

Given the usual difficulty of r_{ib} being equal to zero the shell is then treated as a sphere. In addition the implicit scheme requires the removal of the mass transport to the inner non-existent shell giving Equ.AII-42;

$$\left(\frac{\overline{C_{i,P}^{t+\Delta t}} - \overline{C_{i,P}^{t}}}{(t+\Delta t)-t}\right) = \frac{4\pi r_{ob}^2 D_{app,po} \dfrac{\overline{C_{i,O}^{t+\Delta t}} - \overline{C_{i,P}^{t+\Delta t}}}{r_{MO} - r_{MP}}}{\frac{4}{3}\pi\left(r_{ob}^3 - 0\right)} \qquad \text{AII-42}$$

Simplifying and getting into the form of equation better suited to solving by matrix gives Equ.AII-43.

$$\overline{C_{i,P}^{t}} = \left(\frac{3r_{ob}^2}{\left(r_{ob}^3 - 0\right)(r_{MO} - r_{MP})}\frac{\Delta t D_{app,po}}{1} + 1\right)\overline{C_{i,P}^{t+\Delta t}} - \frac{3r_{ob}^2}{\left(r_{ob}^3 - 0\right)(r_{MO} - r_{MP})}\frac{\Delta t D_{app,po}}{1}\overline{C_{i,O}^{t+\Delta t}}$$

AII-43

Outer shells of the bead

The assumption is made that there is equilibrium at the surface of the bead i.e. at the solid liquid interface and that that the Mass-Action-Law holds to give us the relationship between the resin phase and liquid phase concentrations. As each mass balance equation for each shell is being solved implicitly it is necessary to incorporate an extra shell that represents the bulk

solution associated with each resin bead. Assuming 25 internal shells the external shell representing the bulk is numbered 26.

The basic mass balance for shell number 25 is Equ.AII-44 where the distance from the centre of shell 25 to shell 26 has been halved as this is the distance to the interface. The concentration $\overline{C_{i,26}^{t+\Delta t}}$, is the concentration in the resin at the interface.

$$\left(\frac{\overline{C_{i,25}^{t+\Delta t}}-\overline{C_{i,25}^{t}}}{(t+\Delta t)-t}\right)=\frac{4\pi r_{25b}^{2}D_{app,po}\dfrac{\overline{C_{i,26}^{t+\Delta t}}-\overline{C_{i,25}^{t+\Delta t}}}{(r_{M26}-r_{M25})\frac{1}{2}}-4\pi r_{24b}^{2}D_{app,pi}\dfrac{\overline{C_{i,25}^{t+\Delta t}}-\overline{C_{i,24}^{t+\Delta t}}}{r_{M25}-r_{M24}}}{4/3\,\pi r_{25b}^{3}-4/3\,\pi r_{24b}^{3}} \qquad \text{AII-44}$$

Where

$\overline{C_{i,25}^{t+\Delta t}}$ Concentration in shell 25 at $t+\Delta t$ (*mol/L*)

$\overline{C_{i,26}^{t+\Delta t}}$ Concentration at the interface but in the resin $t+\Delta t$ (*mol/L*)

r_{24b} Radial distance to the outer boundary of shell 25 (*dm*)

r_{25b} Radial distance to the outer boundary of shell 25 (*dm*)

r_{M26} Radial distance to the centre of shell 26 (*dm*)

r_{M25} Radial distance to the centre of shell 25 (*dm*)

r_{M24} Radial distance to the centre of shell 24 (*dm*)

Simplifying Equ.AII-44 and getting it into a form that allows for placement into a matrix gives us Equ.AII-45;

$$-\frac{3r_{24b}^2}{(r_{M25}-r_{M24})(r_{25b}^3-r_{24b}^3)}\frac{D_{app,pi}\Delta t}{1}\overline{C_{i,24}^{t+\Delta t}}$$
$$+\left(1+\frac{3r_{25b}^2}{(r_{25b}^3-r_{24b}^3)(r_{M26}-r_{M25})\frac{1}{2}}\frac{D_{app,po}\Delta t}{1}+\frac{3r_{24b}^2}{(r_{M25}-r_{M24})(r_{25b}^3-r_{24b}^3)}\frac{D_{app,pi}\Delta t}{1}\right)\overline{C_{i,25}^{t+\Delta t}} \qquad \text{AII-45}$$
$$-\frac{3r_{25b}^2}{(r_{25b}^3-r_{24b}^3)(r_{M26}-r_{M25})\frac{1}{2}}\frac{D_{app,po}\Delta t}{1}\overline{C_{i,26}^{t+\Delta t}}=\overline{C_{i,25}^{t}}$$

The boundary condition for the outside of shell 26 (bulk solution associated with each resin bead) is giving in Equ.AII-46;

$$\left.\frac{\partial C_i}{\partial r}\right|_{r=26b}=0 \qquad \text{AII-46}$$

Where

26b Radial distance to the outer bound of the 26th shell (*dm*)

The mass balance equation for shell 26 shows a zero for its outer boundary.

$$\left(\frac{\overline{C_{i,26}^{t+\Delta t}}-\overline{C_{i,26}^{t}}}{(t+\Delta t)-t}\right)=\frac{0-4\pi r_{25b}^2 D_{app,pi}\dfrac{\overline{C_{i,26}^{t+\Delta t}}-\overline{C_{i,25}^{t+\Delta t}}}{r_{M26}-r_{M25}}}{4/3\pi r_{26b}^3-4/3\pi r_{25b}^3} \qquad \text{AII-47}$$

Where

r_{26b} Radial distance to the outer boundary of shell 26 (*dm*)

Simplifying and getting Equ.AII-47 into the correct form for solving by matrix gives Equ.AII-48;

$$-\frac{3r_{25b}^2}{\left(r_{26b}^3-r_{25b}^3\right)\left(r_{M26}-r_{M25}\right)\frac{1}{2}}\frac{D_{app,pi}\Delta t}{1}\overline{C_{i,25}^{t+\Delta t}}+\left(1+\frac{3r_{25b}^2}{\left(r_{26b}^3-r_{25b}^3\right)\left(r_{M26}-r_{M25}\right)\frac{1}{2}}\frac{D_{app,pi}\Delta t}{1}\right)\overline{C_{i,26}^{t+\Delta t}}=\overline{C_{i,26}^{t}}$$

AII-48

Although the concentration of adsorbing ions in shell 26 is considered to be at the boundary of 25 and 26 i.e. the external surface of the resin bead, the concentration is ultimately sustained through the Mass-Action-Law by the presence of the ions in the bulk solution, therefore assuming $\overline{C_{i,(R)}^{t}}=\overline{C_{i,26}^{t}}$ (Equ.AII-37) gives Equ.AII-49;

$$-\frac{3r_{25b}^2}{\left(r_{26b}^3-r_{25b}^3\right)\left(r_{M26}-r_{M25}\right)\frac{1}{2}}\frac{D_{pi}\Delta t}{1}C_{25}^{t+\Delta t}+\left(1+\frac{3r_{25b}^2}{\left(r_{26b}^3-r_{25b}^3\right)\left(r_{M26}-r_{M25}\right)\frac{1}{2}}\frac{D_{pi}\Delta t}{1}\right)C_{26}^{t+\Delta t}=\frac{\alpha\times\overline{C_{D,(R)}^{t}}\times C_{i,t}^{*}}{C_{D}^{t}}$$

AII-49

The term on the right of Equ.AII-49 represents the Mass-Action-Law and is incorporated into the matrix operation with $C_D^t, C_{i,t}^*, \overline{C_{D,(R)}^t}$ being up dated through each time increment in a separate mass balancing algorithm.

ANNEXURE III COMPUTER FLOW DIAGRAMS

Establishing the physical system

This section of the program establishes the physical boundaries of the system and is only used at the beginning of the simulation fitting process. After this part the program moves onto the Hook-Jeeves optimization module

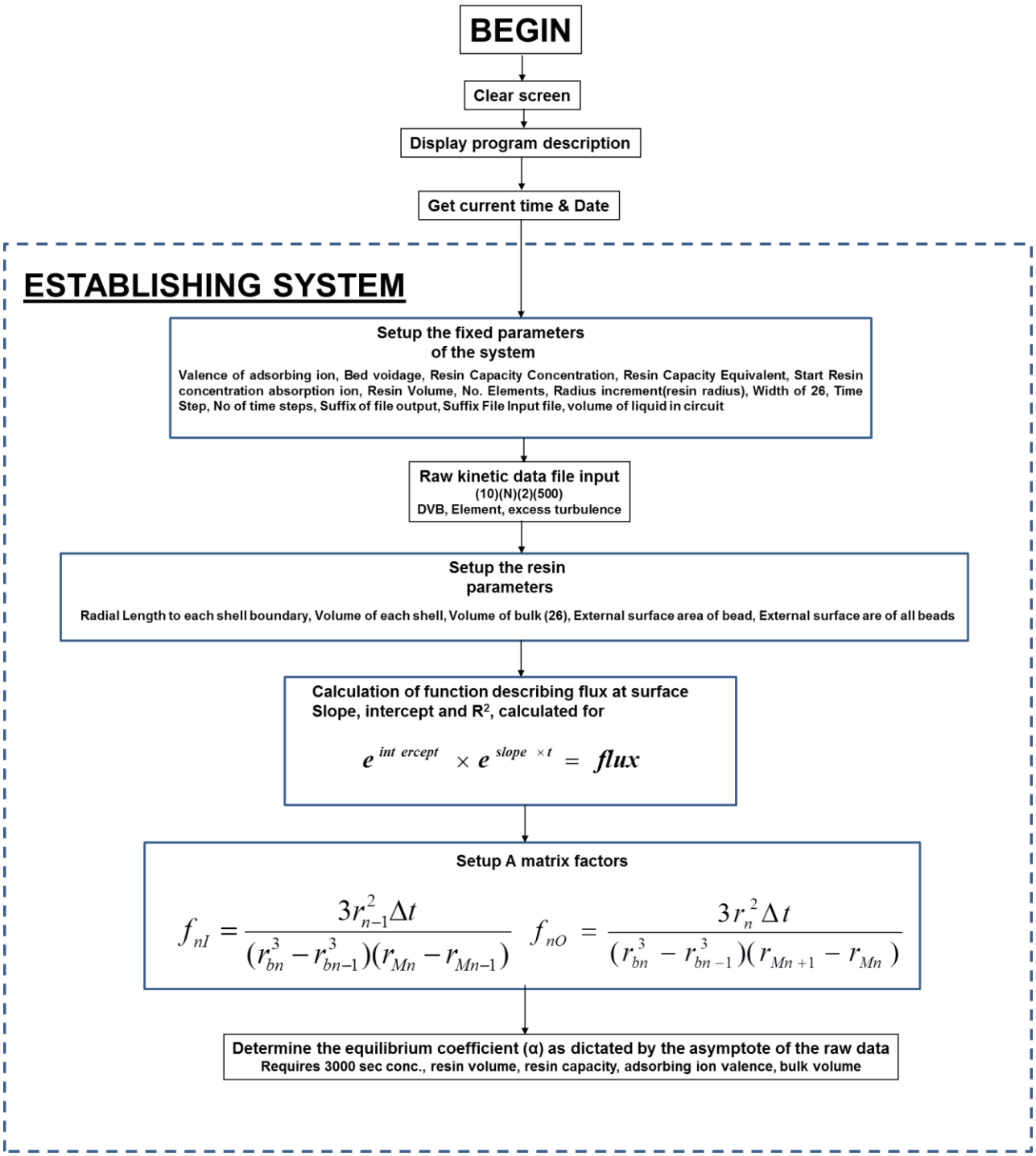

Hook-Jeeves optimisation routine

The Hook-Jeeves optimization algorithm controls the search routine

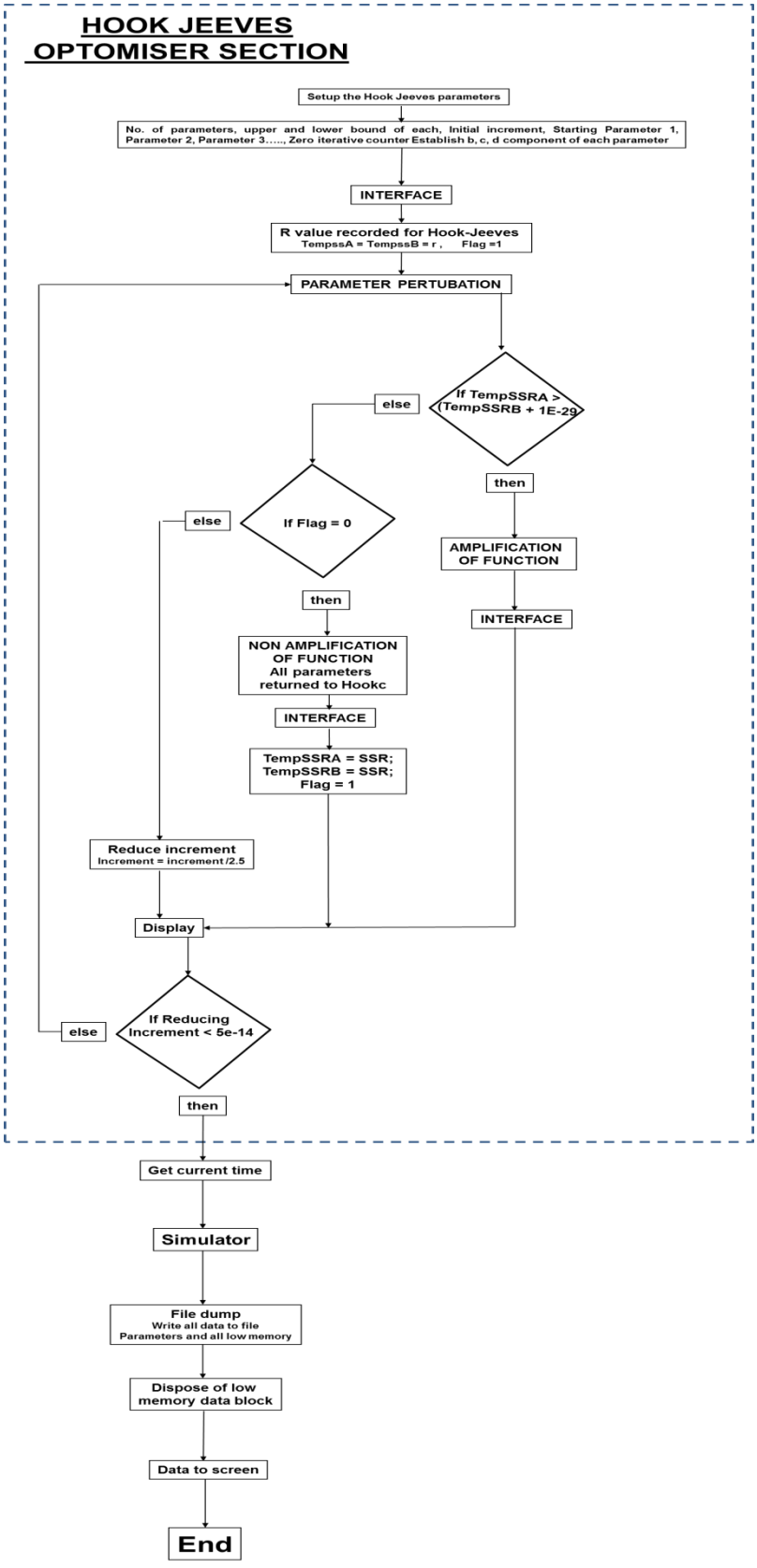

Parameter perturbation

This routine actively undertakes exploratory change to seek better parameter fits and is called upon by the Hook-Jeeves search algorithm

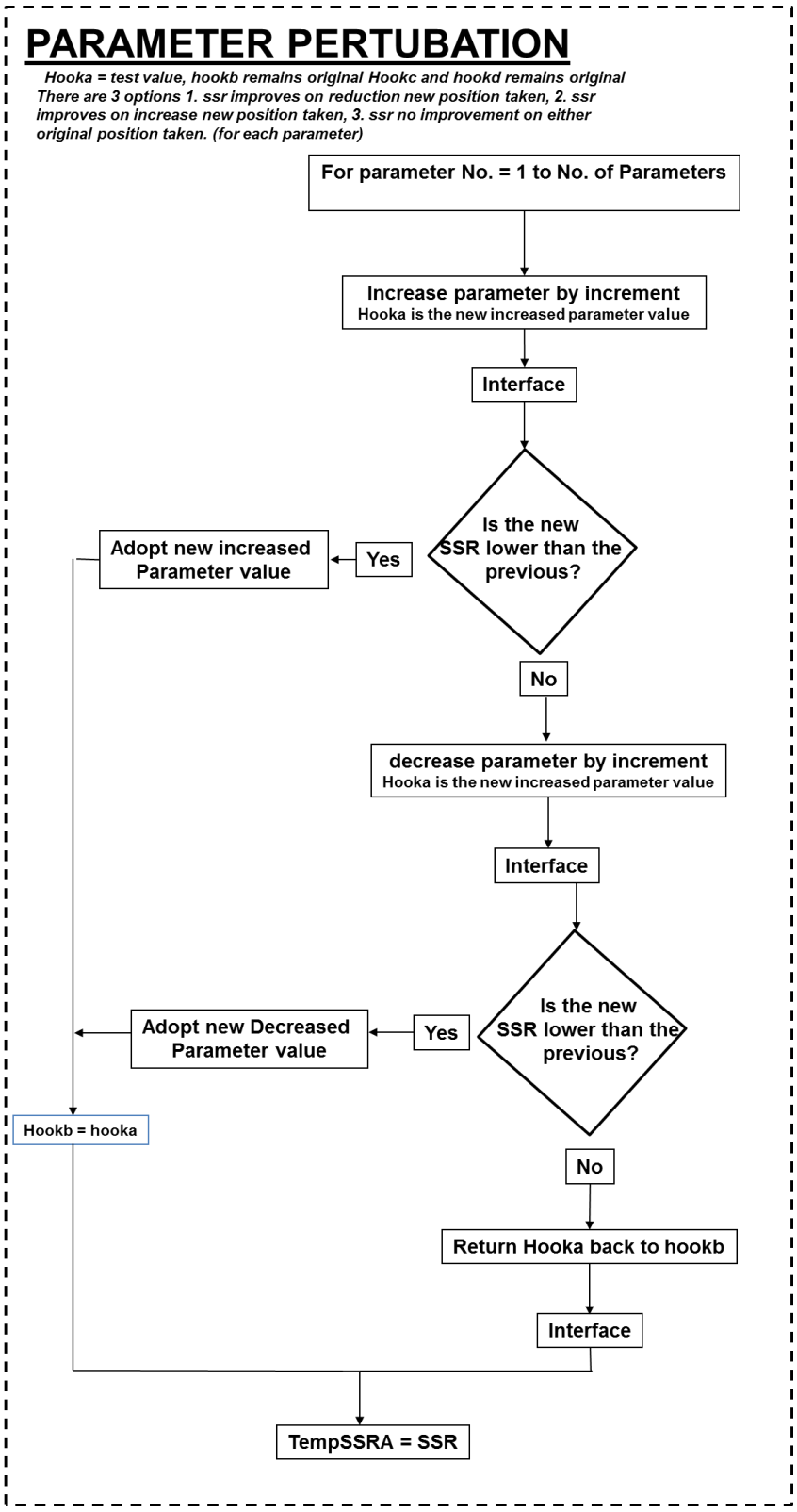

Interface and simulator

The interface interacts between the Hook-Jeeves and simulator algorithms evaluating the degree of improvement/deterioration of fit for each exploratory endeavour.

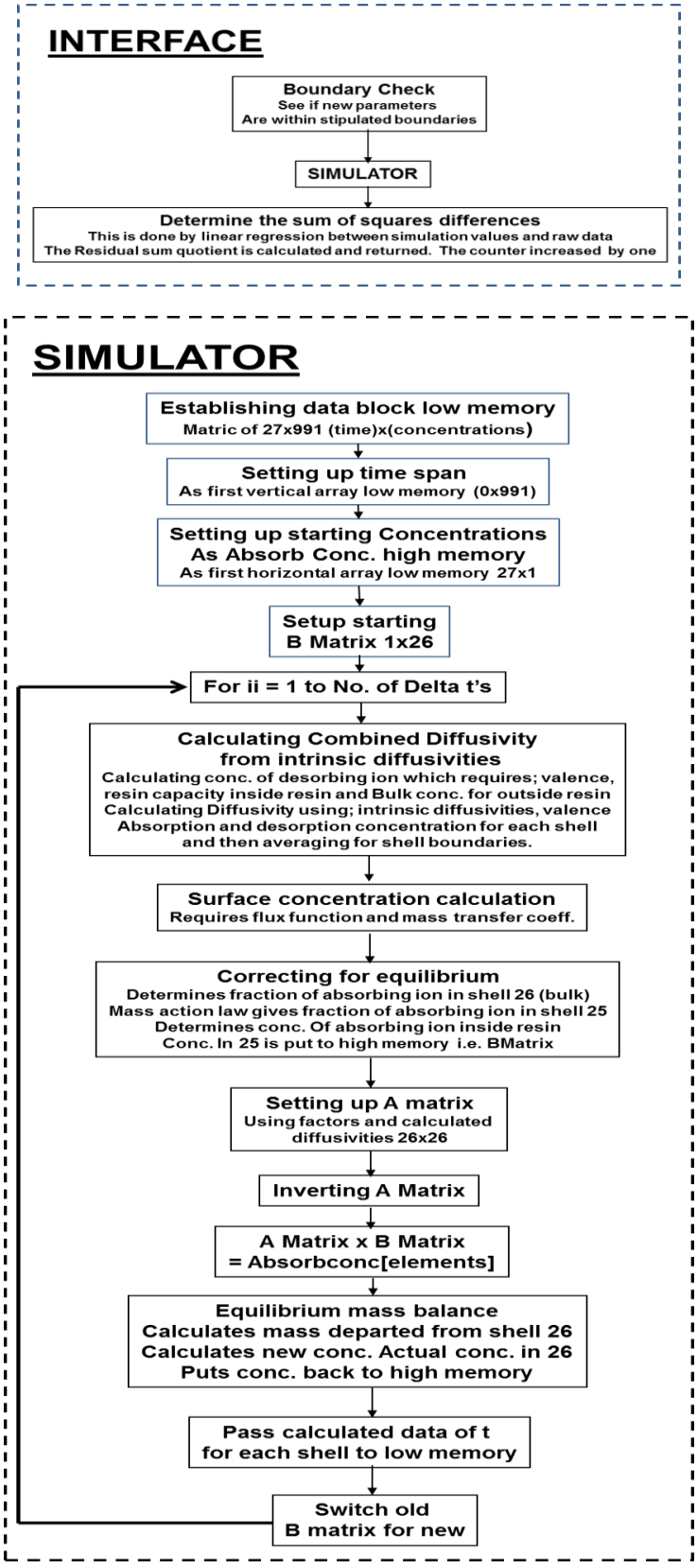

ANNEXURE IV MASS-ACTION-LAW

Calculating the equilibrium coefficient from the final kinetic test concentration

At the end of the transient ($t = \infty$) the desorbing / adsorbing ion concentrations on the resin will be in equilibrium with the desorbing / adsorbing ions in the associated bulk solution and this relationship should be definable by the Mass-Action-Law as described in Equ.5-3. However, as the only measurable variable is the bulk concentration Equ.5-3 needs to be re-configured into the form of Equ.AIV-1.

$$\frac{\dfrac{\boldsymbol{B}-\boldsymbol{E}}{\overline{\boldsymbol{C}_T}}}{1-\dfrac{\boldsymbol{B}-\boldsymbol{E}}{\overline{\boldsymbol{C}_T}}} \times \frac{1-\dfrac{\boldsymbol{E}}{\boldsymbol{E}+(\boldsymbol{B}-\boldsymbol{E})}}{\dfrac{\boldsymbol{E}}{\boldsymbol{E}+(\boldsymbol{B}-\boldsymbol{E})}} = \boldsymbol{\alpha} \qquad \text{AIV-1}$$

Where

$\boldsymbol{E}$	End concentration of adsorbing ions in bulk solution	(*mol/L*)
$\boldsymbol{B}$	Beginning concentration of adsorbing ions bulk solution	(*mol/L*)
$\boldsymbol{C_T}$	Resin ionic capacity of resin co-polymer volume	(*equiv./L*)

Equ.AIV-1 can be simplified to give Equ.AIV-2

$$\frac{(\boldsymbol{B}-\boldsymbol{E})^2}{(\boldsymbol{C_T}-\boldsymbol{B}+\boldsymbol{E})\boldsymbol{E}} = \boldsymbol{\alpha} \qquad \text{AIV-2}$$

It is important to note that if the adsorbing ion has a valence of one and the desorbing ion is hydrogen i.e. also has a valence of one, the calculation of the equilibrium coefficient ($\boldsymbol{\alpha}$) transfer from the concentrations of ions in the bulk solution is relatively easily achieved via

Equ.AIV-2. The bulk concentration change, that is the only measurable variable, gives a direct indication of the number of ions / equivalents adsorbed from bulk solution (***S – E***) and what remains in the bulk solution (***E***).

For multi-valent adsorbing ions it becomes necessary to go back to fundamentals (Equ.AIV-5) as the molar mass of adsorbing and desorbing ions that can be adsorbed onto the resin cannot be equated because of the differing valence and hence this disparity has to be accommodated. If the mass fractions are to be determined in terms of mol fraction then the following holds true:

Mol fraction inside the resin for the adsorbing ion can be calculated using Equ.AIV-3.

$$\frac{\overline{C_i}}{\overline{C_i}+\overline{C_D}} = \frac{(B-E)}{(B-E)+\left[\overline{C_T}-(B-E)\times z_i\right]} \qquad \text{AIV-3}$$

Where

z_i Valence of the adsorbing ion (*dimensionless*)

Mol fraction in the bulk solution for the adsorbing ion can be calculated using Equ.AIV-4.

$$\frac{C_i}{C_i+C_D} = \frac{E}{E+\left[(B-E)\times z_i\right]} \qquad \text{AIV-4}$$

Combining Equ.AIV-3 and Equ.AIV-4 into the Mass-Action-Law (Equ.5-3) and solving for the equilibrium constant (***α***) gives Equ.AIV-5;

$$\frac{\dfrac{(\boldsymbol{B}-\boldsymbol{E})}{(\boldsymbol{B}-\boldsymbol{E})+\overline{\boldsymbol{C}_{\boldsymbol{T}}}-(\boldsymbol{B}-\boldsymbol{E})\times\boldsymbol{z}_{\boldsymbol{B}}}}{1-\dfrac{(\boldsymbol{B}-\boldsymbol{E})}{(\boldsymbol{B}-\boldsymbol{E})+\overline{\boldsymbol{C}_{\boldsymbol{T}}}-(\boldsymbol{B}-\boldsymbol{E})\times\boldsymbol{z}_{\boldsymbol{B}}}}\times\frac{1-\dfrac{\boldsymbol{E}}{\boldsymbol{E}+(\boldsymbol{B}-\boldsymbol{E})\times\boldsymbol{z}_{\boldsymbol{i}}}}{\dfrac{\boldsymbol{E}}{\boldsymbol{E}+(\boldsymbol{B}-\boldsymbol{E})\times\boldsymbol{z}_{\boldsymbol{i}}}}=\boldsymbol{\alpha}_{\boldsymbol{mol}} \qquad \text{AIV-5}$$

Simplifying Equ.AIV-5 gives Equ.AIV-6, from which an equilibrium coefficient can easily be calculated.

$$\frac{\boldsymbol{B}-\boldsymbol{E}}{\dfrac{\overline{\boldsymbol{C}_{\boldsymbol{T}}}}{\boldsymbol{z}_{\boldsymbol{i}}}-\boldsymbol{B}+\boldsymbol{E}}\times\frac{\boldsymbol{B}-\boldsymbol{E}}{\boldsymbol{E}}=\boldsymbol{\alpha}_{\boldsymbol{mol}} \qquad \text{AIV-6}$$

Simplifying further gives Equ.AIV-7 that is similar to Equ.AIV-2 except for the addition of the adsorbing ion's valence as a denominator to the ion exchange resin capacity.

$$\frac{(\boldsymbol{B}-\boldsymbol{E})^2}{\left(\dfrac{\overline{\boldsymbol{C}_{\boldsymbol{T}}}}{\boldsymbol{z}_{\boldsymbol{i}}}-\boldsymbol{B}+\boldsymbol{E}\right)\boldsymbol{E}}=\boldsymbol{\alpha}_{\boldsymbol{mol}} \qquad \text{AIV-7}$$

Interestingly, if the equilibrium coefficient is calculated using either equivalents or mol fractions, the same value is achieved. This is shown in the following section.

Calculating the equilibrium coefficient when multi valent ions are used

The Mass-Action-Law is useful for modelling ion exchange equilibrium between competing ions. However, one of the challenges is its use in finite bulk solution systems where the competing ions have different valences. A fixed quantity of ion exchange resin in a finite bulk solution will hold a constant number of ions measured in equivalents at all times and the associated finite bulk solution will also have a constant number of ions measured in equivalents. But the same will not be true if the competing ions have a different valence and intuitively it is possible that mass fractions based on mol will be different for that based on equivalents. However, it can be shown that the calculation of the Mass-Action-Law equilibrium coefficient (α) is the same value weather it is calculated based on mol mass fractions or equivalent mass fractions. Mol mass fraction of adsorbing ion inside the resin calculated from change in bulk adsorption mol concentration

The original Mass-action-law equation requires the mass fractions in both the resin and bulk phase as shown in Equ.AIV-8.

$$\frac{Resin\ adsorb\ \ Frac}{Resin\ desorb\ \ Frac} \times \frac{Bulk\ desorb\ \ Frac}{Bulk\ adsorb\ \ Frac} = \alpha \qquad \text{AIV-8}$$

Molar fraction in the resin phase is given by Equ.AIV-9

$$\frac{\overline{C_A}}{\overline{C_A} + \overline{C_D}} = \frac{(S-E)}{(S-E) + \overline{C_T} - (S-E) \times V} \qquad \text{AIV-9}$$

Molar fraction in the bulk for the adsorbing resin is given by Equ.AIV-10

$$\frac{C_A}{C_A + C_D} = \frac{E}{E + (B - E) \times V} \qquad \text{AIV-10}$$

The reciprocal or desorbing ion molar fraction in each case will be 1 minus these values.

The **equivalent mass fraction** inside the resin for the adsorbing ion calculated from change in bulk adsorption concentration can be presented as shown in Equ.AIV-11 and simplified

$$\frac{\overline{C_A}}{\overline{C_A} + \overline{C_D}} = \frac{(B - E) \times z_i}{(B - E) \times z_i + \overline{C_T} - (B - E) \times z_i}$$
$$\frac{\overline{C_A}}{\overline{C_A} + \overline{C_D}} = \frac{(B - E) \times z_i}{\overline{C_T}} \qquad \text{AIV-11}$$

The **equivalent mass fraction** in the bulk for the adsorbing ion calculated from change in bulk adsorption ion molar concentration can be presented in Equ.AIV-12 and simplified.

$$\frac{C_A}{C_A + C_D} = \frac{E \times z_i}{E \times z_i + (B - E) \times z_i}$$
$$\frac{C_A}{C_A + C_D} = \frac{E}{B} \qquad \text{AIV-12}$$

Determining the equilibrium coefficient in terms of mol fraction we achieve Equ.AIV-13.

$$\frac{\frac{(B - E)}{(B - E) + \overline{C_T} - (B - E) \times z_i}}{1 - \frac{(B - E)}{(B - E) + \overline{C_T} - (B - E) \times z_i}} \times \frac{1 - \frac{E}{E + (B - E) \times z_i}}{\frac{E}{E + (B - E) \times z_i}} = \alpha_{mol} \qquad \text{AIV-13}$$

Where

α_{mol} Equilibrium coefficient based on mol fractions (*dimensionless*)

Simplifying Equ.AIV-13

$$\frac{\frac{(B-E)}{(B-E)+\overline{C_T}-(B-E)\times z_i}}{1-\frac{(B-E)}{(B-E)+\overline{C_T}-(B-E)\times z_i}}\times\frac{1-\frac{E}{E+(B-E)\times z_i}}{\frac{E}{E+(B-E)\times z_i}}=\alpha_{mol}$$

$$\frac{\frac{(B-E)}{(B-E)+\overline{C_T}-(B-E)\times z_i}}{\frac{(B-E)+C_T-(B-E)\times z_i-(B-E)}{(B-E)+\overline{C_T}-(B-E)\times z_i}}\times\frac{\frac{E+(B-E)\times z_i-E}{E+(B-E)\times z_i}}{\frac{E}{E+(B-E)\times z_i}}=\alpha_{mol}$$

$$\frac{(B-E)}{(B-E)+\overline{C_T}-(B-E)\times z_i-(B-E)}\times\frac{E+(B-E)\times z_i-E}{E}=\alpha_{mol}$$

$$\frac{B-E}{B-E+\overline{C_T}-Bz_i+Ez_i-B+E}\times\frac{E+Bz_i-Ez_i-E}{E}=\alpha_{mol}$$

$$\frac{B-E}{\overline{C_T}-Bz_i+Ez_i}\times\frac{Bz_i-Ez_i}{E}=\alpha_{mol}$$

Finally, achieving Equ.AIV-14 which can be used to calculate the equilibrium coefficient based on mol mass fractions.

$$\frac{Bz_i-Ez_i}{\overline{C_T}-Sz_i+Ez_i}\times\frac{B-E}{E}=\alpha_{mol}\qquad\text{AIV-14}$$

Undertaking the same exercise in terms of ionic / equivalents mass fractions from the original mass-action-law equation we get Equ.AIV-15

$$\frac{\frac{(\boldsymbol{B}-\boldsymbol{E})\times \boldsymbol{z_i}}{\overline{\boldsymbol{C_T}}}}{1-\frac{(\boldsymbol{B}-\boldsymbol{E})\times \boldsymbol{z_i}}{\overline{\boldsymbol{C_T}}}} \times \frac{1-\frac{\boldsymbol{E}}{\boldsymbol{B}}}{\frac{\boldsymbol{E}}{\boldsymbol{B}}} = \boldsymbol{\alpha_{equiv}} \qquad \text{AIV-15}$$

Where

$\boldsymbol{\alpha_{equiv}}$ Equilibrium coefficient based on equivalents (dimensionless)

Simplifying Equ.AIV-15 gives Equ.AIV-16

$$\frac{\frac{(\boldsymbol{B}-\boldsymbol{E})\times \boldsymbol{z_i}}{\overline{\boldsymbol{C_T}}}}{\frac{\boldsymbol{C_T}-(\boldsymbol{B}-\boldsymbol{E})\times \boldsymbol{z_i}}{\overline{\boldsymbol{C_T}}}} \times \frac{\frac{\boldsymbol{B}-\boldsymbol{E}}{\boldsymbol{S}}}{\frac{\boldsymbol{E}}{\boldsymbol{B}}} = \boldsymbol{\alpha_{equiv}}$$

$$\frac{(\boldsymbol{B}-\boldsymbol{E})\times \boldsymbol{z_i}}{\overline{\boldsymbol{C_T}}-(\boldsymbol{B}-\boldsymbol{E})\times \boldsymbol{z_i}} \times \frac{\boldsymbol{B}-\boldsymbol{E}}{\boldsymbol{E}} = \boldsymbol{\alpha_{equiv}}$$

$$\frac{\boldsymbol{Bz_i}-\boldsymbol{Ez_i}}{\overline{\boldsymbol{C_T}}-\boldsymbol{Bz_i}+\boldsymbol{Ez_i}} \times \frac{\boldsymbol{B}-\boldsymbol{E}}{\boldsymbol{E}} = \boldsymbol{\alpha_{equiv}} \qquad \text{AIV-16}$$

Equ.AIV-14 and Equ.AIV-16 are identical proving that the same equilibrium coefficient is measured either using mass fractions based on mol or equivalents, in a finite resin system.

Simplifying the equation further gives Equ.AIV-17 which is then used to calculate the α value at the end of any particular kinetic test.

$$\frac{(B-E)^2}{\left(\overline{C_T}/z_i - B + E\right)E} = \alpha \qquad \text{AIV-17}$$

ANNEXURE V MATRIX OPERATION

Here is presented the implicit mass balance equations for the general equation, the inner most shell (1), the outer most resin shell (25) and the outer most shell representing the bulk solution (26) all in matrix friendly form. The factors for ease of assimilation into the matrix are then presented and finally the matrix operation as a whole. A flow diagram of that part of the overall simulation as presented in the thesis that uses matrix calculation is given.

Implicit mass balance equations

This section follows on from Annexure II and describes the implicit solving of all mass balance equations associated with each shell in the resin bead via a matrix operation. The equation numbering links to and follows on from that presented in Annexure II.

Equation for inner most shell

$$\left(\frac{3r_{ob}^2}{r_{ob}^3(r_{MO}-r_{MP})}\frac{\Delta tD_{app,po}}{1}+1\right)\overline{C_{i,P}^{t+\Delta t}} - \frac{3r_{ob}^2}{r_{ob}^3(r_{MO}-r_{MP})}\frac{\Delta tD_{app,po}}{1}\overline{C_{i,O}^{t+\Delta t}} = \overline{C_{i,P}^{t}} \qquad \text{AII-43}$$

General equation

$$-\frac{3r_{ib}^2\Delta tD_{app,pi}}{\left(r_{ob}^3-r_{ib}^3\right)(r_{MP}-r_{MI})}\overline{C_{i,I}^{t+\Delta t}} + \left(1+\frac{3r_{ob}^2\Delta tD_{app,po}}{\left(r_{ob}^3-r_{ib}^3\right)(r_{MO}-r_{MP})}+\frac{3r_{ib}^2\Delta tD_{app,pi}}{\left(r_{ob}^3-r_{ib}^3\right)(r_{MP}-r_{MI})}\right)\overline{C_{i,P}^{t+\Delta t}} - \frac{3r_{ob}^2\Delta tD_{app,po}}{\left(r_{ob}^3-r_{ib}^3\right)(r_{MO}-r_{MP})}\overline{C_{i,O}^{t+\Delta t}} = \overline{C_{i,P}^{t}} \qquad \text{AII-41}$$

Equation for outer most resin shell (shell No. 25)

$$-\frac{3r_{24b}^{2}}{\left(r_{25b}^{3}-r_{24b}^{3}\right)\left(r_{M25}-r_{M24}\right)}\frac{D_{app,pi}\Delta t}{1}\overline{C_{i,24}^{t+\Delta t}}$$
$$+\left(1+\frac{3r_{25b}^{2}}{\left(r_{25b}^{3}-r_{24b}^{3}\right)\left(r_{M26}-r_{M25}\right)\frac{1}{2}}\frac{D_{app,po}\Delta t}{1}+\frac{3r_{24b}^{2}}{\left(r_{25b}^{3}-r_{24b}^{3}\right)\left(r_{M25}-r_{M24}\right)}\frac{D_{app,pi}\Delta t}{1}\right)\overline{C_{i,25}^{t+\Delta t}} \qquad \text{AII-49b}$$
$$-\frac{3r_{25b}^{2}}{\left(r_{25b}^{3}-r_{24b}^{3}\right)\left(r_{M26}-r_{M25}\right)\frac{1}{2}}\frac{D_{app,po}\Delta t}{1}\overline{C_{i,26}^{t+\Delta t}}=C_{i,25}^{t}$$

Equation for outer most shell (shell No. 26 i.e. bulk solution)

$$-\frac{3r_{25b}^{2}}{\left(r_{26b}^{3}-r_{25b}^{3}\right)\left(r_{M26}-r_{M25}\right)\frac{1}{2}}\frac{D_{app,pi}\Delta t}{1}\overline{C_{i,25}^{t+\Delta t}}$$
$$+\left(1+\frac{3r_{25b}^{2}}{\left(r_{26b}^{3}-r_{25b}^{3}\right)\left(r_{M26}-r_{M25}\right)\frac{1}{2}}\frac{D_{app,pi}\Delta t}{1}\right)\overline{C_{i,26}^{t+\Delta t}} \qquad \text{AII-49}$$
$$=\frac{\alpha\times\overline{C_{D,(R)}^{t}}\times C_{i,t}^{*}}{C_{D}^{t}}$$

Factors for ease of assimilation into matrix

As can be seen from the equation shown in the previous section it's possible to extract common factors. The two common factors that are easily discernible are presented in Equ.AV-50 where f_O is associated with flux through the outer boundary of the shell and f_I is associated with flux through the inner boundary of the shell. In Equ.AV-50 '*n*' refers to the shell number.

$$\frac{3r_{25b}^2\Delta t\ \left[D_{app,O,n}\right]}{\left(r_{nb}^3 - r_{(n-1)b}^3\right)\left(r_{M(n+1)} - r_{Mn}\right)} = f_O \qquad \frac{3r_{25b}^2\Delta t\ \left[D_{app,I,n}\right]}{\left(r_{nb}^3 - r_{(n-1)b}^3\right)\left(r_{Mn} - r_{M(n-1)}\right)} = f_I \qquad \text{AV-50}$$

The equations are now rewritten incorporating these factors.

Inner most shell

$$\left(f_O + 1\right)\overline{C_{i,P}^{t+\Delta t}} - f_O\overline{C_{i,O}^{t+\Delta t}} = \overline{C_{i,P}^{t}} \qquad \text{AV-43}f$$

General equation

$$-f_I\overline{C_{i,I}^{t+\Delta t}} + \left(1 + f_O + f_I\right)\overline{C_{i,P}^{t+\Delta t}} - f_O\overline{C_{i,O}^{t+\Delta t}} = \overline{C_{i,P}^{t}} \qquad \text{AV-41}f$$

Equation for outermost resin shell (shell No. 25)

$$-f_I\overline{C_{i,24}^{t+\Delta t}} + \left(1 + f_O + f_I\right)\overline{C_{i,25}^{t+\Delta t}} - f_O\overline{C_{i,26}^{t+\Delta t}} = \overline{C_{i,25}^{t}} \qquad \text{AV-49b}f$$

Equation for outer most shell (shell No. 26 i.e. bulk solution)

$$-f_I\overline{C_{i,25}^{t+\Delta t}} + \left(1 + f_I\right)\overline{C_{i,26}^{t+\Delta t}} = \frac{\alpha \times \overline{C_{D,(R)}^{t}} \times C_{i,t}^{*}}{C_D^t} \qquad \text{AV-49}f$$

Matrix operations

Equations 41*f*, 43*f*, 49b*f* and 49*f*, can be written in the form of matrix operation Equ.AV-51.

$$[\boldsymbol{A}]\times[\boldsymbol{B}]=[\boldsymbol{C}] \qquad \text{AV-51}$$

Where

$[\boldsymbol{A}]$ Square diagonal matrix incorporating the factor parts of each equation

$[\boldsymbol{B}]$ Single column matrix incorporating the concentrations in each shell at $\boldsymbol{t}+\boldsymbol{\Delta t}$

$[\boldsymbol{C}]$ Single column matrix incorporating the concentrations in each shell at $\boldsymbol{t}$

For the purposes of solving all the equations implicitly to determine the concentration in each shell at $\boldsymbol{t}+\boldsymbol{\Delta t}$, matrix operation Equ.AV-52 can be used, $[\boldsymbol{A}]$ matrix is inverted and multiplied by $[\boldsymbol{C}]$ to determine $[\boldsymbol{B}]$.

$$[\boldsymbol{C}]\times[\boldsymbol{A}]^{-1}=[\boldsymbol{B}] \qquad \text{AV-52}$$

As the diffusivity is a variable, dictated by the Nernst-Plank equation and subject to the changing concentrations of the desorbing and adsorbing ions its values are determined in a separate algorithm that runs parallel to the implicit matrix operation before the inversion of Matrix A. These values are then incorporated into the matrix factors for each time increment.

$$[A]\times[B]=[C]\qquad \begin{bmatrix} 1+f_{1O} & -f_{1O} & 0 & 0 & 0 \\ f_{2I} & 1+f_{2O}+f_{2I} & f_{2O} & 0 & 0 \\ " & " & " & " & " \\ 0 & 0 & -f_{25I} & 1+f_{25O}+f_{25I} & -f_{25O} \\ 0 & 0 & 0 & -f_{26I} & 1+f_{26I} \end{bmatrix} \times \begin{bmatrix} C_1^{\Delta t+t} \\ C_2^{\Delta t+t} \\ " \\ C_{25}^{\Delta t+t} \\ C_{26}^{\Delta t+t} \end{bmatrix} = \begin{bmatrix} C_1^{t} \\ C_2^{t} \\ " \\ C_{25}^{t} \\ C_{26}^{t} \end{bmatrix}$$

$$[A]^{-1}\times[C]=[B]\qquad \begin{bmatrix} 1+f_{1O} & -f_{1O} & 0 & 0 & 0 \\ f_{2I} & 1+f_{2O}+f_{2I} & f_{2O} & 0 & 0 \\ " & " & " & " & " \\ 0 & 0 & -f_{25I} & 1+f_{25O}+f_{25I} & -f_{25O} \\ 0 & 0 & 0 & -f_{26I} & 1+f_{26I} \end{bmatrix}^{-1} \times \begin{bmatrix} C_1^{t} \\ C_2^{t} \\ " \\ C_{25}^{t} \\ C_{26}^{t} \end{bmatrix} = \begin{bmatrix} C_1^{\Delta t+t} \\ C_2^{\Delta t+t} \\ " \\ C_{25}^{\Delta t+t} \\ C_{26}^{\Delta t+t} \end{bmatrix}$$

Where

$$C_{26}^{t}=\frac{\alpha\times\overline{C_{D,(R)}^{t}}\times C_{i,t}^{*}}{C_D^{t}}$$

$$f_o=\frac{3r_{25b}^2\Delta t\quad\left[D_{app,O,n}\right]}{\left(r_{nb}^3-r_{(n-1)b}^3\right)\left(r_{M(n+1)}-r_{Mn}\right)}$$

$$f_I=\frac{3r_{25b}^2\Delta t\quad\left[D_{app,I,n}\right]}{\left(r_{nb}^3-r_{(n-1)b}^3\right)\left(r_{Mn}-r_{M(n-1)}\right)}$$

Simulation algorithm

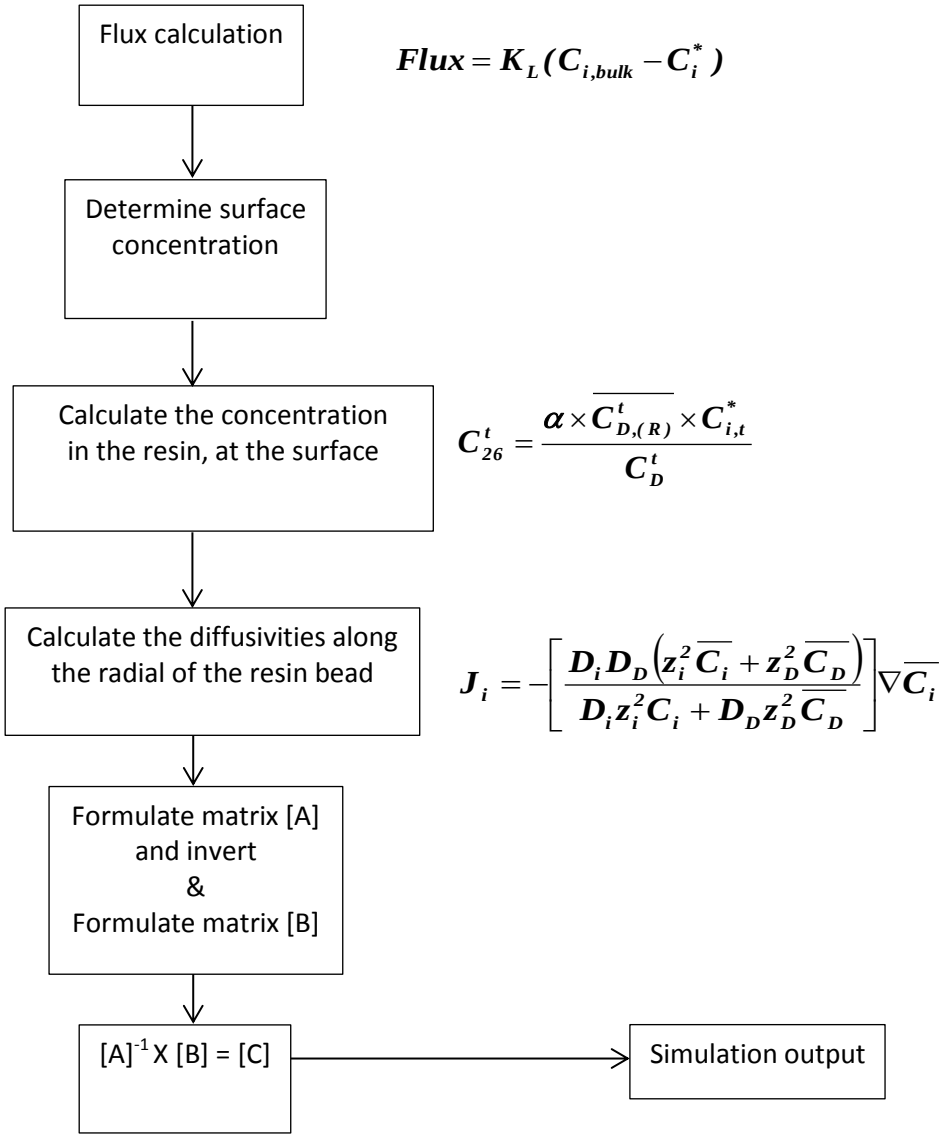

ANNEXURE VI AD/DESORBTION ION RELATIONSHIP IN FINITE MEDIUM

Linking of the disappearance of the adsorbing ion in the bulk to the appearance of the desorbing ion in the bulk via a mass balance, during the transient as displayed in Fig.AVI-1

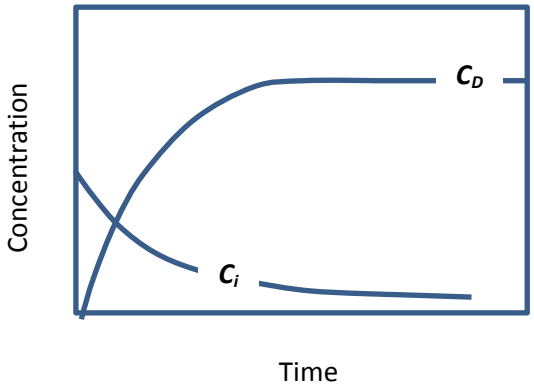

Fig.AVI-1 Transient of an absorbing C_i (valence 2) and desorbing ion C_D

Balance for desorption ion is given in Equ.AVI-1

$$(C_{D,t=\infty} - C_D) + (C_D - C_{D,t=0}) + C_{D,t=0} = C_{D,t=\infty} \qquad \text{AVI-1}$$

Mass balance for desorption and adsorption in a finite system (Equ.AVI-2)

$$C_D - C_{D,t=0} = z_i \left[C_{i,t=0} - C_{i,bulk} \right] \qquad \text{AVI-2}$$

Combining Equ.AVI-1 and Equ.AVI-2 gives us Equ.AVI-3

$$(C_{D,t=\infty} - C_D) + z_i \left[C_{i,t=0} - C_{i,bulk} \right] + C_{D,t=0} = C_{D,t=\infty} \qquad \text{AVI-3}$$

From the mass balance we can also state Equ.AVI-4;

$$C_{D,t=\infty} - C_{D,t=0} = z_i\left[C_{i,t=0} - C_{i,t=\infty}\right] \qquad \text{AVI-4}$$

Substituting Equ.AVI-3 into Equ.AVI-4 gives Equ.AVI-5

$$(C_{D,t=\infty} - C_D) + z_i\left[C_{i,t=0} - C_{i,bulk}\right] = z_i\left[C_{i,t=0} - C_{i,t=\infty}\right] \qquad \text{AVI-5}$$

Simplifying

$$(C_{D,t=\infty} - C_D) = z_i\left[C_{i,t=0} - C_{i,t=\infty} - C_{i,t=0} + C_{i,bulk}\right]$$

$$(C_{D,t=\infty} - C_D) = z_i\left[C_{i,bulk} - C_{i,t=\infty}\right]$$

Its notable that in a kinetic test the concentration of $C_{i,t=\infty}$ will ultimately be equal to C_i*hence giving Equ.AVI-6;

$$(C_{D,t=\infty} - C_D) = z_i\left[C_i - C_i^*\right] \text{ or } \frac{1}{z_i}(C_{D,t=\infty} - C_D) = \left[C_{i,bulk} - C_i^*\right] \qquad \text{AVI-6}$$

In a finite system with no time delays Equ.AVI-7 can be assume to be true;

$$-\left.\frac{dC_{i,bulk}}{dt}\right|_{t=t} = -\frac{1}{z_i}\left.\frac{d\left(C_{D,t=\infty} - C_D\right)}{dt}\right|_{t=t} \qquad \text{AVI-7}$$

Laminar layer model can be stated as Equ.AVI-8;

$$-\frac{dC_{i,bulk}}{dt} = K\left[C_{i,bulk} - C_i^*\right] \qquad \text{AVI-8}$$

Substituting the desorbing differential

$$-\frac{1}{z_i}\frac{d\left(C_{D,t=\infty} - C_D\right)}{dt} = K\left[C_{i,bulk} - C_i^*\right]$$

Substituting from the mass balance

$$-\frac{1}{z_i}\frac{d\left(C_{D,t=\infty} - C_D\right)}{dt} = K\frac{1}{z_i}\left(C_{D,t=\infty} - C_D\right)$$

And therefore the following relationship should hold true if a basic Newton's law of cooling type model is assumed to be true in the same system.

$$-\frac{d\left(C_{D,t=\infty} - C_D\right)}{dt} \propto C_{D,t=\infty} - C_D \qquad \text{AVI-9}$$

KINETIC DATA FROM 6.5% & 10% DVB FRESH RESIN

Each graph contains six curves with the steepest being the highest ZLC flow through and the flattest the lowest ZLC flow through. There are a total of 108 curves which are the sum total of a matrix of tests consisting of three ions (Na^{+}, Mg^{++}, Ba^{++}), two DVB contents (6.5% resin type C100E, 10% resin type PPC100x10), three starting concentrations (20%, 50%, 80% excess) and six volumetric flow rates through the ZLC (60, 100, 200, 300, 400, 500 *mL/min*). The results reported in section *6.2* were calculated from this data.

EXPLANATION OF THE LEGEND AND AXES OF EACH GRAPH

LEGEND

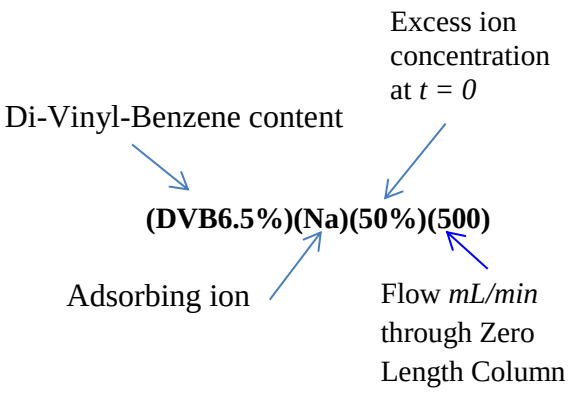

AXES

The vertical axis on each graph is conversion (dimensionless)

The horizontal axis on each graph is time (seconds)

BARIUM ADSORPTION TESTS

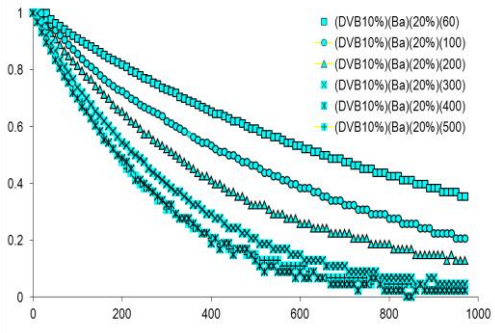

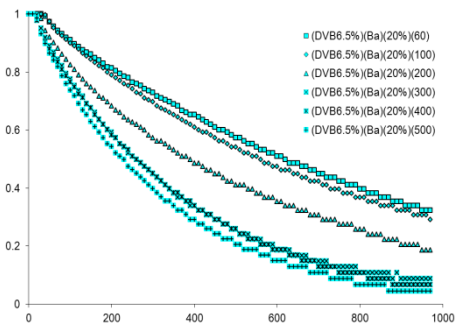

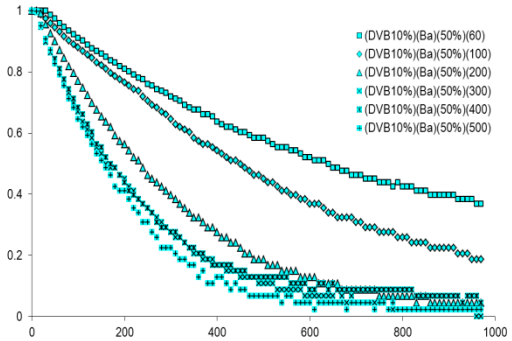

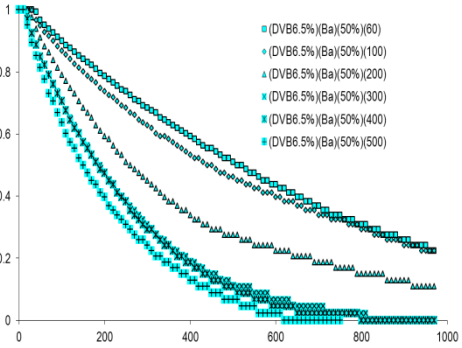

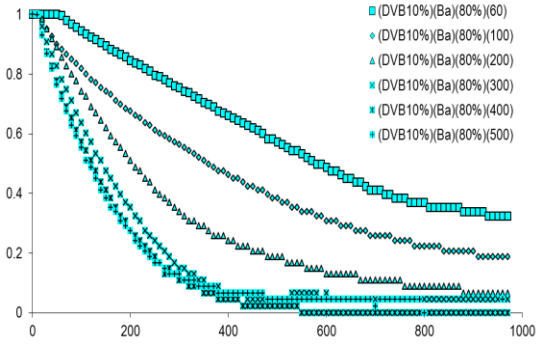

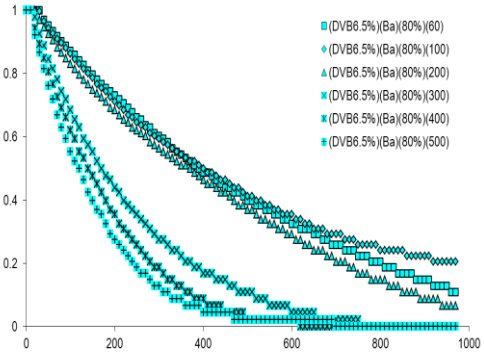

MAGNESIUM ADSORPTION TESTS

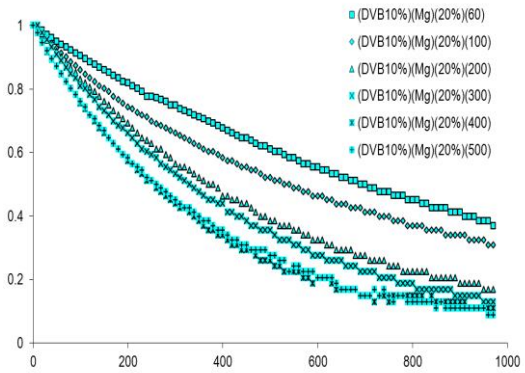

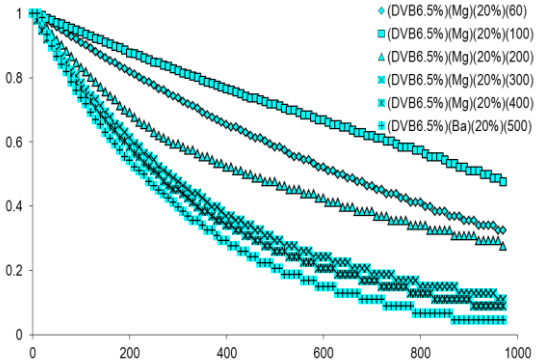

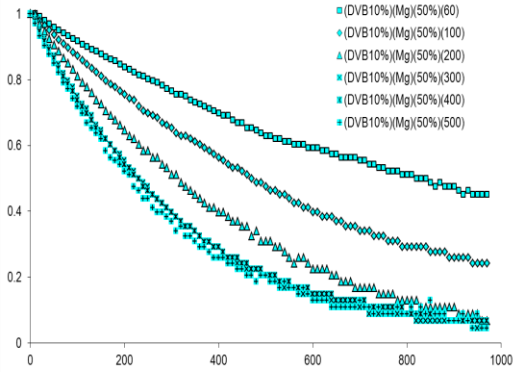

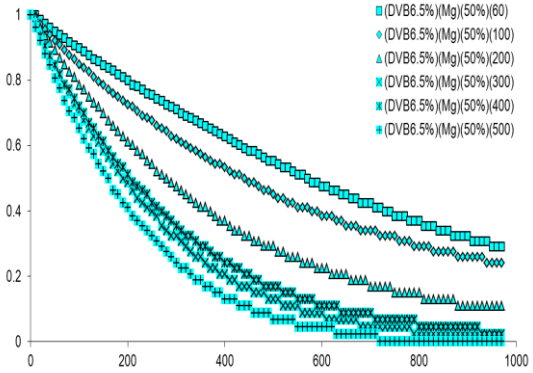

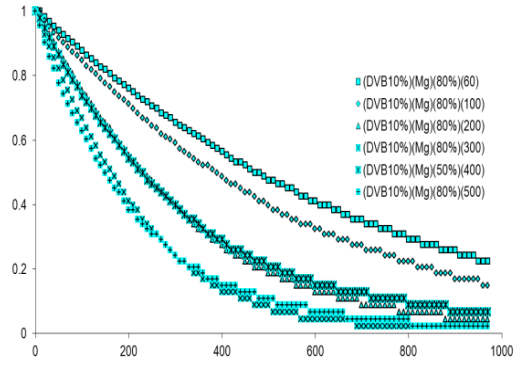

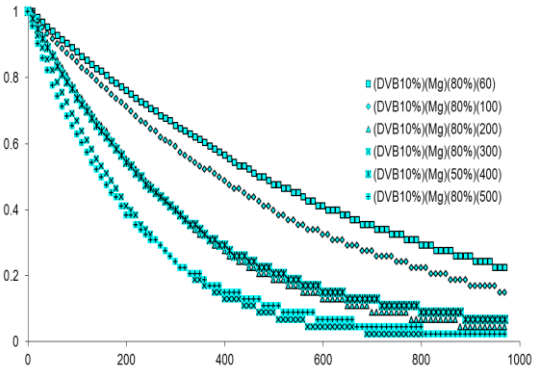

SODIUM ADSORPTION TESTS

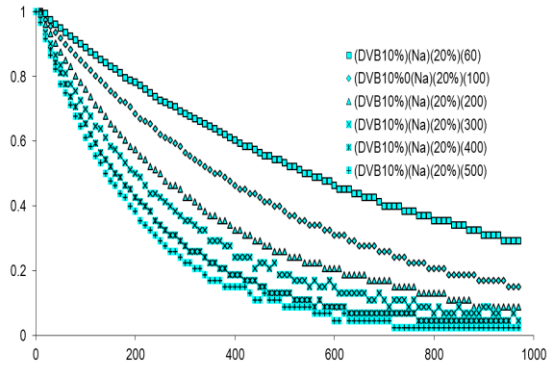

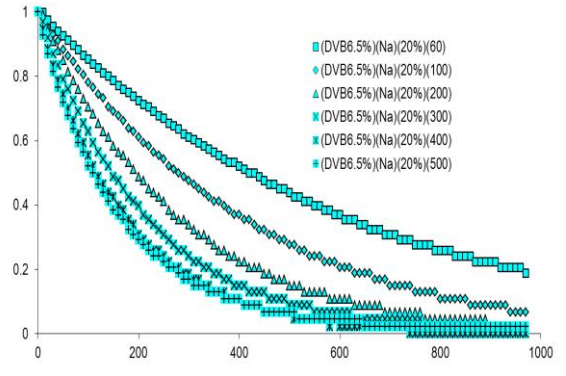

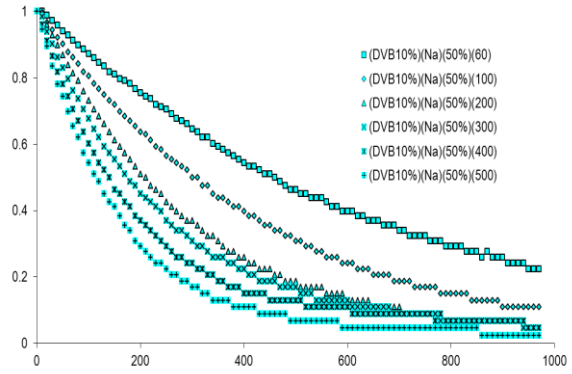

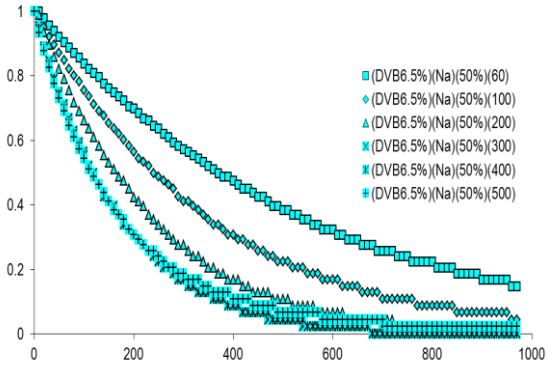

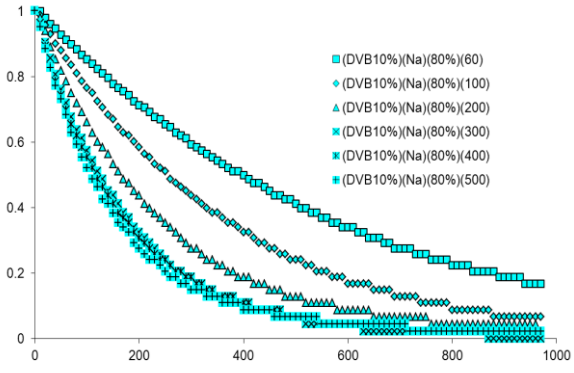

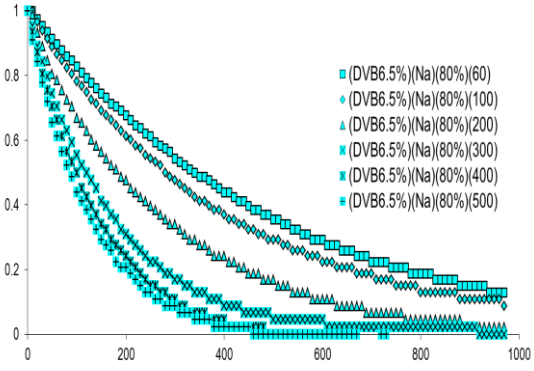

CALCULATED AND MODEL DATA, FRESH RESIN

Where

Re	Reynolds No.
K_L	Mass transfer coefficient
Sc	Schmidt No.
Sh	Sherwood No.
Data	Calculated from Laboratory measurement (Early time data method)
Ka	Model predicted (Kataoka *et al*, 1973)
D&U	Model predicted (Dwivedi & Upadhyay, 1977)
N&M	Model prediction (Nesbitt & Matukela)

(DVB6.5%)(Ba)(20%)							
Linear vel.	***Re***	K_L	***Sc***	***Sh***	***Sh***	***Sh***	***Sh***
dm/s		***m/s***		Data	Ka	D&U	N&M
5.04×10^{-2}	4.0	3.37×10^{-5}	1095	29.6	47.8	23.1	21.1
8.31×10^{-2}	6.6	3.45×10^{-5}	1130	30.8	56.8	30.2	28.3
1.74×10^{-1}	14.2	6.16×10^{-5}	1052	52.8	71.7	46.2	40.7
2.59×10^{-1}	20.3	8.40×10^{-5}	1141	75.2	83.1	59.5	53.2
3.52×10^{-1}	28.2	8.05×10^{-5}	1095	70.5	91.4	72.7	61.5
4.47×10^{-1}	34.1	9.29×10^{-5}	1209	85.8	100.7	85.5	74.2

(DVB6.5%)(Ba)(50%)							
5.00×10^{-2}	3.8	3.28×10^{-5}	1215	30.4	48.6	23.3	22.3
8.44×10^{-2}	6.8	3.90×10^{-5}	1073	33.8	56.6	30.3	27.7
1.72×10^{-1}	13.4	6.40×10^{-5}	1159	57.8	72.8	46.2	42.9
2.60×10^{-1}	20.9	8.32×10^{-5}	1090	72.7	82.5	59.6	51.9
3.55×10^{-1}	28.2	7.81×10^{-5}	1107	68.8	91.8	73.1	62.2
4.52×10^{-1}	40.0	9.69×10^{-5}	881	75.5	95.5	85.9	62.4

(DVB6.5%)(Ba)(80%)							
4.88×10^{-2}	4.1	3.06×10^{-5}	995	25.5	46.5	22.6	19.6
8.55×10^{-2}	7.4	3.08×10^{-5}	925	24.7	55.3	30.2	25.6
1.74×10^{-1}	14.7	4.23×10^{-5}	971	34.8	70.7	46.0	38.9
2.61×10^{-1}	21.6	7.98×10^{-5}	1020	67.3	81.6	59.6	50.1
3.51×10^{-1}	28.2	9.34×10^{-5}	1090	81.6	91.2	72.6	61.3
4.49×10^{-1}	37.0	11.1×10^{-5}	1025	93.9	97.9	85.6	67.8

(DVB6.5%)(Mg)(20%)							
Linear vel.	***Re***	***K_L***	***Sc***	***Sh***	***Sh***	***Sh***	***Sh***
dm/s		***m/s***		Data	Kataoka	D&U	N&M
$4.88x10^{-2}$	3.9	$2.64x10^{-5}$	1315	27.7	50.2	24.2	24.0
$8.40x10^{-2}$	6.9	$1.51x10^{-5}$	1225	15.3	59.4	32.0	31.1
$1.74x10^{-1}$	13.9	$5.34x10^{-5}$	1315	56.0	76.8	49.2	48.5
$2.65x10^{-1}$	22.2	$6.56x10^{-5}$	1189	65.2	86.7	63.9	57.7
$3.53x10^{-1}$	30.1	$7.24x10^{-5}$	1137	70.3	94.6	77.0	65.9
$4.47x10^{-1}$	38.9	$10.1x10^{-5}$	1089	96.2	101.6	90.3	73.2

(DVB6.5%)(Mg)(50%)							
$4.88x10^{-2}$	4.0	$2.39x10^{-5}$	1219	24.1	49.5	24.0	23.0
$8.40x10^{-2}$	6.7	$3.09x10^{-5}$	1328	32.6	60.3	32.2	32.6
$1.74x10^{-1}$	14.5	$5.22x10^{-5}$	1200	52.2	75.4	48.8	46.0
$2.70x10^{-1}$	23.2	$7.20x10^{-5}$	1121	69.3	86.4	64.6	56.4
$3.62x10^{-1}$	28.7	$8.02x10^{-5}$	1342	85.1	98.3	78.7	73.5
$4.48x10^{-1}$	34.3	$8.84x10^{-5}$	1436	97.3	106.8	90.8	85.8

(DVB6.5%)(Mg)(80%)							
$4.94x10^{-2}$	4.0	$2.68x10^{-5}$	1295	27.9	50.3	24.3	24.0
$8.58x10^{-2}$	6.7	$3.89x10^{-5}$	1370	41.7	61.1	32.6	33.6
$1.78x10^{-1}$	14.4	$5.79x10^{-5}$	1275	59.8	76.9	49.7	48.2
$2.70x10^{-1}$	22.2	$7.47x10^{-5}$	1231	75.7	87.8	64.7	59.5
$3.63x10^{-1}$	30.5	$9.70x10^{-5}$	1177	95.9	96.1	78.6	68.3
$4.60x10^{-1}$	36.7	$11.0x10^{-5}$	1315	115.4	106.1	92.4	82.8

(DVB6.5%)(Na)(20%)							
$8.74x10^{-2}$	7.2	$4.82x10^{-5}$	654	26.0	48.9	26.6	19.0
$1.78x10^{-1}$	14.4	$7.09x10^{-5}$	688	39.3	62.5	40.5	28.9
$2.72x10^{-1}$	22.7	$8.42x10^{-5}$	635	44.7	70.9	52.8	34.8
$3.62x10^{-1}$	28.8	$9.82x10^{-5}$	706	55.2	79.5	63.8	43.3
$4.66x10^{-1}$	38.0	$11.8x10^{-5}$	671	64.2	85.7	75.7	48.4

(DVB6.5%)(Na)(50%)							
$4.99x10^{-2}$	4.0	$3.02x10^{-5}$	706	17.0	41.1	19.9	14.5
$8.69x10^{-2}$	7.2	$1.67x10^{-5}$	657	9.0	48.8	26.5	19.0
$1.79x10^{-1}$	14.5	$6.75x10^{-5}$	681	37.2	62.5	40.5	28.8
$2.70x10^{-1}$	22.5	$8.79x10^{-5}$	641	46.9	70.9	52.5	34.9
$3.64x10^{-1}$	29.4	$8.77x10^{-5}$	684	48.5	79.2	64.1	42.7
$4.62x10^{-1}$	38.6	$8.81x10^{-5}$	635	46.8	84.6	75.2	46.7

(DVB6.5%)(Na)(80%)							
Linear vel.	***Re***	***K_L***	***Sc***	***Sh***	***Sh***	***Sh***	***Sh***
dm/s		***m/s***		Data	Kataoka	D&U	N&M
4.97×10^{-2}	4.0	2.95×10^{-5}	702	16.5	41.0	19.8	14.5
8.39×10^{-2}	6.7	3.68×10^{-5}	698	20.6	48.8	26.1	19.2
1.74×10^{-1}	13.4	5.44×10^{-5}	759	31.8	63.1	40.1	30.2
2.62×10^{-1}	20.6	8.37×10^{-5}	728	47.8	71.8	51.7	36.9
3.51×10^{-1}	26.5	8.96×10^{-5}	787	53.4	80.2	62.7	45.3
4.51×10^{-1}	35.1	10.3×10^{-5}	743	59.5	86.4	74.2	50.4

(DVB10%)(Ba)(20%)							
4.86×10^{-2}	3.4	3.71×10^{-5}	1190	30.4	46.2	21.7	20.4
8.51×10^{-2}	6.1	6.17×10^{-5}	1084	48.2	54.8	28.7	26.3
1.73×10^{-1}	11.9	4.72×10^{-5}	1209	39.1	70.8	43.4	41.4
2.56×10^{-1}	16.6	7.74×10^{-5}	1368	68.5	82.4	55.5	55.2
3.50×10^{-1}	23.8	8.07×10^{-5}	1228	67.4	89.8	67.6	61.7
4.44×10^{-1}	29.3	9.85×10^{-5}	1310	85.1	98.2	79.2	72.9

(DVB10%)(Ba)(50%)							
5.00×10^{-2}	3.5	2.70×10^{-5}	1184	22.1	46.6	22.0	20.7
8.52×10^{-2}	6.3	3.95×10^{-5}	1010	29.7	54.1	28.6	25.3
1.73×10^{-1}	12.3	8.52×10^{-5}	1118	67.7	69.8	43.3	39.7
2.63×10^{-1}	19.1	11.0×10^{-5}	1062	1.0	79.5	56.0	48.5
3.57×10^{-1}	24.6	12.7×10^{-5}	1190	104.6	89.8	68.4	61.2
4.47×10^{-1}	31.7	13.9×10^{-5}	1118	110.7	95.7	79.3	66.9

(DVB10%)(Ba)(80%)							
5.10×10^{-2}	3.6	3.20×10^{-5}	1101	25.2	46.3	22.1	20.0
9.70×10^{-2}	6.3	5.97×10^{-5}	1338	52.2	59.4	31.4	31.9
1.76×10^{-1}	11.3	8.06×10^{-5}	1383	71.7	72.9	44.1	45.1
2.63×10^{-1}	17.1	12.6×10^{-5}	1360	110.9	83.1	56.5	55.9
3.56×10^{-1}	26.1	3.56×10^{-5}	1046	27.3	87.8	68.1	56.8
4.47×10^{-1}	30.5	17.2×10^{-5}	1222	143.6	97.3	79.4	70.3

(DVB10%)(Mg)(20%)							
5.01×10^{-2}	3.4	2.64×10^{-5}	1491	26.6	49.9	23.5	24.7
8.38×10^{-2}	6.3	3.70×10^{-5}	1171	32.7	56.8	30.0	28.6
1.70×10^{-1}	11.8	7.25×10^{-5}	1399	71.0	74.2	45.4	46.6
2.58×10^{-1}	16.7	6.69×10^{-5}	1625	70.4	87.6	59.1	64.0
3.51×10^{-1}	23.9	9.90×10^{-5}	1467	98.7	95.3	71.8	71.6
4.40×10^{-1}	29.6	8.17×10^{-5}	1498	82.4	103.2	83.5	82.0

(DVB10%)(Mg)(50%)							
Linear vel.	***Re***	***K_L***	***Sc***	***Sh***	***Sh***	***Sh***	***Sh***
dm/s		***m/s***		Data	Kataoka	D&U	N&M
4.84×10^{-2}	3.3	1.94×10^{-5}	1498	20.0	49.4	23.1	24.3
8.29×10^{-2}	5.8	3.92×10^{-5}	1363	37.6	58.2	30.2	31.0
1.70×10^{-1}	11.6	5.96×10^{-5}	1475	59.6	75.0	45.6	48.2
2.59×10^{-1}	18.6	7.55×10^{-5}	1315	71.1	84.5	58.9	56.9
3.52×10^{-1}	24.4	8.46×10^{-5}	1414	82.7	94.8	71.9	70.2
4.42×10^{-1}	31.0	9.52×10^{-5}	1370	91.5	101.7	83.6	78.1

(DVB10%)(Mg)(80%)							
5.05×10^{-2}	3.3	3.43×10^{-5}	1625	36.1	50.9	23.8	26.0
8.37×10^{-2}	5.4	5.50×10^{-5}	1625	58.0	60.2	30.7	34.4
1.73×10^{-1}	11.2	7.37×10^{-5}	1625	78.0	76.7	46.3	51.3
2.62×10^{-1}	17.0	8.65×10^{-5}	1625	91.1	88.1	59.7	64.6
3.52×10^{-1}	22.2	4.51×10^{-5}	1716	48.0	98.1	72.2	78.3
4.39×10^{-1}	30.3	8.20×10^{-5}	1421	80.5	102.1	83.3	79.5

(DVB10%)(Na)(20%)							
4.86×10^{-2}	3.4	3.62×10^{-5}	759	18.9	39.8	18.7	14.1
8.41×10^{-2}	5.9	4.68×10^{-5}	735	24.1	47.5	24.7	18.7
1.72×10^{-1}	12.8	7.41×10^{-5}	647	35.6	58.9	36.9	25.7
2.64×10^{-1}	19.1	9.10×10^{-5}	684	45.1	68.6	48.3	33.7
3.48×10^{-1}	24.8	9.74×10^{-5}	709	49.2	75.8	57.9	40.1
4.43×10^{-1}	32.1	9.74×10^{-5}	684	48.3	81.6	68.0	44.8

(DVB10%)(Na)(50%)							
4.58×10^{-2}	3.6	2.83×10^{-5}	559	12.6	36.9	17.6	11.4
8.54×10^{-2}	6.6	4.75×10^{-5}	604	22.0	46.1	24.6	16.8
1.72×10^{-1}	12.9	6.54×10^{-5}	628	31.0	58.6	36.9	25.3
2.62×10^{-1}	20.6	8.32×10^{-5}	573	37.5	66.3	47.8	30.3
3.54×10^{-1}	28.0	8.41×10^{-5}	567	37.7	73.2	58.3	35.6
4.51×10^{-1}	35.8	12.0×10^{-5}	559	55.2	79.2	68.6	40.3

(DVB10%)(Na)(80%)							
4.88×10^{-2}	3.6	2.44×10^{-5}	667	11.9	38.9	18.5	13.1
8.45×10^{-2}	6.2	3.67×10^{-5}	667	17.9	46.7	24.6	17.7
1.76×10^{-1}	13.2	5.68×10^{-5}	632	26.9	59.1	37.4	25.7
2.59×10^{-1}	19.3	7.78×10^{-5}	647	37.4	67.6	47.7	32.3
3.57×10^{-1}	26.1	8.24×10^{-5}	671	40.4	75.6	58.8	39.3
4.51×10^{-1}	32.7	8.43×10^{-5}	681	41.6	82.0	68.8	45.1

CALCULATED AND MODEL DATA, AGED RESIN

	(DVB10,Old)(Na)(20%)					
	Linear vel.	***Re***	***K_L***	***Sc***	***Sh***	***Sh***
	dm/s	Data	***m/s***	Data	Data	N&M
	4.47×10^{-2}	3.2	2.57×10^{-5}	1085	20	24
	2.52×10^{-1}	18.4	7.97×10^{-5}	1055	61	56
	4.38×10^{-1}	31.8	8.76×10^{-5}	1061	68	74
	(DVB10,Old)(Na)(50%)					
	4.34×10^{-2}	3.1	2.74×10^{-5}	1067	21	23
	2.50×10^{-1}	18.3	6.75×10^{-5}	1043	52	56
	4.35×10^{-1}	33.7	8.46×10^{-5}	927	61	69
	(DVB10,Old)(Na)(80%)					
	4.35×10^{-2}	2.6	3.13×10^{-5}	844	16	18
	2.52×10^{-1}	14.6	8.29×10^{-5}	937	45	46
	4.40×10^{-1}	26.6	9.92×10^{-5}	849	51	57
	(DVB10,Old)(Mg)(20%)					
	4.42×10^{-2}	2.5	3.81×10^{-5}	1912	41	33
	2.55×10^{-1}	14.4	9.77×10^{-5}	1859	102	78
	4.40×10^{-1}	24.8	10.3×10^{-5}	1859	108	103
	(DVB10,Old)(Mg)(50%)					
	4.41×10^{-2}	2.3	4.00×10^{-5}	1827	38	31
	2.60×10^{-1}	13.6	8.47×10^{-5}	1827	81	75
	4.34×10^{-1}	22.6	10.8×10^{-5}	1827	103	97
	(DVB10,Old)(Mg)(80%)					
	4.41×10^{-2}	2.1	3.12×10^{-5}	1827	27	29
	2.57×10^{-1}	12.2	9.46×10^{-5}	1827	82	71
	4.42×10^{-1}	20.9	9.68×10^{-5}	1827	84	93

ANNEXURE VIII EQUILIBRIUM DATA

Equilibrium data from 6.5% & 10% dvb fresh resin

(All equilibrium test work results associated with section *5.4*)

Barium adsorption tests

Adsorption of Ba^{2+} onto

6.5% DVB resin		10% DVB resin	
Solution	Resin	Solution	Resin
0.000	0.000	0.000	0.000
0.008	0.111	0.021	0.107
0.016	0.171	0.017	0.169
0.018	0.321	0.030	0.305
0.057	0.455	0.017	0.508
0.010	0.694	0.093	0.702
0.165	0.756	0.134	0.831
0.228	0.895	0.233	0.878
0.299	0.946	0.310	0.903
0.280	0.973	0.373	0.928
0.360	0.973	0.444	0.928
0.406	0.973	0.478	0.980
0.448	0.973	0.516	0.980
0.583	0.973	0.556	0.980
1.000	1.000	1.000	1.000

Magnesium adsorption tests

Adsorption of Mg^{2+} onto

6.5% DVB resin		10% DVB resin	
Solution	Resin	Solution	Resin
0.000	0.000	0.000	0.000
0.004	0.111	0.019	0.109
0.024	0.167	0.019	0.171
0.048	0.296	0.050	0.294
0.068	0.443	0.070	0.437
0.149	0.591	0.135	0.617
0.188	0.707	0.195	0.687
0.258	0.795	0.273	0.752
0.331	0.842	0.327	0.842
0.388	0.867	0.525	0.939
0.455	0.892	0.641	0.9721
0.491	0.918	1.000	1.000
0.529	0.918		
0.649	0.918		
1.000	1.000		

Sodium adsorption tests

Adsorption of Na^{+} onto

6.5% DVB resin		10% DVB resin	
Solution	Resin	Solution	Resin
0.089	0.186	0.109	0.180
0.161	0.257	0.175	0.249
0.262	0.371	0.251	0.377
0.333	0.471	0.326	0.480
0.446	0.557	0.425	0.583
0.492	0.614	0.484	0.626
0.544	0.686	0.545	0.686
0.588	0.743	0.589	0.746
0.621	0.800	0.630	0.780
0.669	0.829	0.679	0.809
0.719	0.786	0.709	0.814
0.734	0.829	0.732	0.831
0.809	0.857	0.806	0.874
1.000	1.000	1.000	1.000

ANNEXURE IX FILE NAMING NOMENCLATURE

With the generation of a large number of files of data resulting from the kinetic test work the necessity to develop a file naming nomenclature became apparent. It also made further processing by software more systematic with the suffix changing each time a new file was written. The nomenclature is as follows;

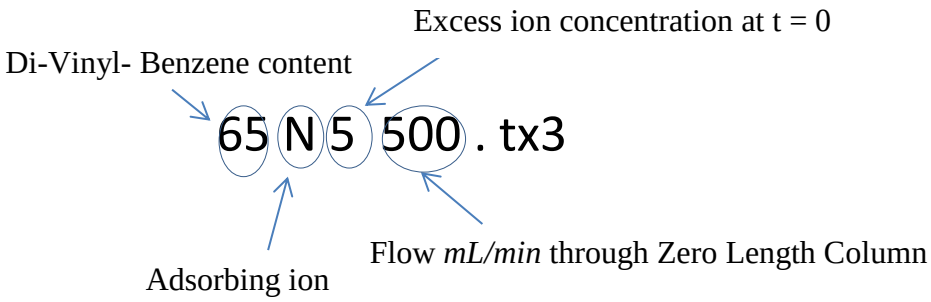

Prefix, Breakdown of the nomenclature for each data set

- The first numerical notations described the starting DVB content of the ion exchange e.g. resin, 10 (10%), 8 (8%) , 65 (6.5%)
- The second notation indicated the ion being adsorbed N (Na), M (Mg), B (Ba)
- The third numerical notation indicated the percentage excess of ions present in the closed circuit 2 (20%), 5 (50%), 8 (80%)
- The fourth notation indicated the volumetric flow rate in the circuit
  60 (60 *mL/min*), 100 (100 *mL/min*), 200 (200 *mL/min*), 300 (300 *mL/min*) etc…

Suffix, Four stages of processing

- **DAT** Raw data file
- **CON** Pre-fitting file
- **TX3** Final fitted simulation output file

ANNEXURE X AGING RESIN DATA

Associated with section *6.4* measured data and fitted model simulations

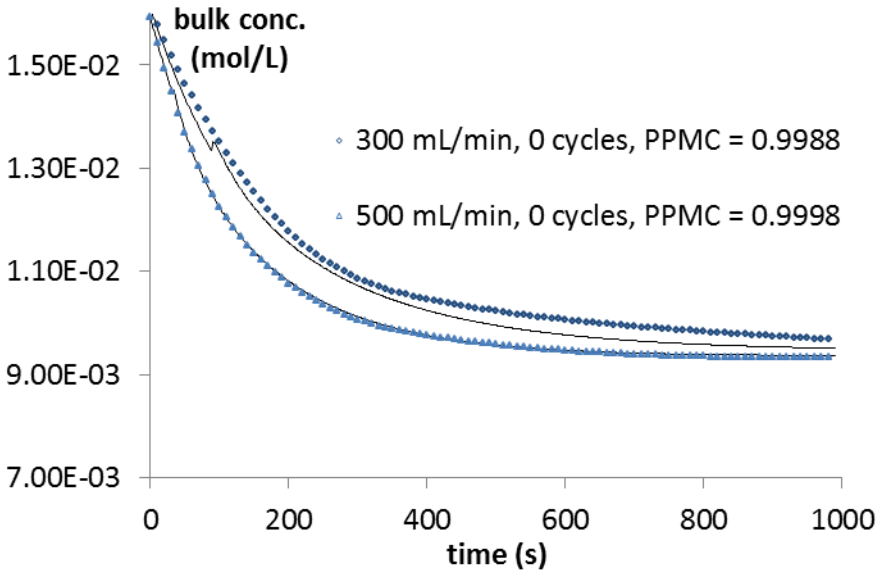

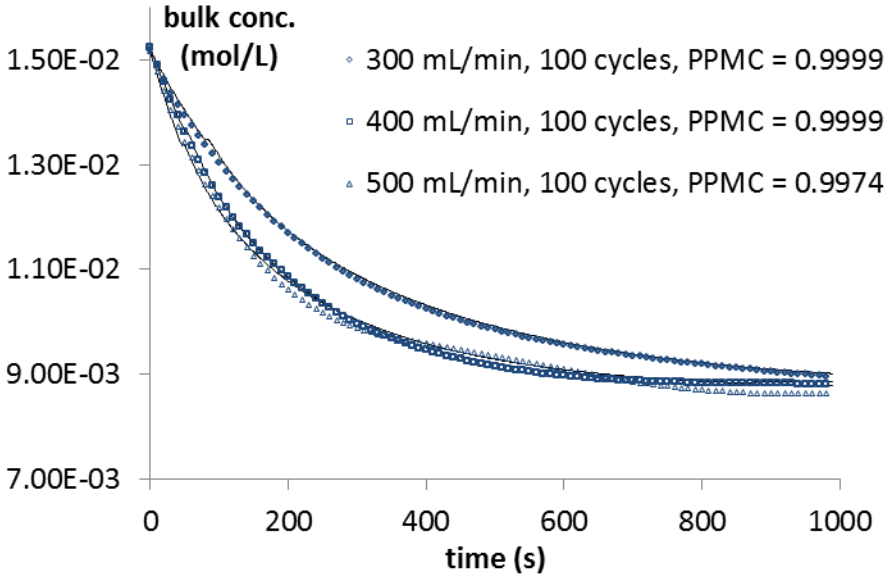

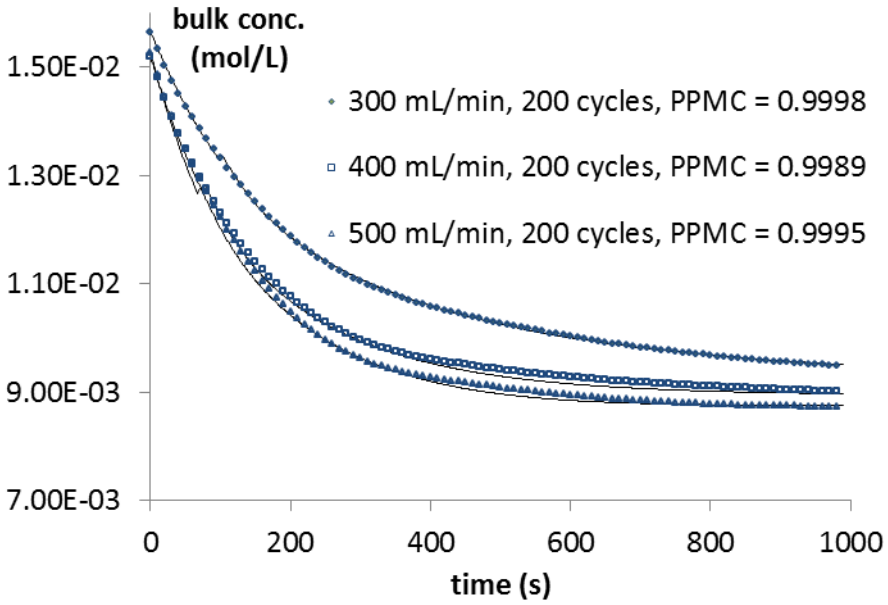
bulk conc.
(mol/L)
1.50E-02
1.30E-02
1.10E-02
9.00E-03
7.00E-03
0
200
400
600
800
1000
time (s)
300 mL/min, 200 cycles, PPMC = 0.9998
400 mL/min, 200 cycles, PPMC = 0.9989
500 mL/min, 200 cycles, PPMC = 0.9995

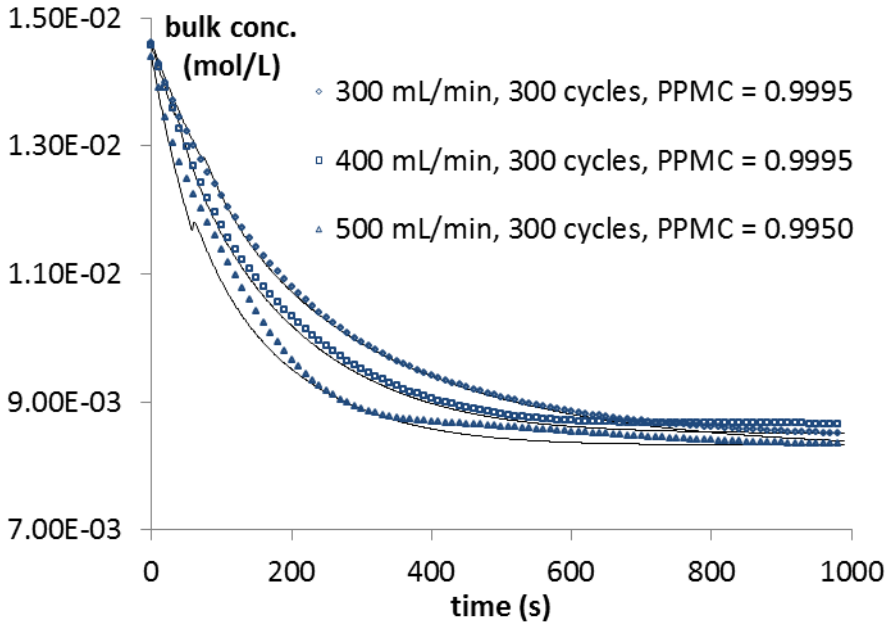
bulk conc.
(mol/L)
1.50E-02
1.30E-02
1.10E-02
9.00E-03
7.00E-03
0
200
400
600
800
1000
time (s)
300 mL/min, 300 cycles, PPMC = 0.9995
400 mL/min, 300 cycles, PPMC = 0.9995
500 mL/min, 300 cycles, PPMC = 0.9950

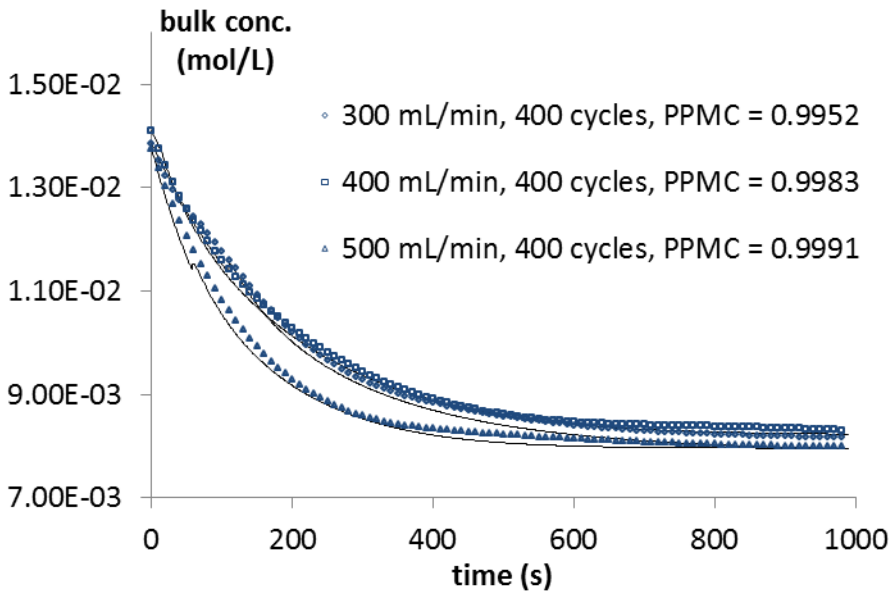
bulk conc. (mol/L)
1.50E-02
1.30E-02
1.10E-02
9.00E-03
7.00E-03
0
200
400
600
800
1000
time (s)
300 mL/min, 400 cycles, PPMC = 0.9952
400 mL/min, 400 cycles, PPMC = 0.9983
500 mL/min, 400 cycles, PPMC = 0.9991

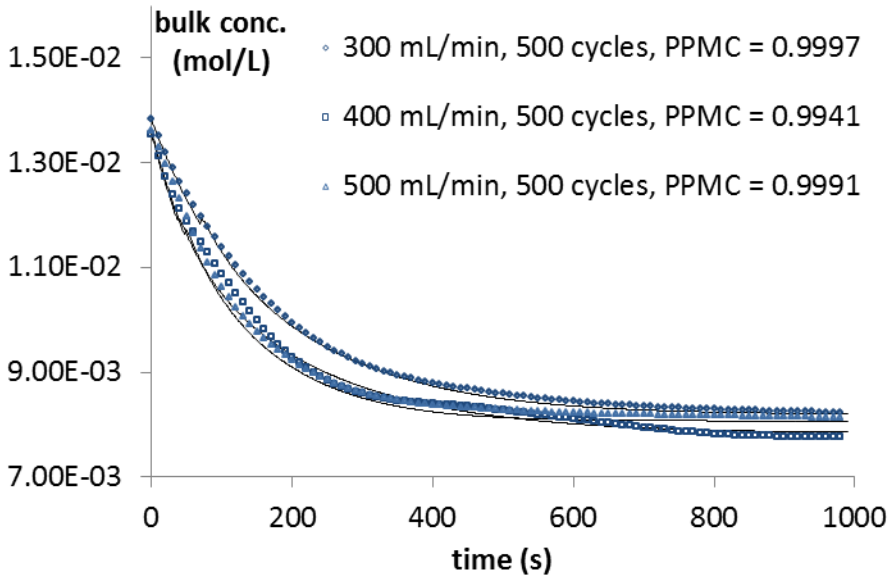
bulk conc. (mol/L)
1.50E-02
1.30E-02
1.10E-02
9.00E-03
7.00E-03
0
200
400
600
800
1000
time (s)
300 mL/min, 500 cycles, PPMC = 0.9997
400 mL/min, 500 cycles, PPMC = 0.9941
500 mL/min, 500 cycles, PPMC = 0.9991

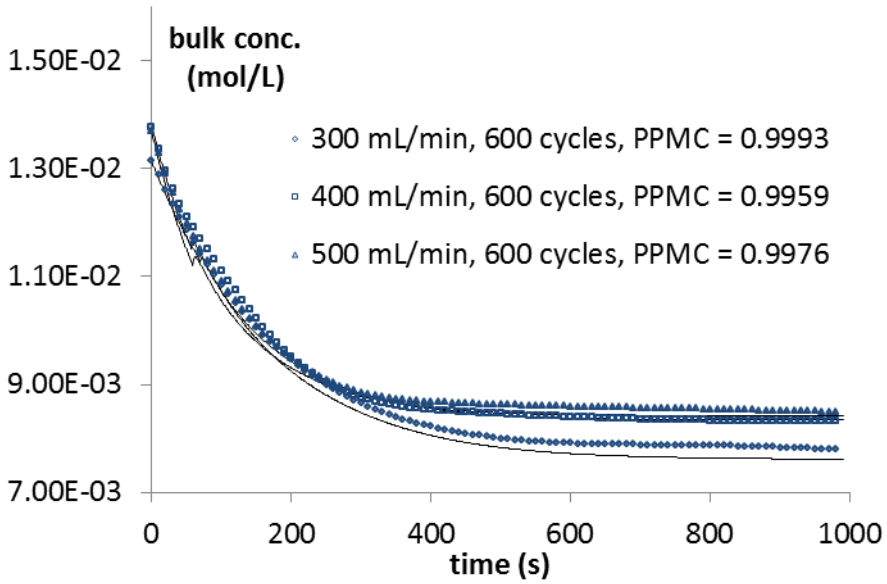
bulk conc.
(mol/L)
1.50E-02
1.30E-02
1.10E-02
9.00E-03
7.00E-03
300 mL/min, 600 cycles, PPMC = 0.9993
400 mL/min, 600 cycles, PPMC = 0.9959
500 mL/min, 600 cycles, PPMC = 0.9976
0
200
400
600
800
1000
time (s)

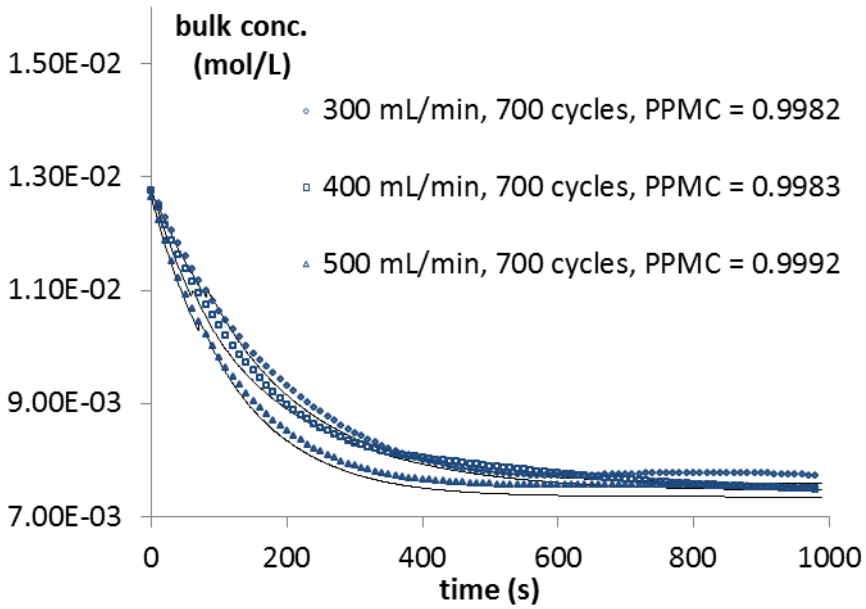
bulk conc.
(mol/L)
1.50E-02
1.30E-02
1.10E-02
9.00E-03
7.00E-03
300 mL/min, 700 cycles, PPMC = 0.9982
400 mL/min, 700 cycles, PPMC = 0.9983
500 mL/min, 700 cycles, PPMC = 0.9992
0
200
400
600
800
1000
time (s)

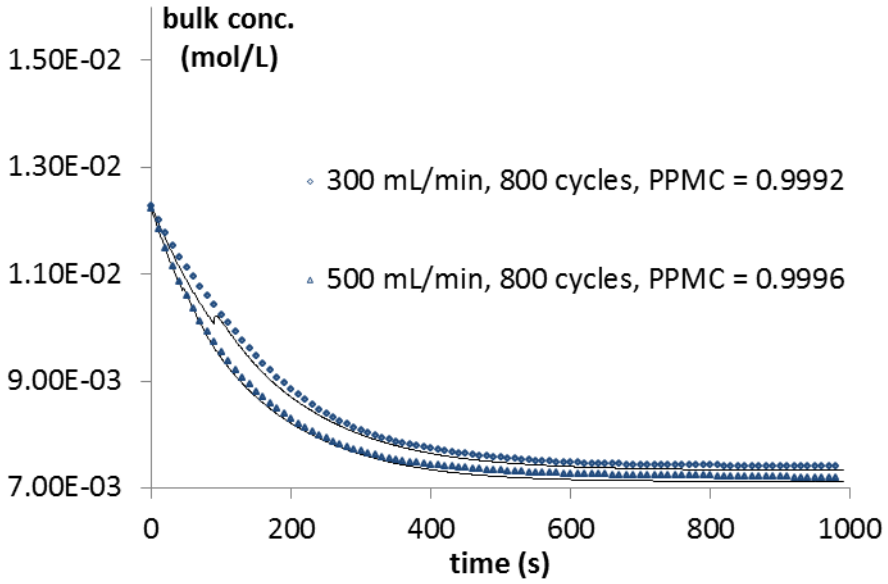
bulk conc.
(mol/L)
1.50E-02
1.30E-02
1.10E-02
9.00E-03
7.00E-03
300 mL/min, 800 cycles, PPMC = 0.9992
500 mL/min, 800 cycles, PPMC = 0.9996
0
200
400
600
800
1000
time (s)

ANNEXURE XI ACCURATE MEASUREMENT OF DIFFUSIVITY

Simulation fitted to data to accurately measure mass transfer coefficients.
The full set of mass transfer coefficients ($\boldsymbol{K_L}$) and intra particle diffusivities ($\overline{D_i}$) for each simulation presented in this annexure are given in Table 5-2a&b.

As explained in section *5.11* a matrix of eighteen tests was undertaken incorporating three DVB contents (6.5%, 8.0% 10.0%) of fresh resins, three ZLC through flowrates (300, 400, 500 *mL/min*) and two starting concentration excesses (50% and 80%). Only the Na^+ ion was used in each adsorption with H^+ desorbing.

The first set of graphs show the data and fitted-bulk-concentration simulation achieved for each test. In addition to giving the concentration in the bulk solution of the finite system the amount Na^+ ions in solution are presented on the secondary vertical axis, as a percentage of the ion capacity of the resin present in the ZLC.

The second set of graphs is the full simulation achieved after the fitting algorithm had completed the fitting process to the raw data and incorporates the change in concentration in each internal shell through the transient.

6.5% DVB content resin

<u>50% excess</u> <u>80% excess</u>

With 300 *mL/min* flow

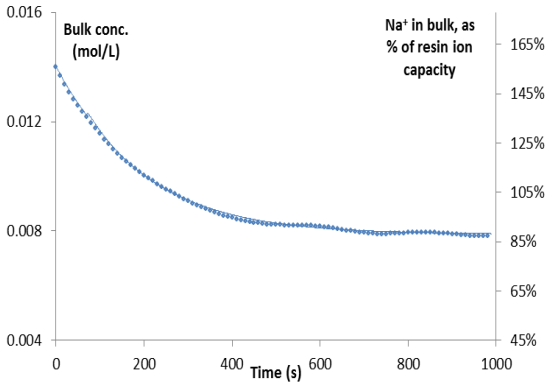

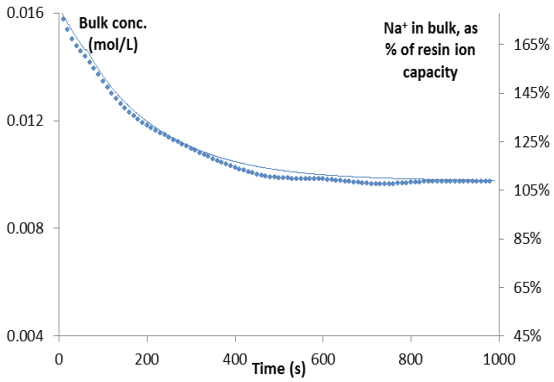

400 *mL/min* flow through

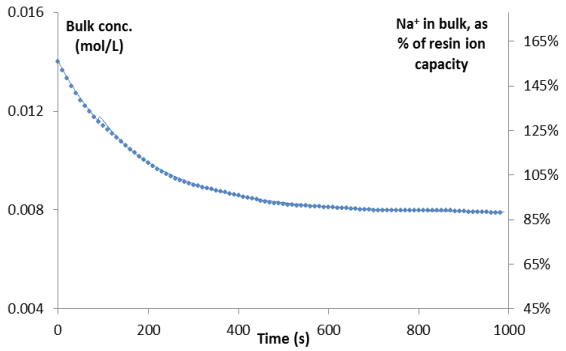

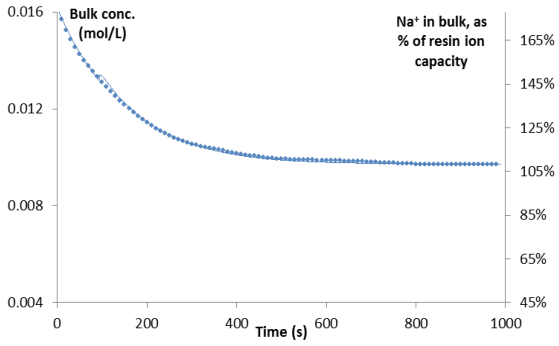

500 *mL/min* flow through

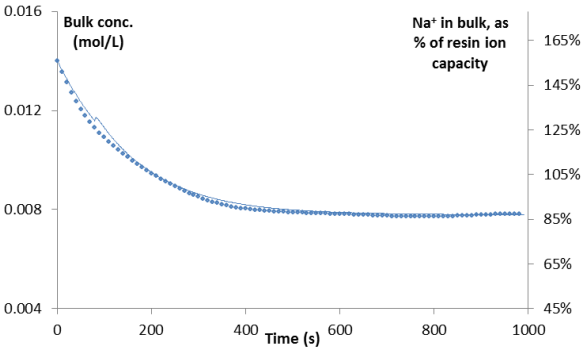

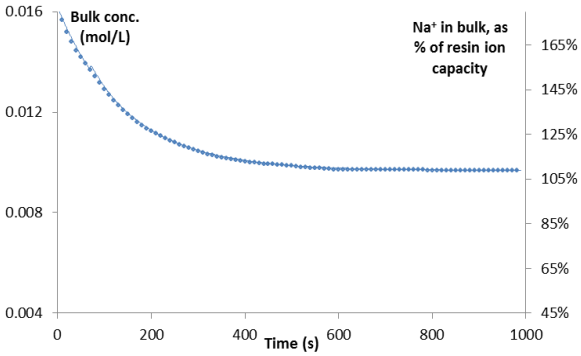

8.0% DVB content resin

50% excess

80% excess

300 *mL/min* flow through

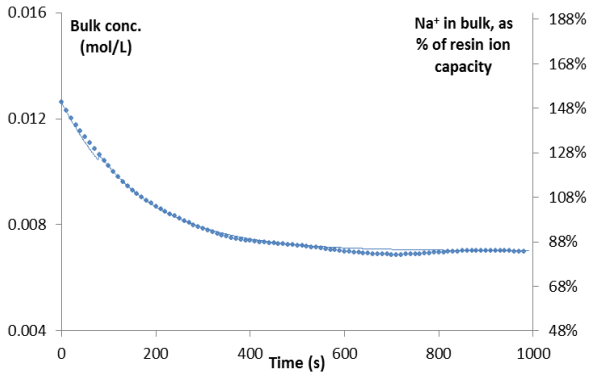

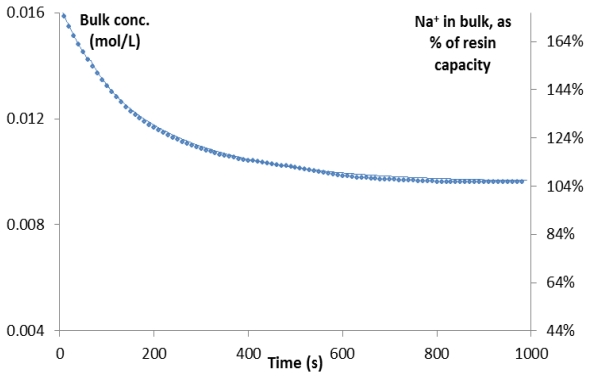

400 *mL/min* flow through

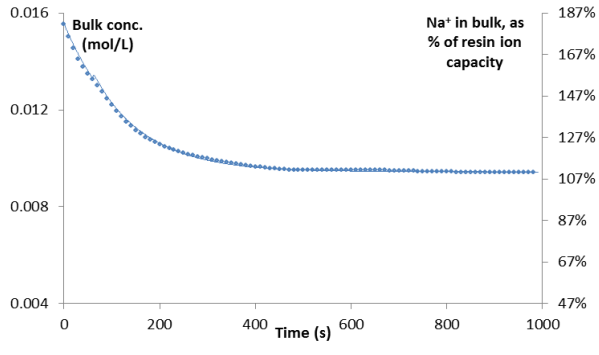

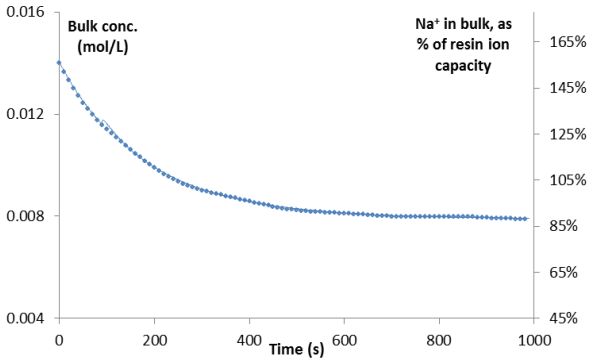

500 *mL/min* flow through

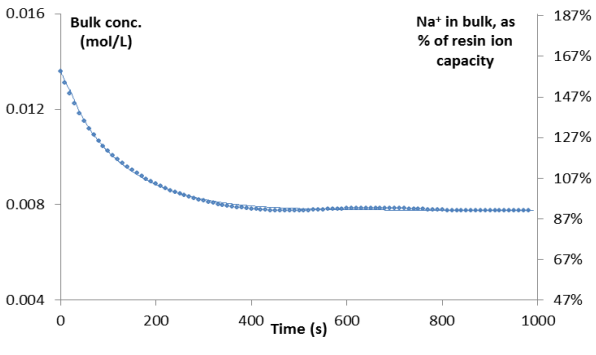

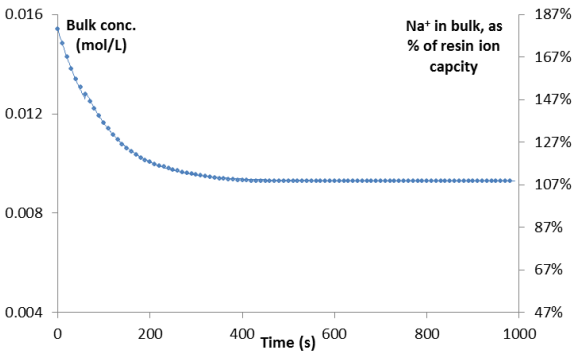

10.0% DVB content resin

50% excess

80% excess

300 *mL/min* flow through

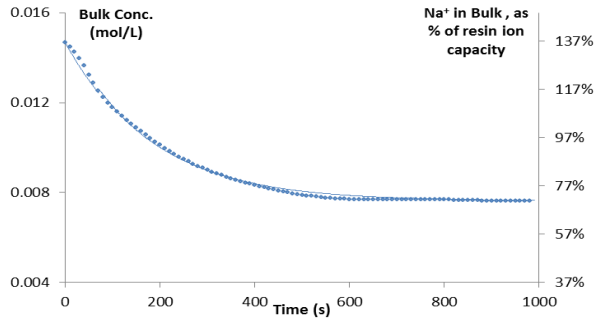

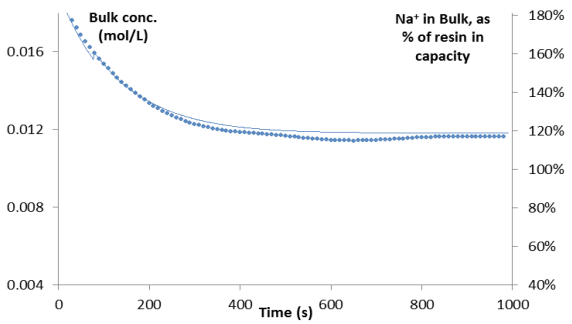

400 *mL/min* flow through

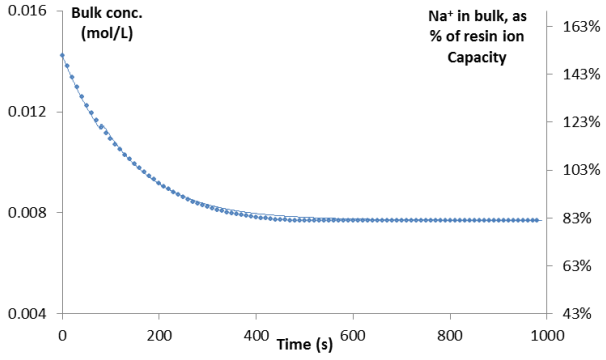

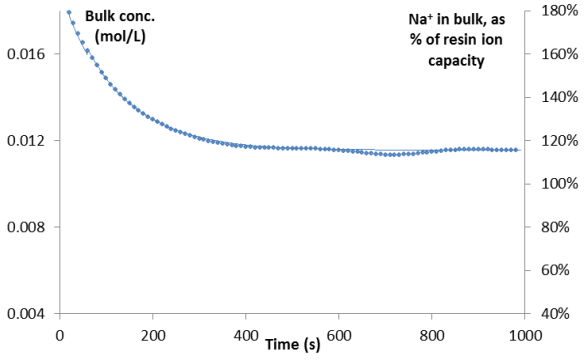

500 *mL/min* flow through

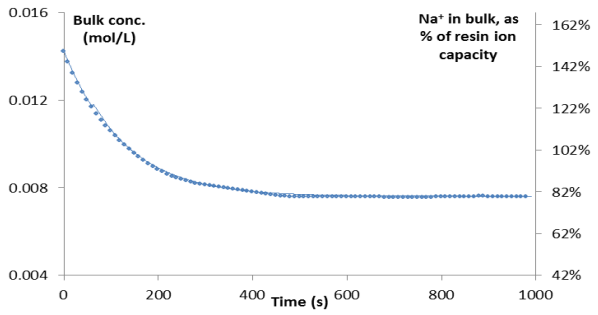

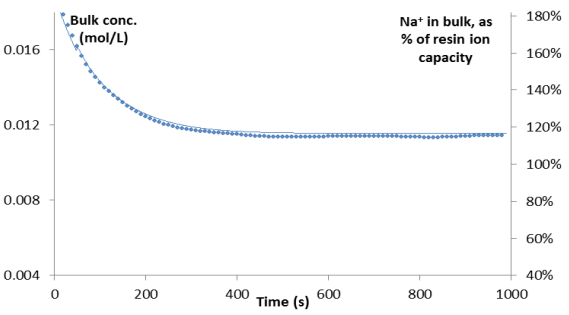

This next section shows the full simulations of each fit to raw data and the change in concentrations inside the resin begins with Fig5-14, which explains the various parts of the simulation and the axes. The left vertical axis is the concentration inside the resin bead and the right axis the concentration in the bulk. The horizontal axis is time. The multiple parallel curvy lines display the concentrations in each of the twenty five concentric shells of each resin bead with the extreme outer shell converting the quickest and the inner taking the longest to convert.

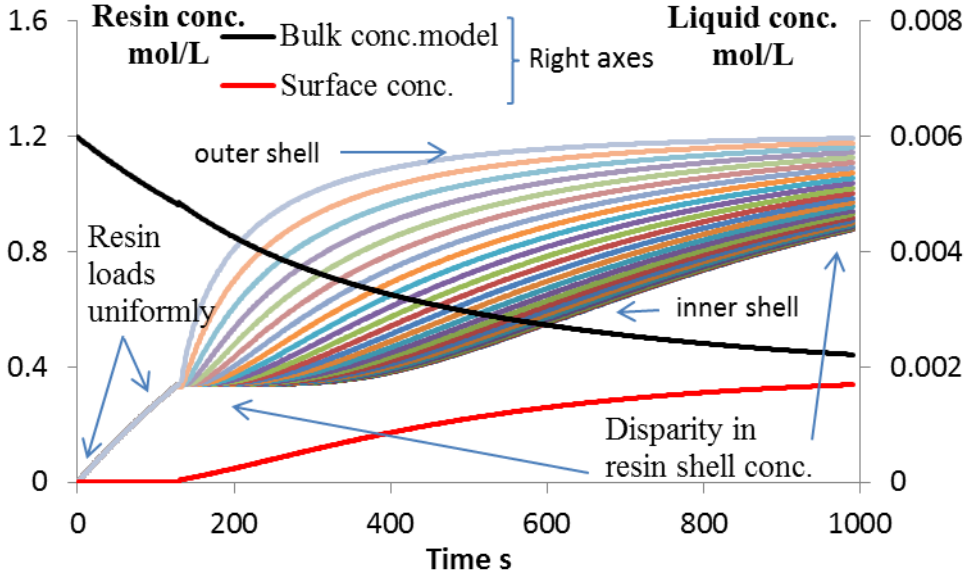

Fig. 5-14 Magnesium adsorption and fitted dynamic model

6.5% DVB content resin

50% excess

80% excess

300 *mL/min* flow through

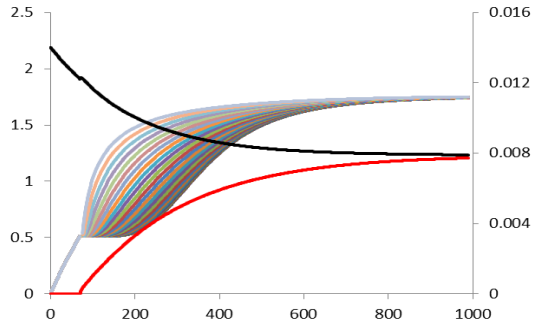

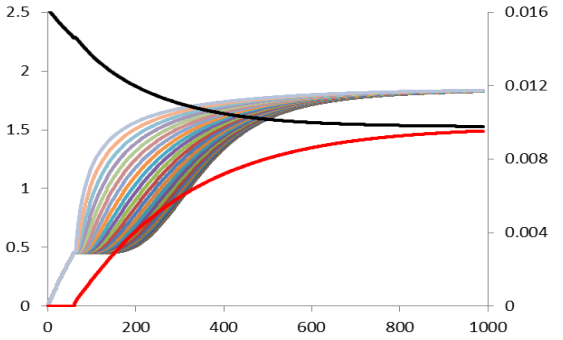

400 *mL/min* flow through

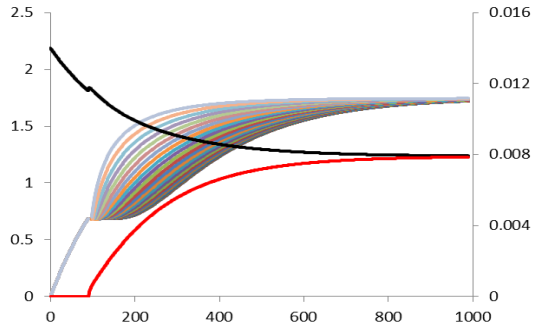

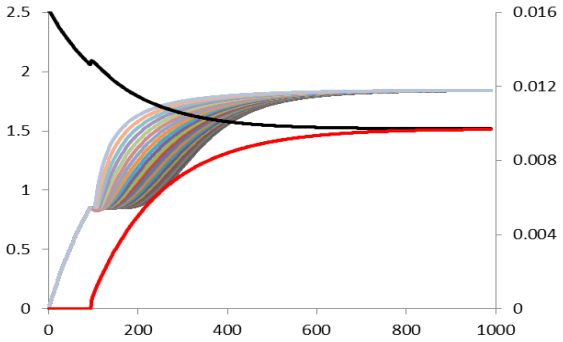

500 *mL/min* flow through

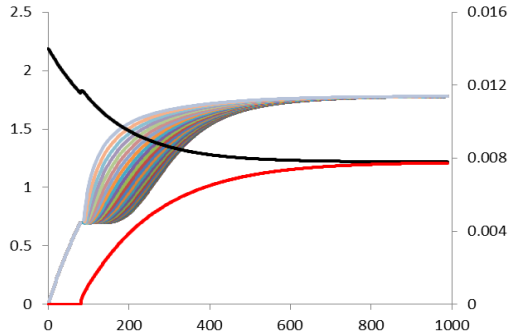

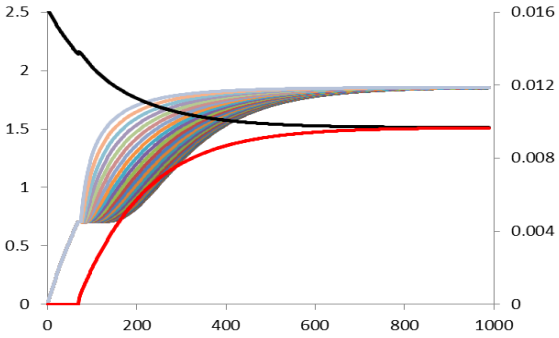

8.0% DVB content resin

50% excess

80% excess

300 *mL/min* flow through

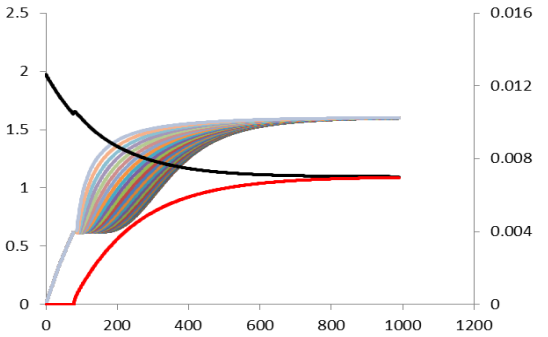

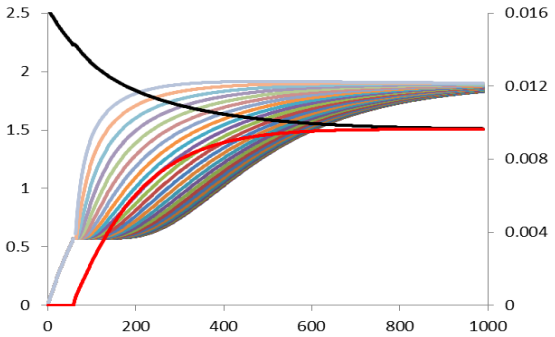

400 *mL/min* flow through

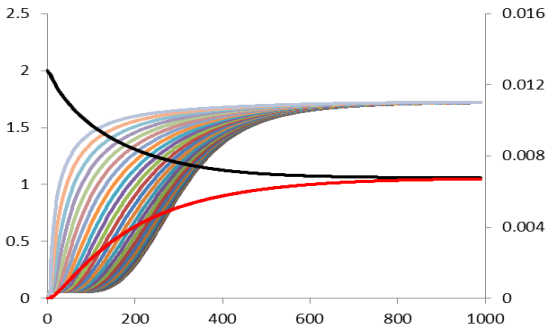

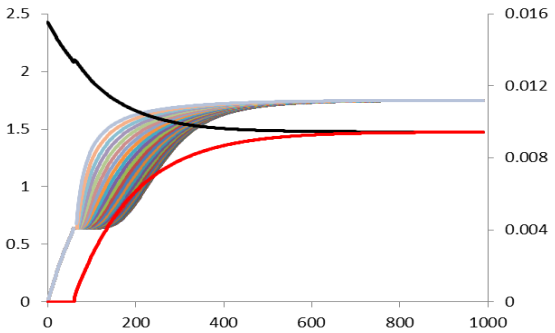

500 *mL/min* through flow

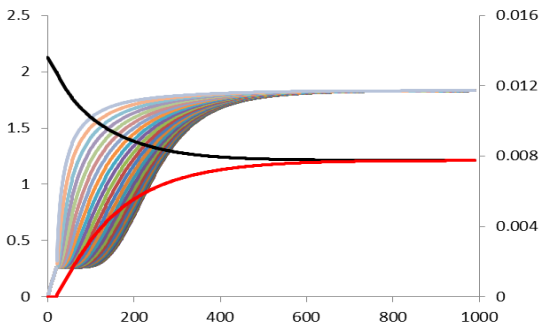

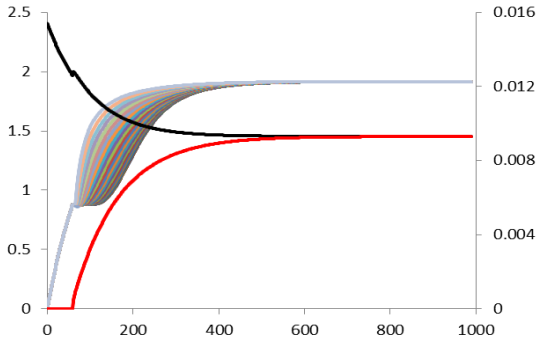

10.0% DVB content resin

50% excess

80% excess

300 *mL/min* flow through

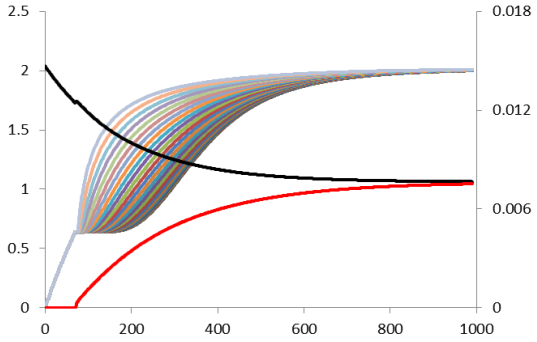

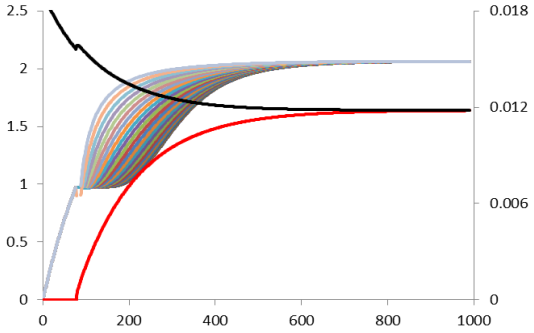

400 *mL/min* flow through

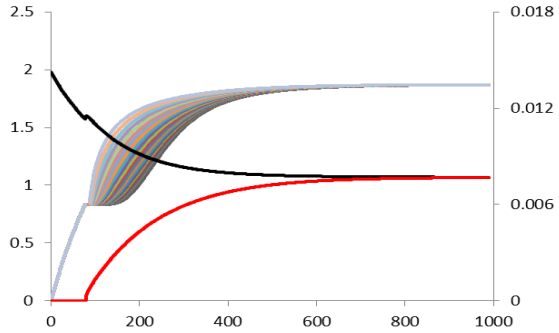

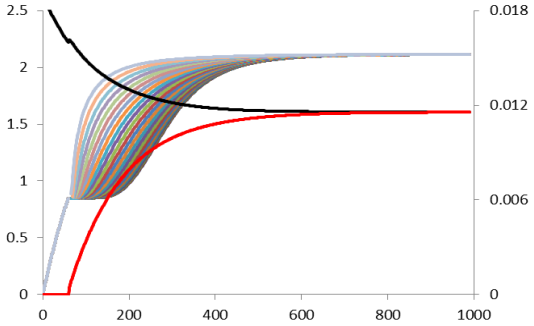

500 *mL/min* flow through

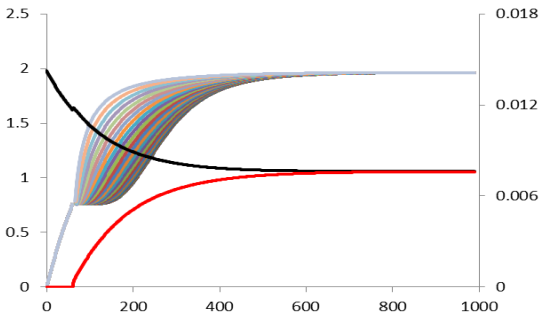

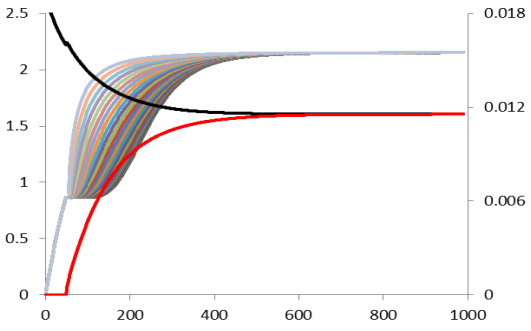

ANNEXURE XII METAL HYDROXIDE NON-PRECIPITATION

Where $\boldsymbol{Met}^{2+}$ represents the bivalent metal i.e. Ba^{2+} or Mg^{2+}, the general case for a bivalent metal gives us the stoichiometric Equ.AXII-1;

$$\boldsymbol{Met^{2+} + 2OH^{-} \Leftrightarrow Met(OH)_2} \qquad \text{AXII-1}$$

The solubility product equation for this is shown in Equ.AXII-2;

$$\boldsymbol{[Met^{2+}][OH^{-}]^2 = K_{sp}} \qquad \text{AXII-2}$$

Incorporating the dissociation of water we have Equ.AXII-3;

$$\boldsymbol{Met^{2+} \times 10^{-2(pH-14)} = K_{sp}} \qquad \text{AXII-3}$$

Finally, a general equation is given in Equ.AXII-4 which gives the relationship between pH and the solubility of the bivalent metal ($\boldsymbol{Met^{2+}}$);

$$\boldsymbol{\log[Met^{2+}] = -2\,pH + 28 + \log[K_{sp}]} \qquad \text{AXII-4}$$

Equ.5-8 and Equ.5-9 are the specific equations for **Mg^{2+}** and **Ba^{2+}** respectively and these functions are plotted in Fig.5-11, clearly showing that no hydroxide is likely to form in pH < 5.

$$\log[Mg^{2+}] = -2\,pH + 17.18 \qquad \textbf{5-4}$$

$$\log[Ba^{2+}] = -2\,pH + 25.70 \qquad \textbf{5-5}$$

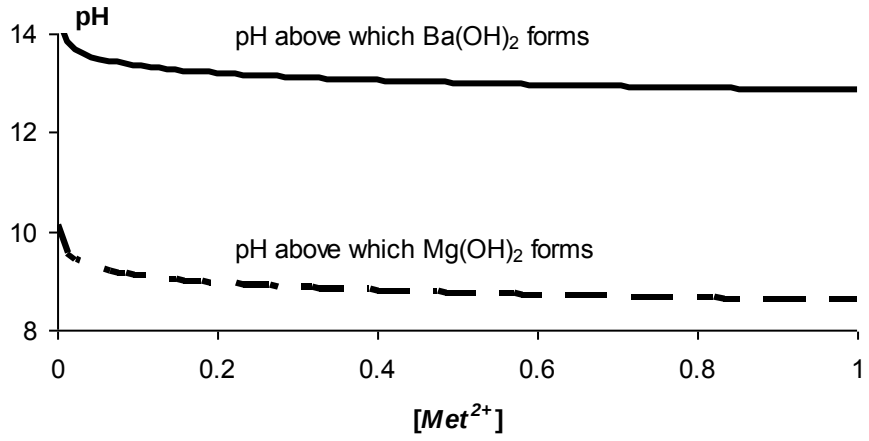

Fig.5-11 Graphical form of Equ.5-8 and Equ.5-9.